Tesis doctoral

Universidad de Granada

Programa de Doctorado en Ciencias de la Tierra

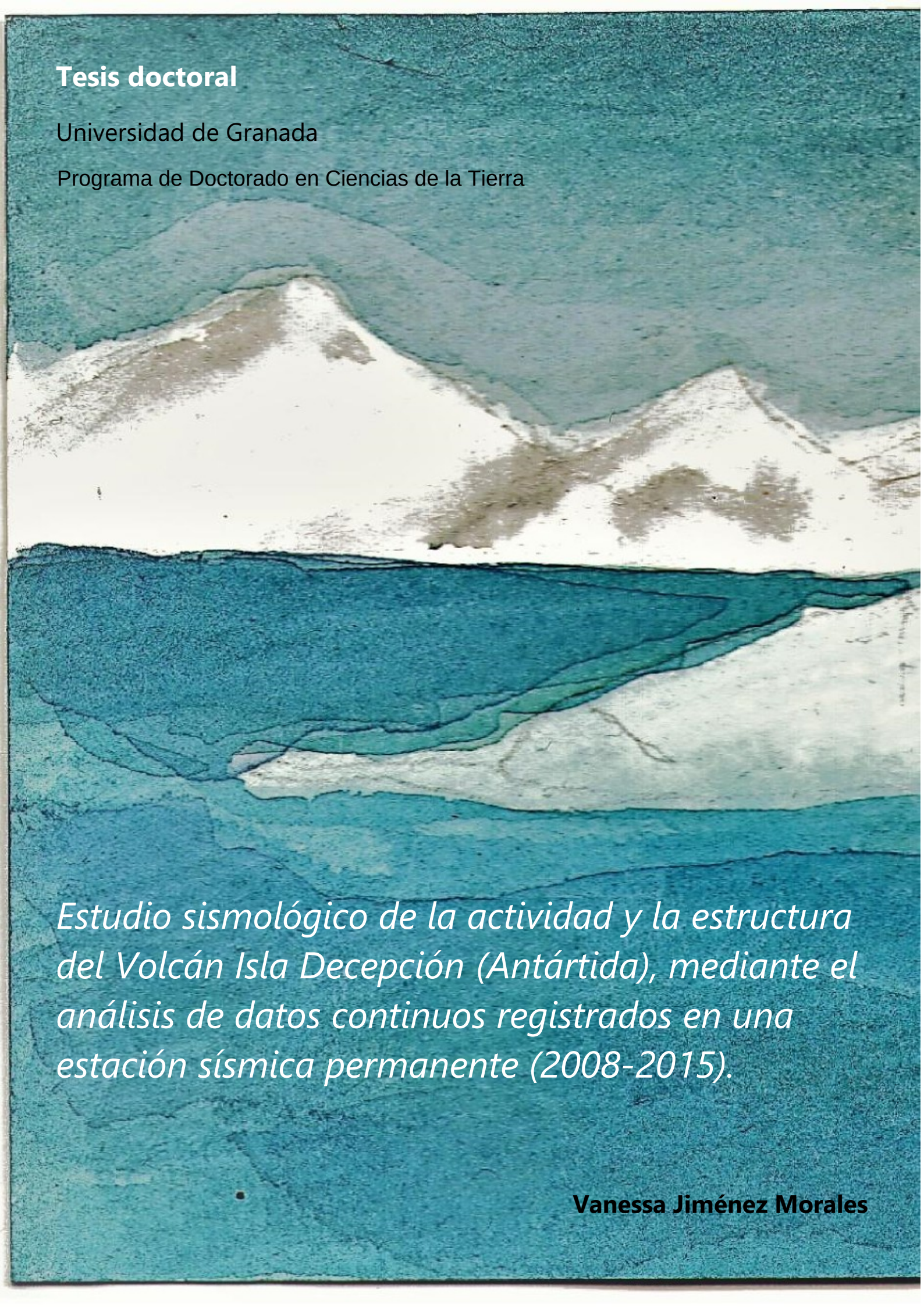

Estudio sismológico de la actividad y la estructura del Volcán Isla Decepción (Antártida), mediante el análisis de datos continuos registrados en una estación sísmica permanente (2008-2015).

Vanessa Jiménez Morales

Estudio sismológico de la actividad y la estructura del Volcán Isla Decepción (Antártida), mediante el análisis de datos continuos registrados en una estación sísmica permanente (2008-2015)

Tesis Doctoral presentada por:

Vanessa Jiménez Morales,

Doctoranda de la Universidad de Granada,
Programa de Doctorado en Ciencias de la Tierra.

Tesis Doctoral dirigida por:

Javier Almendros
Profesor Titular de la Universidad de Granada

Granada, 2021

Editor: Universidad de Granada. Tesis Doctorales
Autor: Vanessa Jiménez Morales
ISBN: 978-84-1117-226-4
URI: http://hdl.handle.net/10481/72869

A mi familia nacida y elegida

Resumen

La Isla Decepción es un volcán activo ubicado en las Islas Shetland del Sur, Antártida. Aunque las últimas erupciones ocurrieron en 1967-1970, el volcán ha experimentado períodos de crisis sísmicas en 1992, 1999 y 2015. La actividad sísmica del volcán Isla Decepción ha sido registrada durante tres meses al año desde 1986 hasta el presente, coincidiendo con el verano austral. En 2008 se instalaron tres estaciones sísmicas permanentes ubicadas en el volcán Isla Decepción (DCP), Isla Livingston y Caleta Cierva (CCV). La presente tesis ha tenido como objetivo utilizar el registro continuo en el volcán de la Isla Decepción (incluidos los períodos invernales australes) desde 2008 para estudiar la actividad sísmica a largo plazo del volcán, para mejorar nuestra comprensión del comportamiento, la sismicidad y los mecanismos que generan la actividad volcánica. Asimismo, nos permite modelar la estructura de la velocidad de las ondas S de las capas más superficiales de Decepción y determinar sus características. A partir de este estudio sismológico de la actividad y estructura del volcán Isla Decepción se ha obtenido:

(1) Un modelo 1D de la estructura poco profunda de la costa y bahía interior de la Isla Decepción. Se ha utilizado series largas de registro de ruido ambiental de diferentes estaciones terrestres y marinas desplegadas en la costa y en el interior de la bahía de Isla Decepción, con lo que se ha mejorado los estudios de ruido observando la estabilidad de los picos.

(2) Identificación de una nueva señal sísmica llamada DLDS utilizando un enfoque basado en la evaluación de la energía sísmica promedio contenido en bandas de frecuencia seleccionadas. Se necesita una cantidad suficiente de datos sísmicos durante todo el año para el análisis de DLDS debido a su larga duración y a su modulación estacional.

(3) Se distingue un enjambre precursor de VT distal al SE de la isla

Livingston que comienza cinco meses antes de la crisis sísmica registrada en Decepción en febrero de 2015.

(4) Reconocimiento de una modulación anual para algunas de las señales sísmicas de Decepción. Esta modulación anual está relacionada con el ciclo estacional y otras variaciones atmosféricas, influenciada por factores externos, que pueden inducir variaciones de presión en los fluidos volcánicos/hidrotermales, o ser un indicador de tendencias climáticas.

(5) Identificación de un aumento y aceleración de la actividad sísmica a partir del 2011 hasta la crisis sísmica registrada en Decepción en 2015.

(6) Se propone un modelo volcánico para el comportamiento del volcán Decepción durante los 7.5 años de registro continuo de DCP. El volcán empieza en un estado dormido en la fase 1 con un bajo nivel de actividad sísmica. En la fase 2 el volcán se despierta con aumento gradual de la actividad sísmica, donde se produce una intrusión magmática profunda que aumenta la cantidad de gas en el edificio volcánico. Finalmente, el volcán se inquieta en la fase 3 con una aceleración de sismicidad hasta llegar a una erupción fallida.

(7) El registro continuo de datos sísmicos en Decepción, incluso en una sola estación (DCP), permite un salto cuantitativo y cualitativo en nuestra capacidad para caracterizar y comprender el comportamiento volcánico. Por lo tanto, se enfatiza la necesidad de una red sísmica permanente en el volcán Isla Decepción para la evaluación de riesgos volcánicos.

Abstract

Deception Island is an active volcano located in the South Shetland Islands, Antarctica. Although the last eruptions occurred in 1967-1970, the volcano has undergone periods of seismic unrest in 1992, 1999, and 2015. The seismic activity of the Deception Island volcano has been monitored three months per year since 1986, coincident with the austral summers. In 2008, three permanent seismic stations were installed at Deception Island, Livingston Island, and Cierva Cove, Antarctica. The present thesis has aimed to exploit the continuous seismic record at Deception Island since 2008 (including the southern winter periods) to study the long-term seismic activity of the volcano, in order to improve our understanding of the behavior, seismicity and the mechanisms that generate the volcanic activity. It also allow us to model the S-wave velocity structure of the shallow layers of the island, as well as their characteristics. From this seismological study of the activity and structure of the Deception Island volcano, we have obtained the following results:

(1) Determination of 1D models of the shallow structure along the coast and inner bay of Deception Island. Long series of ambient noise recordings from different land and marine stations have been used, thereby improving noise studies observing the stability of the peaks.

(2) Identification of a new seismic signal called DLDS, using an approach based on the evaluation of the average seismic energy contained in selected frequency bands. Continuous records from permanent stations are used for DLDS detection. Due to its long duration and seasonal modulation, the analysis of DLDS require a sufficient amount of seismic data throughout the year.

(3) A precursory swarm of distal VT earthquakes has been identified. The

swarm occurred SE of Livingston Island, and started five months before the 2015 seismic crisis at Deception Island.

(4) Recognition of an annual modulation for part of the seismicity at Deception Island. This annual modulation is related to the seasonal cycle and other atmospheric variations, influenced by external factors, which can induce pressure variations in volcanic/hydrothermal fluids, or be an indicator of climatic trends.

(5) Identification of a generalized increase of the seismic activity, starting in 2011 and accelerating during 2011-2014, reaching a climax during the seismic crisis recorded at Deception Island in 2015.

(6) A volcanological model is proposed for the behaviour of Deception Island during the 7.5 years preceding the 2015 crisis. The volcano is in a dormant state up to 2010 (Phase 1), with a low level of seismic activity. In 2011 the activity shifts to an awakening state (Phase 2) characterized by a gradual increase in seismic activity as a consequence of a deep magmatic intrusion that increases the amount of gas permeating the volcanic edifice. Finally, in 2014-2015 the volcano becomes restless (Phase 3) and the activity accelerates, suggesting the occurrence of a failed eruption.

(7) The availability of continuous seismic data at Deception Island, even with just one station (DCP), allows for a qualitative leap in our ability to characterize and understand volcanic behaviour. This emphasizes the need for a permanent seismic network at Deception Island for the assessment of volcanic hazards.

Índice de Contenidos

Índice de Figuras

Índice de Tablas

Capítulo 1

Introducción y motivación

1.1. Descripción general

La Isla Decepción es uno de los volcanes más activos y peligrosos de la Antártida p.ej. [288, 28, 117]. Se sitúa al suroeste de la cuenca del Rift del Bransfield sobre el centro de expansión entre el archipiélago de las Shetland del Sur y la Península Antártica [128, 205] (Figura 1.1). Es una de las zonas más interesantes de la Antártida. Se encuentra en un contexto geodinámico complejo, debido a la confluencia e interacción entre diferentes unidades tectónicas de diferente escala, como son la placa Sudamericana, la placa Antártica y las microplacas de Scotia, Phoenix y Shetland del Sur [24, 107, 108, 121, 139, 183]. Además, es una de las regiones con mayor sensibilidad al cambio climático en la Antártida debido a su localización en la Antártica marítima entre el continente americano y el antártico [264].

Es un volcán activo, con más de la mitad de su superficie cubierta por glaciares (57 %), en el que actúan al mismo tiempo diferentes fenómenos, como actividad hidrotermal, emisiones fumarólicas, episodios de deformación y actividad sísmica [63, 64, 150, 291, 316]. En los últimos 200 años se han documentado varias erupciones. La primera erupción documentada data de 1842 [327] y las más recientes de 1967-1970 [290], que ampliaron y cambiaron la morfología de la isla y destruyeron dos bases antárticas, la chilena "Pedro Aguirre Cerda", y la base británica "B" [p. ej. 234, 291]. Desde entonces en la isla no se han registrado más erupciones, aunque sí se han registrado tres crisis sísmicas en 1992 [236], 1999 [150] y 2015 [10, 11].

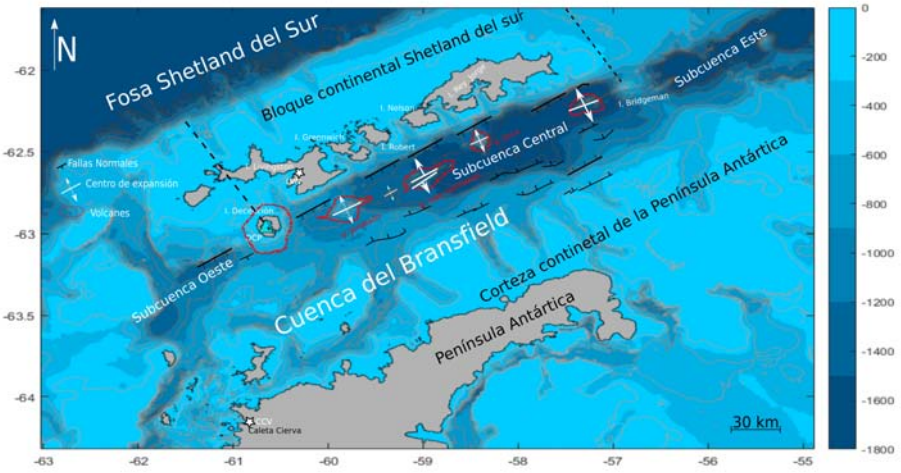

Figura 1.1: Mapa de la región de la Península Antártica y las Islas Shetland del Sur, que muestra la ubicación de la Isla Decepción en el Estrecho del Bransfield. El intervalo de contorno de batimetría (GMRT) es de 200 m. El triángulo cian representa la ubicación de la estación sísmica DCP. La estrellas blancas representan la ubicación de las estaciones sísmicas permanentes LVN y CCV.

Isla Decepción posee una caldera inundada que se abre al mar, formando un puerto natural, que proporciona refugio a las embarcaciones de las duras condiciones climatológicas de la Antártida desde su descubrimiento en 1820. Este puerto seguro se ha utilizado para la actividad comercial en el área desde finales del siglo XIX con los cazadores de lobos marinos, a través de una industria ballenera a principios de siglo XX hasta el turismo en la actualidad, convirtiéndola en el centro del comercio en la Antártida [89].

Las características geotermales de la Isla Decepción favorecen la presencia de diferentes especies de flora de alto interés ecológico (por ejemplo, musgo y líquenes). Muchas de ellas son desconocidas o raras en otra parte de la Antártida [292]. Además, la isla alberga distintas especies de fauna como son: petreles, cormoranes antárticos, págalos, gaviotas, charranes y la mayor colonia de pingüino barbijo [49, 228]. También hay lobos marinos antárticos, distintas especies de focas como las de Weddell, cangrejeras y leopardo y una gran biodiversidad marina (poliquetos, equinodermos, algas, etc.) [27].

En los últimos años Decepción se ha convertido en un laboratorio natural,

idóneo para investigar el cambio climático, la sismicidad, la geología, la flora, la fauna, así como para probar instrumentación experimental, p.ej. [114, 289, 128, 315, 78, 121, 280, 66, 40, 330, 11, 158]. A partir de estos trabajos se ha creado una amplia base de datos científicos que la convierte en una de las áreas mejor estudiadas de la Antártida sobre todo en volcanología, sismología y biodiversidad terrestre [305].

Actualmente la Isla Decepción es visitada por decenas de científicos y personal militar de apoyo, y por miles de turistas, especialmente durante el verano austral [28, 63, 117]. La actividad volcánica puede representar un riesgo para las personas e instalaciones que operan en el área además de para el tráfico marítimo y aéreo. Este hecho resalta la importancia de la vigilancia del volcán para la mitigación de riesgos. Desde 1986 hasta la actualidad, se ha estado vigilando y estudiando la actividad sísmica en la isla durante tres meses al año (verano austral). En 2008, en el marco del Año Polar Internacional, se instalaron tres estaciones sísmicas de banda ancha con carácter permanente en la zona de las Islas Shetland del Sur (Isla Decepción e Isla Livingston) y la Península Antártica (Caleta Cierva). Esto permite tener un registro continuo de la actividad sísmica del volcán Isla Decepción (incluidos los períodos de invierno austral) desde 2008 y así estudiar la evolución a largo plazo del volcán, para mejorar nuestra comprensión sobre el comportamiento, la sismicidad y los mecanismos que generan la actividad volcánica. Este es el objetivo de la presente tesis doctoral.

1.2. Contexto geológico

La Isla Decepción es un estrato-volcán situado en el extremo suroeste del Estrecho de Bransfield, una joven cuenca marginal (<1.4 Ma) [84], orientada NE-SO, de 60 km de ancho y 500 km de largo, situada entre la Península Antártica y las Islas Shetland del Sur. Este estrecho es una cuenca tras-arco formada como consecuencia de la subducción de la Placa Phoenix bajo la Placa Antártica durante el mesozoico-cenozoico superior

[84], y la interacción con el movimiento hacia el oeste del límite de la Placa Scotia-Antártica [121]. El Estrecho del Bransfield está constituido por tres subcuencas adyacentes y caracterizado por presencia de fallas norma-

les y vulcanismo activo [249, 152, 272]. La mayor parte de los terremotos localizados en la región son superficiales (<40 km) [249]. Se han identificado algunos terremotos a profundidades intermedias al noroeste de las Islas Shetland del Sur, lo que es consistente con la subducción de la Placa de Drake [152]. Muchos de estos terremotos poco profundos se agrupan alrededor de centros volcánicos, lo que sugiere que probablemente tienen un origen volcánico o volcano-tectónico, desencadenado por la actividad magmática intrusiva [94, 272]. Estos centros volcánicos los conforman las Islas Decepción, Penguin, Bridgeman y una serie de volcanes sumergidos que están asociados con el centro de extensión del rift del Bransfield (Figura 1.1).

1.2.1. Características geológicas y estructurales de la Isla Decepción

Isla Decepción es un joven estrato-volcán con un diámetro basal que alcanza los 30 km sumergidos [289, 199] y 15 km de diámetro de la zona emergida, limitado en todo su perímetro externo por acantilados verticales de roca y hielo [290] (Figura 1.2). Posee un estrecho canal en el SO llamado Fuelles de Neptuno que da acceso a su caldera inundada (Puerto Foster) de unas dimensiones de 6x10 km y una profundidad de 180 m en el centro y 50 m en los Fuelles de Neptuno. El volcán se eleva ∼1400 m del fondo del marino hasta una altura máxima de 540 m (Monte Pond) sobre el nivel del mar. La edad aproximada de la isla no está clara. Birkenmajer et al. [46] proponen una edad de terciario superior (Eoceno) en base a las observaciones de nanofósiles. Shultz [287] y Keller et al. [170] consideran que el volcán se construyó en los últimos 0,2 Ma, a partir de dataciones radiométricas de algunas rocas. Valencio et al. [311] y Baraldo et al. [23] señalan que todas las rocas expuestas tienen polaridad magnética normal (Período de Brunhes), lo que indica que es menor de 0.75 Ma. Esta conclusión también es compartida por Martí et al. [205] basados en los estudios de estratigrafía y petrología. Los nuevos datos paleomagnéticos en combinación con el estudio de tefra realizados por Oliva-Urcia et al. [232] sugieren que las rocas expuestas de la pre-caldera datan de > 12000 años A.C., que para el colapso de la caldera se data 8300 años A.C., y para las unidades post-caldera de 2000 años A.C.

Antoniades et al. [15] indican que la edad más probable para el evento de formación de caldera es de unos 3980 A.C. según los estudios de sedimentología, tefrocronología y de carbono 14.

Las principales etapas de construcción del edificio volcánico han sido tres; pre-, sin-, y post-caldera [138, 44, 290, 205]. La primera etapa corresponde a la formación del escudo volcánico, con depósitos pre-caldera representados principalmente por el basamento no expuesto de la isla, el cual está formado por rocas basálticas, flujos de lava y diferentes tipos de depósitos estrombolianos [290, 205].

La segunda etapa corresponde al colapso de la caldera, con depósitos sin-caldera representados por la formación de Toba de la Costa Exterior (OCTF) compuesta principalmente por una secuencia gruesa de ignimbritas masivas y depósitos menores de surgencia piroclástica de composición basáltica a andesítica que forman un afloramiento casi continuo en el exterior de la isla que se extiende desde Punta Macarroni hasta el sur de Punta Entrada y alrededor y dentro de Puerto Foster [205].

La tercera etapa corresponde a la evolución desde el colapso de la caldera a la actualidad, con depósitos post-caldera representados principalmente por depósitos estrombolianos y freatomagmáticos, generados por pequeñas bocas eruptivas independientes [290].

El mecanismo de la formación de la caldera central de la isla ha sido un enigma que ha dado lugar a diversos estudios y diferentes hipótesis. (1) La caldera ha sido formada por el colapso del edificio volcánico debido a una o varias erupciones a través de fallas anulares y radiales [233, 138, 44, 45], o por los efectos de la tectónica regional sobre la geología de la isla [289, 315, 237, 290, 201, 39, 205].

(2) La caldera correspondería a una depresión no relacionada con ningún evento eruptivo y formada progresivamente por extensión pasiva (no volcánica) condicionada por el campo regional de esfuerzos a lo largo de conjuntos de fallas normales ortogonales [206, 266, 207].

Hay estudios que han demostrado la ausencia de fallas anulares y radiales [207]. Las anomalías gravimétricas y magnéticas corroboran una tendencia lineal NE-SO [237, 205]. La ubicación epicentral de la sismicidad manifiesta la existencia de fallas activas en el área de la Bahía Fumarolas, con tendencias

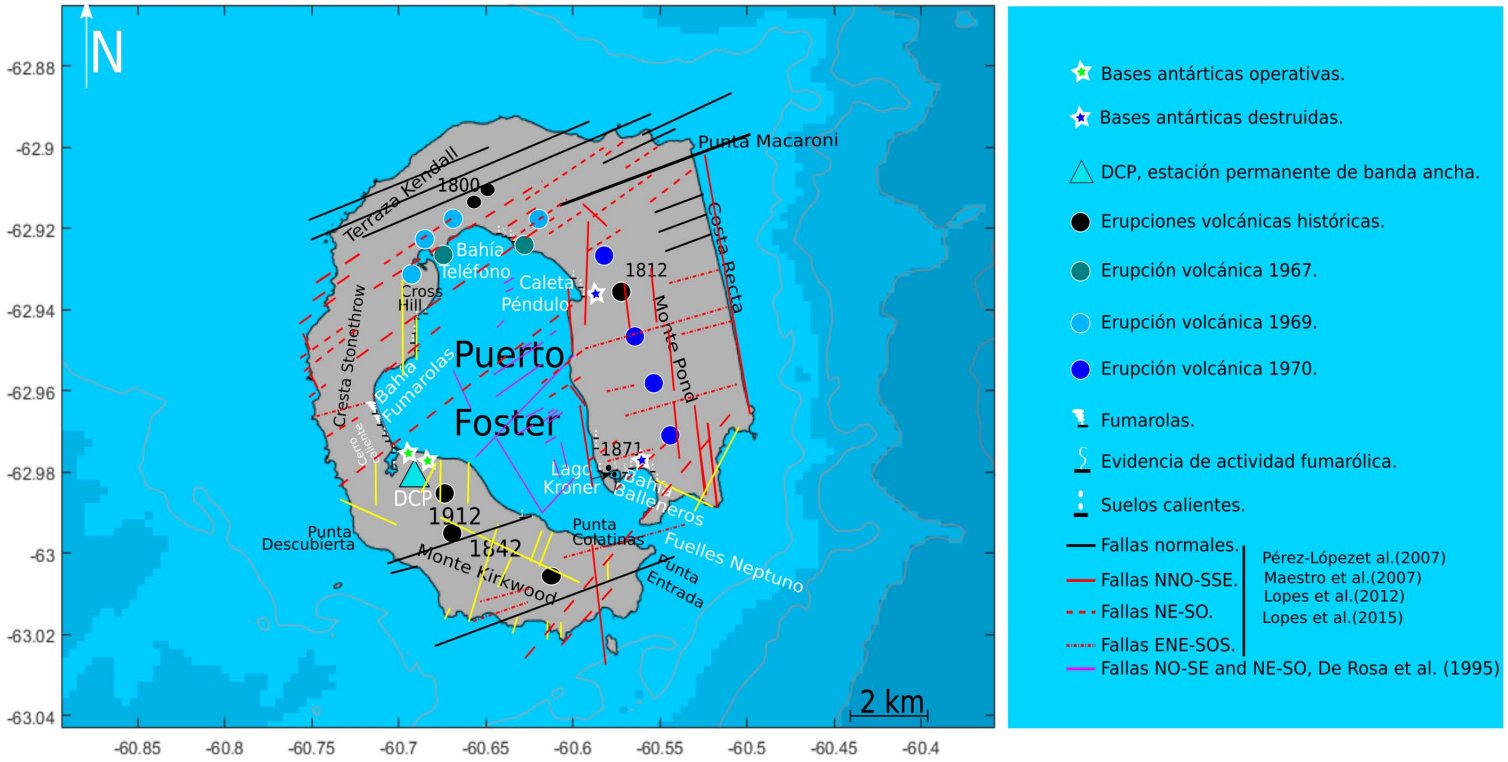

Figura 1.2: Mapa de la Isla Decepción. Disposición de las erupciones históricas y recientes. Principales sistema de fallas principales según [266, 315, 288, 201, 196, 85]. Distribución de fumarolas, suelos calientes y actividad fumarólica a partir del estudio [288]. El triángulo cian representa la ubicación de la estación sísmica DCP.

NO-SE y NE-SO coincidiendo con algunos de los sistemas de fallas principales [64]. Además, se ha demostrado la existencia de un depósito asociado a la formación de la caldera (*Outer Coast Tuff Formation*, OCTF) que podemos encontrarlo en el exterior e interior de la caldera y en otras áreas del Bransfield como la Península de Byers y en la Península Antártica [290, 205, 15]. Por ello, se considera que la formación de la caldera de la isla se debe a una gran erupción con un fuerte control tectónico regional [290, 205].

Nuevas investigaciones han descrito que el colapso de la caldera de la Isla Decepción habría ocurrido en el Holoceno, con un volumen de material eyectado de unos 30-60 km^3 e índice de explosividad volcánica (VEI) de 6 [15].

La estructura tectónica de Isla Decepción (Figura 1.2), presenta tres sistemas de fallas principales. (1) La más predominante es un conjunto de fallas orientadas NE-SO, son casi paralelas al eje de expansión del Estrecho de Bransfield [315, 266].

(2) El sistema de fallas orientado N-S, podría ser la consecuencia de la combinación del eje de expansión del Estrecho de Bransfield junto la compresión de la subducción de la fosa de las Shetland de sur [207]. (3) El sistema de fallas orientado NO-SE, localizadas dentro del borde de la caldera son dominantes en la isla y sus alrededores [266, 207].

Así Rey et al. [266] postula que las causas de las fallas normales orientadas NE-SO de las zonas profundas de la bahía (superiores a 160 m) se deben al hundimiento y la inclinación del lecho de sedimentos volcánicos localizados al N, que está relacionada con la actividad fumarólica. Además, se observa un eje volcánico en el interior de la isla compuesto por varios conos volcánicos con dirección 150°N (Figura 1.2).

La estructura interna de la Isla Decepción estimada a partir de estudios de sísmica, con fuentes tanto activas como pasivas y de correlación de ruido sísmico ambiental, permite conocer la existencia de múltiples heterogeneidades laterales de velocidad [278, 208, 330, 199, 262, 261].

Saccorotti et al. [278] demuestran la existencia de una heterogeneidad lateral de velocidad, entre el exterior y el interior de la caldera, relacionada posiblemente con el sistema de fallas que bordean la caldera y que se extienden en el interior de la isla. Los estudios de atenuación realizados por

Martínez-Arévalo et al. [208] corroboran esta heterogeneidad lateral de velocidad y ponen de manifiesto una alta atenuación y un medio muy fracturado con presencia de fluidos.

Zandomeneghi et al. [330] mencionan que hay fuertes contrastes laterales de velocidad en la isla y alrededores, muchas de ellos supeditados a las direcciones de fallas principales NO-SE y NE-SO. Asimismo, se reconoce una zona de alta velocidad al NO y SO de Isla Decepción. Bajo Puerto Foster existe una zona de baja velocidad. Además, observamos por un lado una amplia anomalía de baja velocidad localizada al Este de la isla y otra anomalía de baja velocidad que se extiende por el Oeste de la isla. La zona de baja velocidad en el interior de Puerto Foster se ha explicado por la presencia de un volumen significativo de fusión parcial, por lo que se interpreta como la existencia de una cámara de magma poco profunda, cubierta por sedimentos, que abarca desde los 2 km hasta al menos 5 km de profundidad [330, 34, 248]. Además, se determina la presencia de un cuerpo de alta atenuación debajo de la Bahía, desde la superficie hasta 4 km de profundidad [262, 261]. Prudencio et al. [262, 261] consideran que la alta atenuación de los dos primeros km dentro de la Bahía Foster, en el centro de la isla, se asocia con un medio muy fracturado con interacciones hidrotermales y depósitos piroclásticos y de sedimentos. La estructura por debajo de 2 km presenta una alta atenuación y una baja velocidad, que puede deberse tanto a la presencia de una cámara magmática como a la de un sistema hidrotermal e incluso la combinación de estos dos modelos.

Martí et al. [205] describen que la erupción formadora de la caldera habría destruido total o parcialmente la cámara magmática poco profunda al vaciarse y que es improbable que se haya creado una nueva cámara magmática única a esa profundidad, sino que se trataría de pequeños reservorios de magma. La anomalía observada en los estudios anteriores la relacionan principalmente con la alteración de las rocas por el sistema geotérmico desarrollado después de la formación de la caldera. Geyer et al. [117] describen que esta anomalía puede deberse al conjunto del sistema de conductos que interconectan pequeños reservorios de magma y no a una sola cámara magmática.

Luzón et al. [199] describen la estructura de velocidad superficial de nueve sitios en la costa interior de la isla, relativamente cerca entre sí. Caracteri-

zaron los primeros 400 m, diferenciando dos capas entre 100 y 300 m, con unas velocidades de las ondas S alrededor de 0.2-0.8 y 0.7-1.1 km/s, respectivamente. Estas capas están compuestas por depósitos piroclásticos y sedimentos, con diferentes grados de compactación. Este estudio señala una marcada diferencia de velocidades S, que están relacionadas con las características intrínsecas de la isla. Por un lado, las velocidades más bajas de onda S se relacionan con la actividad hidrotermal. Por otro lado, las velocidades más altas se asocian a los depósitos pre-caldera.

Otro aspecto revelador de la geología de Decepción es la existencia de acuíferos superficiales propiciados por la presencia de una Bahía interior y el alto gradiente térmico de la isla que favorece el deshielo, la percolación y la acumulación de agua [315]. Estos acuíferos se han deducido de los estudios geoquímicos realizados a las fumarolas y manantiales termales distribuidos por distintos puntos de la isla [209] y por la presencia de rocas alteradas hidrotermalmente en depósitos de piroclastos [204].

1.2.2. Vulcanismo

La isla ha sido construida por sucesivas erupciones volcánicas desde el cuaternario hasta los tiempos recientes (Figura 1.2). Entre las erupciones pre- y post-caldera se distinguen erupciones efusivas tempranas, piroclásticas tempranas, traquíticas y freatomagmáticas [24].

La primera erupción histórica se data en 1842, cuando una expedición norte-americana [327] describió que todo el lado sur de la isla en las cercanías del Monte Kirkwood parecía estar en llamas.

En 1912 y 1917 hubo una serie de erupciones freatomagmáticas en una zona cercana a la bahía de Fumarolas [235]. Roobol [273], mediante comparaciones de distintos mapas topográficos y fotografías aéreas de [171, 138], considera otros procesos eruptivos en 1839 en Caleta Péndulo, 1871 y 1909 en el Lago Króner, en 1927 en el suroeste de la isla, y en 1956 en las proximidades del monte Pond, que no han podido ser verificados.

En 1967, tras un periodo de actividad sísmica de hasta 300 eventos/mes [100], se produjo una erupción de tipo mixto, entre estromboliana y freatomagmática, en la zona de la bahía Teléfono, con dos centros eruptivos, uno

en el mar, que provocó la formación de una nueva isla alargada en dirección NE-SO, y otro en la costa norte de Puerto Foster a 2 km al E de la nueva isla. La erupción fue relativamente corta, de 3 días de duración, con proyecciones aéreas de bloques, bombas, lapilli y cenizas. Los volúmenes estimados son de unos 0.05 km^3 distribuidos por toda la isla. La columna de tefra alcanzó 6 km de altura y cubrió la totalidad de las Islas Shetland del Sur [100, 24, 290].

En 1969, la reactivación de una fractura provocó una nueva erupción en el lado Este de la isla. Esta erupción subglacial tuvo lugar en tres fracturas que se extendieron a lo largo de 5 km, desde el norte de caleta Péndulo, cruzando el glaciar del Monte Pond hasta el sur en Bahía Balleneros. La erupción fue principalmente estromboliana, tuvo una duración de tan solo dos días y se registraron terremotos violentos y tremores diarios antes de la erupción, como sucedió en 1967. El volumen del material eyectado fue de unos 0.03 km^3, formado por lapilli, bombas y escorias. Se generaron lahares y emisiones de piroclastos que destruyeron completamente la base chilena y produjeron graves daños en la base inglesa situada en Bahía Balleneros. La pluma se elevó hasta los 3000 m de altura [100, 24, 241].

En 1970 se produjo un nuevo proceso eruptivo, con una serie de erupciones freáticas y freatomagmáticas derivadas de 13 focos eruptivos terrestres y marinos alineados aproximadamente NO-SE en bahía Teléfono, cerca de los centros eruptivos de 1967. El volumen del material eyectado se calcula aproximadamente de 0.1 km^3, formado por bombas, bloques, flujos piroclásticos y una columna de al menos unos 10 km sobre el nivel del mar. Esta actividad explosiva se clasifica con un índice de explosividad volcánica (VEI) 3. La principal consecuencia de este proceso eruptivo fue la anexión del islote de 1967 a la costa y un desplazamiento de la costa de bahía Teléfono aguas adentro de unos 500 metros aproximadamente. No hay referencia directa de esta erupción ya que la isla estaba deshabitada debido a que se produjo durante el invierno austral, pero se cree que fue de corta duración. Estas erupciones fueron precedidas por movimientos sísmicos, registrados por la base chilena O'Higgins (ubicada a 170 km de la Isla Decepción) [237, 100, 24, 247]

A partir de 1970 no ha vuelto a ocurrir una erupción volcánica, aunque existen varios campos de fumarolas, anomalías térmicas, deformación y actividad sísmica, que demuestran que la actividad del volcán de la Isla

Decepción continúa [63, 64, 150, 291, 316].

1.2.3. Actividad sísmica de Isla Decepción

Una de las herramientas geofísicas más útiles para la vigilancia y el estudio de la actividad volcánica es la Sismología Volcánica [75, 218]. La sismicidad asociada a los volcanes activos tiene una amplia gama de características que revelan la variedad de procesos involucrados en la generación de señales sísmicas. La investigación del origen de los eventos sismo-volcánicos y su relación con los procesos volcánicos constituye una poderosa herramienta para comprender la dinámica y estructura de un volcán, y puede a su vez proporcionar una alerta temprana de erupción volcánica [331].

Las señales sísmicas generadas en un volcán son muy variadas. Las más características del volcán Isla Decepción son las señales de largo periodo (LP) y los terremotos volcano-tectónicos (VT). La sismicidad LP son señales puramente volcánicas que incluyen los eventos LP y los tremores volcánicos (TR). Los eventos LP de Decepción presentan una llegada emergente y una envolvente en forma de huso, con duraciones generalmente inferiores a 60 s. Se caracterizan por un contenido espectral cuasi monocromático a bajas frecuencias por debajo de 3 Hz [148]. Los mecanismos de generación de estos eventos se asocian a interacciones de fluidos como el magma, agua y gas con la roca que los envuelve, por ejemplo, según el modelo de resonancia de grieta propuesto por Chouet [74]. Los TR son señales sísmicas continuas y de larga duración (minutos a días o semanas) que normalmente se registran en áreas volcánicas activas [6, 150, 216]. Muy a menudo muestran características espectrales similares a los eventos LP. Los TR de Decepción generalmente presentan una banda estrecha de frecuencias entre 1-4 Hz, pequeñas amplitudes y duraciones de unas pocas horas. Los TR se pueden interpretar como la superposición de eventos LP que ocurren cerca en el tiempo durante un período de tiempo prolongado [13]. Se ha observado que los eventos LP y TR muestran un área de origen y un espectro similar, aunque la duración de la fuente es mayor para los episodios TR [13, 6, 150]. La sismicidad LP en Decepción se ha localizado en el área de Fumarolas, al norte de Bahía Fumarolas y en la Playa de Obsidianas, que son áreas de anomalías geoquímicas y térmi-

cas en la isla. Se interpreta que los mecanismos que generan los episodios TR y los eventos LP en Decepción, que se asocian al modelo de resonancia de cavidades rellenas de fluido, son originados por la circulación de fluidos en el sistema hidrotermal [13, 6, 150, 65]. Los terremotos VT son terremotos generados dentro del edifico volcánico [74, 216]. Los VT de Decepción presentan un contenido espectral amplio de hasta 30 Hz, con fases bien diferenciadas y rangos de tiempos S-P de 4-5 s. Presentan generalmente bajas magnitudes, aunque se han registrado VT con magnitud superior a 3.5, y suelen ser eventos superficiales [150]. Presentan distribuciones espaciales heterogéneas, se han localizado por toda la isla [315], a lo largo del sistema de fallas NO-SO [146] y en el interior de Puerto Foster [150]. Su origen está relacionado con la activación de sistemas de fracturas en el edificio volcánico debido a cambios en la distribución de esfuerzos locales o regionales, originados por procesos volcánicos [150, 65].

Desde que se restableció la vigilancia sísmica estacional en 1986, después de las erupciones de 1967-1970, el nivel de sismicidad del volcán Isla Decepción presenta una alta variabilidad. Se caracteriza por el dominio de la sismicidad LP sobre los VT, salvo en las crisis registradas en 1992, 1999 y 2015 en los que predominaron los VT. Los eventos LP se registran aislados o en enjambres. Sin embargo, los TR no se registran en todas las campañas, normalmente no aparecen en las campañas de baja actividad. Esta sismicidad parece presentar una distribución temporal con máximos de actividad de tres a seis años de forma recurrente [65]. Los eventos VT presentan dos tipos de distribuciones temporales: de forma homogénea, generalmente con un bajo nivel de actividad, o en enjambres VT que duran unos días [65]. Las campañas más interesantes desde el punto de vista de vigilancia volcánica han sido en las que se ha registrado una actividad anómala, como en las de las campañas de 1992, 1999, 2015 y 2019 que pasamos a detallar.

En enero de 1992 hubo un aumento notable de la actividad sísmica, se registraron un total 776 eventos sísmicos. Más de la mitad de los eventos registrados fueron seguidos por otro evento de características similares en menos de una hora. Se sintieron algunos terremotos (con magnitud superior a 3) e incluso algunos episodios de tremor volcánico. Este aumento en la actividad junto con las anomalías gravimétricas y magnéticas registradas

sugieren que la reactivación del volcán se debió a una inyección magmática de 2 km de profundidad en el área de la Bahía Fumarolas [237, 236, 110, 152]. Sin embargo, la inyección no tuvo suficiente energía para llegar a la superficie. Rosado et al. [274] apoya la hipótesis de la inyección magmática en base a los cambios en las emisiones fumarólicas y al estudio de deformación que refleja un proceso mixto de transición con extensión que ocurrió en la isla desde 1992 hasta la siguiente campaña en el que se tienen datos de deformación en 1995-1996.

A principios de 1999, hubo un nuevo aumento de la actividad sísmica. De enero a febrero, se registraron un total de 3643 eventos sísmicos, de los cuales 2072 fueron terremotos VT, 1556 eventos LP y 15 eventos híbridos [150, 148]. También hubo una serie de episodios de tremor (el 14 de enero se registró un tremor intenso de 24 horas, con un claro cambio de frecuencia de 1 a 2 Hz, el tremor más largo registrado hasta ese momento). La gran mayoría de los eventos de VT ocurrieron cerca de la Bahía Fumarolas, a profundidades entre 1 y 4 km. La magnitud de estos terremotos osciló entre -0,8 y 3,4 [137] y la mayoría de los hipocentros se agruparon en unos 8 km^3. Se observaron dos alineaciones: N 45º E y N 80ºE. La aplicación de técnicas de localización precisa Almendros et al. [9] permitió visualizar algunos de los planos de ruptura responsables de los eventos VT [64]. Las direcciones para la mayoría de estos planos indican una tendencia NO-SE, mientras que un número menor tuvo una tendencia NE-SO. La deformación observada en la isla muestra un proceso de inflación, el más significativo de los registrados en la isla hasta ese momento. Además, se observaron cambios en la composición del gas y anomalías gravimétricas y geomagnéticas [41]. Por tanto, todas las observaciones anteriores sugieren que el origen de la serie sísmica se debió a una inyección magmática profunda [150, 148, 41, 64].

En 2015, el nivel de sismicidad aumentó nuevamente. Se registró una alta tasa de actividad sísmica, tanto de sismicidad LP como VT y regionales. Los terremotos VT se produjeron esporádicamente a principios de diciembre. A partir de diciembre y durante los dos meses posteriores tendieron a ocurrir con más frecuencia y se agruparon en enjambres (por ejemplo, 25 de diciembre de 2014, 17 a 19 de enero y 25 a 26 de enero y 13 a 14 de febrero y 18 a 21 de febrero de 2015). Los terremotos de diciembre se localizaron dispersos

hacia el SO de la isla. En enero, se localizaron algunos terremotos de baja magnitud alrededor de Decepción y los enjambres de los días del 17-19 y 25-26 enero se concentraron a $\sim$ 20 km al SO de la isla. Sin embargo, en febrero abarcaron el edificio volcánico completo. Las mayores magnitudes se produjeron a finales de febrero, hasta 3.2. La mayoría de estos terremotos ocurrieron el 13-14 y el 18-21 de febrero. Además, la sismicidad LP se intensificó en el mes de febrero, registrando eventos LP y episodios de tremor cada vez más grandes y recurrentes. Este comportamiento anómalo en la actividad sísmica de Decepción llevó a los investigadores a recomendar un cambio en el estado de peligro. El Comité Polar Español elevó el nivel de alerta volcánica a amarillo durante unos días en febrero de 2015 [10]. Por otro lado, los estudios de deformación mostraron que se encontraba en un proceso de inflación. La correlación entre la actividad sísmica y el desplazamiento geodésico del suelo muestra que en los procesos de inflación hay un aumento de la actividad sísmica, mientras que en la deflación hay una disminución [274].

Desde entonces la actividad sísmica ha vuelto a su estado normal. La deformación en cambio sí ha sufrido un comportamiento anómalo como en 2019 que se observó un ritmo de deformación muy elevado del orden de 2 cm/mes y se mantuvo más o menos constante durante toda la campaña lo que llevó a los a los investigadores a recomendar un cambio en el estado de peligro.

1.3. Motivación y Objetivo

Isla Decepción es un volcán vigilado desde los inicios de la investigación en la isla en los años 50. La mayoría de los instrumentos sísmicos desplegados en la isla Decepción han sido instalaciones estacionales, que solo podían mantenerse durante las duraciones de las campañas antárticas (2-3 meses en el verano austral) llevadas a cabo por las distintas instituciones y países que han estado vigilando el volcán en las últimas décadas.

En 2008 en el marco del Año Polar Internacional, el proyecto CORSHET liderado por la Universidad de Granada permitió la instalación de tres estaciones sísmicas de banda ancha con carácter permanente en la zona de las Islas Shetland del Sur y la Península Antártica. Este proyecto se enmarcaba

dentro del programa POLENET, que agrupa a diversos proyectos internacionales relacionados con la instalación de nueva instrumentación geofísica para el desarrollo de las Ciencias de la Tierra en zonas polares.

Estas tres estaciones forman un perfil N-S de unos 170 km de largo, que es aproximadamente perpendicular al Rift del Bransfield (Figura 1.2). Las estaciones están ubicadas en diferentes contextos geodinámicos: (1) LVN (62°39 ′ S, 60°23 ′ W) ubicada cerca de la base española "Juan Carlos I" en la Isla Livingston, en la microplaca de las Shetlands del Sur; (2) DCP (62 °59 ′ S, 60 °41 ′ W) cerca de la base española "Gabriel de Castilla" en el volcán Isla Decepción, ubicada en el eje de extensión del Rift del Bransfield; y (3) CCV (64 °09 ′ S, 60 °57 ′ W) cerca de la base argentina "Primavera", en la Placa Antártica, cada estación está equipada con un sismómetro electrolitíco de tres componentes de banda ancha (16 s) Eentec SP400; y un registrador de datos de 24 bits de bajo consumo Eentec DR4000. La idea original es que la alimentación de energía la proporcionara el sistema de baterías, el panel solar y generadores eólicos en las estaciones DCP y CCV (Figuras 1.5 y 1.4) y en LVN el sistema de alimentación de la Base Juan Carlos I (Figura 1.3). Debido a las duras condiciones climáticas de la zona tras el primer año los generadores eólicos se tuvieron que desinstalar, ya que no resistieron las fuertes rachas de vientos. Se observó que con el sistema de baterías y los paneles solares era suficiente para el funcionamiento de la estación en DCP y CCV [63]. Estas estaciones han operado continuamente desde 2008 hasta 2015, excepto por algunos períodos invernales en los que el suministro de energía falló temporalmente como resultado de las duras condiciones ambientales. Esta es la primera vez que las estaciones permanentes sin supervisión han operado de manera eficiente durante varios años en los sitios seleccionados. Este hecho es especialmente importante para la vigilancia sísmica del volcán Isla Decepción.

1.3.1. Objetivos

El conjunto de datos registrados por la estación DCP, brinda la oportunidad única de estudiar la actividad sísmica a largo plazo del volcán Isla Decepción desde 2008 (incluidos los períodos de invierno austral), lo que nun-

Figura 1.3: (arriba) Vista de la localización de la estación LVN cerca de la base española Juan carlos I, en Isla Livinstong. (abajo) detalle del interior de la caja con la batería y el sistema de adquisición de datos de la estación sísmica permanente en febrero de 2008.

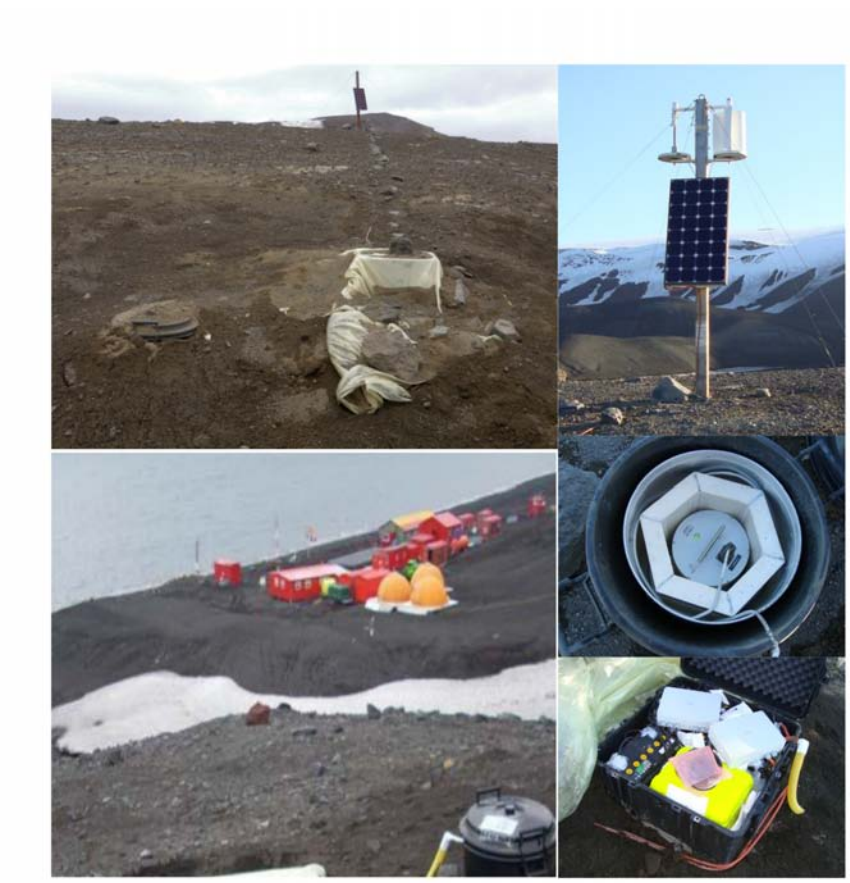

Figura 1.4: (arriba izquierda) Vista del la estación DCP preparada para la invernada. (arriba derecha) vista del panel solar sin los generadores eólicos. (medio derecha) sensor Eentec SP400. (abajo derecha) detalle de la caja Peli con el banco de baterías, sistema de adquisición, antena GPS en febrero de 2008. (abajo izquierda) Vista del la localización de la estación DCP en Isla Decepción cerca de la base española Gabriel de Castilla.

Figura 1.5: (arriba) Vista del panel solar (medio) detalle del interior de la caja con el banco de baterías y el sistema de adquisición de datos, la antena GPS de la estación sísmica permanente en febrero de 2008. (abajo) Vista del la localización de la estación sísmica permanente en Caleta Cierva.

ca se había logrado. Este es el principal objetivo de la presente tesis. Además, se pretende aprovechar toda la señal registrada en DCP aplicando análisis de ruido ambiental y comparar los resultados con los obtenidos por diferentes autores a partir de otros tipos análisis. En concreto, los objetivos específicos a alcanzar son los siguientes:

1. Identificar posibles precursores y estudiar la evolución del volcán Isla Decepción a partir del comportamiento de los eventos volcánicos antes de la serie sísmica del 2015.

2. Utilizar el registro continuo para caracterizar eventos de larga duración como son los tremores volcánicos.

3. Determinar la distribución temporal de los eventos sísmicos a lo largo de los años de registro, observar si hay estacionalidad y efectos externos que afecten a la sismicidad.

4. Caracterizar de forma completa la serie sísmica registrada en 2015, que se extendió temporalmente más allá de la duración de la campaña de vigilancia.

5. Modelar la estructura de la velocidad de las ondas S de las capas más superficiales de la isla, a partir de registros largos de ruido sísmico, así como sus características.

1.4. Esquema de tesis

La presente tesis se divide en 6 capítulos. El Capítulo 1, se describe la geología, tectónica y geodinámica de la región de estudio, así como una introducción a la sismicidad volcánica de Isla Decepción y los motivos para la realización de este estudio.

En el Capítulo 2, se analiza el ruido sísmico de diferentes estaciones desplegadas en Decepción, para poder así obtener un modelo del subsuelo de la isla más completo. Además, se ha comprobado que los estudios de análisis de ruido mejoran notablemente con el uso de series largas y continuas de datos.

Tras realizar el estudio de ruido sísmico y modelar la estructura de velocidad superficial del volcán Isla Decepción, se realiza el análisis de la sismicidad de Decepción donde se observa una señal de larga duración que se registra durante los meses del invierno austral. Para poder investigar el origen de esta

señal en el capítulo 3 se realiza una comparación de la sismicidad de las tres estaciones sísmicas permanentes localizadas en la zona de las Islas Shetland del Sur y la Península Antártica (LVN, DCP y CCV) para caracterizar esta señal de larga duración e identificar su origen y mecanismo. Además, se analiza la evolución en el tiempo de esta señal desde 2008-2015.

El siguiente paso fue analizar los datos de las estaciones permanentes para observar si la crisis sísmica registrada en la campaña 2014-2015 continuaba más allá de los registros de las estaciones desplegadas durante el verano austral en la Isla Decepción. Donde se observa que no sólo continuaba, sino que se detecta una crisis sísmica cerca de la Isla Livisntong meses antes de la contemplada en la campaña. En el Capítulo 4 se analiza los eventos tectónicos de las tres estaciones permanentes (DCP, LVN, CCV) junto a las estaciones temporales desplegadas durante el verano austral en la Isla Decepción en 2015, para determinar y caracterizar el comienzo, la localización y la fuente de la crisis sísmica, además de investigar la evolución espacial y temporal de la sismicidad y las posibles interacciones con la alta actividad sísmica del volcán Isla Decepción.

En el Capítulo 5 se analizan las señales sísmicas registradas en el volcán Isla Decepción por la estación permanente de banda ancha (DCP) durante el período 2008-2015, que precede y abarca a la crisis sísmica del 2015 y, por lo tanto, se aborda la evolución a largo plazo de la sismicidad, la estacionalidad, los efectos externos e internos que afectan a la actividad sísmica y los precursores observados en los datos.

El último Capítulo 6, se resumen las aportaciones más significativas de la presente tesis y se proporciona una perspectiva hacia el trabajo futuro.

Capítulo 2

Nuevos conocimientos sobre la estructura de la Isla Decepción a partir del análisis de ruido ambiental de series largas y continuas de datos

Resumen

La relación espectral horizontal a vertical (H/V) del ruido sísmico ambiental se ha utilizado en muchas aplicaciones, desde ingeniería civil hasta estudios de criósfera, para obtener información sobre la estructura de la superficie. Este método rápido y no invasivo se basa en la interpretación de la relación entre las amplitudes espectrales de las componentes horizontal y vertical de las vibraciones sísmicas de fondo. En este estudio, se aplica el método H/V y la inversión conjunta con curvas de dispersión para estimar la estructura poco profunda de la Isla Decepción, en la Antártida. Hemos utilizado; (1) siete años de registros continuos de ruido para la estación permanente DCP desde 2008-2015; (2) las estaciones de la red desplegada temporalmente durante los meses de verano en la isla desde 2008-2015; (3) un array desplegado temporalmente conformado por cuatro estaciones OBS dentro de Puerto

Foster durante tres meses en el experimento sísmico TOMODEC en 2005. Por otro lado, hemos utilizado las curvas de dispersión determinadas en el estudio de Luzón et al. [199], para mitigar los problemas de no unicidad. El análisis inicial revela variaciones en las tipologías de picos H/V, similares a las encontradas en cuencas geotermales. Se han obtenido modelos 1D locales de la estructura de velocidad sísmica del subsuelo bajo cada estación. Los modelos incluyen capas muy superficiales bien definidas relacionadas con el sistema hidrotermal de la isla. Además, es la primera aplicación del método del H/V en sismómetros de fondo marino (OBS) en Decepción, se han estimado modelos de velocidad del interior de la bahía. Asimismo, se han mejorado los modelos previos existentes para la Isla Decepción.

2.1. Introducción

El método H/V o HVSR (*Horizontal to Vertical Spectral Ratio*) es una herramienta sencilla, económica y no invasiva, a partir de la cual se puede estimar la frecuencia fundamental de resonancia inducida por la estructura superficial local, a partir de mediciones de ruido ambiental. El ruido ambiental se produce por fuentes naturales (interacción de atmósfera-océano-Tierra) o fuentes antropogénicas (tráfico, industrias) que muestran cambios temporales y espaciales, p. ej. [174, 36, 59, 303]. El ruido sísmico de origen oceánico o microsismo comprende las bandas de frecuencias entre 0,05 y 2 Hz, generados por el acoplamiento de la energía de las tormentas entre el océano y la tierra [59]. La curva H/V se calcula a partir del registro de una sola estación sísmica de tres componentes. Consiste en el calculo del cociente espectral entre la componente horizontal (H) y la vertical (V). La componente horizontal la calculamos como la suma de los espectros en las direcciones Norte y Este. Este método se utiliza en distintas disciplinas, desde la ingeniería civil hasta los estudios de la criósfera [306, 174, 294, 329, 251, 131, 111, 253]. El método H/V nos permite explotar la información contenida en el ruido sísmico para evaluar la respuesta sísmica local y los efectos de sitio y, utilizando un modelo físico adecuado para el ruido, caracterizar las propiedades elásticas de la estructura geológica poco profunda [226, 282, 198, 254, 294, 113]. Lunedei and Malischewsky [198] identifican dos líneas de investigación principales; (1)

considerar que la composición del ruido contiene todo tipo de ondas elásticas [197, 282, 294]; (2) considerar que el ruido esta compuesto por ondas superficiales [244, 16] de modo que la forma H/V está gobernada por la elipticidad de las ondas Rayleigh.

La Isla Decepción es un estrato-volcán situado en el extremo suroeste del Estrecho de Bransfield, una joven cuenca marginal orientada NE-SO de 60 km de ancho y 500 km de largo, situada entre la Península Antártica y las Islas Shetland del Sur (Figura 2.1). Este estrecho es una cuenca tras-arco formada como consecuencia de la subducción de la Placa Phoenix bajo la Placa Antártica durante el mesozoico-cenozoico superior [84], y la interacción con el movimiento hacia el oeste del límite de la Placa Scotia-Antártica [121]. El estrecho está caracterizado por presencia de fallas normales y vulcanismo activo [249, 152, 272]. Las Islas Decepción, Penguin y Bridgeman y una serie de volcanes sumergidos están asociados con el centro de propagación del rift del Bransfield.

Isla Decepción presenta una morfología singular en forma de herradura con un diámetro basal que alcanza los 30 km [289, 288] y 15 km de diámetro de la zona emergida, limitada en todo su contorno por acantilados verticales de roca y hielo. Posee un estrecho canal en el SO llamado Fuelles de Neptuno que da acceso a su caldera inundada (Puerto Foster) con unas dimensiones de 6 x 10 km y una profundidad de 180 m en el centro y 50 m en los Fuelles de Neptuno. El volcán se eleva ∼1400 m del fondo del mar hasta una altura máxima de 540 m (Monte Pond) sobre el nivel del mar [288].

La Isla Decepción ha sido un volcán muy activo durante toda su evolución y en la actualidad. Se han documentado más de 20 erupciones en los últimos 200 años [28]. Las erupciones más recientes se produjeron en 1967, 1969 y 1970 [290, 205], además de tres crisis sísmicas en 1992, 1999 y 2014–2015 [236, 150, 10, 11]. También hay emisiones fumarólicas, actividad hidrotermal, episodios de deformación y un nivel moderado y muy variable de actividad sísmica [63, 64, 150, 291, 316]. Se han realizado diversos estudios geológicos, geofísicos, geodésicos y geoquímicos, para poder entender la evolución y la dinámica volcánica de la isla y así, ampliar nuestra capacidad para evaluar los peligros volcánicos [315, 237, 13, 24, 288, 150, 68, 201, 39, 330, 34, 42, 248, 258, 262, 63, 232, 157, 274].

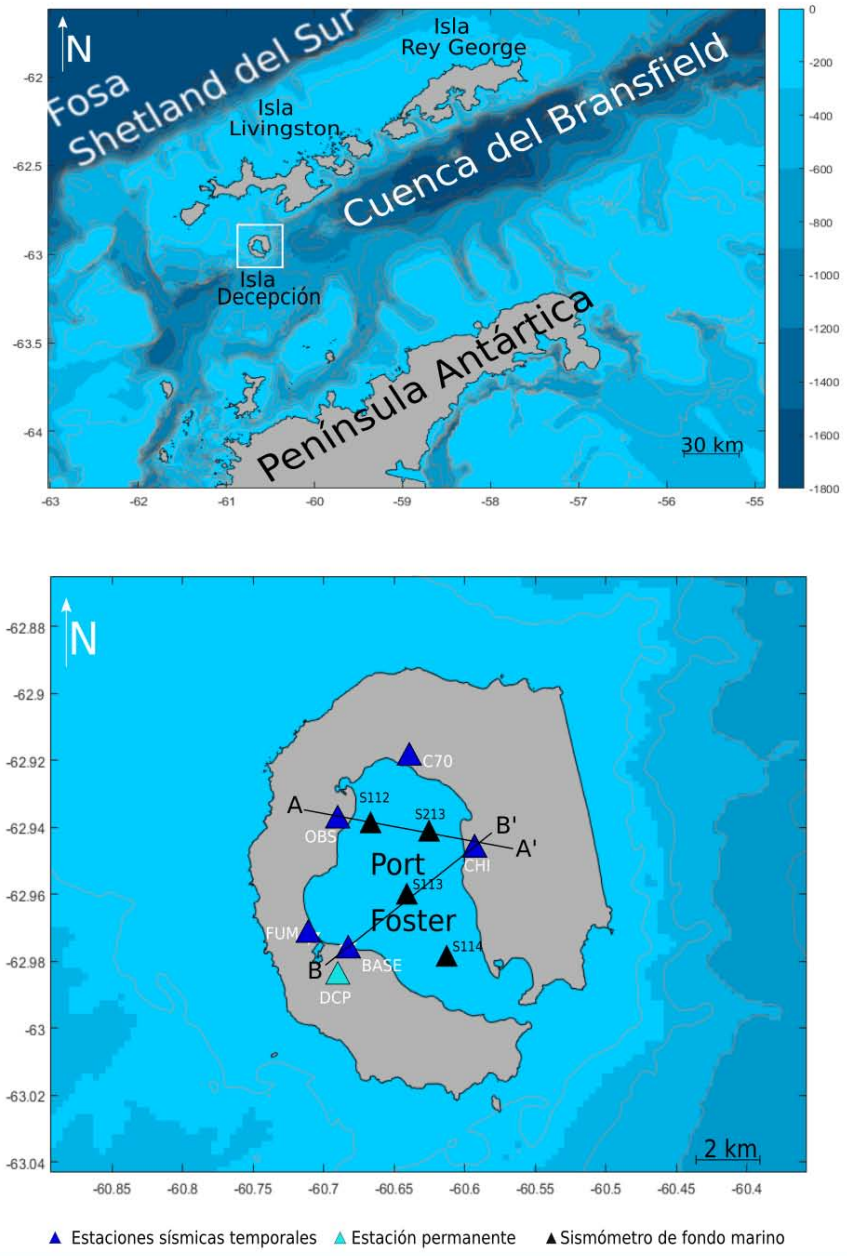

Figura 2.1: (arriba) Mapa del estrecho de Bransfield y ubicación de la isla Decepcion sobre la batimetría (el intervalo de contorno es de 200 m). (abajo) Mapa de la isla Decepción, que muestra la ubicación de las estaciones sísmicas utilizadas en este estudio. Los triángulos indican estaciones sísmicas (cían para estaciones permanentes y azul para estaciones temporales y negro para sismómetro de fondo oceánico).

Asimismo, se han realizado experimentos de sísmica, con fuentes tanto activas como pasivas en el Volcán Isla Decepción que han proporcionado estructuras de velocidad en 2D y 3D, tanto del interior como en el exterior [34, 330, 199, 262, 261]. La estructura de Decepción presenta una heterogeneidad lateral de velocidad entre el exterior y el interior de la caldera, relacionada posiblemente con el sistema de fallas que bordean la caldera y que se extienden en el interior de la isla [278]. Además presenta una alta atenuación y un medio muy fracturado con presencia de fluidos [208]. Asismismo se observan contrastes laterales de velocidad de ondas P en la isla y alrededores entre los 0-10 km de profundidad, muchos de ellos supeditados a las direcciones de fallas principales NO-SE y NE-SO [330]. Igualmente se observa una zona de baja velocidad en el centro de Decepción bajo Puerto Foster, que se relaciona con la presencia de un volumen significativo de fusión parcial. Así, los dos primeros km se asocian a un medio muy fracturado con interacciones hidrotermales y depósitos de piroclástos y de sedimentos [330, 34, 199, 261]. Por debajo de 2 km se interpreta, por un lado como una cámara de magma poco profunda (entre 2 y 5 km de profundidad), cubierta por sedimentos [330, 34, 248, 262, 261]. Por otro lado, con la presencia de un sistema geotérmico, cubierto por sedimentos,[205, 261] e incluso la combinación de estos dos modelos [261]. Estudios recientes proponen que esta anomalía de baja velocidad puede deberse al conjunto del sistema complejo de pequeños reservorios de magma remanentes, enfriados o recientes interconectados entre sí [117].

La estructura de velocidad superficial de los primeros 400 m en la costa interior de la isla presenta dos capas de espesores medios de 100 y 300 m, con velocidades de las ondas S entre 0.2-0.8 y 0.7-1.1 km/s, respectivamente. Estas capas están compuestas por depósitos piroclásticos y sedimentos con diferentes grados de compactación y presentan una marcada variación lateral de velocidades relacionadas con las características estructurales de la isla. Por un lado, las velocidades más bajas de onda S se relacionan con la actividad hidrotermal. Por otro lado, las velocidades más altas se asocian a los productos y las estructuras pre-caldera, revelando la presencia de materiales compactos a poca profundidad [199].

En este trabajo, aportamos más resolución en la determinación de los

principales contrastes de velocidad a partir de la inversión conjunta del H/V y las curvas de dispersión en la costa interior de la isla y en el interior de la bahía, con lo que se mejora la precisión de la profundidad de los principales contrastes de velocidad y las características de las capas que conforman dichas contrastes. Se definen mejor las capas más superficiales, de pocos metros de espesor. Además, es la primera aplicación del método del H/V en sismómetros de fondo marino (OBS) en Decepción, es posible determinar modelos de velocidad del interior de la bahía.

2.2. Método

2.2.1. Metodología del H/V

El método HVSR o H/V se basa en la interpretación del cociente de los espectros de Fourier de las componentes horizontal y vertical del movimiento del suelo. Inicialmente este método fue usado para determinar la frecuencia de resonancia del suelo y estimar la amplificación máxima, lo que se emplea para caracterizar los efectos de sitio en ingeniería civil [226, 189, 301, 26].

El cociente H/V lo calculamos como la raíz cuadrada de la relación entre la densidad espectral de energía de las componentes horizontales (con índices 1 y 2) sobre la dirección vertical (índice 3)[16] :

$$H/V(x,\omega) = \sqrt{\frac{E_1(x,\omega) + E_2(x,\omega)}{E_3(x,\omega)}} \tag{2.1}$$

donde, E es la densidad espectral de la energía, ω es la frecuencia angular y x es la posición.

Podemos encontrar una primera relación matemática entre el H/V y la estratigrafía basándonos en la resonancia de las ondas S en un medio de una capa sobre un semi-espacio:

$$f_0 = \frac{4h}{\beta} \tag{2.2}$$

donde, β es la velocidad de onda S de la capa, h es su espesor y f_0 es la frecuencia del primer pico que se observa en el H/V.

Conforme avanzaban los estudios y los usos de la técnica H/V se fueron desarrollando diferentes modelos matemáticos más completos para interpretar toda la curva del H/V y su relación con la estructura de velocidad bajo el punto de medida [198]. En 2011 Sánchez-Sesma et al. [282] desarrollaron un método matemático basado en la hipótesis de campos difusos (*diffuse field assumption*, DFA) encontrando una conexión del H/V con la función de Green (G) en el dominio de la frecuencia, que representa la respuesta impulsiva del medio [281].

Sánchez-Sesma et al. [282] consideran que el ruido se comporta como un campo difuso que contiene todos los modos de ondas elásticas. Un campo difuso puede ser generado por fuentes lejanas emitiendo ondas con fases y direcciones aleatorias y por *scattering* múltiple. Bajo la DFA se supone que la energía relativa de cada estado sísmico que compone la iluminación cumple el principio de equipartición de energía. Si estas ondas se registran en dos puntos, la correlación del movimiento entre éstos nos permitiría recuperar la función de Green entre ambos y mediante inversión, obtendríamos la estructura de velocidad. Sánchez-Sesma and Campillo [281] explican que la correlación del movimiento entre dos puntos es proporcional a la parte imaginaria de la función de Green entre ellos. Seguidamente, Sánchez-Sesma et al. [282] establecen que para un campo de ondas difuso la autocorrelación media en un punto y en una dirección dada, es proporcional a la densidad de energía direccional en ese punto y, a su vez, a la parte imaginaria de la función de Green para una fuente y un receptor coincidiendo en dicho punto.

Así, el cociente H/V se puede expresar como:

$$H/V(x;\omega) = \sqrt{\frac{2 \cdot P_1(x;\omega)}{P_3(x;\omega)}} = \sqrt{\frac{2 \cdot Im(GF_{11}(x;x;\omega))}{Im(GF_{33}(x;x;\omega))}} \tag{2.3}$$

donde, GF es la función de Green, P es densidad de energía direccional.

Esta expresión relaciona mediciones de campo y propiedades intrínsecas del medio. Permite la extracción de información (inversión) a partir del ruido sísmico de manera rápida y económica [282].

García-Jerez et al. [112], Piña-Flores et al. [254] desarrollaron un código informático llamado HV-Inv (http://www.ual.es/GruposInv/hv-inv/) para el cálculo directo y la inversión de las relaciones espectrales H/V experimentales

del ruido ambiental basado en la hipótesis de campo difuso (DFA). El software admite la inversión conjunta de curvas experimentales H/V y curvas de dispersión para mitigar los problemas de no unicidad y nos permite modelar la estructura de velocidad en capas bajo el sitio de medida a través del ajuste de las curvas mediante el uso de varios algoritmos locales y globales: método de Monte Carlo, *simulated annealing dowhill simplex* e *interior point*. Este software reduce el tiempo y el costo computacional y es una herramienta muy eficaz para los estudios de geofísica.

Asimismo, Lontsi et al. [195] desarrollaron un algoritmo para la interpretación de la curva H/V en el medio marino, ampliando el modelo de campos difusos de Sánchez-Sesma et al. [282]. Este algoritmo se desarrolló para considerar los efectos de la capa de agua y las variaciones que presenta la relación H/V sobre una estructura sólida por la presencia de dicha capa encima de ella. Considerando tres modelos con distintos espesores de la columna de agua (8, 200 y 5000 m) simulan diversos ambientes marinos que abarcan desde las zonas de aguas de escasa profundidad hasta los fondos oceánicos profundos y comparan con la relación H/V en tierra. Se observan pequeñas variaciones para la frecuencia del pico del H/V y variaciones de su amplitud de hasta un 50 % en ambientes de aguas profundas. La disminución de la amplitud del pico se puede interpretar como un efecto de las reverberaciones de las ondas P en la columna de agua.

2.3. Estaciones y datos

En este trabajo, utilizamos datos de distintas estaciones sísmicas que han operado en el volcán Isla Decepción. Por un lado, tenemos una estación permanente (DCP) que consta de un sismómetro electrolítico de banda ancha triaxial EENTEC SP400, con respuesta plana entre 0.06 y 50 Hz; y un sistema de adquisición de datos de 24 bits EENTEC DR4000, con registro local en un disco duro a 100 sps [63, 157]. Por otro lado, tenemos cinco estaciones temporales desplegadas en la isla sólo durante los veranos australes (OBS, FUM, C70, BASE, CHI). No confundir la estación OBS situada en la playa Obsidianas con un sismómetro de fondo marino (Ocean Botton seismometer, OBS). Las estaciones OBS y CHI estaban equipadas con sismómetros Mark-

L4C de 1 Hz. Las estaciones BASE y C70 utilizaron sismómetros Lennartz-3D/5s. Las cuatro utilizaban sistemas de adquisición de datos SARA-SL04 de 24 bits, con un muestreo de 100 sps. La estación FUM tenía un sismómetro de tres componentes Mark-L28 con respuesta extendida a 1 Hz [63, 11]. Era el centro de un array sísmico de pequeña apertura. Los datos se muestrearon a 100 sps mediante un sistema de adquisición de 12 canales y 24 bits [63, 11]. Para finalizar, tenemos 4 OBS instalados en la Bahia Foster (S112, S213, S113 y S114). Cada OBS estaba equipado con un sismómetro autonivelante de tres componentes de banda ancha [330, 151] (Figura 2.1).

Hemos utilizado los registros de ruido obtenidos durante el período de siete años (2008-2015) para las estaciones instaladas en la costa interior de la isla Decepción. Para la estación permanente DCP contamos con un registro continuo. Para las estaciones desplegadas sólo durante los veranos australes (BASE; FUM; OBS; C70; CHI) disponemos de registros de dos a tres meses cada año. Para las estaciones submarinas instalas en interior de la bahía durante la campaña TOMODEC [151] en enero 2005 hemos utilizado unas tres semanas de registro.

Ademas, hemos usado las curvas de dispersión calculadas por Luzón et al. [199] a partir de registros de ruido ambiental obtenidos en varios arrays sísmicos desplegados cerca de la costa interior de la isla Decepción. De este modo, se podrá realizar la inversión conjunta de la curvas de H/V y las curvas de dispersión y así disminuir el problema de no unicidad.

Hemos emparejado cada estación tanto terrestre como marina con la curva de dispersión obtenidas de los array sísmicos desplegados en las áreas más cercanas a nuestras estaciones, o en su defecto, en el medio más parecido al de la estación (Cuadro 2.1).

2.4. Procesamiento de datos

Vamos a usar la estación DCP como ejemplo para explicar el procedimiento utilizado para estimar todas las curvas de H/V y los modelos de velocidad de la Isla Decepción.

Para el procesamiento de datos hemos usado un programa escrito en lenguaje Matlab llamado HV-Process (Piña-Flores y García-Jerez, en proceso

Estación	Coordenadas	Elevación	Curva de dispersión
DCP	62° 59'S, 60° 41'W	25	E
BASE	62° 58.667'S, 60° 40.751'W	40	E
FUM	62° 58.103'S, 602° 42.340'W	12	F2
OBS	62° 56.263'S, 60° 41.228'W	5	F2
C70	62° 55.230'S, 60° 38.011'W	5	J
CHI	62° 56.426'S, 60° 35.597'W	14	G
S112	62° 56' 15,8"S, 60° 39' 47,3"W	-176,13	F2
S113	62° 57' 30"S, 60° 38' 17,7"W	-198,087	E
S114	62° 58' 34",7S, 60° 36' 39,2"W	-147,243	E
S213	62° 56' 24,5" S, 60° 37' 22,9"W	-157,368	G

Cuadro 2.1: Relación de estaciones y curvas de dispersión. Los nombres de las curvas de dispersión se referirán a los modelos proporcionados por Luzón et al. [199]

de publicación). Los registros son divididos en ventanas de longitud 80 s, sin solapamiento, aplicando un taper coseno sobre el 5 % de la ventana. Los espectros son calculados y suavizados según el método de Konno y Ohmachi [175] con un parámetro de suavizado de 40. Calculamos las curvas a frecuencias de 0.1 a 40 Hz, obtenemos sus promedios durante cada hora y los representamos como función del tiempo en un "HVgrama" (Figura 2.2). Retiramos manualmente las ventanas de tiempo de aquellas señales de cualquier tipo que generen perturbaciones en el HVgrama y calculamos la media logarítmica de la curvas de H/V sobre el resto del tiempo. Aplicamos este procedimiento al registro continuo de siete años para la estación DCP. Este procedimiento se repitió para todas las estaciones y los resultados se muestran en la Figuras 2.5 y 2.6.

Usando el software de inversión HV-inv (Figura 2.3), hacemos la inversión conjunta del H/V medio calculado para la estación DCP junto a la curva de dispersión (E) calculada en Luzón et al. [199] (Cuadro 2.1).

Utilizamos como modelos iniciales los propuestos por [150, 330, 199] que se describen en el Cuadro 2.2. En primer lugar ajustamos sus parámetros a partir de éstos modelos de referencia usando una combinación de muestreo de

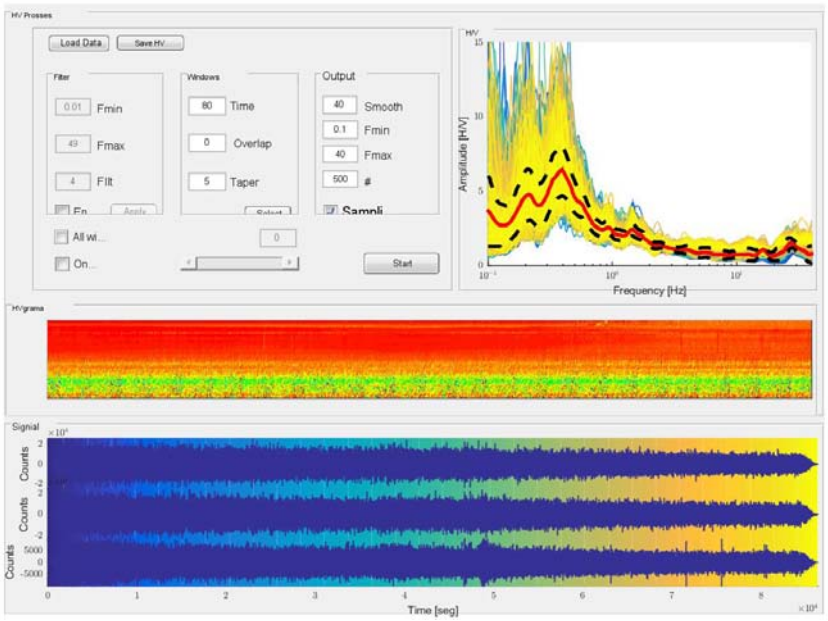

Figura 2.2: Interfaz del programa HV process. (arriba izquierda) Se observa los distintos valores para el filtro, la ventana y el suavizado. (arriba derecha) Se muestra la curva H/V calculada para 24h de registro. (centro) se muestra el HVgrama observando la estabilidad con el tiempo de las curvas. (abajo) Se observa el sismograma de las tres componentes.

Modelo	capa	espesor (m)	V_p (m/s)	V_s (m/s)
Vila et al. [316]	1º	574	1500	
	2º	838	1760	
	3º	6000	4550	
Ibáñez and Carmona [146] and Saccorotti et al. [278]	1º	80	580	310
	2º	490	1500	940
	3º	840	1800	1090
	semi-espacio		4500	2600
Ibáñez et al. [150]	1º	40	900	
	2º	1960	2300	
	3º	6000	4500	
	4º	12000	6000	
	semi-espacio	40	8000	
Zandomeneghi et al. [330]	1º	0	1908.699	
	2º	500	2939.982	
	3º	1000	3640.216	
	4º	1500	3869.476	
	5º	2000	4092.861	
	6º	2500	4405.244	
	7º	3000	4547.313	
	8º	3500	4959.158	
	9º	4000	5220.018	
	10º	4500	5499.106	
	semi-espacio	5000	5806.462	

Cuadro 2.2: Rangos de modelos utilizados en el procedimiento de inversión de curvas H/V.

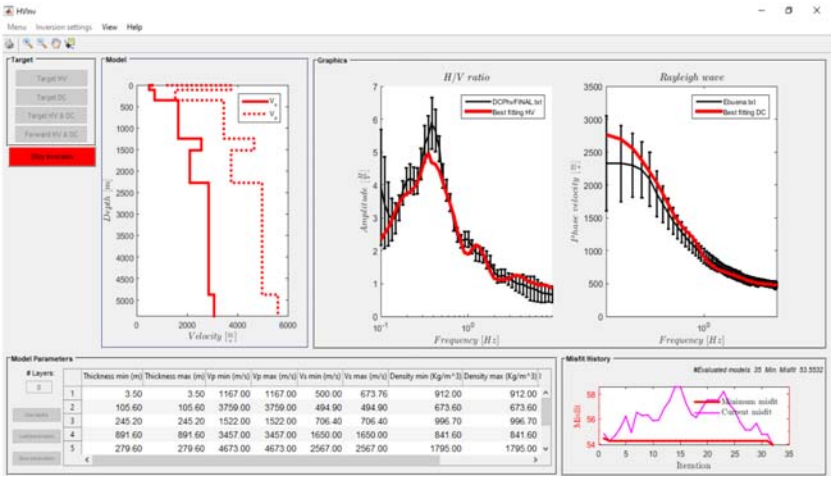

Figura 2.3: Interfaz del programa HV-Inv. (arriba izquierda) Se observan los perfiles de V_p y V_s. (arriba centro) Se muestra la curva H/V calculada y el ajuste del modelo. (arriba derecha) Se muestra la curva de dispersión (DC) calculada y el ajuste del modelo. (abajo izquierda) Se observan los parámetros impuestos para el ajuste. (abajo derecha) Se observa el historial del misfit.

Monte Carlo (en una primera etapa) y la optimización del (*dowhill simplex* e (*interior point* (segunda y tercera etapa). Después se representa el modelo obtenido, con el ajuste de las curvas H/V y la curva de dispersión (E), Figura 2.4, y se manipula el modelo manualmente, modificando las capas, reagrupándolas o dividiéndolas según la necesidad. Para finalizar se vuelve a pasar las interacciones de muestreo de Monte Carlo y optimización (*dowhill simplex*, hasta ajustar la curva teórica a la experimental de la estación DCP. El modelo de capas obtenido para la estación contiene el espesor, la velocidad de la onda P, la velocidad de la onda S y la densidad. Este método se repitió para todas las estaciones y los resultados se muestran en la Figura 2.8.

La función costo (misfit) para cada modelo probado, tanto para las H/V como para las inversiones de la curva de dispersión se basa en la definición:

$$misfit_X(m) = \frac{1}{n_X} \sum_{i-1}^{n_X} \frac{(X_{obs}(\omega_i) - X_{th}(\omega_i, m))^2}{\sigma_X^2(\omega_i)} \tag{2.4}$$

donde m representa un modelo dado, n representa el número de frecuencias de cada observable invertido, X es el observable invertido σ_X es su des-

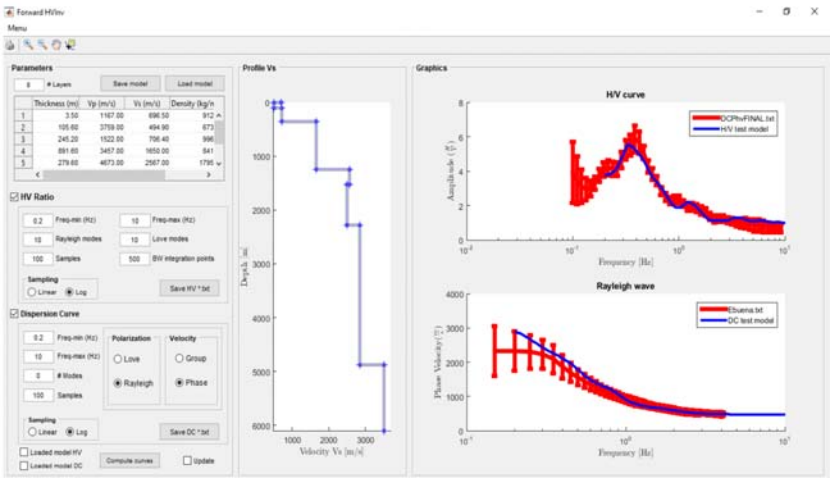

Figura 2.4: Interfaz del programa Forward HV-Inv. (arriba a la izquierda) Se observan los distintos valores del modelo. (arriba a la derecha) Se muestra la curva H/V calculada y el ajuste del modelo. (centro) Se observa el perfil de V_s. (abajo a la derecha) Se observa la curva de dispersión (E) y el ajuste del modelo.

viación estándar y los subíndices obs y th representan valores observados y teóricos.

2.5. Resultados

Las curvas H/V para las diferentes estaciones de tierra de la Isla Decepción se muestran en la Figura 2.5 y para las estaciones marinas de Puerto Foster en la Figura 2.6. Todas las curvas presentan una gran estabilidad en la frecuencia y amplitud del pico a lo largo del tiempo, como se observa en el HVgrama. La estaciones de C70 y CHI presentan una leve variación en la frecuencia en 2015, debido al cambio de ubicación de la estación a unos metros de su localización habitual por la gran cobertura de nieve de ese año en la isla.

En la Figura 2.5 se muestra cómo las curvas H/V de las estaciones de tierra (DCP, BASE, OBS, CHI y C70) presentan un pico prominente f_0 a 0.38 Hz, con amplitudes entre 3 y 7 (Cuadro 2.3). Atribuimos este pico a un contraste de impedancia en la estructura profunda del suelo [26]. La

estación CHI muestra un segundo pico ancho a f_1 3.50 Hz y amplitud 1.78, por lo que no podemos asegurar que corresponda a un contraste importante de velocidades [26]. La curva H/V de FUM presenta dos picos claros f_0 a 1.78 y f_1 a 6.85 Hz con amplitudes mayores a 2, un valle muy pronunciado a 2.86 Hz y un tercer pico a 0.20 Hz con una amplitud de 2.32. Las curvas que presentan picos múltiples se relaciona con varios contrastes importantes de variaciones en profundidad [26].

Las cuatro curvas H/V marinas presentan dos picos claros y con valores de frecuencia y amplitud parecidos. El primer pico lo encontramos entre f_0 a 0.26 Hz y a 0.38 Hz y el segundo entre f_1 a 3.80 y a 5.13 Hz. Todos muestran amplitudes (H/V) mayores a 4. Las curvas que presentan dos picos aparecen cuando existen dos fuertes contrastes de impedancia a escalas diferentes, correspondiendo el pico de baja frecuencia a la estructura profunda y el de alta frecuencia a contrastes más superficiales [26].

En el Cuadro 2.3, representamos las frecuencias de los picos H/V y sus amplitudes. Si nos fijamos en las amplitudes H/V a f_0 de las estaciones tanto terrestres como marinas, observamos que van aumentando de S a N, en mayor o menor medida, excepto en la S112, en que disminuye. Sin embargo, la amplitud a f_1 en las estaciones marinas disminuye de S a N excepto en la S112, donde aumenta.

En la Figura 2.7 se representan todos los curvas H/V y las curvas de dispersión más cercanas a la ubicación de nuestras estaciones calculadas por Luzón et al. [199]. Podemos apreciar que las curvas de H/V en DCP y OBS tienen el mismo valor de f_0 y amplitud de pico, aunque difieren en la forma, siendo el pico de OBS más ancho. C70 y S213, una en tierra y otra en el fondo marino, presentan la misma frecuencia, forma y amplitud del pico f_0, aunque es la estación CHI la más cercana a S213.

Los resultados de las inversiones conjuntas a partir de la curva H/V y curva de dispersión empíricas, muestran un notable ajuste de todas las formas de las curvas H/V (no solo los picos principales) para las estaciones tanto terrestres como marinas junto a las curvas de dispersión en las frecuencias de 0.1 a 10 Hz (Figura 2.8). Tomamos los modelos asociados al mejor ajuste como estimación de la estructura de velocidad bajo cada estación definida por la V_P, V_s , ρ y el espesor de cada capa. En la Figura 2.8 representamos

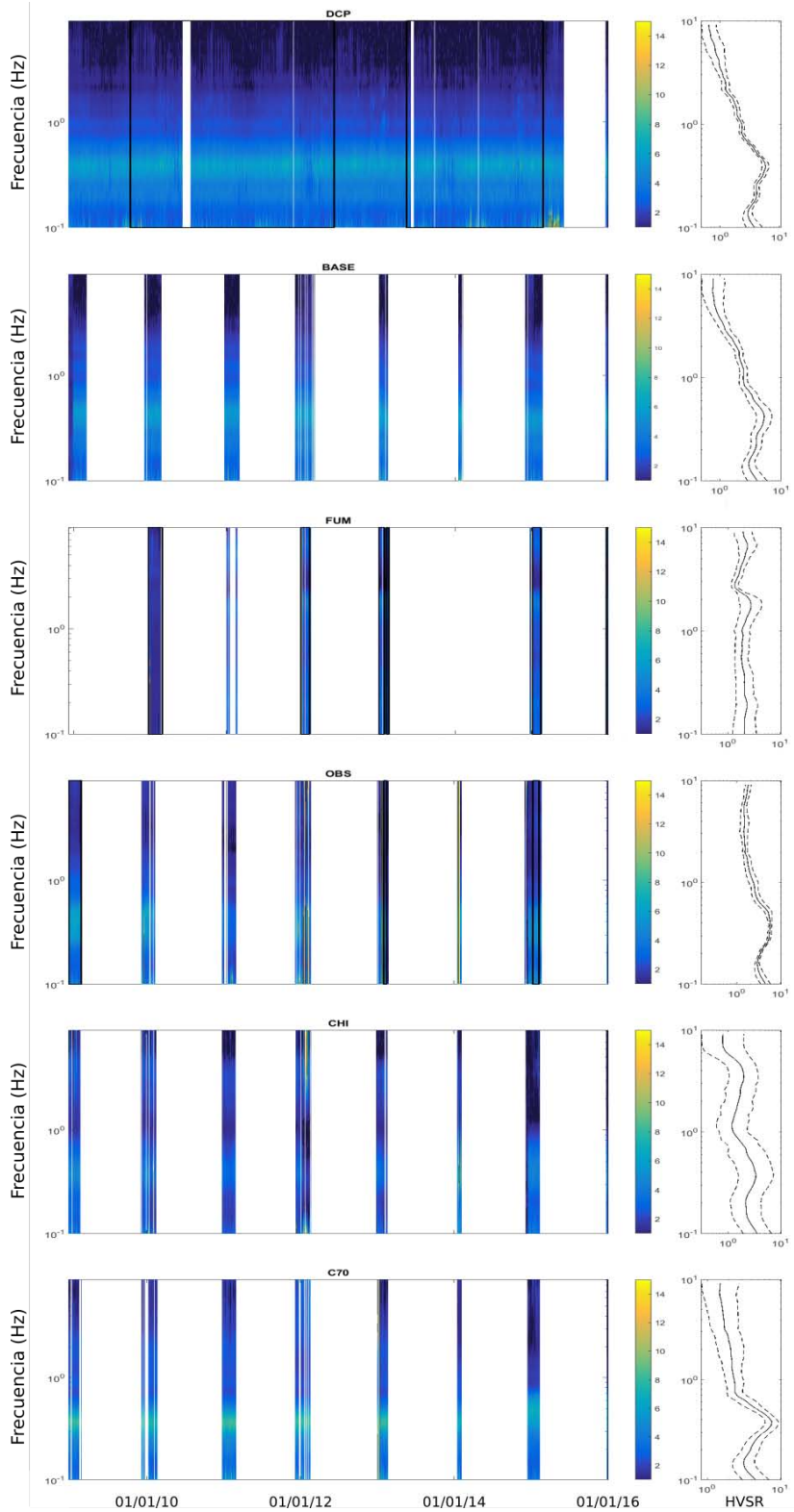

Figura 2.5: HVgrama de las estaciones de tierra que muestran la estabilidad y el H/V de cada estación.

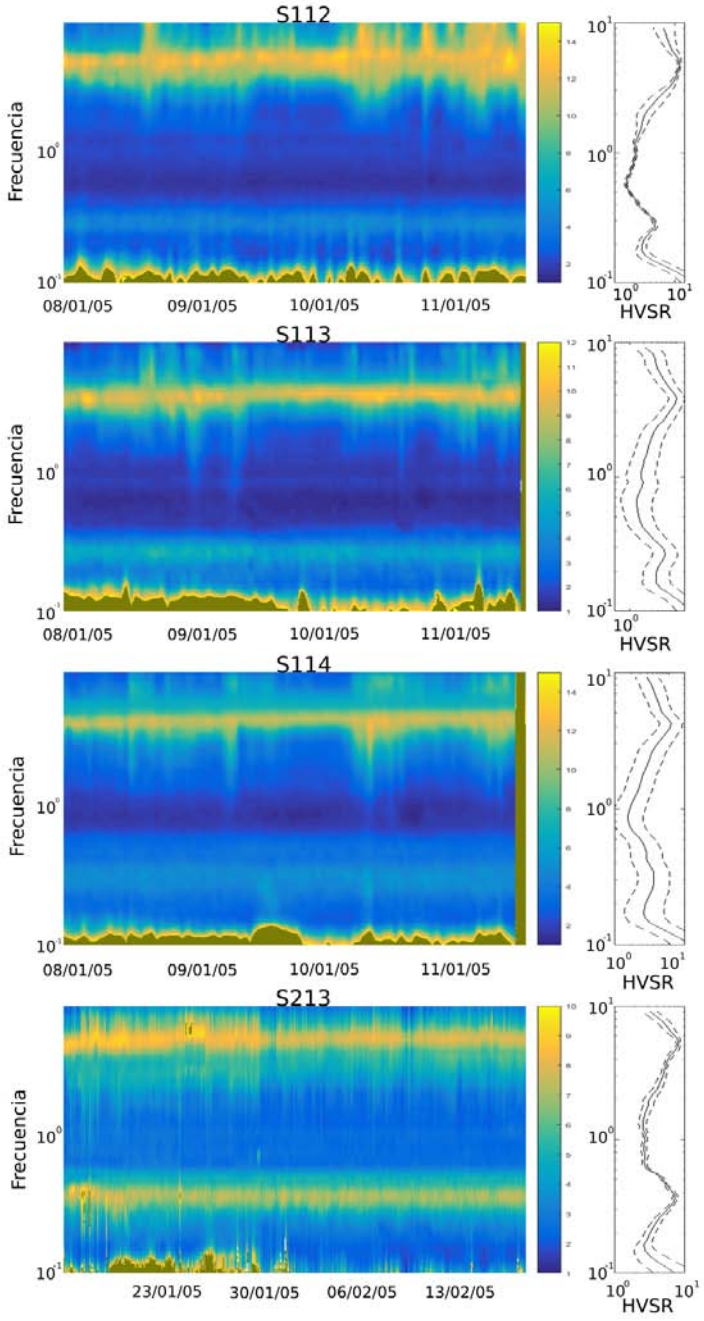

Figura 2.6: HVgrama de las estaciones de fondo oceánico (OBS) que muestran la estabilidad y el HVSR de cada estación.

Estación	Nº máximos	Tipo máximo	f_0 (Hz)	Amplitud f_0	f_1 (Hz)	Amplitud f_1	f_2 (Hz)	Amplitud f_2	f_{valle} (Hz)	Amplitud f_{valle}
DCP	2	pico claro y joraba anterior	0.3837	5.875	0.2156	4.2				
BASE	2	pico claro y joraba anterior	0.4032	5.229	0.2218	3.895				
FUM	3	múltiples picos	1.784	2.763	6.847	2.376	0.1959	2.322	2.885	1.351
OBS	1	pico claro	0.3837	5.823						
C70	1	pico claro	0.3837	7.655						
CHI	2	pico claro pico ancho posterior	0.3837	3.714	3.495	1.784			1.215	1.6262
S112	2	picos claros	0.2877	4.702	4.663	12.08			0.5635	1.517
S113	2	picos claros	0.2613	5.706	3.848	9.98			0.6203	1.427
S114	2	pico ancho pico claro posterior	0.3167	5.289	4.236	11.07			0.9109	1.739
S213	2	picos claros	0.3837	7.227	5.133	8.121				

Cuadro 2.3: Relación de estaciones, curvas de dispersión y características de los máximos de frecuencia H/V

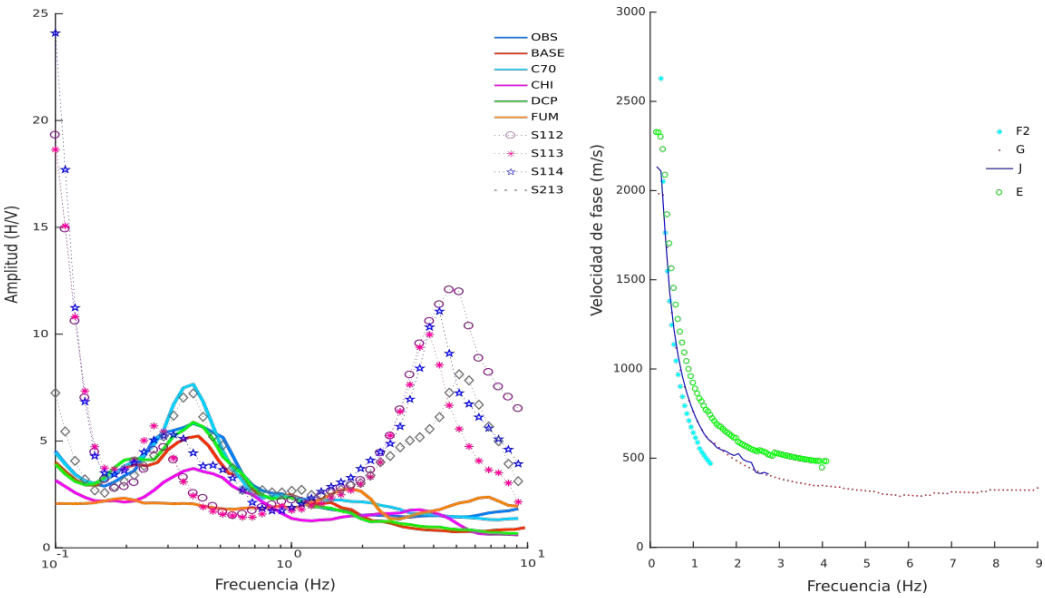

Figura 2.7: Representación de todas las curvas H/V empíricas de las estaciones y de las curvas de dispersión.

los resultados de las inversiones conjuntas a partir de la curva H/V y curva de dispersión empíricas. En la parte izquierda observamos dichas curvas en negro con barras relativas de error, sobre estas se encuentra una línea roja que representa el mejor modelo obtenido. El resto de modelos probados están representados en distintos colores según su misfit. A la derecha observamos los perfiles de velocidades representados de igual modo. Adicionalmente se representa el modelo medio en línea negra gruesa (promedio de los modelos muestreados, considerando para cada uno un peso o probabilidad dependiente del misfit).

Se observa que los perfiles medios de velocidad obtenidos son semejantes al del mejor modelo obtenido, lo que es de esperar cuando se está muestreando el entorno de un único mínimo del misfit. Los modelos que presentan diferencias entre el modelo medio y el mejor modelo (dentro de las barras relativas de error del modelo medio) son DCP y C70 a profundidades de 4500 y 3000 m, respectivamente. Esto muestra que la resolución disminuye con la profundidad de estos modelos. Sin embargo, los modelos CHI, S113 presentan diferencias en los primeros 10 y 150 m de profundidad. Esto mues-

tra una baja precisión en la determinación de la estructura del subsuelo a profundidades superficiales e intermedias, para las estaciones CHI y S113, respectivamente. Cabe destacar que cada modelo alcanza una profundidad diferente. El que presenta mayor profundidad es el de la estación OBS, de hasta 6000 m, y el más superficial es el de la estación FUM con 1500 m (Figura 2.8) y (Cuadro A.2). Además, se pueden diferenciar contrastes de velocidad y heterogeneidades laterales para los modelos obtenidos.

La velocidades estimadas de las ondas S para la mayoría de los modelos de tierra presentan dos contrastes notables, uno en los primeros 100 m y otro entre los 1100 y los 2600 m de profundidad. Se distinguen varias capas bien definidas. Para los modelos de tierra, las estaciones DCP, BASE y C70 presentan 8 capas y para las estaciones de OBS, FUM y CHI presentan siete capas. Las velocidades V_S de los modelos varían de 202 m/s para la capa menos profunda bajo la estación FUM y 3100 m/s para la capa más profunda bajo la estación C70.

Las estaciones marinas presentan cinco capas. Las velocidades de los modelos presentan 100 m/s para la capa más superficial bajo la estación S114 y 2391 m/s para la capa menos superficial bajo la estación S213. Se diferencian cuatro distribuciones de velocidad para los modelos de las estaciones que heterogeneidades laterales (Figura 2.9).

(i) Las estaciones de la costa oeste de la isla (DCP, BASE y OBS) presentan una distribución de velocidades V_S similares. Las capas más superficiales de los modelos son capas blandas (capa 1, 2 y 3, para DCP y BASE; capa 1 y 2, para OBS) con velocidades de la onda S entre 300 y 720 m/s, se extienden hasta unos 350 m de profundidad. Las capas intermedias (capa 4) presentan velocidades de 1400 a 1700 m/s con una potencia de unos 900 m de espesor extendiéndose hasta los 1250 m de profundidad. Seguidamente encontramos unas capas más profundas (capa 5, 6 y 7 para DCP y BASE; capa 5 y 6, para OBS) con velocidades restringidas entre 2300 y 2900 m/s, con un espesor entre 600-4000 m llegando hasta los 4800 m de profundidad. Las ultima capa (capa 8 para DCP y BASE; capa 7, para OBS que corresponden con las velocidades del semi-espacio las velocidades oscilan entre los 3000 y 3400 m/s. El modelo de BASE y DCP presentan pocas diferencias debido a que están muy cerca las estaciones, separados por unos 76 m. Presentan dos inversiones

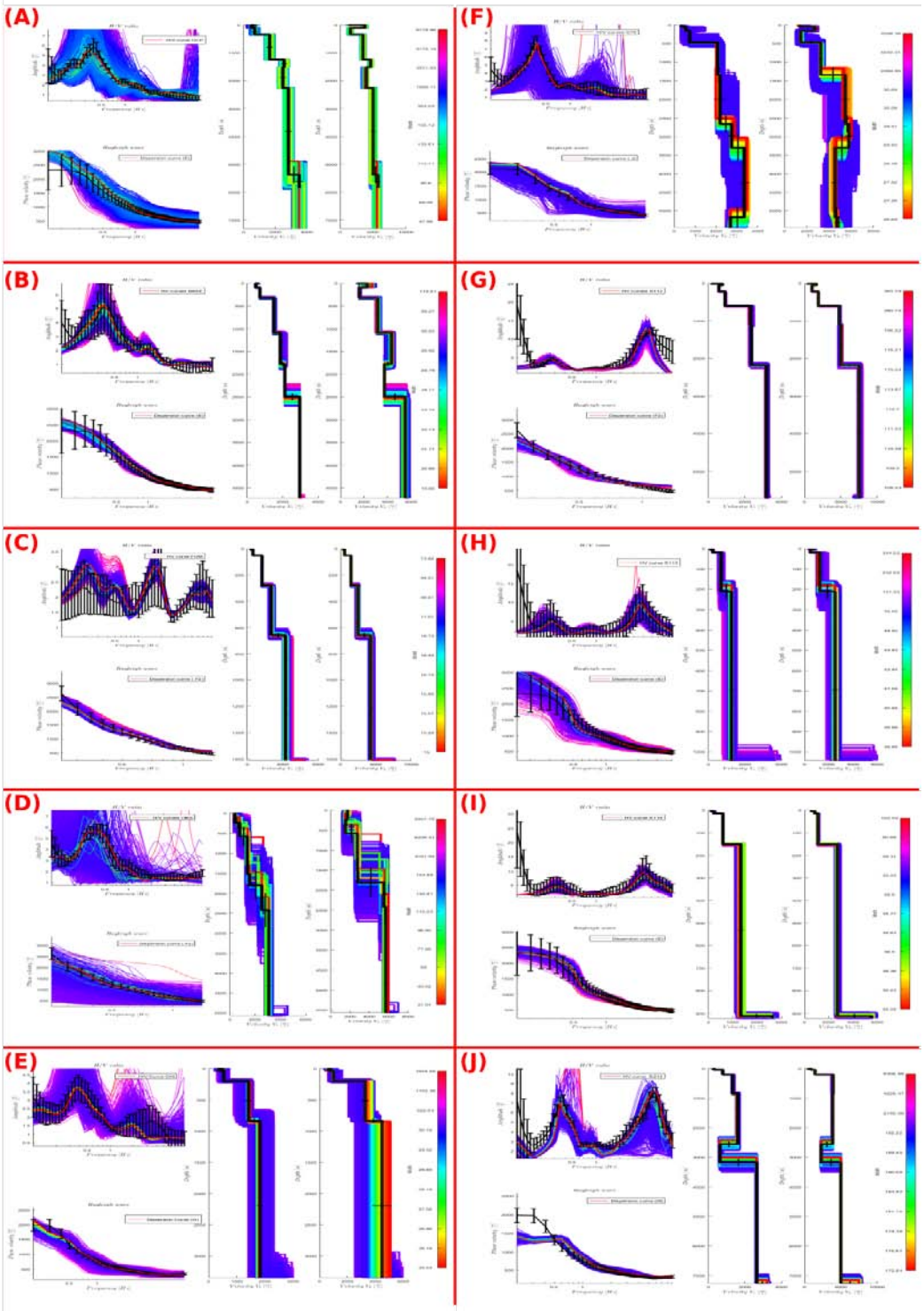

Figura 2.8: Resultados de inversiones conjuntas a partir de curvas empíricas de H/V y dispersión (líneas negras) para todas las estaciones. Las curvas teóricas se colorean como sus correspondientes modelos de velocidad y densidad. El mejor modelo conseguido se resalta en rojo.

de velocidad a unos 7 m y a 1800 m. El modelo OBS no presenta inversiones de velocidad y es más lento que los de DCP y BASE en los primeros 2000 m. Se observan contrastes laterales de velocidad entre estos modelos a unos 100, 350 y 2200 m de profundidad (Figura 2.9 a y a').

(ii) Para las estaciones de las costa noreste de la isla (C70, CHI), la distribución de velocidad es similar salvo entre los 200 y 1200 m de profundidad. Las capas más superficiales (capa 1, 2 y 3 para C70; capa 1, 2, 3 y 4 para CHI) presentan velocidades de la onda S entre 280-760 m/s, se extienden hasta los 200 m y 500 m de profundidad para CHI y C70, respectivamente. Las capas intermedias (capa 4 y 5 para C70; capa 5 para CHI) presentan velocidades de onda S de 1300-2100 m/s con un espesor de 500 a 1300 m, extendiéndose hasta los 800 m para CHI y los 2640 m de profundidad para la estación C70. Se observan capas más profundas (capa 6 y 7 para C70; capa 6 para CHI) con un amplio rango de velocidades de onda S entre 900-3100 m/s, con un espesor de 550 a 1890 m de potencia y se extienden hasta los 5000 m y 2500 m de profundidad para C70 y CHI, respectivamente. Finalmente la última capa (capa 8 para C70; capa 7 para CHI) que corresponde con el semi-espacio presenta velocidades de onda S entre 2470-2744 m/s. El modelo de C70 presenta una inversión de velocidad a 1200 m y este modelo es más rápido que el modelo de CHI. El modelo de CHI presenta una inversión de velocidad en los primeros 50 m de profundidad (Figura 2.9 b y b').

(iii) El modelo de velocidad de FUM no se asemeja al resto de modelos de tierra, siendo un modelo más rápido y con capas más delgadas. Las capas más superficiales (capa 1 y 2) son capas blandas, presentan una velocidad de onda S entre 202 y 313 m/s, se extienden hasta los primeros 52 m de profundidad. Las capas intermedias (capa 3 y 4) presentan una potencia de espesor entre 77 y 136 m, con velocidades de onda S muy restringidas entre 957-1091 m/s, se extienden hasta los 265 m de profundidad. La capas más profundas (capa 5 y 6) presentan un amplio rango de velocidades de onda S entre 1332 y 2120 m/s con espesores de 316 y 922 m, extendiéndose hasta los 1500 m de profundidad. finalmente la ultima capa (capa 7) que corresponde al semi-espacio presentan velocidades de onda S de 2799 m/s. El modelo no muestra inversiones de velocidad como el resto de modelos de tierra excepto OBS (Figura 2.9 c y c').

(iv) Los modelos de velocidad de las estaciones del interior de la bahía presentan una distribución de velocidad V_S similar presentan contrastes laterales a unos 150 m y 1500 m entre las estaciones. Las capas superficiales (capa 1) presentan velocidades de onda S muy bajas a 100-140 m/s, espesores de 4 a 7 m. La capa intermedia (capa 2) es una capa blanda, presenta velocidades de onda S de 224 a 301 m/s, extendiéndose hasta los 15 m en S113, 16 m en S112, 17 m en S114 y 27 en S213 m de profundidad. Seguidamente se observa una capa (capa 3) presentan un espesor mayor que las capas anteriores de 130-187 m, con V_S en un amplio rango de velocidades entre 1100 y 1800 m/s, extendiéndose entre los 150 y 220 m de profundidad. La capa más profundas (capa 4) presenta valores de velocidad que varían entre los 2300 y 2830 m/s, con espesores entre los y los 900 m de potencia, se extienden hasta los 900 y 1200 m. La útima capa (capa 5) que pertenece al semi-espacio presentan velocidades que varían entre 2888 y 3966 m/s. Los modelos de las estaciones de S112 y S113 en el semi-espacio presentan velocidades de onda S por encima de los 3400 m/s (Figura 2.9 d y d').

2.6. Discusión

La técnica H/V aplicada a mediciones de ruido sísmico ambiental registrado en la isla Decepción revela sitios que presentan curvas de H/V con distintas características. En función de éstas podemos agrupar las curvas en tres grupos o patrones diferentes: (1) las estaciones terrestres instaladas en la costa del interior de la isla, a excepción de FUM, que presentan un pico claro y ancho a baja frecuencia ($\sim$ 0.4 Hz), con amplitudes generalmente grandes (5-7); (2) las estaciones marinas en el interior de la bahía, con dos picos claros y estrechos: uno a baja frecuencia ($\sim$ 0.2-0.4 Hz) y otro a frecuencia media-alta ($\sim$ 4-5 Hz), con grandes amplitudes, siendo las del segundo pico (8-12) generalmente mayores que las del primero (4-7); (3) la estación de tierra (FUM) instalada en una llanura aluvial en la costa del interior de la isla, que presenta múltiples picos anchos, uno a frecuencia baja ($\sim$ 0.2 Hz) y dos a frecuencias medias-altas ($\sim$ 1.8 y 7 Hz), con amplitudes por encima de 2.

En general, la forma y los valores de frecuencia de los picos se relacio-

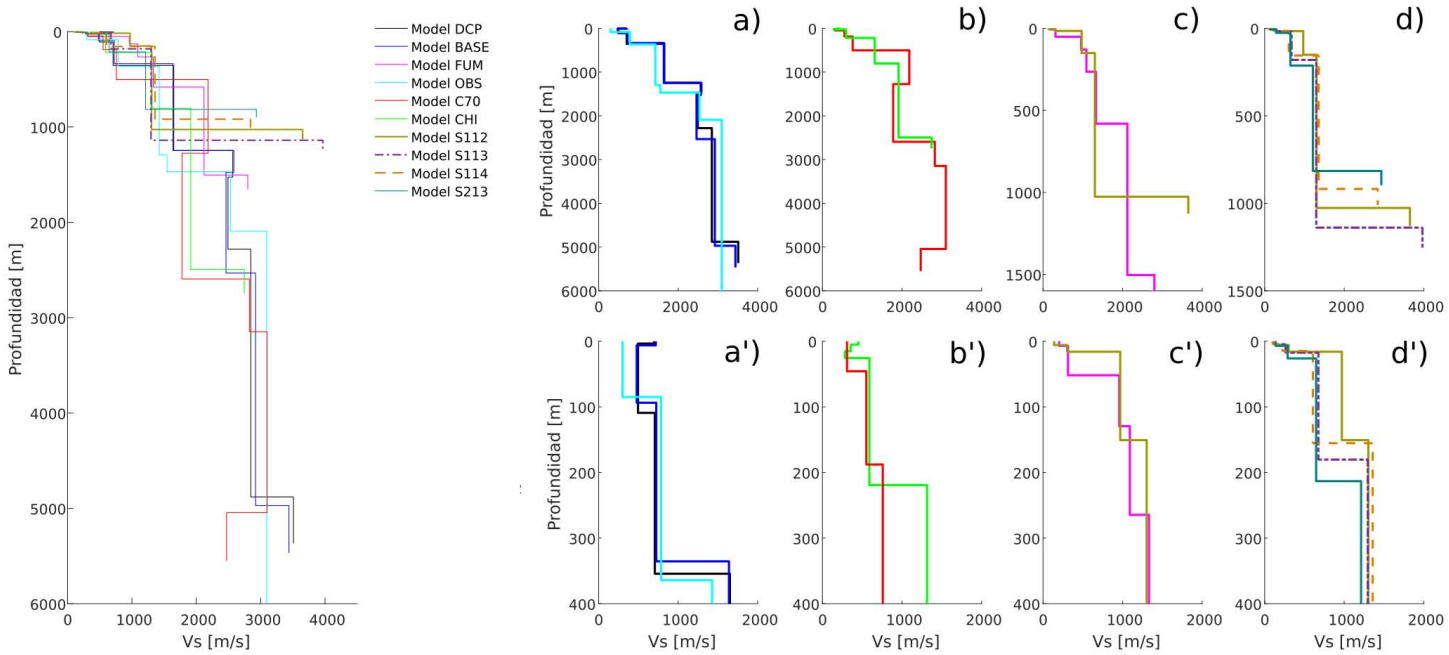

Figura 2.9: (izquierda) Representación de todos los modelos de velocidad obtenidos a partir de la inversión conjunta. (derecha) Representación de las cuatro distrubicines de los modelos de velocidad. a) Modelos de la costa oeste (DCP, BASE, OBS). a') zoom de los primeros 400 m de los modelos de la costa oeste. b) modelos de FUM y S112 al Noroeste de la isla. b') zoom de los primeros 400 m de los modelos Fum y S112. c) Modelos de la costa este (C70, CHI). c') zoom de los primeros 400 m de los modelos de la costa este. d) modelos del interor de Puerto Foster. d') zoom de los primeros 400 m de los modelos del interor de Puerto Foster.

nan con las características de la estructura superficial. Si consideramos una zona en la que la serie estratigráfica sea semejante, la frecuencia pico f_0 se relacionará con el espesor de las capas blandas superficiales (habitualmente sedimentarias). Los picos de menor frecuencia indican un mayor espesor de los depósitos y viceversa. Por otro lado, se relacionan los picos de gran amplitud con un fuerte contraste de impedencia entre estratos (p.e. entre los sedimentos y el lecho rocoso). Los picos de mayor anchura suelen asociarse transiciones más paulatinas entre las velocidades propias del sedimento y las del basamento (p.e. [106, 245]).

En estudios previos, los picos claros de baja frecuencia, < 1 Hz, se han relacionado con cuencas sedimentarias [332, 245, 165], calderas [227], áreas geotermales [106, 300, 19, 132] o con glaciares [252, 173] y los picos de frecuencias medias-altas $> 1Hz$, con capas poco profundas de sedimentos [332, 245, 165] o con permafrost [252].

En estudios de HVSR centrados en entornos volcánicos se han observado curvas de H/V con picos anchos de frecuencia fundamental f_0 (la frecuencia más baja) entre 1 y 7 Hz y una amplitud máxima entre 2 y 12, con las zonas centrales del cráter presentando valores f_0 menores que las laderas interiores del cráter [251, 293, 307, 227]. Así, en estos entornos volcánicos encontramos depósitos con mayor espesor en las zonas centrales que en las laderas, con un contraste de impedancia moderado.

Los valores de f_0 menores de 1 Hz, suelen aparecer en depósitos de sedimentos con mayor potencia que los encontrados en los entornos volcánicos descritos anteriormente, como por ejemplo en cuencas sedimentarias y geotermales o glaciares gruesos.

Las cuencas sedimentarias profundas presentan picos claros de baja frecuencia, < 1 Hz, en las zonas centrales con espesores mayores y va aumentando la frecuencia f_0 conforme se van adelgazando los espesores de sedimentos al acercarnos a los márgenes de la cuenca, típicamente con valores de f_0 de 1-5 Hz. Habitualmente se pueden observar variaciones laterales en f_0 y de la estructura o el espesor sedimentario en distancias cortas [332, 165]. Asimismo, las áreas termales como la cuenca de Eugenea, en el norte de Italia, presentan picos de frecuencia entre 0.78 a 1.9 Hz, tanto estrechos y de gran amplitud como picos más anchos con amplitud menor. Los picos amplios y de baja

amplitud se asocian con las áreas de suelo blando sobre rocas fracturadas que facilitan la circulación hidrotermal de aguas más calientes y presentan una transición suave de impedancia [106].

Estos valores de f_0 menores de 1 Hz suelen aparecer también en glaciares gruesos con espesores de hielo de 700-1000 m y picos normalmente anchos con frecuencias f_0 que oscilan entre 0.83-0.91 Hz [252].

Decepción presenta una caldera central inundada de agua de mar, con sistemas de fumarolas y suelos calientes que bordean la costa del interior de la bahía. La isla está constituida por depósitos piroclásticos de diferentes erupciones y depósitos de aluvión, playa y pedregales [290, 205]. Las estaciones de tierra de nuestro trabajo en Decepción están localizadas en el interior de la costa de Puerto Foster, generalmente en playas abiertas, laderas o llanuras aluviales, algunas de ellas en áreas cercanas a fumarolas y suelos calientes de la isla. La distancia entre estaciones es de aproximadamente 2-4 km, siendo éstas de fácil acceso, ya que su principal función es la vigilancia volcánica (Figura 2.1). Sin embargo, no se han instalado sobre los distintos glaciares que conforman la isla debido a la dificultad de acceso y a que interferiría con su función principal. Nuestros datos muestran que los picos de las estaciones de tierra son anchos con valores de amplitud similares a los estudios mencionados. Las estaciones marinas presentan dos picos estrechos con valores de amplitud altos. La frecuencia fundamental sigue una distribución espacial también similar, con valores menores en el centro de la bahía (estaciones marinas) y aumentando en el margen de la depresión de la caldera (estaciones de tierra). Sin embargo, las frecuencias f_0 son menores de 1 Hz.

Así, nuestros resultados de las curvas de H/V experimentales presentarían unas características y distribución similar a las de las cuencas geotermales. Las estaciones marinas (S112, S231, S113 y S114) presentan picos estrechos de baja frecuencia mientras que las estaciones de tierra (DCP, BASE, FUM, OBS, C70 y CHI) presentan picos anchos de bajo valor de frecuencia de pico f_0 (un poco mayores en frecuencia que los de la bahía). En consecuencia, el interior de la bahía presentaría un mayor espesor de los depósitos y un mayor contraste de impedancia entre el sedimento y el basamento, que en el margen de la depresión de la caldera en la costa interior de la isla. Además, los picos de FUM y CHI, localizadas cerca de las áreas de fumarolas y suelos

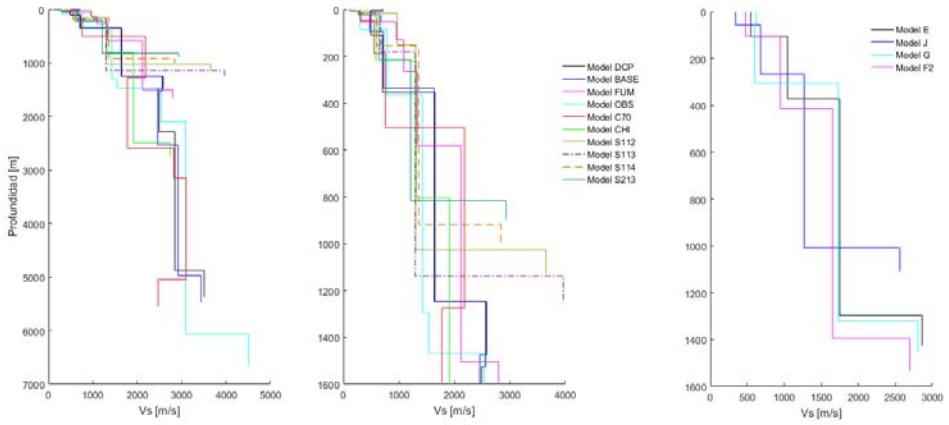

Figura 2.10: (derecha) Representación de todos los modelos de velocidad obtenidos a partir de la inversión conjunta. (Centro) zoon de los primeros 1600 m de todos los modelos de velocidad. (Izquierda) representación de los modelos obtenidos a partir de las curvas de dispersion por [199]

.

calientes, son anchos y de baja amplitud, por lo que se relacionarían con áreas de sedimentos sobre rocas fracturadas que favorecen la circulación de agua caliente.

En la Figura 2.10 y Figura 2.11, se muestran todos los modelos obtenidos a partir de la inversión conjunta y los modelos estimados por las curvas de dispersión calculadas por Luzón et al. [199]. Se observa que los modelos calculados con la curva E (DCP, BASE, S113 y S114) muestran la misma tendencia, con algunas diferencias. La primera es que los modelos de las estaciones marinas S113 y S114 son más rápidos, mientras que los modelos de tierra DCP y BASE son más lentos que el modelo E. Los modelos alcanzan resoluciones diferentes, de 1500 m y 5500 m de profundidad para las estaciones marinas y estaciones de tierra, respectivamente. Esta diferencia de resolución se debe a que las curvas de dispersión usadas para la inversión se han calculado para áreas más cercanas a las estaciones de tierra que para las marinas. La segunda diferencia radica en las capas poco profundas de baja velocidad que se estiman en los primeros 20 m para los modelos del interior de la bahía y la capa superficial de alta velocidad a unos 7 m en los mode-

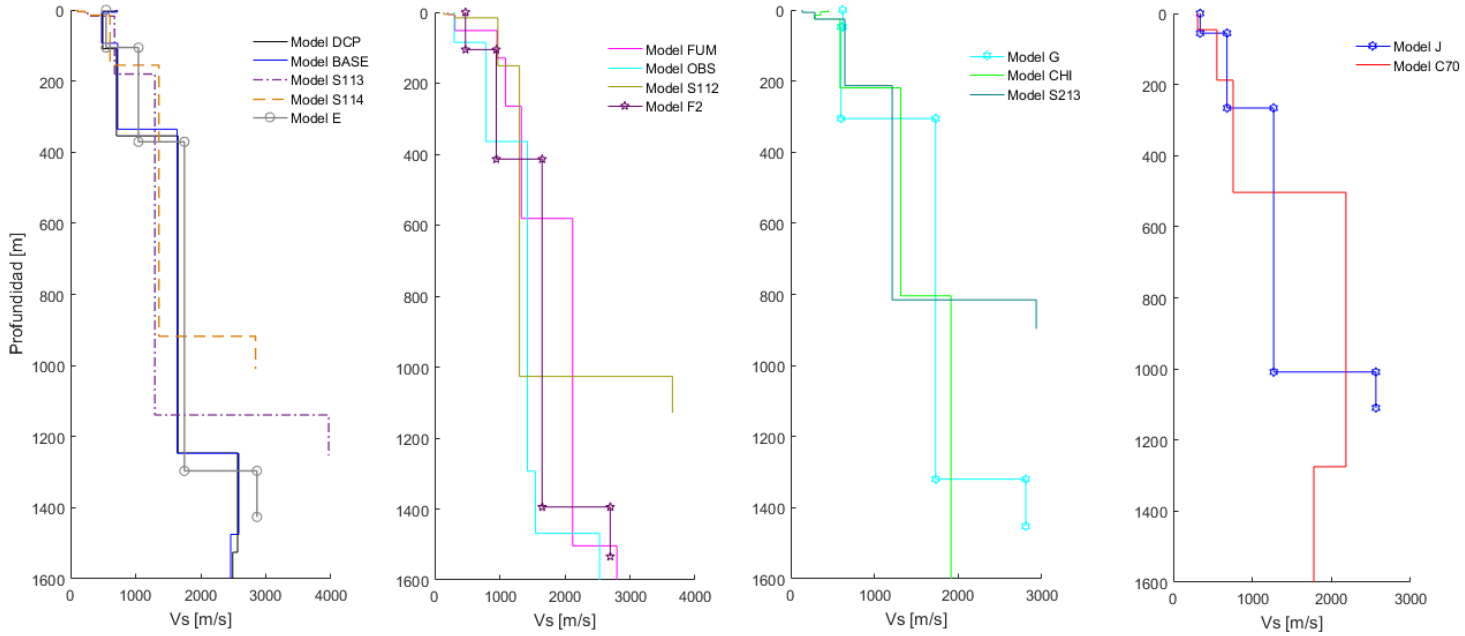

Figura 2.11: Representación de todos los modelos de velocidad obtenidos de la inversión conjunta junto al modelo estimado por Luzón et al. [199] a partir de la misma curva de dispersión (modelos E, G, J, F2); (a) representación de los modelos de BASE, DCP, S113 y S114 junto al modelo E (basado sólo en la curva de dispersión); (b) modelos FUM, OBS y S112 junto al modelo F2; (b) representación de los modelos de CHI y S213 junto al modelo G; (d) representación del modelo de C70 junto al modelo de la curva de dispersión J

.

los de las estaciones de tierra, que no aparecían en el modelo E. La tercera diferencia es que el contraste a 100 m del modelo E desaparece en los modelos de tierra mostrando una estructura más homogénea en los primeros 350 m, mientras que se mantiene el contraste a 1200-1300 m. Estas diferencias son las aportaciones de la curva experimental H/V a los modelos. La curva de dispersión controla la tendencia general ("suavizada") de la velocidad de onda S al aumentar la profundidad, mientras que la presencia de grandes contrastes de velocidad tiene efectos más claros en el H/V (generación de picos). Por tanto, las curvas H/V pueden definir mejor las capas más superficiales y determinar su espesor. Así se mejora el modelo previo del oeste de la costa interior realizado por Luzón et al. [199].

Para los modelos calculados con la curva de F2 (FUM, OBS y S112) se observa una tendencia común, con capas más delgadas que las estimadas para el modelo F2. Los modelos de OBS y F2 son muy similares, mientras que los modelos de FUM y S112 presentan diferencias más notables en los primeros 400 m. Estas diferencias consisten en que el modelo de OBS no presenta contraste superficial, al igual que el modelo F2, mientras que sí se muestra en los modelos de FUM y S112. Este contraste en el modelo es requerido por la presencia de picos de altas frecuencias en las curvas H/V de FUM y S112 que definen esas capas más superficiales. La curva de dispersión F2 no llega hasta muy altas frecuencias, mientras que la curva H/V resalta las diferencias en las capas superficiales. Por otro lado, el modelo F2 se estimó de un array instalado en una zona más cercana a la estación OBS que FUM y S112. Asimismo, se observan diferencias entre las estaciones OBS y FUM separadas por no más de 2 km, que revelarían la presencia de heterogeneidades laterales a 300 m y entre los 600 y los 1300 m de profundidad, siendo el modelo de FUM más rápido que el de OBS.

Para los modelos cuya inversión consideró la curva G (CHI y S213) se observa una semejanza entre ellos, mostrando diferencias con el modelo G. La primera diferencia la encontramos en las capas superficiales, donde el modelo S213 presenta una capa de unos pocos metros de profundidad de baja velocidad y el modelo CH presenta una inversión de velocidad en la segunda capa. Sin embargo, el modelo G presenta una capa superficial de mayor velocidad que las mostradas en los modelos anteriores y de gran espesor, hasta

los 300 m de profundidad. Estas capas superficiales en los modelos de CHI y S213 se corresponden con los picos de alta frecuencia mostrados en las curvas experimentales H/V de cada modelo. La segunda diferencia son los contrastes de velocidad del modelo G a 300 m y a 1300 m, que los modelos de S213 y CHI presentan a unos 200 m y 800 m. Como se ha mencionado anteriormente, las curvas H/V precisan mejor la magnitud de los contrastes en las capas superficiales que las curvas de dispersión.

Finalmente, para el modelo invertido con la curva J (C70), se observa una tendencia de velocidad similar entre modelos, pero con los contrastes de velocidad a menor profundidad en el modelo de C70 que en el modelo J. Estas diferencias de posición de los contrastes de velocidad van aumentando con la profundidad. De este modo, se observa un gradiente más suave de crecimiento de la velocidad con la profundidad en el modelo J, mientras que el modelo de C70 presenta un alto contraste a unos 500 m profundidad consecuencia del pico de baja frecuencia de la curva H/V. En el modelo de C70 por debajo de 500 m de profundidad nos encontramos ya velocidades de onda S similares a las máximas de la curva de dispersión Rayleigh, por lo que las capas inferiores presentan algunas incertidumbres al estar determinadas, en esencia, sólo determinadas por el H/V.

En general, nuestros modelos mejoran los modelos previos y definen mejor las capas más superficiales. Se definen con mayor resolución los primeros 5000 m para las estaciones de BASE, DCP y OBS, los 2500 m para las estaciones de CHI Y C70 y los primeros 1000 m para las estaciones del interior de la bahía, las capas del semi-espacio en C70 y estaciones marinas presentan varias incertidumbres.

2.6.1. Modelos de las estaciones de tierra

Los modelos de las estaciones en tierra se pueden agrupar en tres distribuciones de velocidad diferentes: modelos de la costa este, modelos de la costa oeste y el modelo de Fumarolas. En las primeras capas presentan un rango de velocidades V_S entre 202 y 760 m/s. Son capas blandas con un espesor alrededor de 400 m, exceptuando la estación FUM en que presenta un espesor de sólo 52 m. La profundidad a que aparece esta discontinuidad

varía entre los 100 y los 350 m, siendo el contrate entre las capas consistente con los valores dados por diferentes autores [146, 280, 199] que muestran una capa superficial de unos 100 m con Vs entre 200 y 800 m/s compuesta por depósitos de piroclastos post-caldera y sedimentos sueltos. Esta diferencia de espesor de las capas de baja velocidad entre los autores antes mencionados y nuestro rango refleja las limitaciones de los métodos usados. Por ejemplo, en [280, 199] sólo se calculan las curvas de dispersión, por lo que tienen menos resolución en determinar la profundidad de los contrastes de velocidad que la inversión conjunta con el H/V.

Existen diferencias en las capas superficiales de nuestros datos incluso en estaciones cercanas. Por ejemplo, las estaciones FUM, OBS, C70 y CHI presentan velocidades muy bajas de V_S, en la capa más superficial, que van aumentando de una estación a otra de oeste a este. Estas estaciones se encuentran ubicadas cerca de las áreas caracterizadas por actividad hidrotermal, (FUM y CHI) o suelos calientes (OBS y C70) [290]. La circulación de agua caliente y sus efectos en los sedimentos que la rodean pueden ser responsables de las bajas velocidades de onda S observadas en estos sitios [199]. En las estaciones FUM y CHI estas capas son más lentas y más delgadas que en OBS y C70. Esta diferencia puede ser debida a la geología de la superficie, ya que las estaciones OBS y C70 están localizadas en playas caracterizadas por la presencia de sedimentos marinos no consolidados, depósitos de pedregales y aluviales indiferenciados [205], mostrando una estructura más homogénea en los primeros 50-90 m.

En cambio, las estaciones FUM y CHI presentan varias capas delgadas en los primeros 50 m. Esta diferenciación entre las capas poco profundas se puede corresponder a una capa muy superficial de sedimentos de la erosión del borde de la caldera y de derrubios de ladera para FUM y CHI, respectivamente seguida de una capa de sedimentos piroclásticos más consolidados de post-caldera.

Las estaciones DCP y BASE muestran una capa superficial delgada de alta velocidad. Esta capa se puede deber a los sedimentos de piroclastos consolidados de depósitos post-caldera [290].

Martí et al. [205] interpretan estas capas superficiales descritas bajo las estaciones de tierra, como propias de depósitos de avalanchas de escombros

formados por el colapso gravitacional de la pared de la caldera, depósitos volcánicos post-caldera o depósitos de pedregales y abanicos aluviales.

Las capas intermedias presentan velocidades de onda S entre 1300 y 2100 m/s, con espesores de 800 a 1700 m, son capas más duras que se extienden hasta 1250 m de profundidad para los modelos de la costa oeste y entre los 800 y 2600 m de profundidad para los modelos de la costa este (CHI y C70, respectivamente). Estas capas intermedias se pueden corresponder con los depósitos de la formación de la caldera (*Outer Coast Tuff Formation*, OCTF), compuestos principalmente por una secuencia gruesa de ignimbritas masivas y depósitos menores de surgencia piroclástica de composición basáltica a andesítica, caracterizadas por velocidades mayores al comportarse como una roca dura [205]. Para el modelo de FUM la capa intermedia presenta velocidades de ondas S más bajas (957-1091 m/s) y capas más delgadas (77 y 135 m), que se extienden hasta los 265 m de profundidad. Esta capa intermedia se corresponde en velocidad de la onda S con las capas descritas por [199] entre 100-400 m que interpretan como depósitos post-caldera más consolidados.

Las capas más profundas presentan variaciones significativas tanto en espesor como en velocidad de las ondas S de un modelo a otro. Esto responde al carácter complejo de la estructura superficial para Decepción. Los modelos de la costa oeste presentan velocidades de V_S de 2300-2900 m/s, con espesores entre los 600 y 2500 m. Sin embargo, los modelos de la costa este presentan velocidades de V_S que varían entre los 1900 y los 3100 m/s y espesores de 1600-1900 m. Para el modelo de FUM las velocidades se encuentran dentro del rango de los modelos de la costa oeste (1350-2100 m/s) pero a profundidades menores (1500 m). Estas capas duras con altas velocidades y diferencias de espesores pueden corresponder con los depósitos basálticos formadores del volcán en escudo y con la distribución irregular de éstos [205].

2.6.2. Modelos de las estaciones del fondo marino

Los modelos de velocidad para el interior de la bahía presentan una capa superficial (capa 1) muy delgada (de unos pocos metros) y muy lenta (100-140 m/s). Estos valores coinciden con los calculados para las curvas de

dispersión de las ondas superficiales asociados a sedimentos pocos profundos de espesores entre 3- 21 m y velocidades de onda S de (120 m/s) por Overduin et al. [239], para el estudio de ruido sísmico del fondo marino alrededor de la isla de Muostakh en el Mar Central de Laptev, Rusia. Las profundidades a las que están instalados los OBS de Puerto Foster son mayores que los usados por [239], aunque este estudio no determina la dependencia de la profundidad con la velocidad de la onda S.

Así, la capa 1 de puerto Foster se puede considerar una capa delgada de muy baja velocidad compuesta por sedimentos no consolidados saturados en agua procedentes del aporte de relleno de la bahía reciente. La siguiente capa (capa 2) es una capa blanda delgada (entre 10-20 m de espesor) con velocidades de onda S entre 224-301 m/s, las estaciones más al noroeste de la bahía, S112 y S213, presentan velocidades parecidas a las de las capas superficiales de los modelos de la costa este (288-301 m/s), esta similitud probablemente se deba a la cercanía entre las estaciones de tierra y marinas, por lo que los mismos materiales erosionados de las áreas donde se encuentran las estaciones de tierra, serían depositados dentro de la bahía bajo las estaciones marinas. Estos depósitos pueden corresponder a los sedimentos no consolidados post-caldera característicos por presentar bajas velocidades y depósitos volcánicos recientes producidos durante las erupciones [266, 34].

Las capas intermedias (capa 3) presentan velocidades muy restringidas entre 606-675 m/s, excepto en la estación S112 que presenta velocidades de 970 m/s, esta capa tiene mayor velocidad y espesor (100 m), esta diferencia con las capas más superficiales puede deberse a que nos encontramos ante materiales compuestos por sedimentos de post-caldera más consolidados [128, 34]. La capa más profunda (capa 4) es una capa gruesa entre 600- 960 m de espesor y muy rápida con velocidades de onda S entre los 1212- 1358 m/s, esta capa dura se puede deber a los depósitos de materiales intra-caldera de OCTF compuestos principalmente por un gran volumen de ignimbritas producida durante la erupción de la formación de la caldera en el Holoceno [205].

Diferentes estudios realizados en la bahía interior de Decepción describen que su estructura interna compuesta por una capa rellena de sedimentos de unos 2 km, asociada a un medio muy fracturado con circulación de fluidos

hidrotermales, por encima de una cámara magmática comprendida entre los 2-5 km de profundidad [330, 34, 248, 262, 261]. La capa superior compuesta por sedimentos se ha descrito en tres unidades geofísicas principales; (1) la unidad superior de $<$ 100 m de espesor está compuesta por sedimentos de post-caldera y depósitos de las recientes erupciones [128, 34, 205] (2) la unidad central con un espesor de unos 1200 m está compuesta por depósitos de piroclasto más consolidado o depósitos inta-caldera de la formación de la caldera (OTCF) con velocidades de 2.5-3.5 km/s [128, 34, 205], (3) la unidad inferior con velocidades de 4.5 km/s, compuesta por depósitos más duros pre-caldera [128, 34, 205].

En nuestros resultados, esta capa de sedimentos de 2000 m de espesor comprende 4 capas. Las dos primeras se corresponden con depósitos post-caldera y erupciones recientes caracterizados por bajas velocidades de onda S, donde diferenciamos la capa 1 con materiales sueltos saturados de agua procedentes del proceso de relleno de la bahía y la capa 2, que presenta una variación de velocidad suave respecto a la capa 1 y se puede interpretar como sedimentos de igual composición con menor contenido en agua o por las interacciones del sistema hidrotermal con los sedimentos procedentes de los depósitos post-caldera, caracterizados por bajas velocidades de onda S. El contraste de velocidad existente a unos 100 m marca la transición de materiales blandos (las dos capas superiores) a más rígidos, y se refleja en el pico a altas frecuencias de las curvas H/V de las estaciones del interior de la bahía. Estas dos capas poco profundas extendidas hasta los 100 m se corresponderían con la unidad superior descrita anteriormente por [128, 34, 205].

Hay que aclarar que al modelar el pico de altas frecuencias estamos sobrestimando en alguna medida su amplitud ya que no hemos contemplado los efectos de la capa de agua sobre las estaciones. Al considerarla, se obtendría un pico de alta frecuencia de menor amplitud [195]. Esta reducción de amplitud en el pico depende de la altura de la columna de agua, pudiéndose reducir hasta un 50 por ciento en columnas de varios kilómetros. Esto repercute en que, en el modelo obtenido, las dos capas superficiales presentarían un contraste de velocidad sobre la tercera algo más bajo que el real (o, dicho de otro modo, el gradiente de crecimiento de la velocidad con la profundidad

obtenido sería más suave que el real).

La capa 3 se constituye posiblemente de materiales más consolidados debido a la subsidencia, pertenecientes a depósitos post-caldera. La transición de materiales blandos a más duros se produce a unos 200 m de profundidad, en la interacción de la capa 3 con la capa 4 que es más rápida y con espesores mayores que el resto. Esta discontinuidad de velocidades se corresponde con el pico de menor frecuencia en las curvas H/V. La capa profunda se puede componer de materiales depositados por la formación de la caldera (intra-caldera OTCF), compuestos por un volumen más o menos constante de ignimbritas masivas que se comportan como roca dura, con velocidades mayores a 1500 m/s. La velocidad en la capa 4 es más baja debido a la presencia de materiales muy fracturados y el sistema hidrotermal, que se caracteriza por alterar las rocas y disminuir la rigidez, disminuyendo así la velocidad de la onda S. De este modo, esta capa puede pertenecer a la unidad central descrita anteriormente por [128, 34, 205].

La última capa que corresponde con el semi-espacio presenta heterogeneidades verticales y laterales con velocidades de 2800-4000 km/s. Aunque la resolución del método para estas capas es muy limitada al sobrepasar las velocidades obtenidas con las curvas de dispersión, presentando grandes incertidumbres, posiblemente están relacionadas con estructuras y productos pre-caldera, correspondientes a la tercera unidad descrita por [128, 34, 205].

La inversión conjunta de las curvas experimentales H/V y de dispersión nos ha permitido definir el modelo hasta los primeros 1500 m de profundidad en el interior de la bahía caracterizando bien las capas de sedimentos que se encuentran encima de la cámara magmática, sin embargo, no se ha llegado a la profundidad donde se encuentra la cámara magmática. Esto se debe principalmente a que hemos utilizado curvas de dispersión que no son propias del interior de bahía. Para poder llegar a la profundidad de la cámara recomendamos desplegar una red de OBS más densa con estaciones de tierra que operen simultáneamente y calcular una curva de dispersión experimental propia de la bahía o realizar correlaciones entre las estaciones de los arrays de tierra (usado para el estudio de ruido sísmico en Luzón et al. [199]) para llegar a frecuencias más bajas en la curva de dispersión experimental.

En la Figura 2.12 se observan perfiles de la velocidad de A- A' con di-

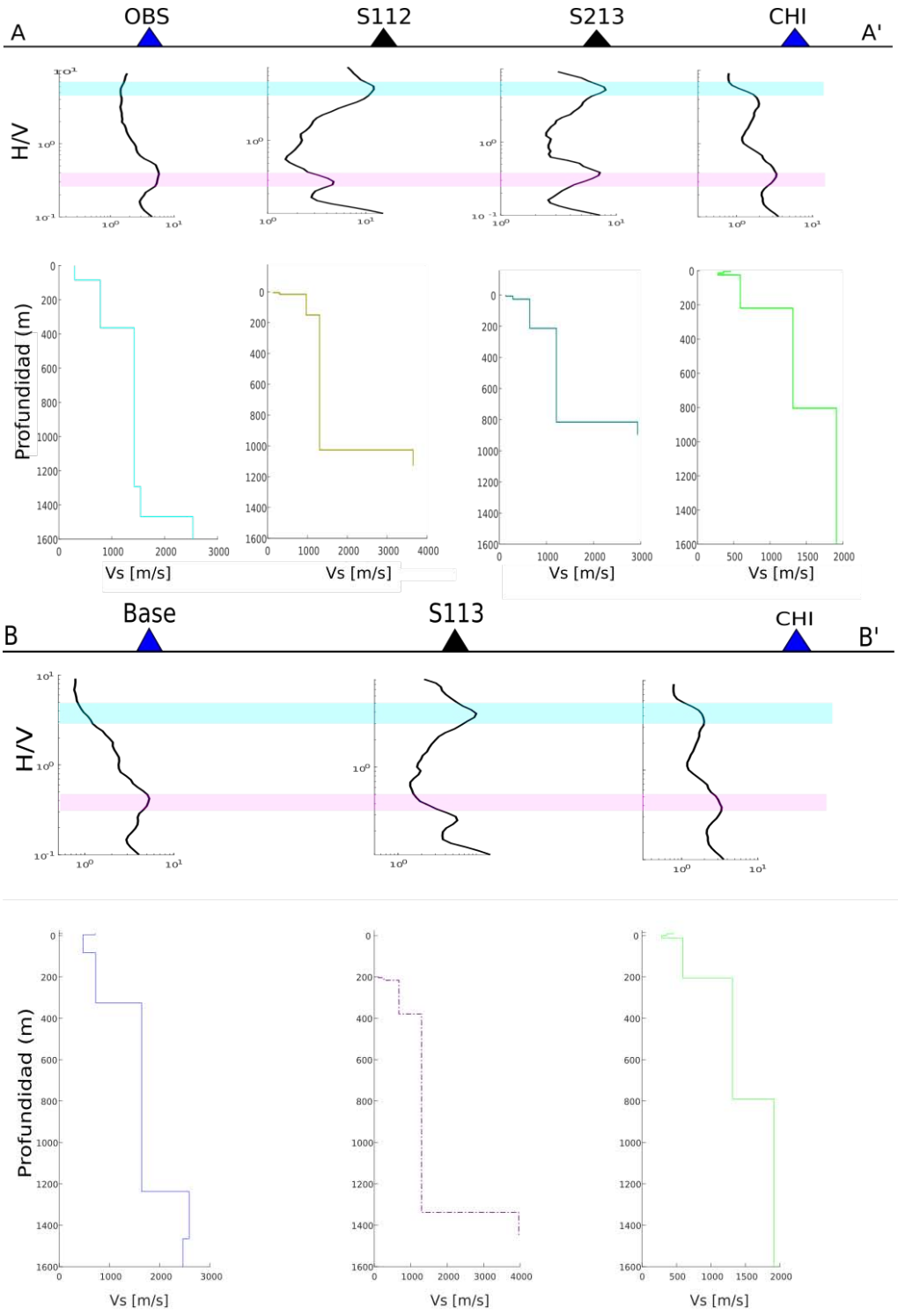

Figura 2.12: Muestra los perfiles que se han señalado en la Figura (2.1). (arriba) Perfíl de A-A' que contiene las estaciones OBS, S112, S213, CHI. Muestra las curvas H/V y modelos de velocidad de onda S para cada estación. (abajo) perfíl de B-B' que contiene las estaciones DCP,BASE, S113, CHI. Muestra las curvas H/V y modelos de velocidad de onda S para cada estación.

rección NNO-NNE que comprenden las estaciones OBS, S112, S213 y CHI y B-B' con dirección NO-NE que contienen las estaciones DCP, BASE, S113 y CHI marcados en la Figura 2.1, donde se muestran las curvas H/V y los modelos de velocidad para cada estación del perfil. Se recalcan las heterogeneidades laterales y verticales entre estaciones relativamente cercanas.

En las curvas de H/V de los perfiles se observan que los picos de baja frecuencia disminuyen de valor conforme nos acercamos al centro de la bahía, lo que revela un mayor espesor de sedimentos en el centro de la bahía o una velocidad menor. Los valores de la amplitud de este pico disminuyen de NNO-NNE. Esto refleja un contraste de velocidad moderado en las estaciones de tierra y más bajo en las estaciones marinas, las capas que controlan este contraste de velocidad se encuentran entre los 800 y 1500 m de profundidad.

Los modelos de velocidad presentan variaciones laterales entre capas conforme nos movemos del borde de la caldera al interior de ésta. Se observan dos capas comunes en los primeros 1600 m de profundidad entre las estaciones, con características similares, donde la velocidad disminuye y el espesor aumenta en el centro de la bahía. Además, se observa un espesor menor y más capas superficiales diferenciadas en el parte este que en la parte oeste del borde de la caldera.

Estas diferencias de espesores de depósitos de igual material y capas en el lado este se pueden deber a la superposición de materiales nuevos generados por las erupciones recientes y a la distribución heterogénea de los productos y lavas de las erupciones que han formado la isla [22, 288, 247]. Por ejemplo, las últimas erupciones del 1967-1970 se localizan en el norte, cerca de las estaciones de OBS, C70 y CHI. Así las capas muy delgadas y superficiales de la parte noreste de las estaciones de C70 y CHI se podrían deber a los depósitos de los materiales de estas erupciones recientes, que en las estaciones del oeste (DCP y BASE) no se encuentran.

Por otro lado, se describen tres cuencas submarinas que conforman Puerto Foster [77, 265]: la Subcuenca 1, que ocupa todo el norte de la bahía, separada de la Subcuenca 2, que va desde el *Stanley Patch* a bahía Balleneros por una monoclina en ENE relacionada con una falla NNO-SSE [77], y la Subcuenca 3 localizada en la bahía Fumarolas. Las subcuencas están rellenadas por distintas capas de sedimentos. Se observa que la Subcuenca 1, que alcanza

mayores profundidades, está hundida y se interpreta que el hundimiento de su parte suroeste fue acompañado por un levantamiento en la zona noreste [265]. En los perfiles de la Figura 2.12 se observa este levantamiento de bloque en la parte este, donde las capas de iguales características van apareciendo a menores profundidades cada vez y reduciendo sus espesores. Además, hay que tener en cuenta que, en la zona noreste, hasta Fumarolas, se centra el sistema hidrotermal, donde encontramos las estaciones OBS, S112, y CHI. Las curvas H/V de estas estaciones presentan picos anchos de baja amplitud, que se relaciona con un medio muy fracturado por el que circulan aguas calientes. Estos picos controlan un contraste de velocidad moderado entre los 800 y 1500 m de profundidad. Así el sistema hidrotermal se extendería hasta los 1500 m de profundidad. Como se ha mencionado anteriormente, el sistema hidrotermal altera los materiales con los que interacciona y puede que la reducción de espesor en el este se deba a dicha interacción.

2.7. Conclusiones

En este trabajo se aplica la técnica de H/V basada en la interpretación de la relación entre las amplitudes espectrales de las componentes horizontal y vertical de las vibraciones sísmicas de fondo y la inversión conjunta con curvas de dispersión para mitigar los problemas de no unicidad. Este método rápido y no invasivo se ha utilizado para estimar la estructura poco profunda de la Isla Decepción, en la Antártida. Se han utilizado series largas de registro de ruido ambiental de diferentes estaciones terrestres desplegadas en la costa interior y un array de estaciones marinas en el interior de la bahía de Isla Decepción, con lo que se han mejorado los estudios de ruido observando la estabilidad de los picos y se ha obtenido un modelo del subsuelo de la costa y bahía interior de la Isla más completo. Lo que aporta más información sobre las propiedades del medio cuyo conocimiento es importante para mejorar la interpretación de la actividad sísmica del volcán como por ejemplo la actividad de largo periodo que es más superficial relacionada con el sistema hidrotermal de la isla [6].

Se observa un patrón de picos que responde al comportamiento de una cuenca geotermal con los picos estrechos de menor frecuencia en el centro

de la bahía y aumentando un poco las frecuencias y la anchura de pico en el borde en la costa interior de Puerto Foster. Por lo que presentarían un mayor espesor de los depósitos y un mayor contraste de impedancia entre el sedimento y el basamento en el interior de la bahía, que en el margen de la depresión de la caldera en la costa interior de la bahía. Además, los picos de FUM y CHI tienen baja amplitud y son anchos, por lo que se relacionan con áreas de sedimentos sobre rocas fracturadas que favorecen la circulación de agua caliente.

Se mejora el modelo previo obtenido por Luzón et al. [199] para las capas más superficiales del área de los sitos de la costa interior de la bahía donde están localizadas las estaciones y para las estaciones de fondo marino del interior de la bahía. Esta mejora la aporta la curva experimental H/V que recalca la presencia de contrastes de velocidades. Así, las curvas H/V definen mejor las capas más superficiales y nos permiten explorar los primeros km de la corteza.

Se aplica el método H/V a estaciones de fondo marino instaladas en el interior de la bahía. Se definen cuatro capas superficiales de sedimentos en los primeros 1500 m, con la restricción de que las curvas de dispersión no son justo las del sitio donde se localizan los OBS y no contemplamos los efectos de la capa de agua, por lo que el contraste que controla el pico de alta frecuencia sería más fuerte al mostrado. No se ha resuelto el modelo para la profundidad de 2000 m donde se encontraría la anomalía de baja velocidad descrita por [330]. Recomendamos realizar curvas de dispersión con el array de estaciones de fondo marino y con muchos puntos de medición.

Se diferencian tres grupos de modelos de tierra: modelos de la costa este, modelos costa oeste y modelo FUM. Se observa heterogeneidades laterales y verticales entre las estaciones. Los modelos de la costa oeste presentan capas de mayor espesor y más rápidos. Se identifican varias capas; una capa superficial de depósitos post-caldera más o menos consolidados, una capa intermedia depósitos de OCTF y una capa profunda de depósitos de pre-caldera. Los modelos de la costa este presentan capas de menor espesor y más lentos. Se observa unas capas superficiales afectadas por el sistema hidrotermal constituidas por depósitos post-caldera más o menos consolidados y una capa intermedia de depósitos de OCTF. El modelo FUM presentan

capas más superficiales, delgadas y rápidas.

Se encuentran evidencias del sistema hidrotermal en las estaciones FUM, OBS, CHI Y S112, S113, S114 desde la parte NE cruzando la bahía y en el NO. El sistema hidrotermal se extiende al menos hasta los 1500 m en el interior de la bahía y en las estaciones de tierra hasta 2500 m profundidad en CHI y 1500 m en OBS.

Capítulo 3

Detection of long-duration tremors at Deception Island volcano, Antarctica

Summary

We analyze seismic data from permanent seismic stations located on Deception Island volcano, Livingston Island, and Cierva Cove, Antarctica, and identify a type of signal named Deception long-duration signals (DLDS). They are characterized by low amplitudes, long durations (several hours to days), frequency content limited to the 0.5–5 Hz band, and are detected only at Deception Island. We develop a semi-automated method to systematically detect the occurrence of DLDS during February 2008–January 2015. We identify 276 DLDS episodes with amplitudes in the range of 0.5–2 μm/s and durations from 3 h to 13 days. The temporal distribution shows an annual modulation, suggesting a seasonal effect. DLDS activity generally increases during the austral winter, although the annual distributions display two different behaviors. Some of them have a single maximum in the winter, while others are bimodal and show a second maximum during spring. Several mechanisms can explain the occurrence of long-duration signals. However, the only mechanism that explains the spectral content, duration, temporal distribution, and station coverage of the DLDS is the occurrence of volcanic tremors. Tremor generation at Deception Island has been explained by the resonance of fluid-filled conduits within the hydrothermal and/or shallow vol-

canic conduits. However, the long durations of the DLDS require a triggering mechanism that could be active for a long time span. The seasonal modulation of the DLDS suggests the influence of external effects. Most DLDS episodes can be related to periods with high-amplitude oceanic microseisms, which can induce an external forcing and introduce pressure variations in the volcanic/hydrothermal fluids. However, in some cases DLDS occur independently from oceanic noise amplitude. These cases precede summer surveys with large numbers of seismic events, indicating an increasingly restless state of the volcano. They can be produced by triggering mechanisms of internal, volcanic origin, such as the occurrence of changes in the stress distribution in the volcano edifice induced by magma dynamics, or fluctuations in the rate of volcanic gas supply.

3.1. Introduction

Seismic signals with long durations (hours or days) are a common occurrence in seismic records throughout the world. They originate from several, different dynamic processes that lead to the continuous release of elastic energy in the shallow crust. Long-duration signals include: microseisms generated by atmosphere-ocean-land interactions; volcanic tremors produced at volcanoes; non-volcanic tremors related to fault creeping in subduction zones; vibrations produced by wind gales and other local meteorological phenomena; ground motions induced by glacial dynamics, and anthropic noise generated by human activities.

All these signals have been traditionally regarded as seismic noise, mainly due to our inability to extract useful information from them. However, the definition of seismic noise is subjective. A particular seismogram may be referred to as signal or noise, depending on the purpose of the study.

In fact, many of these long-duration signals, previously treated as noise, are currently being re-evaluated, using newly developed methods and capabilities, for applications including investigations about the Earth's structure [76, 155, 156, 243, 317], detailed dynamics of tectonic motions in subduction zones and strike-slip faults [37, 276, 286] interactions between the atmosphere-ocean-land systems[322, 36, 215, 212, 18], and ice dynamics in

glacial environments [94, 318].

In particular, volcanic tremor is a continuous signal recorded at most volcanoes around the world. The analysis of volcanic tremors is crucial to characterize the volcano plumbing systems and identify active portions; understand the interactions between the volcanic fluids and the surrounding crust; and even to produce eruption forecasts [75, 176, 217]. Additionally, it has forced the development of several techniques for seismic source tracking and location, such as array methods[12, 7, 86, 120, 220, 280] and amplitude locations[30, 29, 179].

In this paper, we analyze seismic data from permanent seismic stations located on Deception Island volcano, Livingston Island, and Cierva Cove, Antarctica. We observe the occurrence of long-duration signals with different characteristics. In particular, at Deception Island volcano we find the occasional occurrence of low-amplitude, sustained seismic signals with energy confined within the 0.5–5 Hz frequency range and variable durations up to a few days. For these signals, we investigate waveforms, spectral contents and temporal distribution. We compare them with the data from other sites, and conclude that at least some of these signals are volcanic tremors.

3.2. Geological setting

The area of the Bransfield Strait is among the most interesting regions in Antarctica, from a geodynamic point of view (Figure 3.1). It is located in a complex regional tectonic framework characterized by the confluence of two main plates (South American and Antarctic) and three microplates (Scotia, Phoenix and South Shetland) [24, 107, 108, 121, 139, 183]. The Bransfield Strait separates the South Shetland and Antarctic plates. It constitutes a spreading center aligned in NE-SW direction through three adjacent basins, and it is characterized by the presence of normal faults and active volcanism [249, 152, 272]. Most earthquakes in the region are shallow, with depths b40 km [249]. A few deeper earthquakes have been identified NW of the South Shetland Islands, which is consistent with the subduction of the Drake Plate [152]. Many of these shallow earthquakes are clustered around volcanic centers,which suggest that they probably have a volcanic or volcano-tectonic

origin, triggered by intrusive magmatic activity [94, 272]. Subareal volcanoes

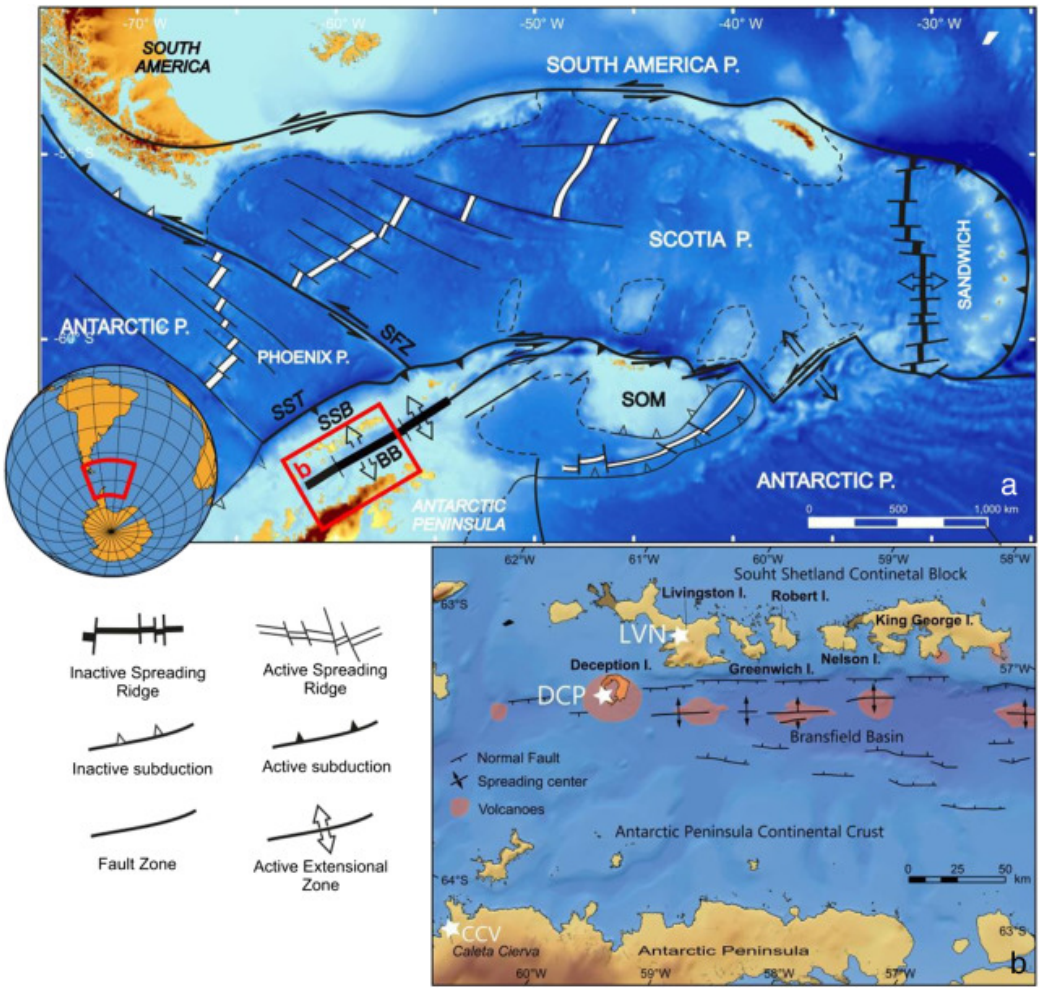

Figura 3.1: (a) Map of the Scotia area, showing the most important plate boundaries and the area of study (red box). SST = South Shetland Trench; SSB = South Shetland Block; SFZ = Shackleton Fracture Zone; BB = Bransfield Basin; SOM = South Orkney Microcontinent. (b) Map of the Bransfield Strait, displaying the positions of normal faults, spreading centers, and volcanic edifices. The seismic stations used in this study are depicted by white stars.

in the Bransfield Strait are Deception, Penguin, and Bridgeman Islands. There are also several submarine seamounts and remnant volcanic centers south of Livingston, Greenwich, and King George Islands [e.g. 185, 290]. Recent vol-

canic in this region has been dominated by the eruptions of Deception Island, which is among the most active and hazardous volcanoes in Antarctica. 20 eruptions have been documented in the 19th and 20th centuries [28, 235, 290]. The last eruptions occurred in 1967, 1969 and 1970 [e.g. 290]. There are also fumarolic emissions, hydrothermal activity, deformation episodes, and a moderate, highly variable, level of seismic activity [63, 64, 150, 291, 316]. Deception Island is one of the busiest zones in Antarctica, especially during the austral summer. It is visited annually by dozens of scientists and military personnel, and thousands of tourists. This fact highlights the importance of volcano monitoring for hazard mitigation [28, 63].

3.3. Instruments and data

The data we use come from a permanent network set up by the Andalusian Institute of Geophysics of University of Granada, Spain (IAGUGR). Three broadband seismometers were installed in February 2008 in the area of the Bransfield Strait. They form a N-S profile about 170 km long, which is approximately perpendicular to the Bransfield Rift. Stations are located within different geodynamical contexts:(1) LVN (62°39′S, 60°23′W) located near the "Juan Carlos I" Spanish base at Livingston Island, in the South Shetlands micro-plate; (2) DCP (62°59′S, 60°41′W) near the "Gabriel de Castilla" Spanish base at Deception Island volcano, located on the extension axis of the Bransfield Rift;and (3) CCV (64°09′S, 60°57′W) near the "Primavera" Argentinean base, on the Antarctic plate (Figure 3.1).Each station is equipped with an electrochemical, three-component, broadband (16 s) seismometer Eentec SP400; and a low power, 24-bit data-logger Eentec DR4000. Stations are powered with batteries and solar panels [63].

Seismic data are recorded in miniseed format [2] on a hard disk with an estimated capacity for 20 months of data. The amount of data generated is around 10 GB per year and station. The stations are visited once a year to perform basic maintenance and recover the seismic data.

These three stations have operated continuously since 2008, except for a few winter periods when the power supply temporarily failed resulting from the harsh environmental conditions. This represents the first time that

unsupervised, permanent-recording stations have operated efficiently for several years at the selected sites. This fact is especially important for the seismic monitoring of Deception Island volcano. The only precedent is the SEPA experiment carried out in the Bransfield Strait area between 1997 and 1999 [272]. Since 1994, Deception has been monitored intermittently, during summer surveys (December–February) under the Spanish Polar Program [63, 146, 148]. The present dataset provides the unique opportunity to study the long-term seismic activity of Deception Island volcano and the Bransfield Strait area since 2008 (including the austral winter periods), which has never been achieved.

3.4. Data analysis

We perform a preliminary analysis of the seismograms based on the SEISAN package [135]. Seismic data are incorporated into a continuous database, and a visual inspection of the seismograms is carried out using 30-minute windows. This allows for the identification of different types of seismic events, and the characterization of their waveforms, durations, spectral contents, temporal distributions, etc.

During this process, unusual signals were identified at DCP, that were not recorded at LVN or CCV. These signals have low amplitudes and may last for a long time (several hours or days). (Figure 3.2) shows seismograms and spectrograms of the ground motion recorded at the three stations for a ten-day-long time interval. Focusing on the 0.5–5 Hz band, there is virtually no energy recorded at LVN and CCV, while at DCP there is a signal lasting for N8 days. We refer to this kind of signals as Deception long-duration signal (hereinafter DLDS). The DLDS is a continuous signal with average amplitudes varying slowly over time scales of hours. However, zooming in their waveforms (Figure 3.3), it becomes evident that they are formed by a continuous series of energy packets. Particle motions are basically chaotic and do not show any preferred polarization, apart from a general dominance of the horizontal motions. The amplitude of the vertical component is generally around 60 % of the horizontal amplitudes (Figure 3.4). Due to their low amplitudes and sustained durations, DLDS are hardly identifiable during the

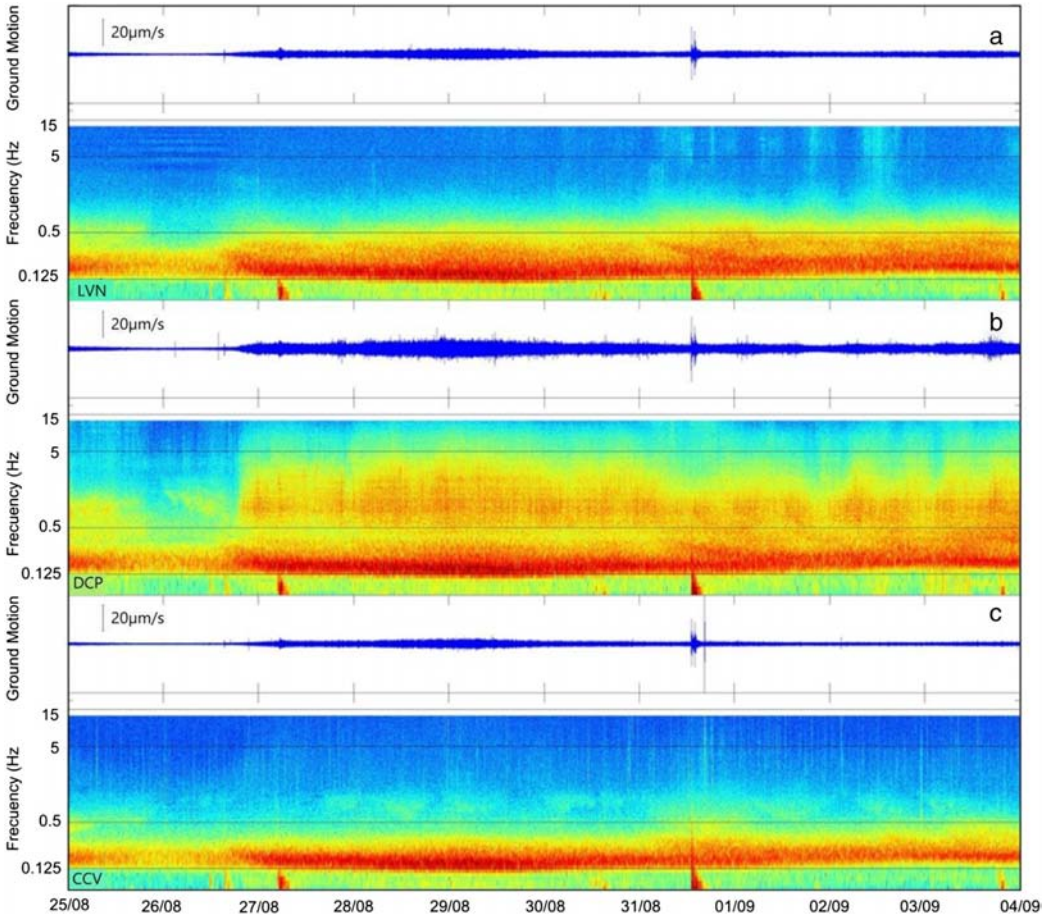

Figura 3.2: Examples of vertical-component velocity seismograms and spectrograms for the three stations LVN (a), DCP (b), and CCV (c). The horizontal lines indicate the frequency bands selected for the analysis. Notice that the frequency axis in the spectrogram is displayed in logarithmic scale. The data correspond to ten days starting on 25/08/2012.

routine inspection of seismograms. The comparison between data from LVN, DCP, and CCV, is essential to achieve the identification of these signals.

For our study, we selected a continuous seismic dataset extending from February 2008 to January 2015. This dataset is long enough to identify the average characteristics of the DLDS and their temporal behavior patterns.

Given the large amount of data, an efficient procedure is required in order to identify and quantify the occurrence of DLDS.

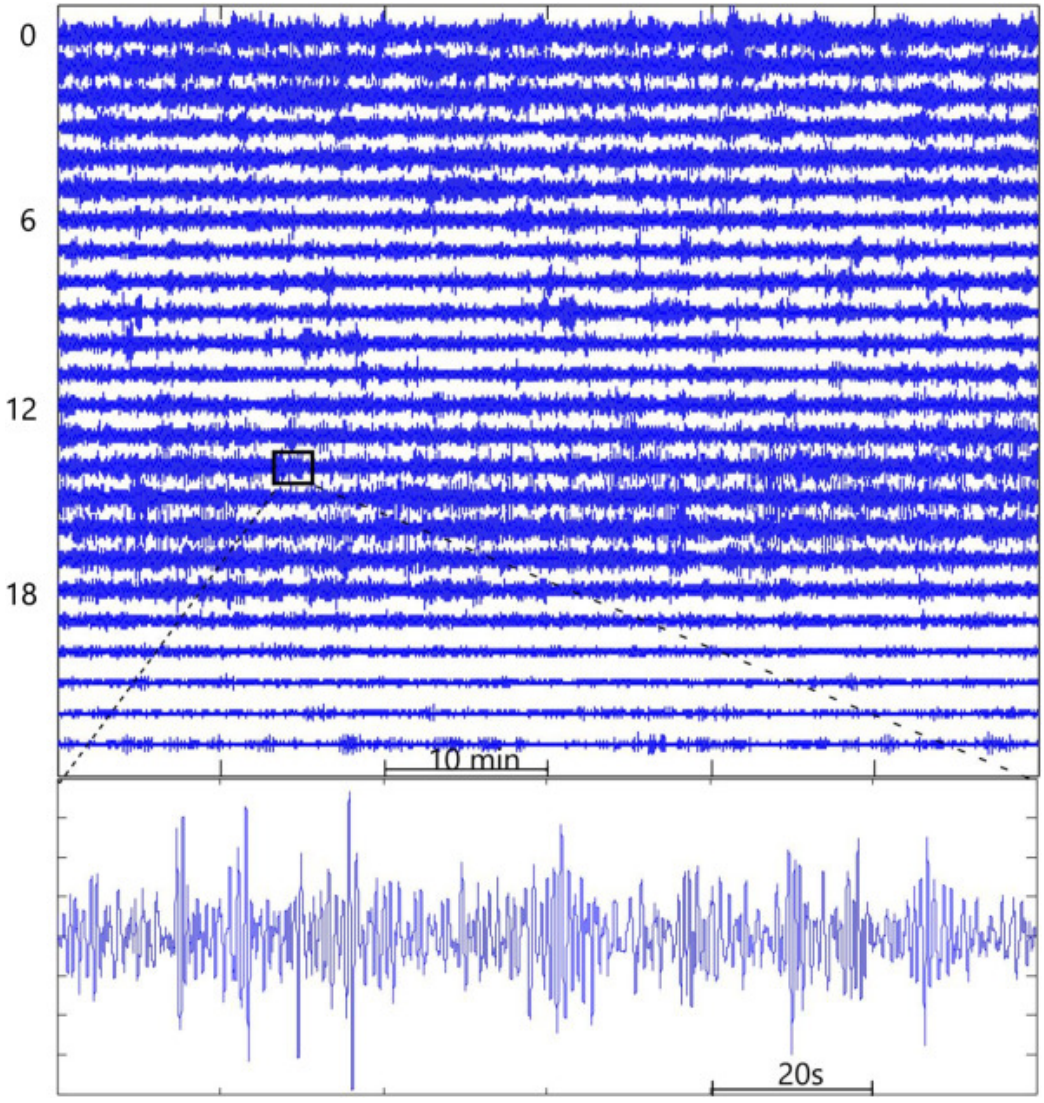

Figura 3.3: Example of the waveform of the final stages of a DLDS recorded at DCP. We show the vertical-component seismogram recorded on 20/09/2009. The top panel corresponds to 24 h; the bottom panel displays 2 min of data.

Several methods can be applied to detect DLDS with limited computational and operational efforts. Some of them are based on the parameterization of the characteristics of seismic events, in order to achieve an automatic detection and classification [32, 33, 43, 61, 82, 92, 119, 149]. Other methods use

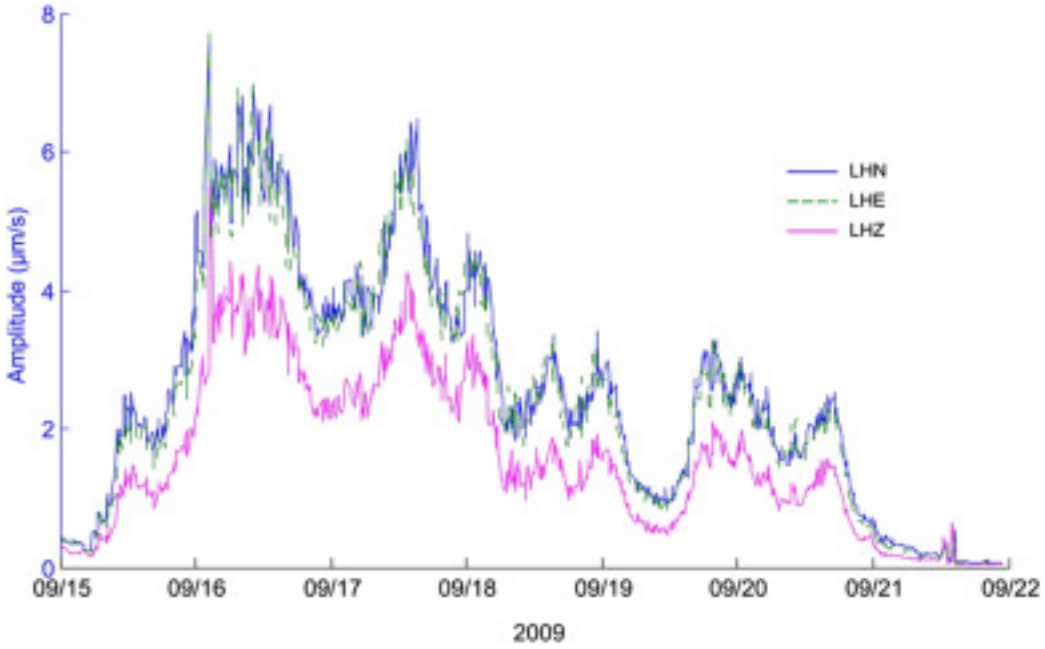

Figura 3.4: Comparison of the average amplitudes on the three components of ground motion for a DLDS episode recorded at DCP between15/09/2009 and 21/09/2009.

simpler approaches based on the variations of the seismic amplitude envelope, which do not require any training or a priori information. For example, the real-time seismic amplitude measurement (RSAM) method [96, 256] evaluates the average seismic amplitude in long-duration time windows, independent of the seismicity they may contain. Related to the RSAM method is the seismic spectral amplitude measurement (SSAM) method [190, 257, 297], in which, the amplitude information obtained from the signal spectrum is averaged in several narrow frequency bands.

In this work, we adapt the essence of the RSAM and SSAM philosophies and develop a semi-automated method to detect the occurrence of DLDS. This method is based on the distribution of seismic energy in a few, selected frequency bands. The choice of these frequency bands is crucial. It is based on the knowledge of the different types of events recorded and the expertise accumulated during our work on Deception Island since 1994. The method calculates the seismic energy density of the vertical-component seismogram

in the selected frequency bands, averaged in long-duration windows.We will refer to this energy as "filtered and averaged seismic energy" (FASE). We make a careful selection of the frequency bands, so that each band represents particular types of seismic signals. This focused selection simplifies the interpretation of the results and constitutes an improvement over the RSAM or SSAM methods, where the average energy was blindly calculated in a single band (RSAM) or in multiple narrow bands (SSAM).

We select four bands for the FASE calculations. The lower limit is defined by the instrumental response of the seismometer, which in our case is flat between 16 s and 50 Hz.

The first band (F1) extends from 0.07 to 0.125 Hz (8–15 s). In this band, the only signals that may contribute are teleseismic events or very-long-period (VLP) volcanic signals. At Deception Island volcano broadband seismometers have been occasionally deployed, but no VLPs have been ever reported [65]. Therefore, we expect that the F1 FASE will correlate with the occurrence of teleseisms.

The second band (F2) ranges from 0.125 to 0.5 Hz (2–8 s). In this band we find the dominant contribution to be oceanic noise. This microseismic noise constitutes a background signal that is recorded everywhere in the Earth [17, 177, 298, 299], originating from perturbations in the ocean-atmosphere system.

The third band (F3) extends from0.5 to 5 Hz. This frequency band is generally named "long-period" in Volcano Seismology [e.g. 74, 75, 217]. Long-period (LP) events and volcanic tremor, which are among the most characteristic signals in active volcanoes, are quasi-monochromatic signals with dominant frequencies in the 0.5–5 Hz range. At Deception Island, several studies indicate that LP events and volcanic tremors also lay within this frequency band [6, 65, 63, 146, 150].

The fourth band (F4) ranges from 5 to 15 Hz. A variety of seismic events can contribute to this high-frequency band, for example, tectonic and volcano-tectonic (VT) earthquakes, hybrid events, ice-quakes and glacial dynamics [5, 97, 122, 123, 124, 150, 182]. These signals usually have a wide frequency content, occasionally extending well below and above the F4 band. Other sources of seismic energy that may be present in this band are

noise produced by local weather (wind and storms), cultural noise, etc.

For each of these bands, we calculated FASE as the spectral power density of the vertical-component seismogram in the selected frequency band, averaged in long time windows. We used a moving window of 10 min, with an overlap of 5 min, for the whole 7- year study period. This analysis is principally focused on long-lasting signals, and prevents the detection of isolated transient signals such as local earthquakes, icequakes, etc. However, they may still be detected when they occur closely in time, forming seismic swarms.

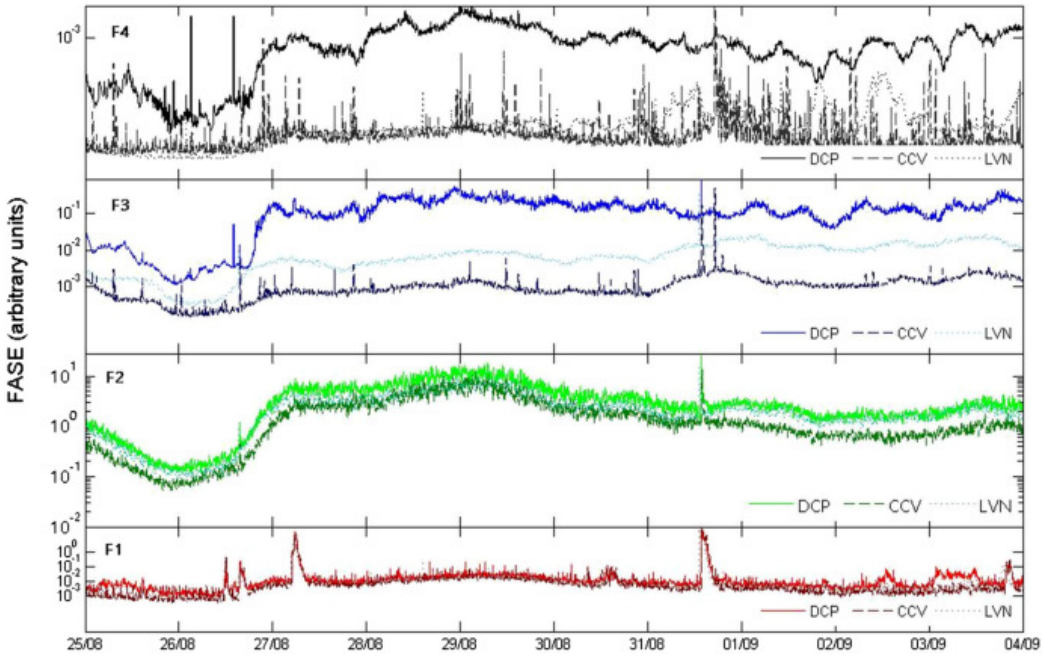

Figura 3.5: Example of FASE measured in the F1, F2, F3 and F4 bands for the three stations LVN, DCP, and CCV. The time window extends for ten days, starting on 25/08/2012 (the data shown in Figure 3.2). The FASE axes are displayed in logarithmic scale.

Figure 3.5 shows an example of FASE estimates for the LVN, DCP and CCV stations. The dominant seismicity patterns can be identified from the relative importance of the FASE in the different bands.

About 90 % of the time, there is a clear energy prevalence of the F2 band, corresponding to a seismic wave field dominated by the contribution of oceanic microseism. The level of energy can be so large that it occasionally leaks

into the adjacent bands (F1 and F3). In the F2 band, the seismic data show long-lasting wave trains with slowly varying amplitudes, and consequently FASE displays smooth variations. In the F1 band, FASE is characterized by the occasional occurrence of narrow peaks with durations smaller than a few hours, corresponding to teleseismic surface waves. In the F3 and F4 bands, we observe sporadic signals lasting several hours or days. The F4 band generally displays the smallest values of FASE. The F3 and F4 bands are very variable, sometimes following similar trends.

If we compare the FASE results for the three stations LVN, DCP and CCV, we observe that they are basically identical in the low-frequency bands F1 and F2, while we find notable differences in the high frequency bands F3 and F4 (Figure 3.5). These similarities and differences are also evident in the spectrograms (Figure 3.2). The similarity of the level and temporal variations of FASE calculated at stations separated by several tens of kilometers suggest the contribution of a common, distant seismic source located at regional distance. In contrast, FASE differences among stations instead point to dominant contributions from local sources.

Stations LVN and CCV usually present a similar trend in the F3 band, although the absolute values of FASE can be different. However, station DCP sometimes shows a completely different amplitude pattern compared to the other stations, with much higher FASE values and an independent energy trend (Figure 3.5). These differences are related to the occurrence at DCP of DLDS, which are basically confined to the F3 and are not recorded at LVN and CCV. Finally, in the F4 band, the three stations show different FASE patterns and absolute values. At DCP, FASE in the F3 and F4 bands sometimes show similar trends.

3.5. Results

Using the procedure described above, we have identified the occurrence of DLDS searching for periods when FASE in the F3 band is high at DCP, and shows a different trend compared to the F2 band, which generally contains the highest energy density. We have also compared the results with stations LVN and CCV, to corroborate that the detected signals are indeed DLDS. In

this way, we have identified 276 DLDS episodes during the period between 2008 and 2015.

Although DLDS are basically contained within the F3 band, they have slightly different frequency contents. For example, we find signals extending from 3 to 5 Hz (Figure 3.6a) and from 0.5 to 5 Hz (Figure 3.6b, c). For some DLDS, part of the energy may occasionally leak into the F4 band. The FASE peaks in the F3 band usually coincide with periods of high FASE in the F2 band. However, this is not always the case, and we occasionally find peaks in the F3 FASE that are not temporally related to high F2 FASE (Figure 3.6b).

DLDS are characterized by low amplitudes (in the range 0.5–2 μm/s; Figure 3.7a) and highly variable durations (ranging from3 h to $>$ 13 days;Figure 3.7b). The most frequent durations are around 15–40 h. These long durations suggest a remarkably stable source mechanism. Both amplitude and duration remain within similar limits during the whole period analyzed, and there is no evident temporal pattern. Similarly, there is no clear relationship between duration and amplitude of the DLDS.

The temporal distribution of the DLDS between 2008 and 2015 is shown in Figure 3.7 and Figure 3.8. In Figure 3.7 we show the occurrence of individual DLDS episodes, while in Figure 3.8 we present the cumulative duration of DLDS computed on a monthly basis. Given the large variability of the DLDS durations, we believe that this representation provides an improved picture of the overall DLDS activity. We observe that DLDS occur during the whole period, with activity of up to 200–600 cumulative hours (8–24 days) per month. These numbers indicate that DLDS are a common occurrence at Deception Island volcano.

The most striking characteristic of the temporal distribution of DLDS is the annual periodicity. Most part of the DLDS are recorded in the period from June to October (around the austral winter),which suggests a seasonal effect. The annual maximum is reached in winter in 2008, 2009 and 2012; in late autumn in 2010; and in early spring in 2011, 2013 and 2014.

In addition, we find two types of annual distributions. In the first pattern, there is a single dominant peak around the winter. This is observed in 2008 (July) and 2010 (June). In the second pattern,we find a bimodal distribution

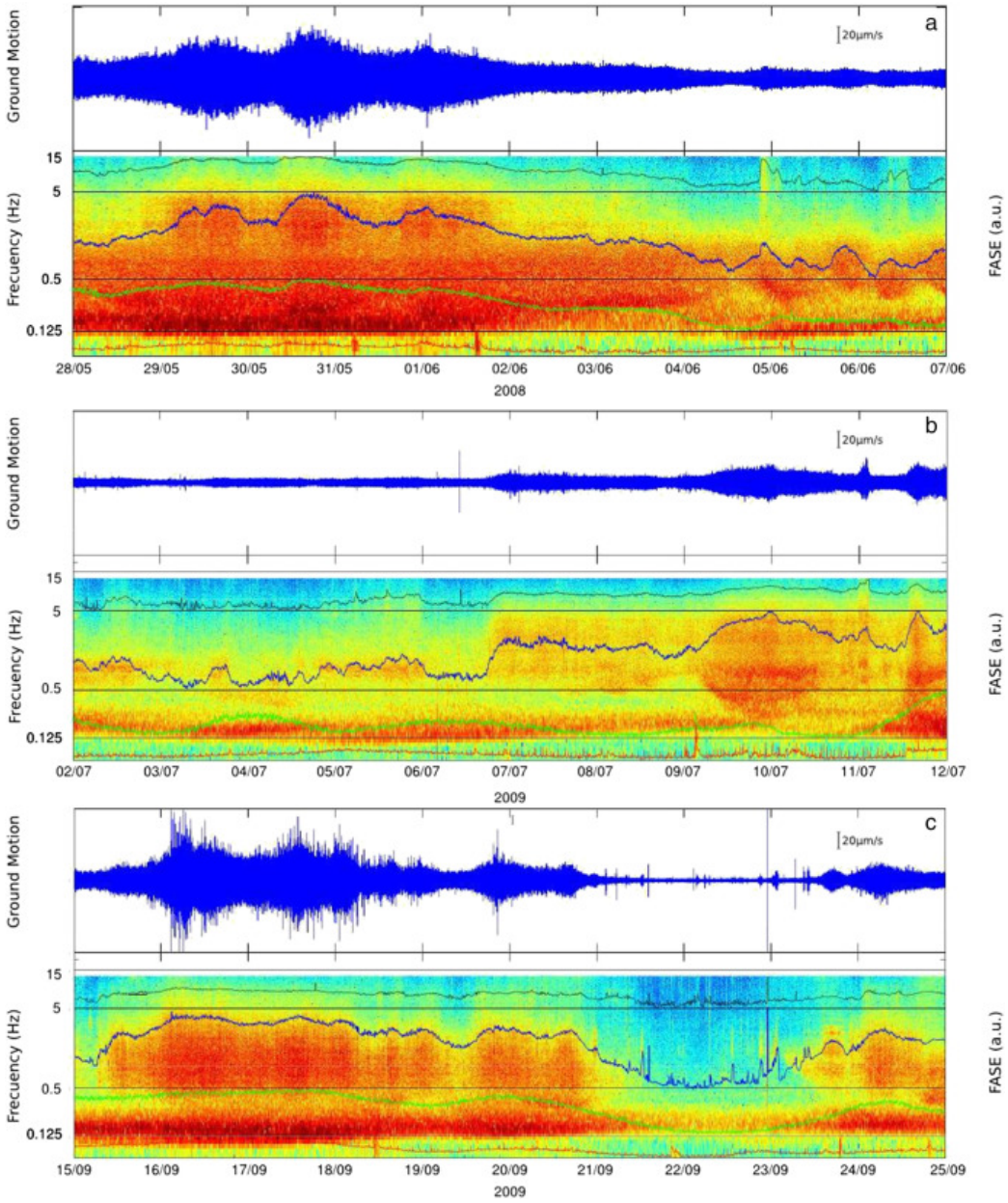

Figura 3.6: Examples of seismograms and spectrograms of DLDS recorded at DCP. The horizontal lines indicate the frequency bands selected for the analysis. The frequency axes in the spectrograms are displayed in logarithmic scale. Within each band, we plot FASE in a relative scale. FASE colors are the same than in Figure 3.5.

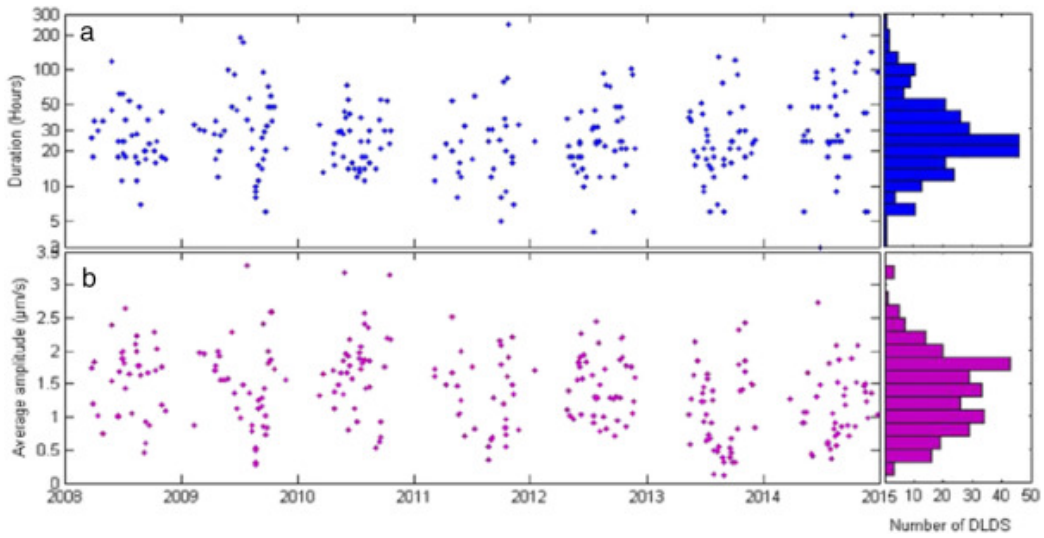

Figura 3.7: Representation of: a) the durations (top) of the DLDS as a function of time and histogram (right); b) average amplitudes (bottom) of the DLDS as a function of time and histogram (right). Notice that the durations are represented in logarithmic scale.

with two separate peaks. This occurred in 2009, 2012, 2013 and 2014. These peaks are observed in August and October in all cases except in 2009, when they occur in July and October. Although they are not observed exactly in the same months, in these years, there is one peak in winter and another peak in early spring. The distribution of DLDS during 2011 is quite peculiar and different from the distributions for the other years. There is very small DLDS activity during most of the year, including the winter. The maximum rate occurs very late in the year, and the DLDS activity decreases sharply immediately thereafter.

The minimum DLDS rates are consistently observed during the austral summer. In these periods there are some seismic sources that may effectively increase the noise level and reduce our ability to detect the DLDS. Thus, the question of whether the observed annual cycle might be an apparent effect related to the low detectability of DLDSs during the summer should be addressed.

The Gabriel de Castilla Base is located at roughly 500 m from station

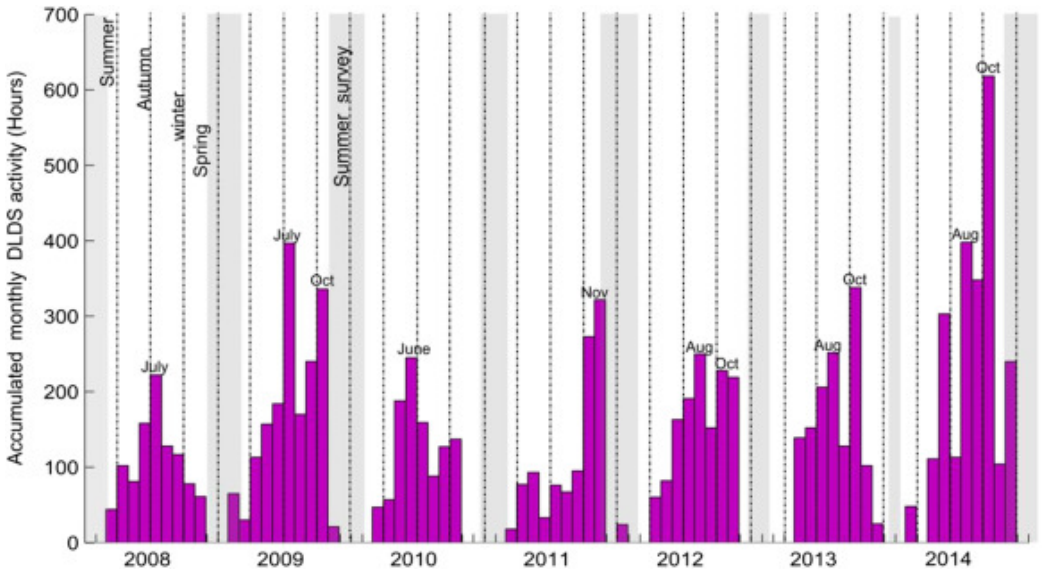

Figura 3.8: Temporal distribution of the DLDS activity recorded at DCP from February 2008 to January 2015. The bars show the total duration of all DLDS recorded during each month. The gray bands indicate the periods of operation of the Gabriel de Castilla Base during the summer surveys.

DCP and it operates from the end of spring to the end of the summer, providing support for 10–40 people. The base operations include electric generators, machinery, tow trucks, small vehicles, etc., which produce anthropic noise that may partially mask the DLDS, making them difficult to detect and identify.

Wind storms and other local meteorological effects can be another source of noise that mask the DLDS. In Figure 3.9, we show measurements of wind speed provided by the Spanish Meteorological Survey (AEMET). We observe that wind is a highly variable phenomenon, but in general, both the average wind speed and the wind speed variability increase during the winter. Nevertheless, the level of seismic noise actually recorded by the station during the winter is likely reduced due to the snow and ice coverage that isolates the seismometer from the external atmospheric conditions. It is possible that the station records more wind noise during the summer, even if the wind speed is not especially high, contributing to a greater amount of noise a reduced DLDS detectability during the summer.

We observe that often there are no DLDS around the summer, even in periods when the Gabriel de Castilla Base is closed to people. This occurs, for instance, in November 2010, March 2012, March–April 2013, and April 2014 (Figure 3.8). During these periods the DCP station has no nearby sources of anthropic noise. Unfortunately, these periods generally coincide with high-speed winds (Figure 3.9).

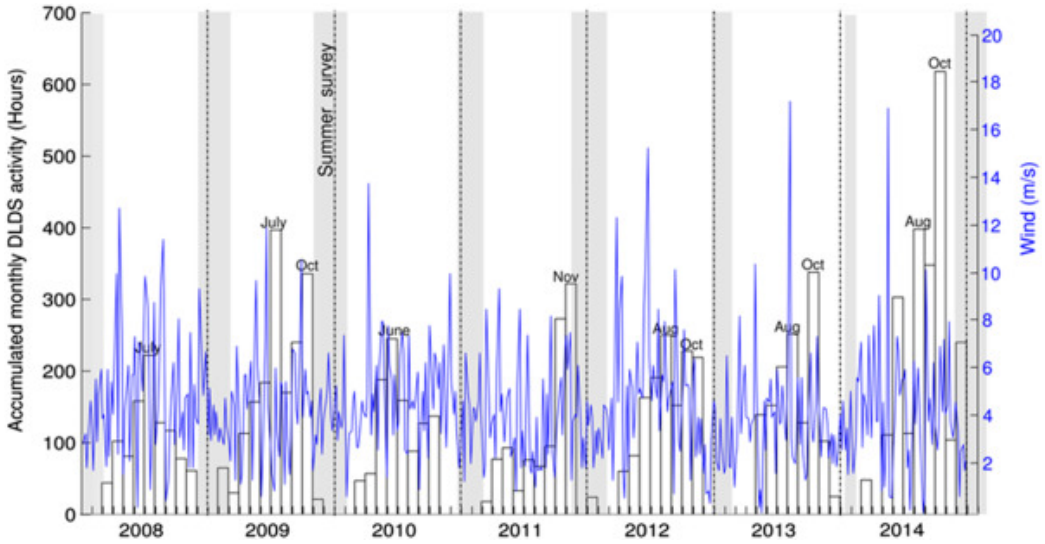

Figura 3.9: Comparison between DLDS activity at DCP (empty bars) and wind speed measured at a meteorological station located on Livingston Island (blue line). The wind speed plot has been smoothed using a median algorithm with a window length of ten days. The gray bands indicate the periods of operation of the Gabriel de Castilla Base during the summer surveys.

The detection capabilities should be homogeneous during the winter half of the year as there is no human activity nearby, and the seismometer is efficiently isolated from the local windstorms. Nevertheless, we find that the DLDS activity is not constant, and there seems to be a modulation related to the annual cycle of the seasons.

We conclude that, although anthropic and meteorologic noise may play an important role in the detectability of DLDS, there are some hints that the general decrease of DLDS activity during the summer is, to some extent, a real feature. Therefore, there is a seasonal effect in the temporal distribution

of the DLDS, although it may not be as remarkable as it appears in Figure 3.8.

3.6. Discussion

We analyzed continuous seismic data recorded at three stations located in the Bransfield Strait, Antarctica, during 2008–2015. Using an approach based on the calculation of the average seismic energy in selected frequency bands, we have identified a type of signal named DLDS, with the following characteristics: (1) they have long durations between several hours and several days; (2) they have small amplitudes and their energy is mostly limited to the F3 band; (3) they are recorded only at Deception Island; and (4) they show a seasonal trend with maximum rates during the austral winter.

3.6.1. Seismic sources producing long-duration signals

There are several processes that may generate seismic signals with long durations at Deception Island volcano, including teleseisms, ocean-atmosphere interactions, storms, wind, glacial dynamics, or volcanic processes.

Teleseisms, as mentioned above, produce low-frequency surface wave trains that may last up to a few hours with energy mostly in the F1 frequency band (Figure 3.2 and Figure 3.5). We have identified a few hundreds of these peaks, which correspond to catalogued teleseisms.

The atmosphere-ocean-land interactions are generally regarded as the origin of microseismic noise in the Earth [36, 59, 134, 169, 194, 215, 303, 322]. Atmospheric pressure variations couple with the ocean, and induce seismic waves in the seafloor, producing a continuous signal in the 2–8 s band. Temporal variations in the microseismic frequency band are related to oceanic storms [20, 21, 60, 116]. In our data, we isolate the microseismic noise in the F2 band. FASE in the F2 band correlates negatively with pressure (Figure 3.10), confirming the atmospheric oceanic origin of these signals. Nevertheless, another possibility is that DLDS could be related to the interactions of oceanic microseisms with the peculiar ring-shaped morphology of Deception Island. Seismic waves could be trapped within the inner bay, producing a re-

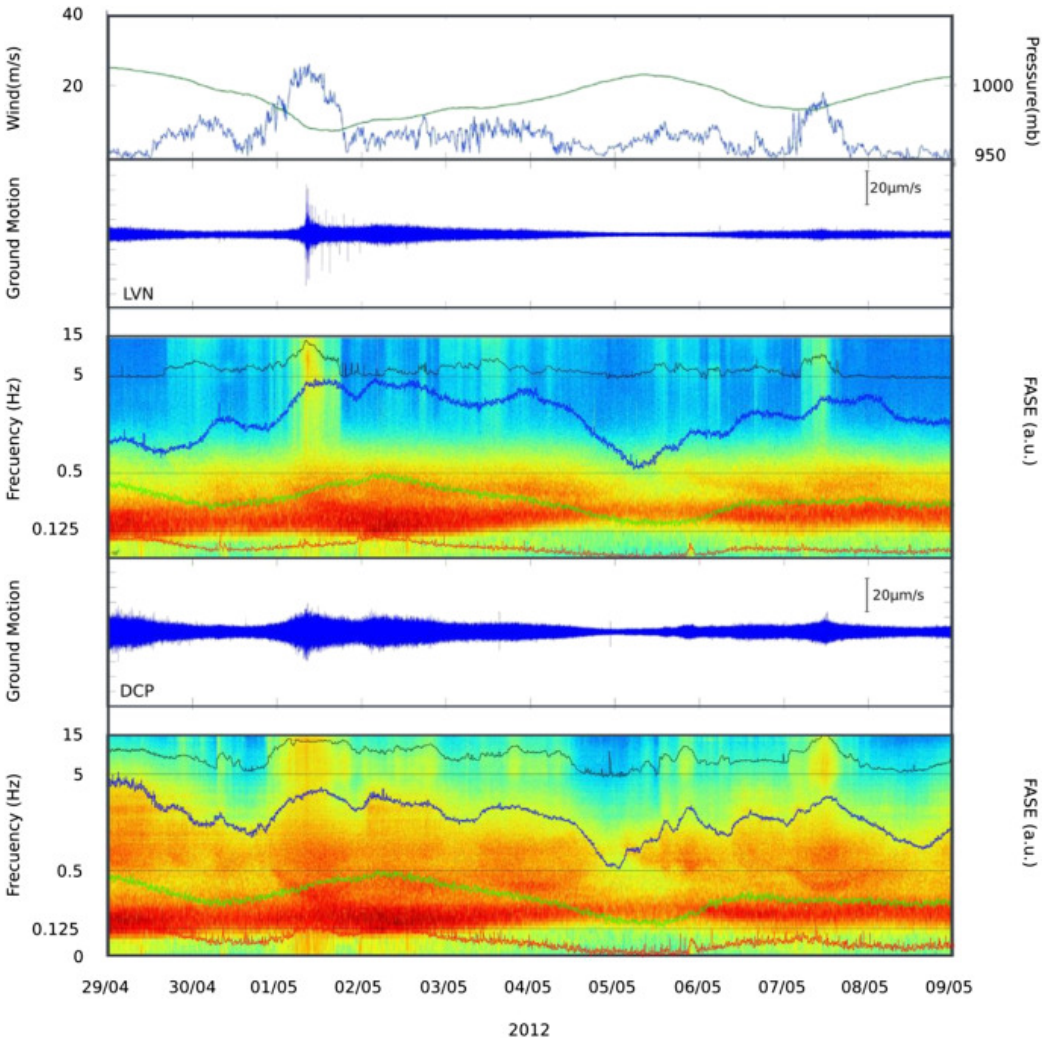

Figura 3.10: Comparison between measurements of wind speed (blue) and atmospheric pressure (green) at Livingston Island (top), provided by the Spanish Meteorological Survey (AEMET); and seismograms, spectrograms and FASE at LVN (middle) and DCP (bottom). FASE colors are F1 (red), F2 (green), F3 (blue) and F4 (black). The frequency axes in the spectrograms are displayed in logarithmic scale.

sonance that, under certain conditions, might result in an increase of energy in the F3 band.

Wind storms produce irregular bursts of local seismic noise. According to Dziak et al. [93], seismic noise above 10 Hz in the Bransfield Strait area is

dominated by the effect of wind. Therefore, we expect to find the contribution of local weather in the F4 band. In fact, F4 FASE can be directly correlated with wind speed (Figure 3.10). Moreover, we observe that F4 FASE at LVN and DCP stations display similar trends. These stations are just 40 km apart (compared to 132 km between DCP and CCV), which explains the coincidence of FASE peaks originating from wind noise.

Glacial dynamics can also produce long-duration seismic signals. Several ice-related phenomena may produce vibrations that propagate as seismic waves, for example, glacier calving, thaw water flow, ice shelf motions, iceberg detachment and disintegration, or iceberg scraping on the seafloor [255]. Some of these phenomena generate transient icequakes, although long-duration tremors have been reported as well [224, 200]. These ice-related tremors show a strong seasonal variation, reflecting the freezing-thawing cycle, and reach a maximum level in the austral summer [94, 93]. They often display a monochromatic or even harmonic character, with smoothly varying frequencies (frequency gliding). The frequency content of glacial tremors is highly variable, although the main contributions are generally found in the 0.5– 10 Hz range [71, 200, 302, 328].We therefore expect to observe these signals in the F3 and F4 bands.

Volcanic processes are another likely source of continuous signals at the Deception Island volcano. Volcanic tremors are long-duration signals (from minutes to days or weeks) typically recorded in active volcanic areas. Virtually all eruptions are accompanied by tremors, probably caused by pressure fluctuations of degassing magma [216]. However, they may also occur at volcanoes with no eruptive activity.

Several models have been developed to explain the origin of volcanic tremors, such as: the resonance of fluid-filled conduits [101, 72, 74], fluctuations in the flow of volcanic or hydrothermal fluids [164, 163], viscoelastic reaction of the magma to bubble growth and collapse [176, 270, 269], or repetitive transients produced by flow instabilities and/or stick-slip [145, 191, 283]. Volcanic tremors have energy mostly in the 0.5–5 Hz band [74], and therefore they lay fully within our F3 band.

Finally, tectonic (or non-volcanic) tremors are a continuous signal detected at active tectonic areas such as subduction zones and large trans-

form faults. They have been reported, for example, in Japan, Cascadia, and Mexico, although their global distribution is still being ascertained [276]. Tectonic tremors originate in deep (30 km) sections of major faults [e.g. 181, 214, 231]. Source models invoke slow frictional interactions at the plate interface, although several observations suggest that fluids may play an important role as well [166, 231]. Tectonic tremors may last for days and weeks, which coincides with our observations of DLDS. Moreover, tremor energy is generally contained in the 1–10 Hz range [37], which approximately coincides with our F3 band.

3.6.2. Origin of Deception long-duration signals

All mechanisms reported above are able to produce long-duration signals. However, some of them are limited to frequency ranges that do not coincide with the F3 band containing the DLDS. For example, teleseismic surface waves are confined to the F1 band; oceanic microseisms lay in the F2 band; wind noise and local storms are mostly contained in the F4 band.

The focusing effect of the morphology of Deception Island on oceanic microseisms could explain why DLDS are just recorded at DCP. However, we observe that not all strong microseisms produce DLDS, and some DLDS are uncorrelated with oceanic noise (Figure 3.6b). Therefore, there is not a clear relationship between these effects.

Glacial tremors may be contained in the F3 band. However, in our data the most common glacial signals are transient icequakes with broadband energy in all frequency bands F1–F4 (Figure 3.11). They are recorded primarily at LVN and CCV stations, which is consistent with their locations being surrounded by great glaciers. At the DCP station the ice coverage is very small compared to the other two sites. We have identified some ice-related tremors at CCV, but they are rare and have never been recorded at DCP. Additionally, glacial activity should reach a maximum during the summer, which is not observed in the DLDS.

Non-volcanic tremors have frequencies within the F3 band, as observed for the DLDS. However, this type of event should respond to a regional-scale source related to the roots of hypothetical large faults existing in the area, for

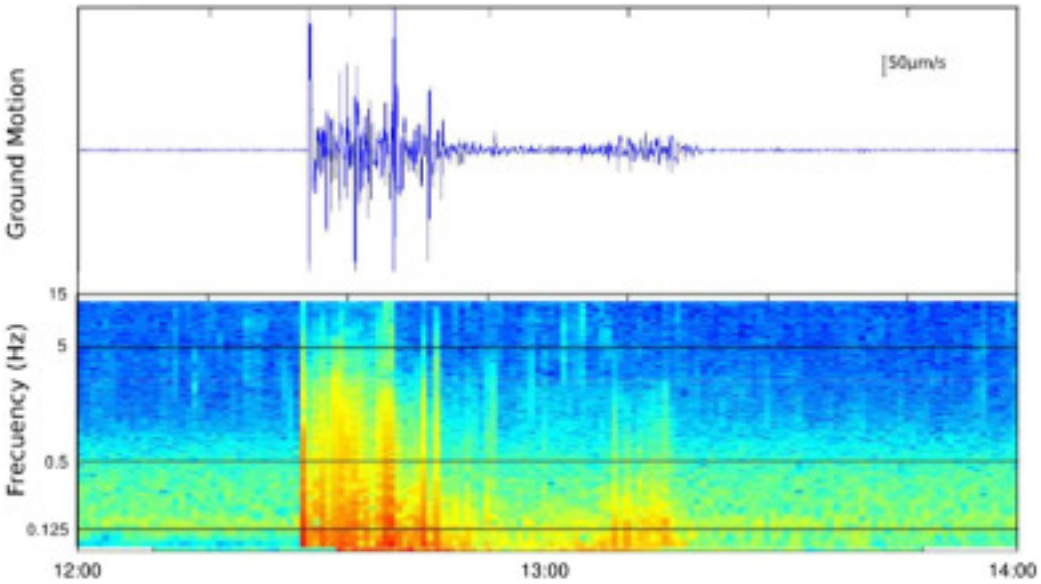

Figura 3.11: Seismogram and spectrogram of 2 h of data containing glacial signals recorded at CCV on 11/04/2010. The frequency axis in the spectrogram is displayed in logarithmic scale.

example in the South Shetland subduction zone. If the source of the DLDS were located near the base of the crust, at depths of tens of kilometers, then the DLDS should be detected at distances on the order of the source depth. Therefore, we cannot explain why DLDS are only recorded at DCP. The absence of DLDS in LVN and CCV ensures that their source process must occur within the shallow crust of Deception Island.

Therefore, we can exclude most of the effects discussed in the previous section. The only mechanism that is able to explain the duration, amplitude, spectral content, temporal distribution, and station coverage of the DLDS is the occurrence of volcanic tremors at Deception Island.

The seismic activity of the Deception Island volcano has been monitored by the IAG-UGR during summer surveys since 1994, usually from early December to late February, using seismic networks and arrays [146, 148, 65, 63]. Volcanic tremors have been reported in several of these surveys, generally identified by visual inspection of the seismograms. For example, during 1999–2011 volcanic tremor was identified in all surveys, except those with the

lowest activity (2004–2005, 2008–2009) and the 2010–2011 survey [65]. Volcanic tremors are described as quasi-monochromatic signals with frequencies between 1 and 4 Hz, although some episodes of spasmodic tremors displayed energy in two frequency bands: 1–3 Hz and 4–8 Hz [13, 150, 148, 315]. Tremor amplitudes are generally small compared to other types of seismicity [63]. Reported tremor durations range between less than a minute and a few hours [150]. The longest duration was observed during the 1999 seismic crisis, when volcanic tremor exceptionally reached a duration of around 24 h [148]. Although tremor source locations are difficult to identify, the application of array techniques has allowed for the determination of a few tremor source areas at the Deception Island volcano. They are generally associated with zones with a high thermal gradient and fumarolic emissions, such as Cerro Caliente, Fumarole Bay, Telefon Bay, and Obsidianas area [13, 6, 65, 87, 146, 150, 219, 240].

Volcanic tremor generation can be explained by the resonance of fluid-filled conduits, which is the source model that best suits the characteristics of the observed tremors at the Deception Island volcano [6, 65, 146]. Sustained seismic radiation results from the trapping of energy within volcanic cracks and conduits filled with magmatic or hydrothermal fluids, which produce sharp impedance contrasts with the surrounding elastic medium [74, 75]. In order to achieve the long durations observed in volcanic tremors, the excitation mechanism has to remain active during long time spans.

The DLDS reported here and the volcanic tremors previously described at the Deception Island volcano share similar characteristics. First, we observe that they are both sustained signals with long durations. Tremor durations reported during the annual surveys are short compared to DLDS, although this might be due to the difficulties associated with the visual detection of weak, long-duration signals characterized by very emergent onsets. Second, they share a similar range of frequencies, contained within our F3 band (0.5–5 Hz) which is the typical frequency band for LP seismicity reported at volcanoes around the world. Third, they are both recorded only at Deception Island; they are not detected at Livingston Island or Cierva Cove, located in non volcanic environments. Therefore, the DLDS source process must occur within the shallow crust of the Deception Island volcano. Taking into

account all of these observations, we conclude that the DLDS are indeed volcanic tremors.

However, if the DLDS are volcanic tremors, then we have yet to explain why volcanic tremors have an annual periodicity, as shown in Figure 3.8. To address this point, we must consider the mechanisms that might trigger volcanic tremors at Deception Island.

There are several phenomena that can give rise to volcanic tremors in an active, unstable volcanic system such as Deception Island. Some of them are internal factors, like the mechanisms triggering tremors in other volcanoes.We may think of the instabilities induced by the presence of a near-surface magma chamber, the circulation of magma and other fluids within the volcanic conduits, or stress changes, related to local deformation, or to the activation of local and regional fault systems [64, 146, 330]. However, internal mechanisms are unable to explain the observed seasonal modulation of the DLDS activity.

Consequently, we have to consider external (non-volcanic) effects that might modulate the volcanic and/or hydrothermal activity with the required periodicity. Interactions between unstable volcanic systems and external phenomena have been described in the literature. For example, there are reports about volcanic activity triggered or modulated by intense rainfalls, large earthquakes, tides, changes in crater lake levels, pressure variations, etc. [83, 109, 167, 213, 222, 229, 246, 250, 267, 304]. Some of these external effects may display annual cycles, and therefore could be invoked to explain the observed seasonal modulation of the DLDS (Figure 3.8). For example, the interactions of shallow aquifers with the hydrothermal system [150] are affected by seasons. At Deception Island, the amount of liquid water percolating the shallow structure is larger during the summer than in the winter when most surface water is frozen. The extra thaw water may alter the equilibrium within an unstable hydrothermal system, and thus more tremors would be expected during the summer [13]. However, our results point to the opposite effect, since we observe more tremors during the winter (Figure 3.8).

External effects modulating the seismic activity at the Deception Island volcano have also been described by Stich et al. [298]. They studied series of rhythmic LP events with stable inter-event times recorded at Deception

Island in 2009. They compared the LP event production rate with the dominant frequency of the oceanic microseisms, and concluded that the LP series was triggered by the effect of oceanic microtremors with amplitudes of 1–6 μm on an unstable hydrothermal system.

Although this mechanism has been proposed for LP events,we must keep in mind that LPs and tremor are originated by the same processes [12, 75, 176, 331]. At Deception Island, volcanic tremors and LP events are similar in terms of waveform, spectral content, wave polarization, and source locations [13, 6, 148]. Tremors only differ from LP events in their much longer duration. Therefore, external effects modulating LP activity may also trigger volcanic tremors (i.e. DLDS).

The energy of oceanic microtremors varies during the year. These variations may induce a seasonal behavior in the seismic activity of Deception Island, and in volcanic tremors in particular. At high-latitudes in both hemispheres, microseismic energy is larger during the local fall and winter [130, 299]. However, in Antarctica the trend can be reversed due to the sea ice coverage which softens the effect of ocean waves and efficiently suppresses the local sources of micro-seismic noise [14, 20, 130].

We use the F2 FASE as a measure of the oceanic microseism energy at Deception Island (Figure 3.12). We can see that there are annual oscillations with minima during the austral summer, although the amplitudes and precise distributions are quite irregular. These variations can be linked for example to peculiarities in the ice coverage. For example, the 2008 and 2010 winter maxima in F2 FASE occur when the Bransfield Strait is partially free of ice (Figure 3.13). In the remaining years, there is no winter peak, and accordingly the ice coverage is larger. The same effect can be observed in the spring of 2009, 2010, and 2011.

Figure 3.12 compares the DLDS activity (volcanic tremors) and the F2 FASE representing the amplitude of oceanic noise. The oscillations of microseismic energy are often correlated with variations in the DLDS activity. There are periods of high F2 FASE that coincide with intense DLDS activity. For instance, this happens during the DLDS maxima in July 2008, October 2009, June 2010, and October–November 2011. Examples can also be seen in Fig. 5a and c. Following Stich et al. [298], we propose that in these ca-

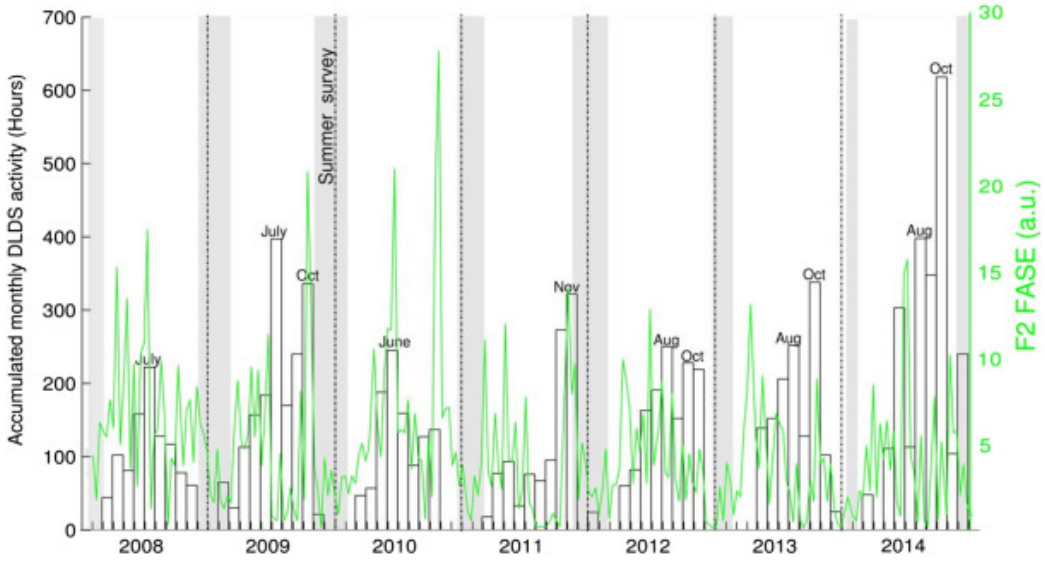

Figura 3.12: Comparison between DLDS activity (empty bars) and amplitude of the oceanic microseism, represented by the F2 FASE (green line). The gray bands indicate the periods of operation of the Gabriel de Castilla Base during the summer surveys.

ses, volcanic tremors are triggered by the small instabilities induced in the hydrothermal system by high-amplitude microseisms generated by oceanic pressure variations. Microseism amplitudes are in the range 0.1–10 μm/s, which are comparable with the results of Stich et al. [298].

Periods with high F2 FASE but small DLDS activity are also observed, for example in April 2008, October 2010, and April 2013 (Figure 3.12). In these cases, we have to keep in mind that the presence of high amplitude microtremors is a necessary condition to trigger DLDS, but it is not sufficient as adequate instabilities of a susceptible volcanic system are also required. The threshold levels in internal pressure variations required to actually trigger volcanic tremors may be different at different times. These thresholds may become larger when the conditions within the volcanic system are stable. As a consequence, the level of DLDS activity may be small even in the presence of high amplitude microtremors.

These observations suggest that high-amplitude microseismic noise may constitute a feasible trigger mechanism for volcanic tremors, thus explaining

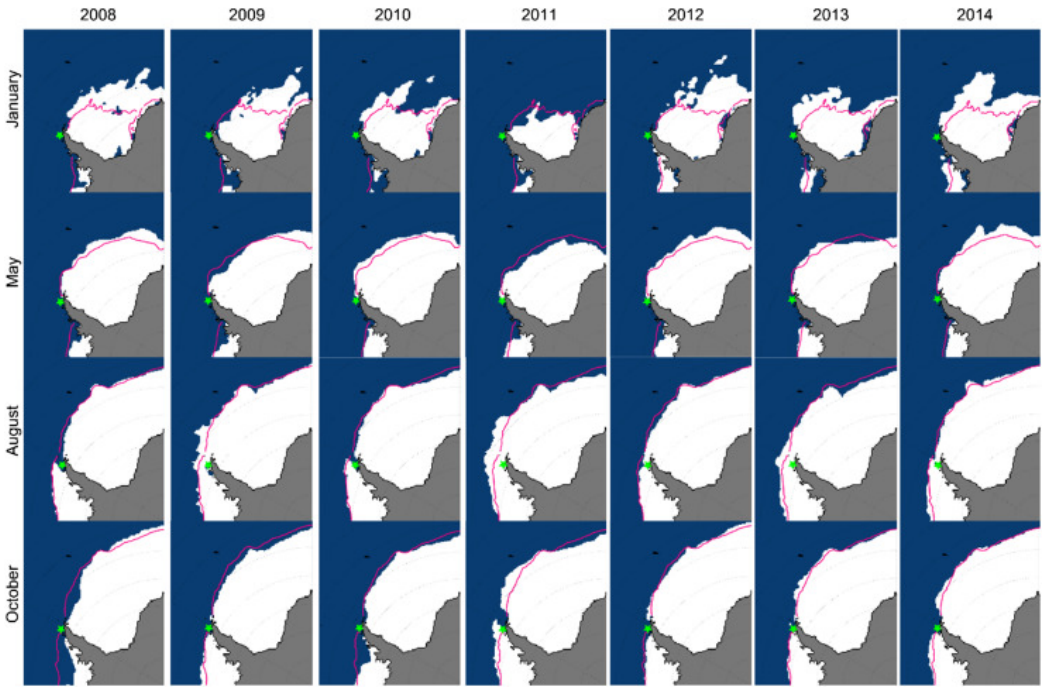

Figura 3.13: Images of ice coverage for January, May, August and October of each year since 2008 to 2014. Purple line median ice edge 1981–2010 (modified from the NSIDC Sea Ice Index, [102].

the general features of the temporal distribution of DLDS activity. Nevertheless, in some cases we find intense DLDS activity that does not coincide with high levels of F2 FASE. This happens in July 2009, August–November 2012, July–October 2013, and August–October 2014. Figure 3.5b is also an example of a DLDS event uncorrelated with the F2 FASE. These cases are most interesting. If the only triggering mechanism were the presence of oceanic microtremors, DLDS should not be produced during these quiet periods, even assuming a lowered triggering threshold. Therefore the origin of this particular DLDS activity must be related to another triggering mechanisms, probably related to the internal dynamics of the Deception Island volcano.

To corroborate this point, we compare the DLDS activity with the seismic activity recorded during the summer surveys at Deception Island volcano (Figure 3.14). We use the number of seismic events as a proxy to characterize the volcanic activity at Deception Island [65, 63]. In this case, we can see that

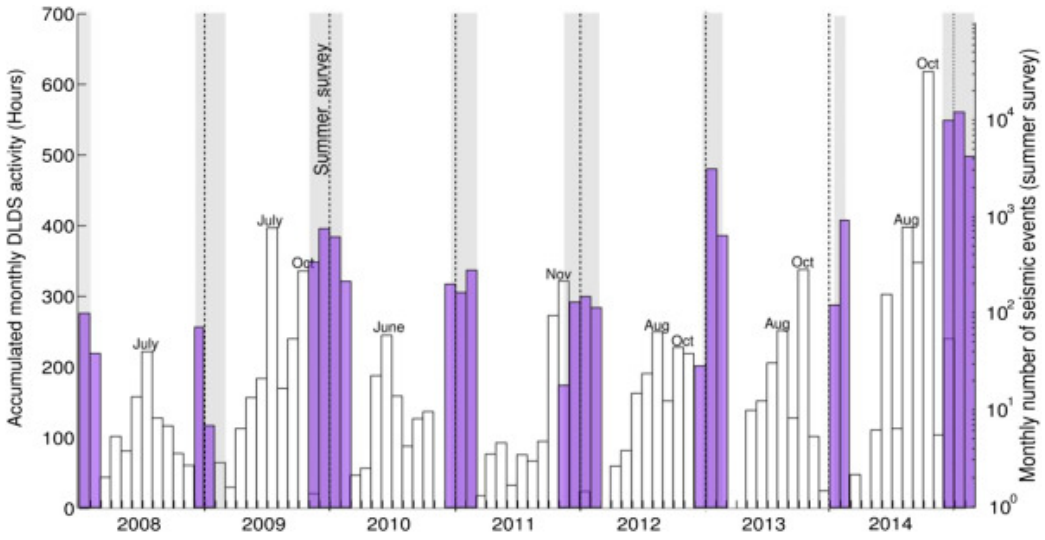

Figura 3.14: Comparison between DLDS activity (empty bars) and number of seismic events recorded during the temporal surveys at Deception Island (purple bars). The gray bands indicate the periods of operation of the Gabriel de Castilla Base during the summer surveys. Notice that the number of events is displayed in logarithmic scale.

2009–2010, 2012–2013, 2013–2014 and 2014–2015 are the most active surveys in the seven years analyzed.We observe that a few DLDS are present during most surveys, except for 2010–2011. In this survey, there was a low level of seismic activity, with no reported observations of volcanic tremors. But in general, the relationship between DLDS activity and number of events recorded during the surveys is far from obvious.

However, if we focus just on DLDS activity uncorrelated with oceanic microseisms, we find that it clearly precedes the most active surveys. The July 2009 DLDS peak precedes the 2009–2010 survey, which is among the most active in the 1999–2011 period [65]. Likewise, the DLDS activity during the winter/spring of 2012, 2013 and 2014 precedes the ensuing 2012–2013, 2013–2014, and 2014–2015 surveys, which display a high (and increasing) level of activity [10]. These years are precisely those showing a bimodal distribution with two separate peaks of DLDS activity. On the contrary, the quietest surveys (2008–2009, 2010–2011, and 2011– 2012) occur after years with a single peak of DLDS.

Therefore, our interpretation is that DLDS are volcanic tremors occurring in response to sustained mechanisms that are able to trigger the tremor source continuously for long time spans. In most cases the excitation seems to be related to the influence of oceanic microtremors on an unstable hydrothermal system, as evidenced by the coincidence of DLDS activity peaks and periods of high F2 FASE. However, in some cases there is no such relationship, and we believe that the excitation must be then produced by a different, probably internal, mechanism.

In particular, there are at least two triggering mechanisms that may account for the generation of these ocean-noise-uncorrelated DLDS. The first one is the occurrence of changes in the state of stress of the volcanic edifice. These changes can be shown, for example, by volcano-tectonic earthquake series and also by static deformation of the free surface, and both phenomena have indeed been observed at Deception Island [10, 39, 99, 148, 237]. Stress changes can modify the pressure distribution and alter the equilibrium in the shallow volcanic and hydrothermal conduits, thus facilitating the occurrence of long duration tremors. Stress changes can be originated by local and regional tectonics. Regional tectonics are dominated by extension of the Bransfield rift, which produces normal fault systems parallel to the rift direction [107, 121]. Local tectonics at Deception include several other fault systems, and are greatly influenced by the magma dynamics [98, 225, 248].

A second triggering mechanism could be related to the volcanic gas supply. DLDS could be triggered either by fluctuations of the net gas flux and/or by the interactions with the complex plumbing system. This mechanism has been invoked to explain long-period events and tremor at volcanoes [72, 164, 268] and hydrothermal tremors at geysers [168, 313]. Gas emissions are common at Deception Island volcano. The most prominent fumaroles are located at Fumarole Bay, with temperatures around 100°C and sulfur-rich gases [68, 67, 180]. Diffuse emissions of CO2 are also reported at sites around the coast of Port Foster, where significant thermal anomalies are also found [237, 240]. In previous analyses, we have found that there is a close relationship between LP seismicicty and gas emissions, at least for some time periods. For example, changes in the chemical composition of fumarolic gases and deposits were documented during the 1999 seismic crisis [148, 68].

The same observation was also reported during the 2003–2004 seismic survey [67], which was one of the most active in the 1999–2011 period [65]. Additionally, detailed array analyses of LP seismicity during the 2009–2010 survey demonstrated a clear temporal correlation between the activity of a seismic source near Cerro Caliente and diffuse CO2 measurements at Fumarole Bay [240]. Fluctuations in the gas flux through the hydrothermal system and shallow volcanic conduits of Deception Island can be produced by the supply of fresh, undegassed magma into the system, either as deep or shallow intrusions [148, 240]. These fluctuations may occur over long time scales, and constitute a primary triggering mechanism for long-term volcanic tremors.

3.7. Conclusions

Using an approach based on the evaluation of the average seismic energy contained in selected frequency bands, we have identified the occurrence of 276 DLDS episodes between February 2008 and January 2015. Their main characteristics are: (1) they have very long durations, between several hours and several days; (2) their energy content is mostly centered in the F3 band (0.5–5 Hz); they have low amplitudes, which are uncorrelated to the duration of the events; (4) they are recorded only at Deception Island, and not at nearby (30 km) stations; and (5) they apparently show a seasonal modulation, with minima of activity during the austral summers.

Several mechanisms can potentially be invoked to explain the generation of long-lasting signals at the Deception Island volcano. However, only a few of them generate signals whose frequency is limited mainly to the F3 band. We can mention the seismic signature of glacial and iceberg dynamics, and the occurrence of tectonic tremors. However, none of them can explain the fact that DLDS are detected exclusively at Deception Island.

We conclude that the DLDS are volcanic tremors, most likely originating from instabilities in the hydrothermal system and/or shallow volcanic conduits. The triggering mechanism may be related to pressure variations induced by the effect of oceanic microseisms [298], which results in the annual modulation. However, some peaks of tremor activity are uncorrelated with the amplitude of oceanic noise. They correspond to one of the peaks of

the bimodal distributions of DLDS observed in 2009, 2012, 2013 and 2014. In these cases, we notice that they precede summer surveys with a high level of seismic activity. This suggests that they may be triggered by internal, purely volcanic mechanisms, and thus reveal the state of volcanic activity of Deception Island volcano.

This is the first time that this type of long-lasting volcanic tremor is reported at Deception Island volcano. Surely this does not mean that they had never occurred before, only that they had not been detected until now. The reasons for this are twofold, and involve both technical advances and the development of new methods. On one hand, DLDS is easiest to identify during the winter, when the signal to noise ratio is largest. Seismic data at Deception Island are available since the late 80s, but limited to temporal surveys carried out during the austral summers. Continuous records from permanent stations are only available since 2008. The analysis of DLDS has not been feasible until now, when a sufficient amount of year-round seismic data has become available. On the other hand, the low amplitudes and long durations of the DLDS make them very difficult to identify in routine analyses of seismic data. A specific method focused on the long-period band is required to distinguish these signals from variations in the background seismic noise.

Consequently, these long-duration tremors have never been considered in any of the previous evaluations of the seismic activity of the Deception Island volcano. Our results indicate that tremors at Deception are more common than previously assumed, to the extent of being almost continuous during some periods. The actual significance of these low-amplitude signals in terms of the overall dynamics of the volcano has yet to be ascertained.

The period corresponding to the 2014–2015 summer survey was especially active, to the point that a change in the volcanic alert level from green to yellow was issued by the Spanish Polar Committee [10]. The increasing volcanic tremor activity observed since 2012 might be considered a precursor to this activity. However, the confirmation of this point requires a continued analysis over a longer time period.

The procedure described in this analysis is a fast and effective method for the detection of long-duration signals with limited frequency content. It is therefore very well suited for the detection of volcanic tremors at active volcanic areas. It could be helpful as a routine monitoring tool to identify and

evaluate the volcanic tremor activity, which is very important for volcanic hazard assessment.We have used this procedure to facilitate the identification and quantification of hundreds of tremors recorded at Deception Island during 7 years (2008–2015). However, it can be easily adapted to any other volcanic system, using the knowledge about the frequency content of the different signals recorded in the area to establish the most adequate frequency bands.

Capítulo 4

Volcano-Tectonic Activity at Deception Island Volcano Following a Seismic Swarm in the Bransfield Rift (2014–2015)

Summary

In September 2014 there was a sharp increase in the seismic activity of the Bransfield Strait, Antarctica. More than 9000 earthquakes with magnitudes up to 4.6 located SE of Livingston Island were detected over a period of 8 months. A few months after the series onset, local seismicity at the nearby (∼35 km) Deception Island volcano increased, displaying enhanced long-period (LP) seismicity and several outbursts of volcano-tectonic (VT) earthquakes. Before February 2015, VT earthquakes occurred mainly at 5-20 km SW of Deception Island. In mid-February the numbers and sizes of VT earthquakes escalated, and their locations encompassed the whole volcanic edifice, suggesting a situation of generalized unrest. The activity continued in anomalously high levels at least until May 2015. Given the spatial and temporal coincidence, it is unlikely that the Livingston series and the Deception VT swarm were unrelated. We propose that the Livingston series may have produced a triggering effect on Deception Island volcano. Dynamic stresses associated to the seismic swarm may have induced over pressure in the unstable volcanic system, leading to a magmatic intrusion that may in turn have

triggered the VT swarm. Alternatively, both the Livingston earthquakes and the VT swarm could be consequences of a magmatic intrusion at Deception Island. The Livingston series would be an example of precursory distal VT swarm, which seems to be a common feature preceding volcanic eruptions and magma intrusions in long-dormant volcanoes.

4.1. Introduction

The Bransfield Strait, Antarctica, is located between the Antarctic Peninsula and the South Shetland Islands (Figure 4.1). It is a region dominated by an extensional regime, promoted by the separation of the South Shetland microplate and the Antarctic plate [107, 69, 202]. The Bransfield rift has a NE-SW direction, forming a series of extensional basins. Several volcanic edifices can be found along the rift, some of them subaereal and some submarine.

Deception Island is a prominent volcano of the Bransfield rift (Figure 4.1). It is among the most active volcanoes in Antarctica, with more than 20 eruptions documented in the last two centuries [28]. Recent eruptions took place in 1967-1970 [e.g., 290]]. Other signs of volcanic activity include an extensive hydrothermal system, fumaroles, gas emissions, surface deformations, and a generally moderate but highly variable level of volcano seismicity [236, 150, 65, 10]

In the framework of the Spanish Polar Program, the Andalusian Institute of Geophysics, University of Granada (IAG-UGR) has carried out research projects at Deception Island since 1994 to investigate the seismic activity and structure of the volcano and surrounding areas [e.g. 152, 13, 6, 146, 150, 148, 35, 330, 64, 114, 199, 65, 262, 63, 261, 151, 157] The IAG-UGR also monitors the seismic activity of Deception Island volcano, and provides scientific advice for the management of the volcanic alert system. Seismic monitoring is based on a temporary seismic network deployed generally from December to February, coinciding with the operation of the Gabriel de Castilla Base. Moreover, since 2008 three permanent broadband stations are maintained in the region, at Cierva Cove, Deception Island, and Livingston Island [63].

Two major seismic crises have been reported since 1986, when seismic

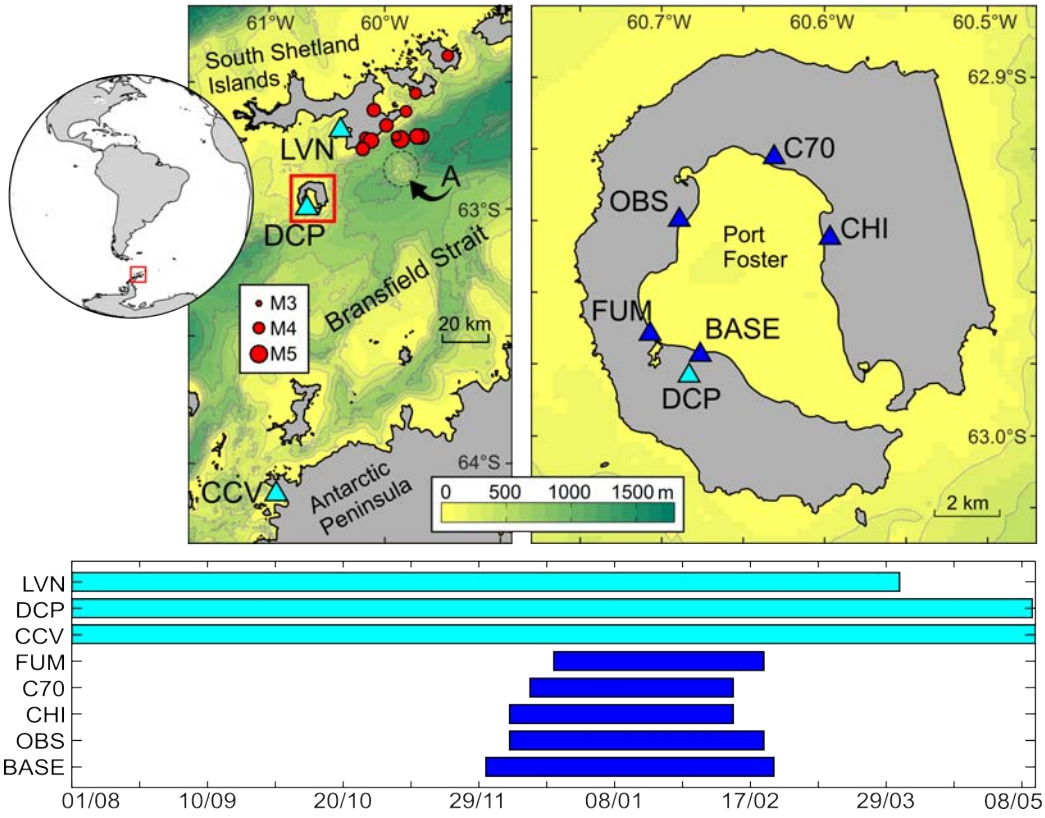

Figura 4.1: (top) Map of the Bransfield Strait and Deception Island, showing the locations of the seismic stations used in this study. Red squares mark the areas zoomed in the next plot. Triangles indicate seismic stations (cyan for permanent stations, blue for temporary stations). Notice that OBS is the name of a station, and does not refer to an ocean-bottom seismometer. Red dots in the left panel show the epicenters of earthquakes reported by the International Seismological Center [153] in the period 2014-2015. Bathymetry contour interval is 200 m. The dashed circle indicates a submarine volcanic feature labelled Edifice A by Gracia et al. [126]. (bottom) Operating periods of the seismic stations.

monitoring was re-established at Deception Island after the 1967-1970 eruptions. They occurred in 1992 [236] and 1999 [148] and were characterized by a sharp increase in the number and magnitude of volcano-tectonic (VT) earthquakes, reaching rates of tens of earthquakes per day and maximum magnitudes around 3. They have been interpreted as consequences of aborted magmatic intrusions.

After 1999, the seismic activity was relatively quiet, with a general dominance of long-period (LP) seismicity and occasional bursts of LP seismic activity, for example in the 2003-2004 and the 2012-2013 surveys [65, 10].

This behavior changed drastically in the 2014-2015 survey, when a very large number of earthquakes of tectonic and volcanic origin was detected. The number of events was one order of magnitude larger than the sum of all earthquakes recorded in the previous 15 years. During the survey, data from the temporary seismic network was preliminarily analyzed in near real-time. LP seismicity was unusually frequent and intense. Tectonic and VT earthquakes also occurred in large numbers. In the last weeks of the survey, the number of local earthquakes at Deception Island escalated. At the same time, LP seismicity became conspicuous, displaying increasingly larger and more recurrent LP events and tremor episodes. These observations, in the context of extensive seismo-volcanic activity, led to a change in the volcanic alert system. The Spanish Polar Committee established the volcanic alert level at yellow (enhanced monitoring to corroborate the observed anomalies) for a few days in February 2015 [10]. In the present work we analyze the seismicity of Deception Island and surrounding areas during the period August 2014-May 2015, using both temporary and permanent stations. We investigate the spatial and temporal evolution of the seismicity, and assess the possible interactions with the activity of Deception Island volcano.

4.2. Instruments

Since February 2008 the IAG-UGR maintains three permanent seismic stations (LVN, DCP and CCV, see Figure 4.1) at Livingston Island, Deception Island, and Cierva Cove [63, 157]. Additionally, from December 2014 to February 2015 a temporary network composed of five short-period seismic

stations [1, 323, 63, 136] was set up at accessible areas around Port Foster (Figure 4.1). For further details about these instruments, see Supplementary Text S1.

4.3. Data analysis and results

We analyze the seismic activity in the Bransfield Strait area during the period August 2014-May 2015. We combine data with different spatial and temporal coverages: (1) permanent stations with a sparse spatial distribution, but continuous recording [11]; and (2) temporary stations with a dense spatial coverage of Deception Island volcano, operating between December 2014 and February 2015 [8]. The details of the earthquake detection and location procedures are described in the Supplementary Text S2
[192, 135, 146, 137, 330, 136, 199, 314, 309, 63].

4.3.1. Permanent station data

The permanent station data reveal the occurrence of a seismic swarm comprising several thousand earthquakes in a time frame of a few months. P and S arrival times were obtained for 9526, 2535, and 513 earthquake records at LVN, DCP, and CCV, respectively. Some earthquakes are large enough to be included in global catalogs (see Figure 4.1).

In most cases, earthquake amplitudes were largest and S-P delays shortest at station LVN. Thus the main focus of earthquake activity was closest to Livingston Island. Most earthquakes have S-P delays in the range 2.9-3.5 s at LVN (Figure 4.2a). Some of these earthquakes were also detected at DCP, with smaller amplitudes and S-P delays of 6.9-7.5 s (Figure 4.2b, blue). Only the largest earthquakes were detected at CCV, with S-P times of ∼19.5 s. Estimated magnitudes range up to 4.6, and are characterized by a b-parameter of ∼1 (Figures S1 and S2). There is no dominant earthquake, and there are 12 events with magnitudes above 4.0, mostly during September. The total seismic moment is $7.8 \cdot 10^{16}$ Nm, equivalent to a magnitude 5.2 earthquake.

The seismic activity began with two short-lived pulses of small-magnitude earthquakes on August 15 and 22, 2014. On August 31, the number of earth-

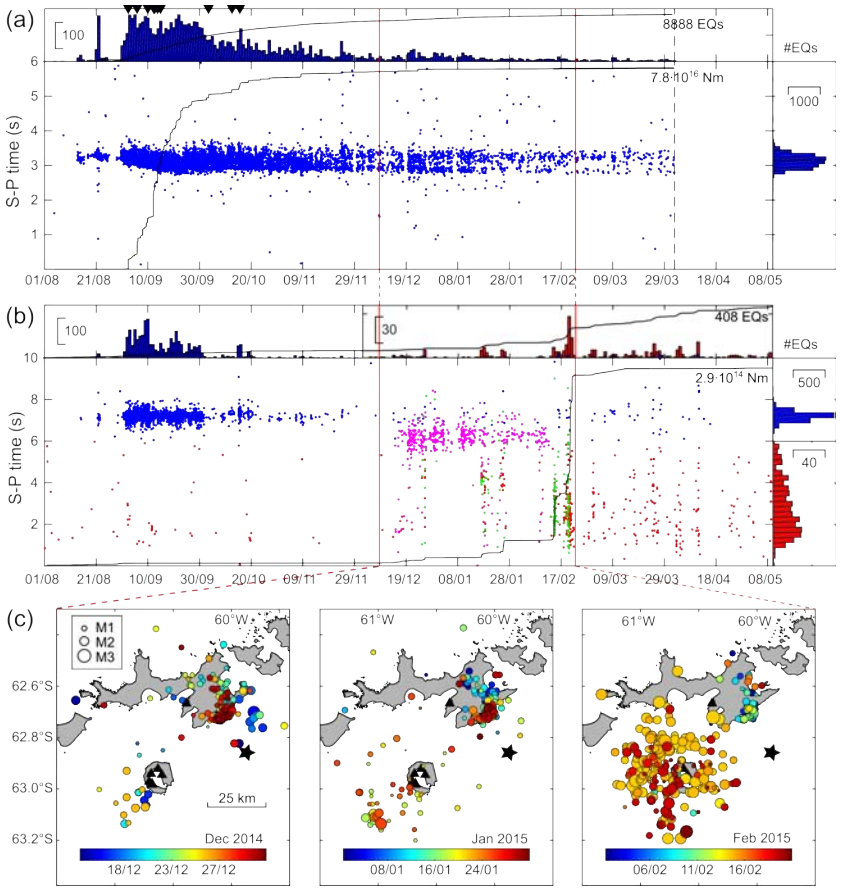

Figura 4.2: (a) S-P times at station LVN during the period August 2014-May 2015. The panels show the S-P delays versus time (center); the daily number of earthquakes (top); and the S-P time distribution, with a bin width of 0.25 s (right). A dashed line marks the end of the recording period. Inverted triangles denote 12 earthquakes reported by ISC. Red vertical lines indicate the span of the temporary network operations. Black lines show the evolution of the number of earthquakes (top) and cumulative seismic moment (center). (b) Same than (a) for DCP. Colors identify local ($t_{SP} < 6$ s, red) and distant ($t_{SP} > 6$ s, blue) earthquakes. Green and magenta dots correspond to OBS and C70, respectively. Black lines displaying the evolution of the earthquake number and moment are calculated using VT earthquakes only (red dots). Note the change in scale in the histograms for times after December 1 and S-P times below 6 s. (c) Epicenter locations in December (left), January (center), and February (right). Dot colors are coded by time and dot sizes are scaled by magnitude. Triangles indicate station locations. The black star marks the position of the submarine volcano Edifice A (see Figure 4.1).

quakes increased again, and remained very high for about a month. This is the most intense period of the swarm, in terms of earthquake rates and seismic moment. By October 4, the series had already produced 50 % of the earthquakes and 87 % of the total moment release. Earthquake rates diminished slowly during the following six months, with some irregular bursts on October 15, November 24, and December 20, 2014. Station LVN stopped functioning in April 1, 2015, although by that time the series had practically faded out.

At DCP, several earthquakes belonging to the Livingston series have been detected (blue dots in Figure 4.2b). Nevertheless, there are also earthquakes characterized by smaller S-P times, in a broad range spanning 1-5 s (red dots in Figure 4.2b). The small S-P times indicate that they are local, VT earthquakes, occurring within the volcanic edifice of Deception Island. P and S arrivals for 408 VT earthquakes were identified, although many other earthquakes were too small for reliable phase identification. This number is small compared to the activity recorded at Livingston Island. However these events are highly significant, because they may represent a seismic reactivation of the volcano.

VT earthquakes occurred sporadically up to early December. Later on, they tended to occur more frequently and were grouped in clusters (e.g., December 25, 2014, January 17-19 and 25-26, February 13-14 and February 18-21, 2015). The highest magnitudes occurred in late February (Figures 4.2b and S3). The activity continued through March and April, with two clusters (April 2-5 and 9-12) displaying even lower S-P delays. This indicates events located near or within the Deception Island caldera. The seismic activity decayed by the end of the recording period (May 10, 2015). However, although the magnitudes are low, the number of earthquakes is still relevant, and we cannot establish precisely how long this series may have continued.

4.3.2. Temporary network data

Basic location capabilities were maintained from December 8 to February 22 (red lines in Figure 4.2). In this period, the network detected a part of the Livingston Island series, and several bursts of local VT seismicity at De-

ception Island volcano (Figure 4.2b). Very often VT earthquakes were very small, and could be detected only at the closest stations. Therefore they cannot be located, although they can be counted and their S-P times measured to have a rough idea of their temporal and spatial distribution. For example, green and magenta dots in Figure 4.2b correspond to VT earthquakes at station OBS and C70. It can be noticed that the February 13-14 cluster is most active at OBS, and thus its source should be closest to OBS. Similarly, at C70 there is more activity in the December and January clusters. Since C70 is closer to Livingston, more Livingston swarm earthquakes are detected, with slightly smaller S-P times (∼6 s).

Figure 4.2c shows the results of the source location procedure. A total of 835 earthquakes have been located, and several features of the spatial and temporal distribution of the earthquakes can be noticed. For example, there is a relevant seismogenetic zone located near the E tip of Livingston Island at about (62°7′S, 60° 0′W) This area comprised ∼50 % of the located earthquakes, with magnitudes in the range 1.0-2.0, and was active during the whole summer survey (December-February). The distribution of earthquakes around Deception Island is more irregular. In December, there were just a few earthquakes scattered towards the SW. Most of them occur around December 25. In January, a few low-magnitude earthquakes were located around Deception. There was also a small cluster ∼20 km SW of Deception, comprising the earthquakes occurring in January 17-19 and 25-26. But in February the situation changed. First, there were many more earthquakes near Deception Island volcano, close to or within the caldera. Second, the epicenters encompassed the complete volcanic edifice. Finally, many earthquakes have large magnitudes up to 3.2. Most of these earthquakes occurred in two clusters, on February 13-14 and 18-21.

Calculated earthquake depths are mostly limited to the first 10 km of the crust, although a few solutions suggest the presence of deeper sources, down to 20-25 km, both in the Livingston cluster and near Deception Island volcano. Therefore, these earthquakes seem to occur in the shallow crust. However the depth resolution is limited due to the irregular station coverage, and further interpretations should be avoided.

4.4. Discussion

4.4.1. The 2014-2015 Livingston seismic swarm

The Bransfield Strait is an area of active seismicity. Despite the poor permanent station coverage, the ISC catalog [153] comprises ∼200 earthquakes with magnitudes above ∼4.0 since 1960. In the past decades, a few detailed studies have revealed a significant background of low-magnitude microseismicity around the Bransfield rift [249, 152, 272, 94]. Most earthquakes are shallow (<10 km), but intermediate-depth earthquakes have been also identified [152, 272]. They are interpreted as a consequence of the subduction of the Drake plate under the South Shetland continental block.

The seismicity of the Bransfield Strait often takes the form of spatio-temporal clusters [272, 148, 94]. They are localized near volcanic features, including not only volcanic islands such as Bridgeman and Deception, but also submarine structures such as Orca volcano and other fissure-like ridges. The close relationship between seismic swarms and volcanic structures suggests that these earthquakes could be originated by ongoing magmatic activity [272, 94].

In this context, our data demonstrate the occurrence of an intense seismic swarm near Livingston Island in 2014-2015. It is the most numerous swarm ever reported in the Bransfield area, comprising ∼9000 earthquakes detected along a period of 8 months. The swarm started in early September 2014, following some precursory seismicity in August. The largest earthquakes (up to magnitude 4.6) and earthquake rates (up to ∼180 events per day) took place in the early stages of the series (September-October). There were two phases of maximum earthquake production during September, although large earthquakes were also recorded in October. After September, the number of earthquakes decayed slowly with time, with occasional bursts of activity (Figure 4.2). The seismicity lasted for 8 months, until it faded out in April-May 2015. The operation of a seismic network at Deception Island during 2.5 months (Figure 4.1) allowed for the location of a small part of the series. The results identify a source region near the eastern tip of Livingston Island (Figure 4.2c). Given the stability of the S-P times displayed in Figure 4.2, we

hypothesize that this is also the source region of the whole Livingston series. The small variability of the S-P delays also suggests that the earthquakes occurred within a spatially limited source area.

The Livingston swarm could be originated either by tectonic stresses acting on the shallow crust, due to the opening of the Bransfield Rift, or by instabilities caused by a localized magmatic intrusion. Both processes are likely to happen in that area off Livingston Island. On one hand, the region is under an extensional tectonic regime. Geodetic studies have shown that the Antarctic Peninsula and the South Shetland Islands are moving apart at a rate of 7-10 mm/year [90, 38]. Thus the occurrence of series of tectonic earthquakes is expected, similar to those produced at other oceanic ridges [e.g. 277]. On the other hand, the region displays active volcanism [188]. Earthquake swarms generally occur near volcanic structures, which suggest that most of them may have a volcanic origin [150, 272, 94]. The presence of shallow magma reservoirs along the Bransfield Rift is also supported by results from seismic profiles [129, 76], seismic tomography [34, 330], magnetotelluric data [248], and gravity and magnetic surveys [69, 70].

The b-parameter of the series, near 1, seem to favor a tectonic origin. It is generally accepted that volcanic sequences have a larger b-parameter; however there are many exceptions to this rule [271], and therefore this observation does not completely exclude a volcanic origin.

Nevertheless, the duration of the Livingston swarm is very long, and displays a relatively slow decay of the earthquake rates (Figure 4.2a). In general, tectonic series responding to a mainshock-aftershock sequence show a faster decay in the number of earthquakes. They usually follow the modified Omori law, with p-values between 0.7 and 1.5, and c-values of a small fraction of a day [e.g. 172, 310]. In our case, a good fit between the earthquake rates and the modified Omori law cannot be found. This suggests that the Livingston swarm is not a mainshock-aftershock series, responding to the re-accommodation of the stress field after a large fracture event. Instead, it may be a continuous process involving heat and fluid flow within the shallow crust in the source region, induced by magmatic activity. A similar result was obtained for the June 1999 seismic sequence of the Endeavour Segment of the Juan de Fuca Ridge [50, 51]. The anomalously large number of earthquakes,

long duration of the series, and absence of a clearly dominant mainshock were interpreted as a demonstration of the volcanic origin of the series.

Another indication comes from the variations in the S-P times observed in Figure 4.2. First, there is a slight drift in the S-P times at the beginning of the series (Figure 4.2a). At the series onset, earthquakes have S-P times near 3.2 s, that reduce gradually to ∼2.9 s in late September. No equivalent changes are observed at DCP. Second, there is a splitting of the S-P times, starting in late October, with average values around 2.9 and 3.2 s. This can be also observed in the data from C70 (Figure 4.2b). The first observation suggests a propagation of the source, that becomes slightly closer to LVN with time. Source migration could be explained by multiple phenomena, including fault propagation, diffusive processes, and fluid and magma motions [279, 29, 52, 88]. The second observation implies the simultaneous activation of two nearby sources. This is not common in tectonic sequences, and would suggest the interplay with hydrothermal or volcanic fluids.

Finally, it is remarkable that the swarm location is apparently unrelated to any volcanic structure. Detailed analyses of the bathymetry show the presence of normal faults in the source region, aligned with the Bransfield rift [25], while the closest volcanic structure is further south [127]. However, the location uncertainties must be considered. Moreover, we have used a simple layered model based on the Deception Island structure. There are evidences that the seismic velocity in the South Shetland continental block is faster than near the rift [34, 330]. Therefore, if the source-LVN path were faster than the source-DCP path, the source might be actually located further from LVN than imaged in Figure 4.2c. This could place the source closer to Edifice A, that could be held responsible for the earthquake swarm.

4.4.2. Relationship with the VT swarm at Deception Island volcano

Exceptionally intense VT activity occurred at Deception Island volcano a few months after the onset of the 2014-2015 Livington swarm. Source locations encompass the whole volcanic edifice, revealing a situation of generalized unrest.

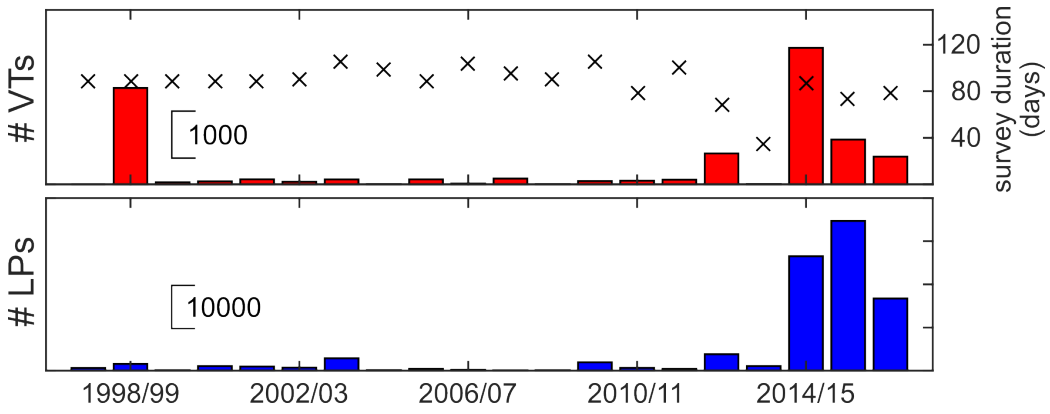

Figura 4.3: Total number of VTs (red) and LPs (blue) recorded during the temporary seismic surveys carried out between 1997 and 2017. Event counts were performed at stations CHI and OBS, respectively. The number of VTs includes many earthquakes that are too small to be located. Crosses in the top panel indicate the durations of the surveys in the scale shown by the right-hand y-axis.

This episode of VT seismicity is similar to those reported in 1992 and 1999 [236, 150, 148, 65]. In 1992, 776 earthquakes were recorded in two months, with a maximum magnitude of 3.4, including four felt earthquakes [236]. In 1999, 2072 VT earthquakes were recorded during two months, with maximum rates of 80 earthquakes per day and maximum magnitude of 3.4, including two felt earthquakes [150]. In 2015, a few thousand earthquakes are reported over a period of five months [10], although most of them are too small to be identified at more than one station. About 400 VT earthquakes have been located, with maximum rates of 45 earthquakes per day and a maximum magnitude of 3.2. Thus we could hypothesize that the 2015 VT swarm may be also related to the stress changes induced by a magmatic intrusion at shallow depths, as proposed for the other two episodes [236, 148].

However, there are two noticeable differences. On one hand, the 1992 and 1999 series died off after a few months. The seismicity levels at Deception Island volcano after the 2015 swarm have been anomalously high, not only during the swarm itself, but during the following years as well. Figure 4.3 shows the total numbers of VT earthquakes and LP events reported during summer surveys from 1998 to 2017. The network configuration and detec-

tion capabilities have been basically the same since 2001 [63], and therefore these numbers are readily comparable. The activity increased in 2015 and has continued in anomalous levels also in the 2015-2016 and 2016-2017 surveys, although it seems to be decaying back to normal thresholds. On the other hand, seismic activity during the 1992 and 1999 episodes was localized solely at Deception Island. The 2015 VT activity occurred after the largest seismic swarm (in terms of number of earthquakes and earthquake rates) ever reported in the Bransfield area. Given the relatively close temporal and spatial coincidence, it is unlikely that these two events could be completely unrelated. Deception Island is a highly fractured volcanic edifice with an extensive hydrothermal system [e.g. 236, 64, 205] in a unstable state, as revealed for example by the VT series described above and the conspicuous presence of LP seismicity [65, 63]. In the last years, this instability seems to be increasing. For example, there are evidences that pressure variations related to high-amplitude microtremors are able to trigger long-duration tremors [157] and induce regular series of LP events [298], what had not been observed before. Moreover, Jiménez-Morales et al. [157] noticed that between 2012 and 2014 the number and durations of volcanic tremors at Deception Island had been growing steadily. In this scenario, the occurrence of the Livingston swarm could have had a triggering effect on Deception Island volcano. Earthquake-generated dynamic stresses traveling as seismic waves are capable of triggering additional earthquakes at remote, critically stressed faults [see 140, and references therein]. Triggering is not always immediate, and time delays of hours to days are common [104, 58]. Similarly, static and dynamic strains produced by earthquakes can induce pressure changes in distant magma bodies. In certain situations, these pressure variations might drive volcanic activity, including seismic swarms, enhanced gas emissions, thermal anomalies, deformation, and even volcanic eruptions [193, 143, 210, 160, 203, 133, 187, 321, 320, 53, 54, 3, 105, 230]. For earthquake-volcano interactions, longer time delays are reported, ranging up to several years [210, 230]. Proposed mechanisms include triggering by frictional failure, where dynamic stresses can be large enough to exceed the frictional strength of faults; and triggering through excitation of crustal fluids, where dynamic strains are thought to induce fluid transport and chan-

ges in pore pressure, reducing the effective normal stress in the fault plane and lowering the threshold required for failure [e.g. 56, 58, 140]. Additional mechanisms focusing on the interactions with magmatic and hydrothermal fluids include the rectified diffusion and advective overpressure models; enhanced bubble nucleation in a supersaturated magma; and detachment and sinking of crystal-rich aggregates [57, 143, 203, 140]. In our case, a direct dynamic triggering of the VT earthquakes by the Livingston swarm can be ruled out, given the long delay between the start of the Livingston series and the seismicity at Deception Island [e.g. 144, 104, 296, 142, 58]. [e.g. 144, 259, 104, 296, 142, 58]. Maximum peak dynamic strains at Deception Island are on the order of $10^{-6} - 10^{-7}$ [144, 285], which exceed the triggering thresholds reported in some cases [e.g. 321, 312]. We hypothesize that these strains may have induced pressure variations in the Deception Island volcanic system, by some of the mechanisms described above. In due time (months), the critically pressurized magma could build up sufficient overpressure to trigger a response in the form of a magmatic intrusion [143, 203, 140]. Static stress changes would then affect the brittle regions of the volcanic edifice, and generate the VT swarm.

Alternatively, the Livingston swarm and the VT activity at Deception Island can both be consequences of magmatic processes taking place at the volcano. However, the notion that the most distant swarm starts months before the local seismicity at the volcano seems largely counterintuitive. Nevertheless, White and Mccausland [324] demonstrate that distal VT swarms located at distances of 2-40 km are usually the earliest precursors preceding volcanic eruptions in long-dormant volcanoes. These earthquakes have a swarm-like nature, and start days to years prior to the magmatic eruptions. White and Mccausland [324] also report magmatic intrusions preceded by distal VT earthquake swarms, and infer an empirical relationship between the cumulative seismic moment and the intruded volume. In order to justify why distal VT seismicity precedes volcanic activity, Coulon et al. [81] simulated the propagation of heat and pressure pulses through the volcanic hydrothermal system. Their results show that, even with modest horizontal/vertical anisotropy, pressure changes associated with a magmatic intrusion can affect distal regions before significant effects are produced in the volcanic edifice.

Therefore, the 2014-2015 Livingston swarm could be another example of a distal VT swarm accompanying a magmatic intrusion at Deception Island volcano. Pressure pulses would propagate laterally, reaching the region SE of Livingston Island, where the interaction with critically stressed faults may have produced the seismic swarm. Local VT earthquakes and LP seismicity at Deception Island were initiated later, when the pressure pulses reached the shallower levels of the volcanic edifice. The volume-moment relationship of White and Mccausland [324] implies that the volume intruded is $\sim 5 \cdot 10^7\ m^3$.

These two models assess the relationship between the Livingston swarm and the VT activity at Deception Island volcano. They share a common feature: the occurrence of a magmatic intrusion beneath Deception Island volcano, that originates the local VT activity. This mechanism was also proposed for the 1992 and 1999 seismic swarms [236, 150, 148]. The models differ in considering the Livingston swarm as a cause or an effect of the intrusion. The main drawbacks are, respectively, the small magnitudes of the Livingston earthquakes, and the absence of distal VT swarms in 1992 and 1999. In any case, these interpretations suggest that Deception Island is in a highly susceptible and unstable state, and confirm the dynamic interactions that can be expected at an active volcanic system. The results also underline the importance of seismic monitoring at Deception Island, to provide quantitative bases for volcanic hazards assessment.

Capítulo 5

Long-term evolution of the seismic activity preceding the 2015 seismic crisis at Deception Island volcano, Antarctica (2008-2015)

Summary

Deception Island is an active volcano located in the South Shetland Islands, Antarctica. Although the last eruptions occurred in 1967-1970, the volcano has undergone periods of seismic unrest in 1992, 1999, and 2015. In this work, we analyze continuous seismic data obtained by a permanent station for the period 2008-2015 preceding the 2015 unrest. We identify different types of seismic signals including tectonic and volcano-tectonic (VT) earthquakes and long-period (LP) seismicity, using a combination of visual and automated techniques. The temporal evolution of the seismicity displays three differentiated stages. In Phase 1 (2008-2010) the volcano was in a dormant state characterized by a moderate level of seismicity dominated by low-energy LP seismicity, and very few VT earthquakes. In Phase 2 (2011-2014), there was a gradual increase in the level of LP events and tremor, and an acceleration of the number and energy of VT earthquakes. In Phase 3 (2014-2015) the seismicity reached a climax, with the occurrence of seismic

swarms comprising thousands of earthquakes, displaying maximum activity in September-October 2014 and February 2015. We propose that the change from Phase 1 to Phase 2 was due to a magmatic intrusion into the plumbing system at Moho depths. The emplacement of fresh magma increased the amount of gas (and heat) permeating the volcano edifice, triggering VT earthquakes in brittle regions and favoring the occurrence of LP seismicity in the shallow hydrothermal system. During Phase 2 the intrusion became increasingly shallower, as evidenced by the acceleration of the seismicity rates, the detection of thermal anomalies, and a change in the deformation pattern that for 2013-2015 corresponded to an inflation process. Finally, in Phase 3 the intrusion reached its shallowest point before stalling at a depth of 6-10 km. The stress perturbations propagated through crustal fluids and produced a distal VT swarm SE of Livingston, as well as proximal VT swarms and very intense LP seismicity at Deception Island.

5.1. Introduction

There are over a thousand active volcanoes worldwide and about 500 million people exposed to volcanic hazards. Throughout history, researchers have developed different techniques and instrumentation for volcano surveillance and monitoring, in order to understand how volcanoes work and, whenever possible, provide timely warnings to the population [211]. Volcano seismology is among the most useful volcano monitoring techniques [e.g. 75, 218]. The seismicity associated with active volcanoes has a wide range of characteristics that reveal the variety of processes involved in the generation of seismic signals. The investigation of the origin of the seismo-volcanic events and their relationship to volcanic processes constitutes a powerful tool to understand the dynamics and structure of a volcano, and may in turn allow us to forecast a volcanic eruption [331].

Deception Island (Figure 5.1) is one of the most active volcanoes in Antarctica, with ∼20 eruptions documented in the last 200 years [28]. Other signs of volcanic activity include the presence of fumarolic emissions, hydrothermal activity, deformation cycles, and a moderate, highly variable level of seismic activity [316, 150, 65]. The last eruptions (1967-1970) led to the destruction

of two Antarctic Bases operating on the island [e.g. 234, 291]. The impact of a potential volcanic eruption at Deception Island is additionally maximized by the presence of scientific personnel and tourists, which visit the island in ever-increasing numbers, especially during the summer [28].

Since 1994 researchers from the Andalusian Institute of Geophysics, University of Granada, Spain, in collaboration with other Spanish and international teams, are involved in seismic monitoring at Deception Island volcano. Monitoring surveys coincide with the activity and operation of the *Gabriel de Castilla* Spanish Base, with is a summer-only facility. Therefore, seismic monitoring at Deception Island has been essentially discontinuous, covering just ∼25 % of the time. In spite of this, a significant amount of research about the structure and dynamics of the Deception Island volcanic system has been carried out [13, 6, 146, 64, 115, 199, 65, 219, 240, 87], including the investigation of two major seismic crises in 1999 and 2015 [150, 11].

In the framework of the International Polar Year 2007-2008, we addressed several technological updates to the Deception Island monitoring network [63]. Among them, we achieved the deployment of a permanent, broadband seismometer based on a low-power acquisition system, that has been in operation since February 2008.

In this paper, we analyze the seismic activity recorded at Deception Island during the years preceding the 2015 unrest (from February 2008 to May 2015). For the first time, we use a 7.5-year-long time series of continuous seismic data, and thus we can address the long-term trends, the evolution of the seismicity, the possible precursors, and the general behaviour of the volcano seismicity before the last seismic crisis. The results deepen our knowledge of the seismic activity of Deception Island, and improve the overall understanding of the volcano.

5.2. Seismicity of Deception Island volcano

The local seismic activity of Deception Island volcano comprises different types of earthquakes. The most conspicuous signals are volcano-tectonic (VT) earthquakes and long-period (LP) seismicity, which includes seismic signals such as LP events and volcanic tremor [13, 150, 65].

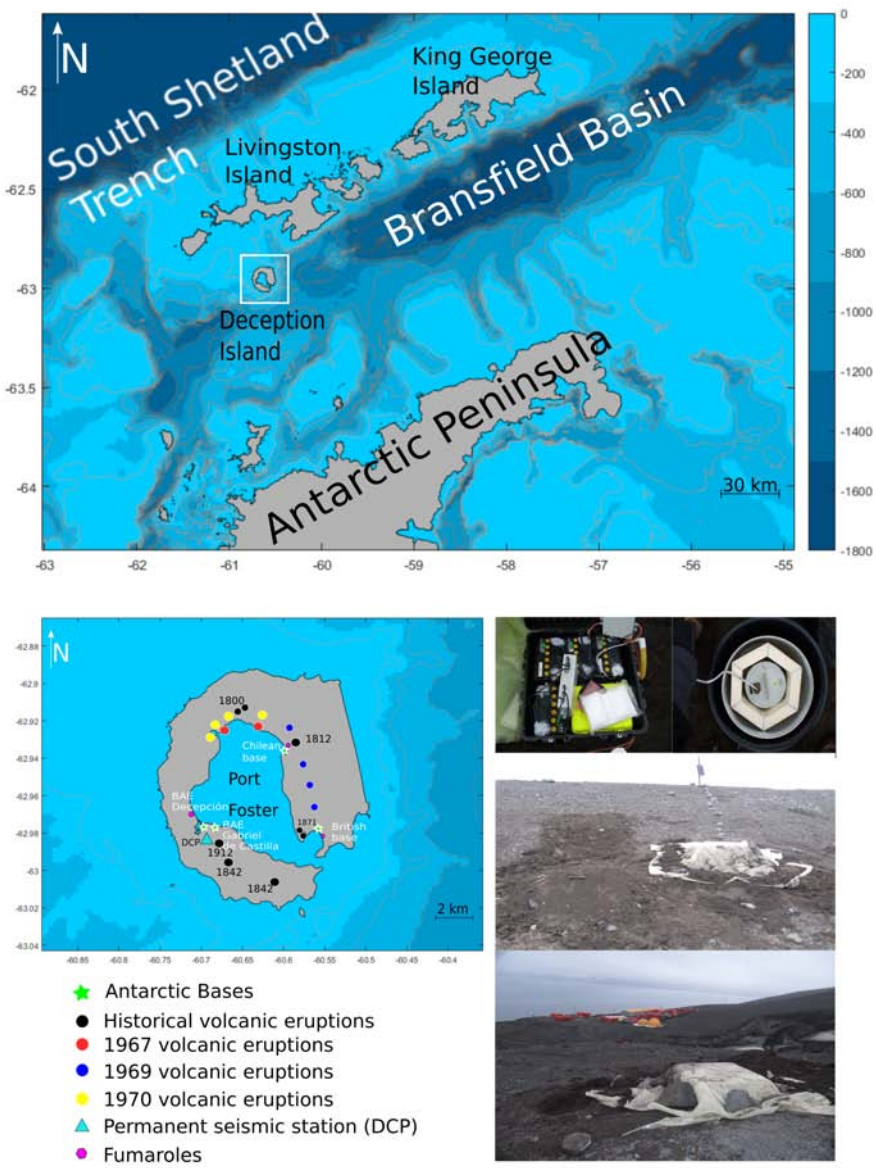

Figura 5.1: (top) Map of the Antarctic Peninsula and South Shetland Islands region, showing the location of Deception Island in the Bransfield Strait. The bathymetry (GMRT) contour interval is 200 m. (bottom left) Map of Deception Island. The cyan triangle represents the location of the seismic station DCP. (bottom right) Photos of the permanent seismic station DCP.

VT earthquakes are consequences of brittle fractures that occur within the volcanic edifice. At Deception Island volcano, VT earthquakes present a broad spectral content, up to 30 Hz, and S-P times below ∼4 s (Figure 5.2). Their source is related to the activation of fracture systems in the volcanic edifice due to changes in the distribution of local stresses, originated by volcanic processes. Several mechanisms have been proposed to explain the stress changes causing VT earthquakes at Deception Island, such as the instabilities induced by a shallow magma reservoir [64] and the dynamics of shallow aquifers, where partial sealing may produce an increase of pressure inside the micro-fractures [68, 64]. However, during unrest periods the most likely cause is the intrusion of magma at depth [236, 150, 11].

LP events (Figure 5.2) are the dominant type of seismicity at Deception Island volcano. They present an emergent arrival and spindle-shaped envelope, with durations generally shorter than 60 s. They are characterized by a quasi-monochromatic spectral content at low frequencies below 3 Hz [148]. However, LP events with frequencies above that limit have been occasionally reported [6]. For example, since 2009 LP events with frequencies up to 8 Hz are relatively common [65].

Volcanic tremors are continuous, long-lasting seismic signals (minutes to days or weeks) normally recorded in active volcanic areas [6, 150, 216]. They very often display spectral characteristics similar to LP events. Tremors recorded at Deception Island are generally narrow-band signals, with frequencies limited to the 1-4 Hz band, small amplitudes, and durations shorter than a few hours (Figure 5.2). However, some tremor episodes showed energy in other frequency bands. For example, episodes of spasmodic tremor contain energy at frequencies up to 8 Hz [13, 150, 148, 316, 63]. Similarly, some tremor episodes last much longer, from several hours to several days. Jiménez-Morales et al. [157] analyzed these episodes, initially termed Deception long-duration signals (DLDS) and concluded that they are volcanic tremors.

Previous studies evidence that LP events and tremor share similar source regions and processes [13, 12]. Thus, tremor and LP events are assumed to be different manifestations of the same source process [150]. Volcanic tremor is often understood as the result of the overlapping of simple events that occur closely in time during a long time span [13].

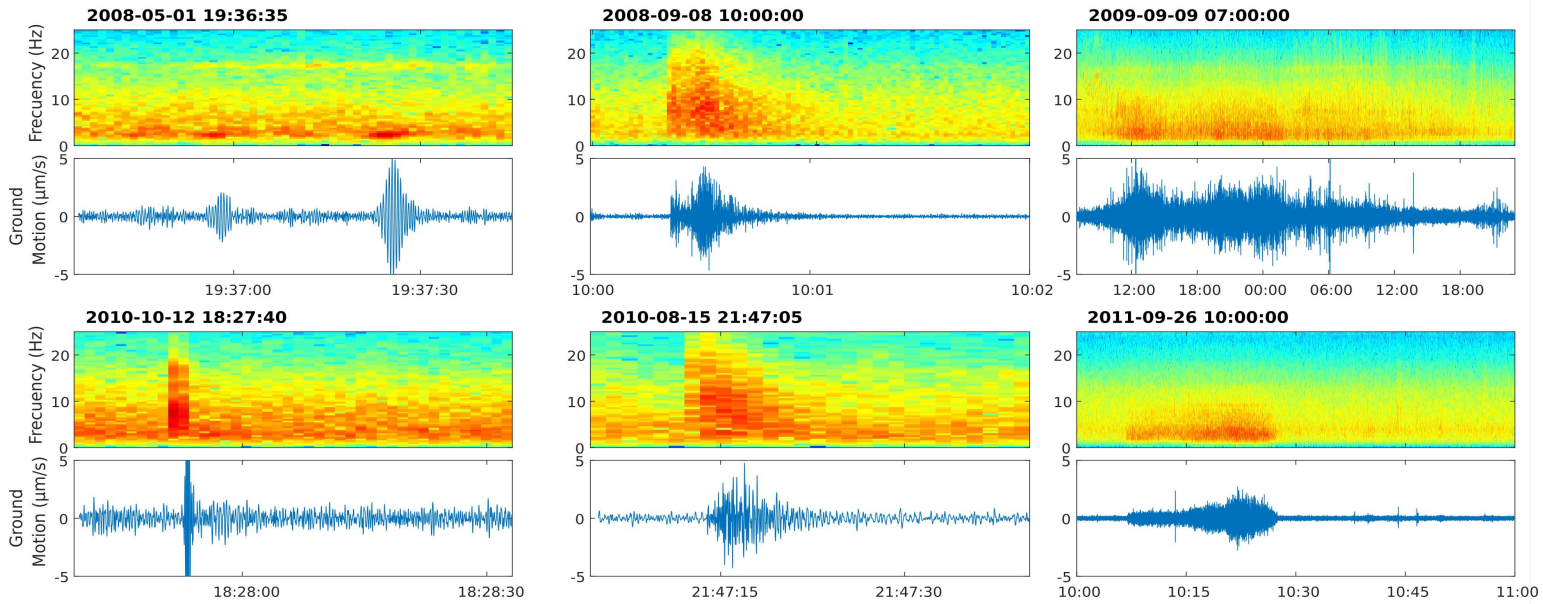

Figura 5.2: Examples of seismic signals recorded at Deception Island volcano: (A) Long-period event, LP; (B) Regional earthquake, RE; (C) Long-duration tremor, DLDS; (D) Short-period event, SP; (E) Volcano-tectonic earthquake, VT; (F) Tremor episode, TR. In all panels, we show the vertical-component seismogram, and the corresponding spectrogram on top. The times on the top axis are the start times of the windows displayed.

LP events have been extensively studied in different volcanoes, and several mechanisms have been proposed to explain their origin. The most accepted source model is the resonance of fluid-filled cavities, activated by pressure changes [5, 73, 74]. Other models invoke non-linear fluid flow phenomena [164, 163], and bubble dynamics and magmatic degassing [270, 186, 161]. A more recent model suggests that LP events could be produced by slow failures in the unconsolidated material of the upper volcanic edifice [31].

The model that best suits the LP seismicity of Deception Island volcano is the resonant crack model [13, 6, 150, 65]. LP sources are shallow, and associated to areas with a high thermal gradient and fumarolic emissions, such as Cerro Caliente, Fumarole Bay, Telefon Bay and Obsidians Beach [6, 65, 87, 146, 150, 219, 240]. Therefore, LP seismicity most likely originates from instabilities in the hydrothermal system and/or shallow volcanic conduits [6].

Additionally, there are other types of events at Deception Island. They might not be as common as LP seismicity, or as significant for the volcano dynamics as VT earthquakes, but still they are frequently detected in the seismograms, specially in recent years. For example, we can mention short-period (SP) events and harmonic tremors (HTR). SP events are characterized by very short signal durations ($\sim$3 s), a broad spectral content reaching very high frequencies, and a strikingly fast attenuation with distance. Harmonic tremors (HTR) are sustained signals characterized by a harmonic spectrum with equispaced overtones of a fundamental frequency. These types of events have not been described quantitatively before, although they are briefly mentioned in some works. Ibáñez and Carmona [146] and Carmona et al. [65] reported the occurrence of SP events during summer surveys. Based on qualitative similarities and the fact that about 60 % of the surface of Deception Island is covered by glaciers, they proposed that SP events are icequakes [260, 295, 62]. Similarly, Almendros [6] reported the detection of harmonic tremor episodes during the period 1994-1996. Harmonic tremors have been related to geothermal areas and volcanic environments in different eruptive phases [145, 283, 176, 191, 7]. They appear as well in ice-related phenomena such as iceberg and glacial dynamics [71, 200, 302, 328]. Additionally, they can be originated by artificial sources [e.g. 95].

The level of seismic activity at Deception Island volcano is highly variable. Based on the observations from seismic monitoring surveys between 1994 and 2011, Carmona et al. [65] proposed that there are two regimes of activity: dormant and restless. The dormant state is characterized by the dominance of LP seismicity, although there might be also some VT earthquakes in response to changes in the local stress distribution, and other signals. The restless state is characterized by a high level of volcanic seismicity, in particular a large number of VT earthquakes. This state implies an important change in the stress distribution, and thus drastic modifications in the conditions of the volcano interior that could eventually end up in an eruptive process.

Deception Island has been restless at least three times (1992, 1999, 2015) since 1986 when seasonal seismic monitoring was re-established after the 1967-1970 eruptions. From December 1991 to February 1992 there was a notable increase in seismic activity [236]. A total of 766 seismic events were recorded by a seismic station operating near the Argentinian Base. Some of them were felt, with magnitudes higher than 3. Although the epicentral area of the recorded activity could not be determined with precision, indirect evidence shows that the source area was probably located in Port Foster, only 2-3 km from the coast. In January 1999 there was a new increase in seismic activity [150, 148]. A total of 3643 seismic events were recorded in two months. More than half were VT earthquakes, with magnitudes ranging between -0.8 and 3.4 [137]. Again, the two largest earthquakes in the series were felt by personnel of the Spanish Base. The hypocenters were roughly aligned from Fumarole Bay to Pendulum Cove, at depths between 1 and 4 km. In early 2015, VT activity increased again [11]. A few thousand VT earthquakes were recorded at Deception Island in a period of 5 months, from December 2014 to April 2015, with a maximum magnitude of 3.3. About 400 VT earthquakes were located, but in this case the epicentres were spread throughout the volcanic edifice at depths down to 10 km and more. LP seismicity was unusually frequent and intense [10]. Additionally, the VT series was preceded by an intense seismic swarm SE of Livingston Island, that started in September 2014 and extended for at least 8 months. In all three cases, the seismic series have been interpreted as a consequence of the stress changes induced by magmatic intrusions [236, 150, 11].

5.3. Instruments and data acquisition

We use data from a permanent seismic station (DCP) operating at Deception Island volcano since February 2008 [63, 157, 11]. The station is based on a triaxial, electrolytic broadband seismometer EENTEC SP400, with flat response between 0.06 and 50 Hz; and a 24-bit data acquisition system EENTEC DR4000. The seismometer is located at 62° 59'S, 60° 41'W, near the Spanish base Gabriel de Castilla (Figure 5.1). The datalogger samples the three channels of the seismometer at 100 sps, and seismic data are stored locally in miniseed format. Power is provided by a 95 W solar panel, connected to a bank of 12 V batteries with a combined capacity of ∼600 Ah. Absolute timing is obtained by GPS. The station includes a monitoring system for temperature, battery voltage and power consumption (Figure 5.3), developed by University of Granada technicians. The total power consumption is very low (about 1 W), which allows the station to survive through the winter, when low-light conditions greatly reduce the panel efficiency and battery recharge.

In any case, despite the low temperatures and extreme weather of Deception Island, the station has operated reasonably well for many years. Figure 5.3 shows that DCP operated continuously during the period 2008-2015, except for short interruptions caused by annual servicing and data download, and a timing problem in October 2009. In May 2015 the station stopped due to a failure in the automatic re-start system after a temporary loss of power, and it did not record again until December.

5.4. Data analysis

We select 7.5 years of seismic data, from February 2008 when the station was deployed at Deception Island volcano, to May 2015, after the 2015 seismic crisis. The large volume (140 Gb) of miniseed seismic data has been processed using the SEISAN software [238]. SEISAN is a package designed for seismic database management and analysis. The database is built of seismic events linked to files containing the event information, including phase pickings (arrival times, amplitude, period, azimuth and apparent velocity)

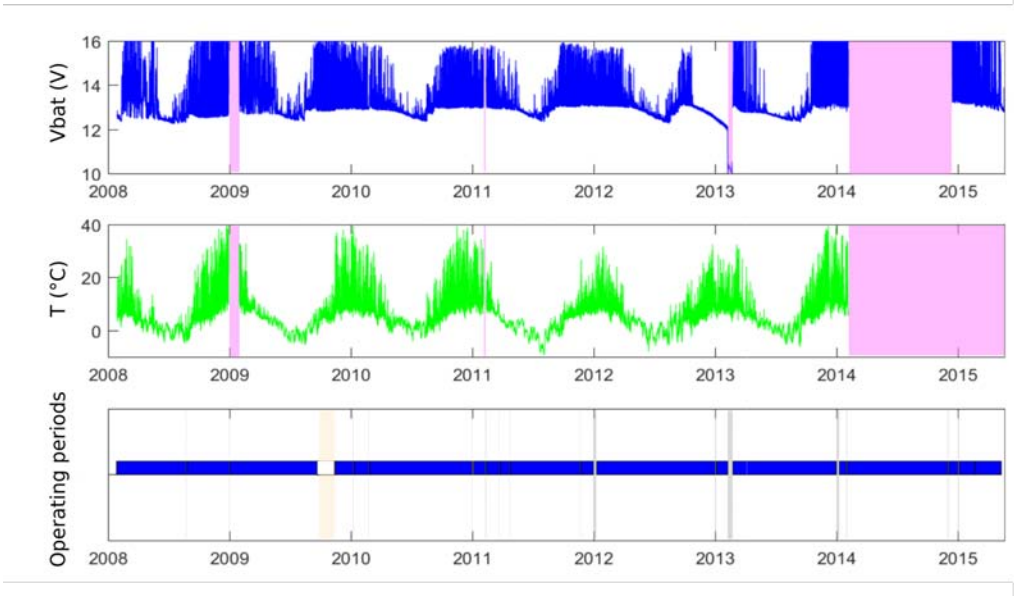

Figura 5.3: (top) Battery voltage during the operation of the station. (middle) Temperature measured at the station. (bottom) Operating periods of the seismic station. Pink areas indicate malfunction in the voltage/temperature datalogger; gray areas represent lack of seismic data due to station maintenance; and the salmon area corresponds to a period when the GPS malfunctioned and seismic data had inaccurate time.

and waveform data. SEISAN includes several tools to visualize seismograms, identify seismic events, determine spectral parameters, assess magnitudes, locate earthquakes, plot epicenters, etc.

The event identification procedure is based on a visual inspection of the seismograms. Although the level of microseismic noise varies with weather and ocean conditions, it is usually the dominant feature of the seismogram, specially at frequencies below 1 Hz. On the other hand, the cultural noise is low, despite the occasional presence of human activity on the island. In the frequency band where seismo-volcanic events have relevant content (0.5-10 Hz), the signal-to-noise ratio is generally good and high-quality records have been obtained. We use different filters to improve the signal-to-noise ratio and enhance our ability to identify seismic events. First, we visualize the vertical-component seismogram using a 0.5-10 Hz filter, with a 5-minute window and

a 12-line setup (1 hour) simultaneously on screen, for a quick overview and an efficient identification of broadband events such as volcano-tectonic and regional earthquakes. Then, we use 2-8 Hz filter, with a 2-minute window and 10-line setup (20 minutes), adequate for the identification of long-period events and short-duration volcanic tremor episodes.

Seismic events were classified in five groups characterized by different waveforms, durations, and spectral contents: long-period events (LP); tremor episodes (TR); volcano-tectonic earthquakes (VT); regional earthquakes (RE); and short-period events (SP). Additionally, we include high-frequency LP events (LPH), a subgroup of LP events with high dominant frequencies above 4.5 Hz; and harmonic tremors (HTR), a subgroup of tremors characterized by spectra with harmonic characteristics. Teleseismic earthquakes have been also identified, although they are not analyzed in this study. The classification is based on the combined visualization of seismograms and spectrograms, which allows us to observe simultaneously the evolution of the signal and its spectrum, and quickly assess the relationship between waveform and frequency content.

In order to quantify the characteristics of the seismic events, we estimated the signal durations and maximum amplitudes using the waveform envelopes. For long-period seismicity, we also calculated the dominant frequencies from the maximum of the smoothed amplitude spectrum. For tectonic and volcano-tectonic earthquakes, durations and amplitudes can be used to calculate the earthquake magnitude. Additionally, we measured the delay between the P and S phase arrivals, which is related to the hypocentral distance.

Source locations of tectonic and volcano-tectonic earthquakes could be roughly estimated from a single, three-component station using the azimuth to the source (obtained from the particle motion of the first P-wave arrival) and the distance to the source (obtained from the difference between the P and S wave arrivals). Unfortunately, for most earthquakes the incidence angles are high, and the retrieved source directions have large uncertainties, which in practice prevents us from obtaining reliable source locations. Nonetheless, we can still estimate the source distance from the difference between the P and S wave arrivals, $t_P - t_S$. The method requires a model of the crustal velocities of the area. For Deception Island volcano, there are several

studies about the local velocity structure [278, 330, 199]. However the spatial extents of these 3D models are limited to the shallow structure of Deception Island, and cannot be extrapolated to the Bransfield Strait, where the velocity structure is quite different [e.g 76]. Source locations reported in the area have been based on average, flat-layered velocity models [146, 65, 11]. To characterize the relationship between S-P times and distance, we use an empirical approach. We selected all available source locations obtained with a local seismic network during austral summer surveys in the period 2000-2015 [65, 11]. Using the source coordinates, we calculate the distances to station DCP and compare these values to the S-P times (Figure 5.4). These data are adequately fitted by a second-order polynomial given by:

$$D = 0.48 \cdot (t_S - t_P)^2 + 3.62 \cdot (t_S - t_P) \tag{5.1}$$

which is valid for distances up to 150 km (S-P times of 14 s). We use this equation to obtain estimates of source distances for all earthquakes recorded at DCP.

We estimated the magnitudes of tectonic and volcano-tectonic earthquakes using a duration magnitude scale. This type of magnitude is based on the observation that, for local earthquakes, the duration of the seismogram is relatively independent of the nature of the seismic source or the epicentral distance, but strongly dependent on the magnitude of the seismic events [184, 47, 48, 4].

Lee et al. [184] proposed a formula to estimate the earthquake magnitude based on the duration of the signal:

$$M = 2 \log \tau - 0.87 \tag{5.2}$$

where τ is the earthquake duration in seconds. Note that there should be also a distance-dependent term; however for local earthquakes it is very small and can be neglected without significant errors. Although originally proposed for California, this formula is widely used to estimate earthquake magnitudes in other regions as well.

Havskov et al. [137] proposed a specific duration magnitude scale for

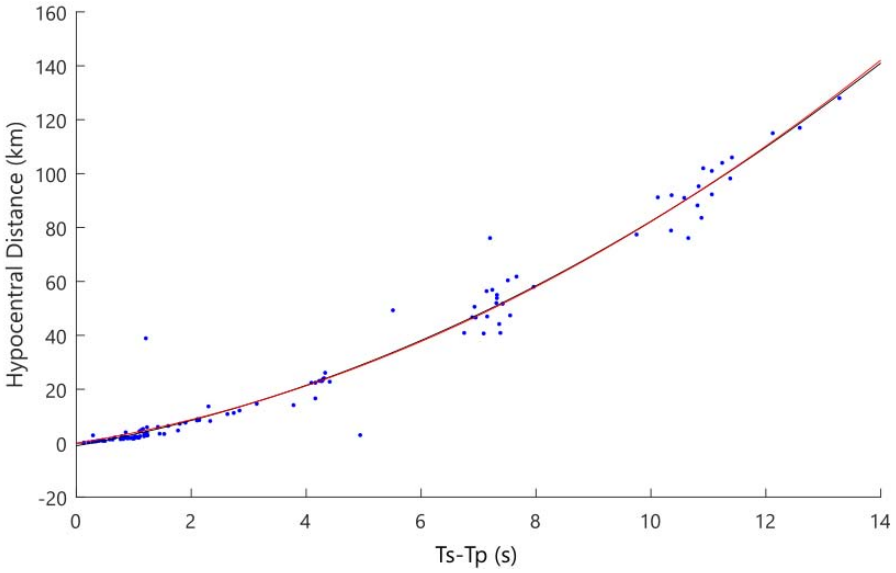

Figura 5.4: Earthquake distances versus S-P times for tectonic and volcano-tectonic earthquakes (blue dots) located by a local seismic network during the summer surveys in 2000-2015 at Deception Island. The red line represents a polynomial fit of the data.

Deception Island volcano:

$$M = 2.8 \log \tau - 2.7 \tag{5.3}$$

where τ is the earthquake duration in seconds. They calibrated this formula using local earthquakes at small distances up to ∼20 km, recorded during the 1999 seismic series [150].

In our analysis, we use the duration-magnitude formula of Havskov et al. [137] for very local earthquakes (S-P times below ∼5 s) that propagate basically in the highly fractured and attenuating crust within or around Deception Island volcano. For earthquakes at distances of 30-150 km (S-P times above ∼5 s), that propagate mostly within the Bransfield Basin and the South Shetland crust, we used instead the equation proposed by Lee et al. [184].

5.5. Results

The analysis of the 2008-2015 dataset at station DCP yielded a database of about 150000 seismic events. There are different event types characterized by a variety of frequency contents, waveforms, durations, amplitudes, magnitudes, etc. Table 5.1 shows the total number of events detected for each event type, as well as the number of events detected during each year. LP events (LP, LPH) constitute the most common type of seismicity (Table 5.1) representing about 86 % of the recorded events. The remaining event types are less numerous, although they are also significant. For example tectonic and volcano-tectonic earthquakes (RE, VT) constitute about 7.5 % of the signals, but their magnitudes can be large and therefore they are very important to understand the release of seismic energy at Deception Island. Similarly, tremor episodes (TR, HTR) constitute just about 4 % of the signals, but given their long durations their contribution to the release of energy can still be significant.

5.5.1. Long-period events (LP, LPH)

LP events with dominant frequencies below 4.5 Hz are conspicuous all over the recording period, with a total of 120586 events. Nevertheless, in recent years LP events with higher dominant frequencies (LPH events) have been recorded as well (Figure 5.5). LPH events are relatively uncommon, comprising just 9282 events (7 % of the total number of LP events). Figure 5.6 shows a summary of the results for LP events, including their temporal distribution, amplitudes, dominant frequencies, and durations. The most obvious feature of their temporal distribution is a remarkable increase in the number of LP events after 2011. Most LPH events are recorded during this period as well. Maximum LP activity generally occurs in the same time of the year (September-October). Maximum event rates are 4115 event/month in 2011, 3770 events/month in 2013, and 11415 events/month in 2014. Maximum event rates for LPH are one order of magnitude lower, e.g. 417 events/month in 2011, 397 events/month in 2012, and 2110 events/month in 2013. LP durations range between 5 and 60 s. The most usual durations are around 8-10 s. LPH durations tend to be shorter, with average values around 4-6 s. Event

	2008	2009	2010	2011	2012	2013	2014	2015	Total
LP	1799	5950	4292	19846	11972	26659	42626	7442	120586
LPH	176	346	84	1382	829	5170	559	736	9282
TR	84	378	138	302	241	594	3045	331	5113
HTR	15	102	36	80	119	42	22	16	432
SP	3	62	171	141	511	1805	774	124	3591
VT	33	50	97	154	191	634	1536	1279	3974
RE	19	35	36	40	28	111	6579	277	7125
VT M_0 (10^{12}Nm)	10.1	36.4	14.8	18.5	21.0	61.3	277.7	196.3	636.1
RE M_0 (10^{14}Nm)	20.4	7.8	4.9	11.7	5.1	32.0	424.4	9.4	515.6

Cuadro 5.1: Number of seismic events recorded for each event type and total seismic moment (M_0) for VT and RE earthquakes. Purple cells highlight the maximum for each event type.

amplitudes are usually small (1-4 μm/s), although they may reach higher values up to 25 μm/s. For example, we find many LP events with amplitudes above 5 μm/s in October-November 2014, also with durations longer than usual (Figure 5.6).

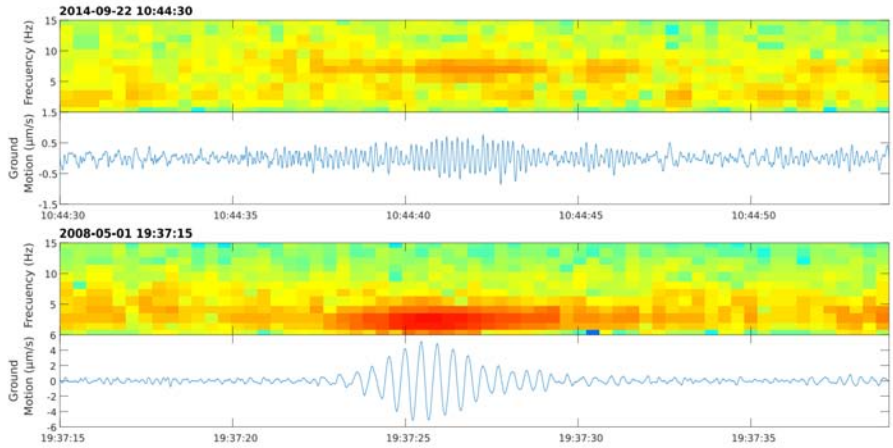

Figura 5.5: Examples of LP events recorded at DCP, with dominant frequencies of 2-3 Hz (bottom) and 6-8 Hz (top). In both panels, we show the vertical-component seismogram, and the corresponding spectrogram on top.

The number of LP events shows temporal variations with annual period that suggest a seasonal effect. Two different seasonal behaviours are observed in the seven years of study. In 2008 and 2009, the maxima are reached in the austral summer. After 2010, the maxima are instead reached in September and October, during the austral spring, while the minima occur during the austral summer months. This trend is clearest in 2011, 2013 and 2014 (Figure 5.6). During the first three years, LPH events were scarce and tended to occur in the summer months. Since 2011, they are scattered along the year, and the seasonal trend is less clear. In any case, we find higher concentrations in the winter/spring months (Figure 5.6).

LP events often occur in series that last for minutes to hours (Figure 5.7). These series can occasionally present evenly-spaced events (rhythmic LPs) as described by Stich et al. [298]. They are characterized by events with very similar waveforms, durations around 8 s, frequencies of 2-3 Hz, and fixed inter-event times in the range of 10-20 s. They may occur at any

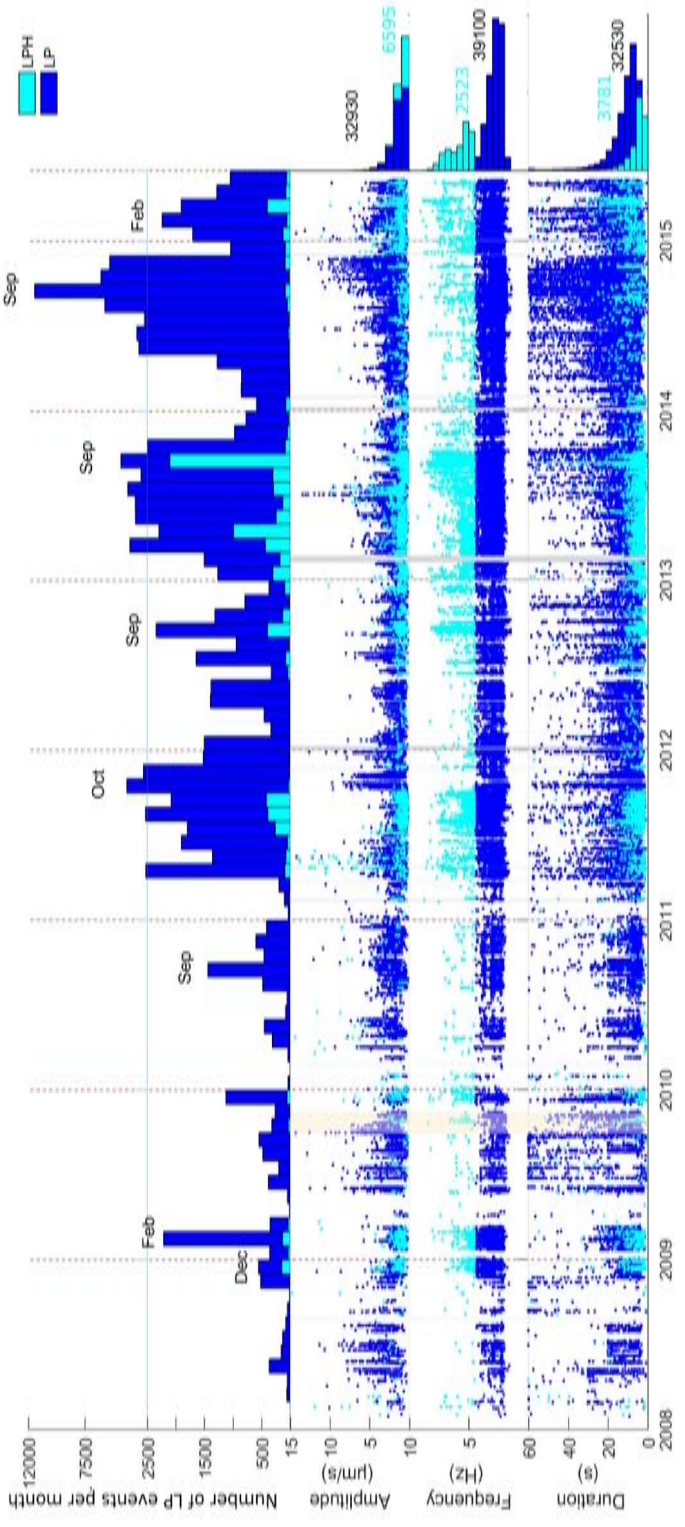

Figura 5.6: Summary of results for LP and LPH events at station DCP during 2008-2015. From top to bottom we show the number of events per month, maximum amplitudes, dominant frequencies, and event durations of LP (blue) and LPH (cyan) events. The labels in the top panel represent the month when the annual maximum is reached. On the right, we display histograms of the distribution of these characteristics. The lengths of the cyan bars representing LPH events have been multiplied by 5 for visibility. Numbers indicate the maximum values reached in each case.

time throughout the year, although they are most common during the austral spring months (September-October). Sometimes, rhythmic LP series are discontinuous, appearing as minute-long packages of five overlapping events characterized by slightly longer durations and broader spectra.

5.5.2. Tremor episodes (TR, HTR)

Volcanic tremors (TR) constitute a common form of seismic activity at Deception Island volcano, with 5113 episodes during 2008-2015. Although their numbers are much smaller than LP events, tremors are long-lasting signals, therefore their energy is important as well. These signals have been always present at Deception Island volcano since the start of seismic monitoring in the 1950s, and often reported after the opening of the Gabriel de Castilla base in 1986 [315, 236, 150]. TR episodes show energy basically in the 1-9 Hz range. They present different spectral characteristics (Figure 5.8). Some of them are relatively broadband, with no clear dominant frequency. Others display energy in a narrower frequency band below 4-5 Hz. Spasmodic tremors characterized by a continuous low-frequency band and discontinuous high-frequency energy packets are also identified. Finally, a very interesting observation is the detection of 432 harmonic tremors (HTR) with a fundamental frequency between 1-3 Hz and regular overtones up to 18 Hz, which decrease in intensity as they increase in frequency.

Figure 5.9 shows the main characteristics of TR episodes, including maximum amplitudes, dominant frequencies, and durations. We observe that amplitudes are mostly limited to 1-10 μm/s. Harmonic tremors tend to be smaller, with amplitudes of 1-3 μm/s. The dominant frequencies cluster in the 2-3 Hz band, although they may reach up to 8-9 Hz. TR durations vary from minutes to one hour. We cannot identify longer-duration tremors due to the limitations of the applied method (i.e. analysis window of 1 hour). Most of the detected TR episodes are relatively short and last less than 15 minutes. HTR are even shorter, basically with durations below 5 minutes. Jiménez-Morales et al. [157] developed a specific method optimized for the detection of long-duration signals, and reported 276 long-duration (hours to days) tremors at Deception Island between 2008 and 2015, with amplitudes

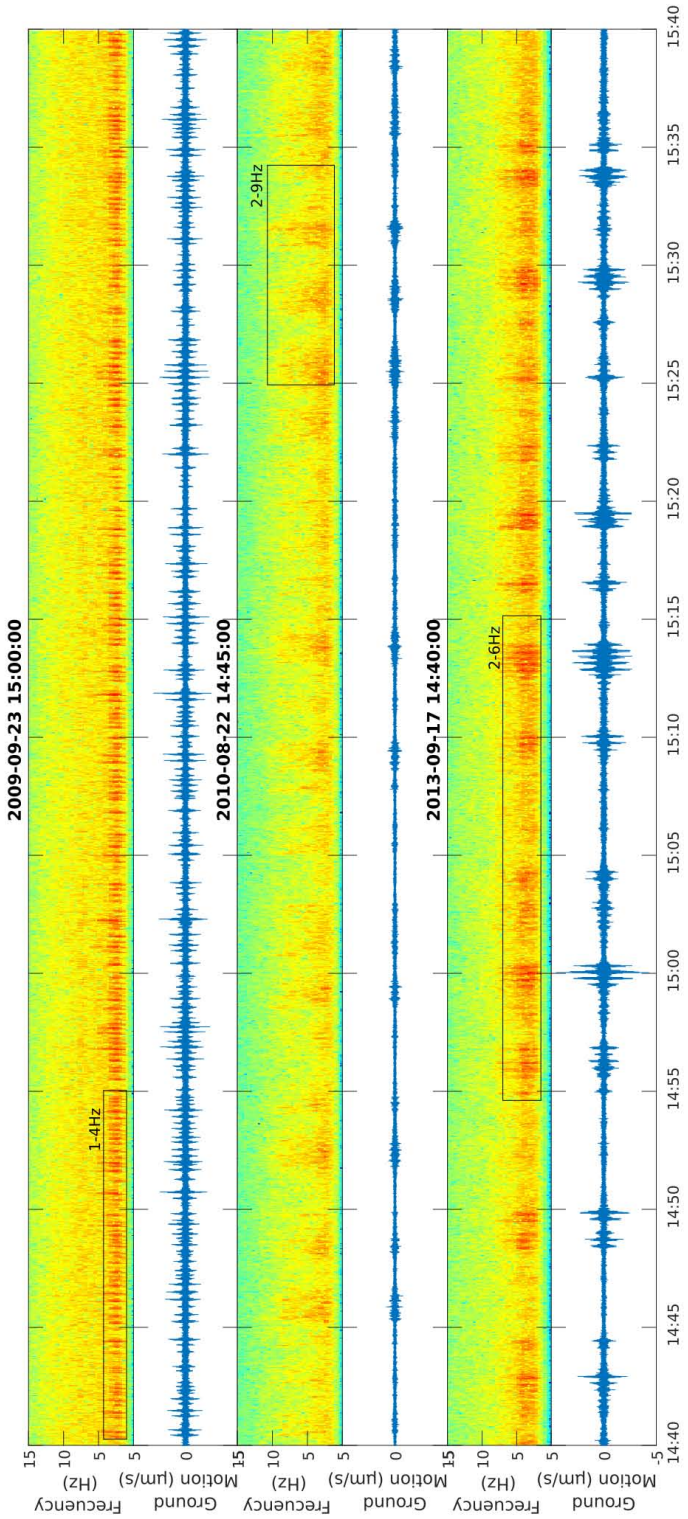

Figura 5.7: Examples of different types of LP series recorded by the DCP station. In all panels, we show the vertical-component seismogram, and the corresponding spectrogram on top. The times on the top axis are the start times of the windows displayed. Black boxes highlight the dominant frequencies of LP series.

in the range of 0.5-2 μm/s, and frequency content limited to the 0.5-5 Hz band. These data are not included in our results, but will be added later for the discussion. We observe no clear relationship among TR frequencies, amplitudes, and durations (Figure 5.9). For example, we find TR episodes with similar durations and different dominant frequencies (Figure 5.8).

TR episodes occur during the entire period of study, with rates up to several hundred events per month. They present a heterogeneous temporal distribution, with three maxima in 2009 (133 episodes/month), 2013 (223 episodes/month) and 2014 (730 episodes/month). These maxima occur approximately in the same time of the year (around September). Relative maxima of 50-80 tremors/month are also found occasionally during the austral summer months. Except for the above mentioned peaks, from 2008 to 2013 the number of events does not exceed 100 per month, with an average of 24 events/month. However, in 2014 we identified a sudden increase in the TR activity, compared to previous years (Table 5.1). A high rate of occurrence of volcanic tremor episodes (about 200 episodes/month) was observed from February to November 2014, except for September and October when there were over 700 events/month. The minimum rate during this period (115 events/month) was larger than the average of the previous years. In December 2014 there was a significant decrease in TR activity to 40-50 episodes/month, with rates similar to the pre-2014 levels.

Harmonic tremors are rare events at Deception Island, that barely reach maximum rates of a few tens of events per month. They have a striking temporal distribution, with most part of the HTR episodes concentrated in the austral summer months (Figure 5.9). We find some exceptions, for example during the winter of 2009, but their temporal behavior is strikingly regular. In the period 2008-2013, maximum activity reached 20-60 events per month. After 2014, the maximum number of events becomes lower (5-15 events/month). Except for these maxima, the monthly number of harmonic tremors did not exceed 14, with an average of about 5 events/month.

The spectral characteristics of some tremors are similar to those observed for the LP signals. In some cases, we can even identify wave packets that can be interpreted as LP events, although we cannot isolate their onset or end due to the close overlapping. In fact, we observe a continuous gradation from

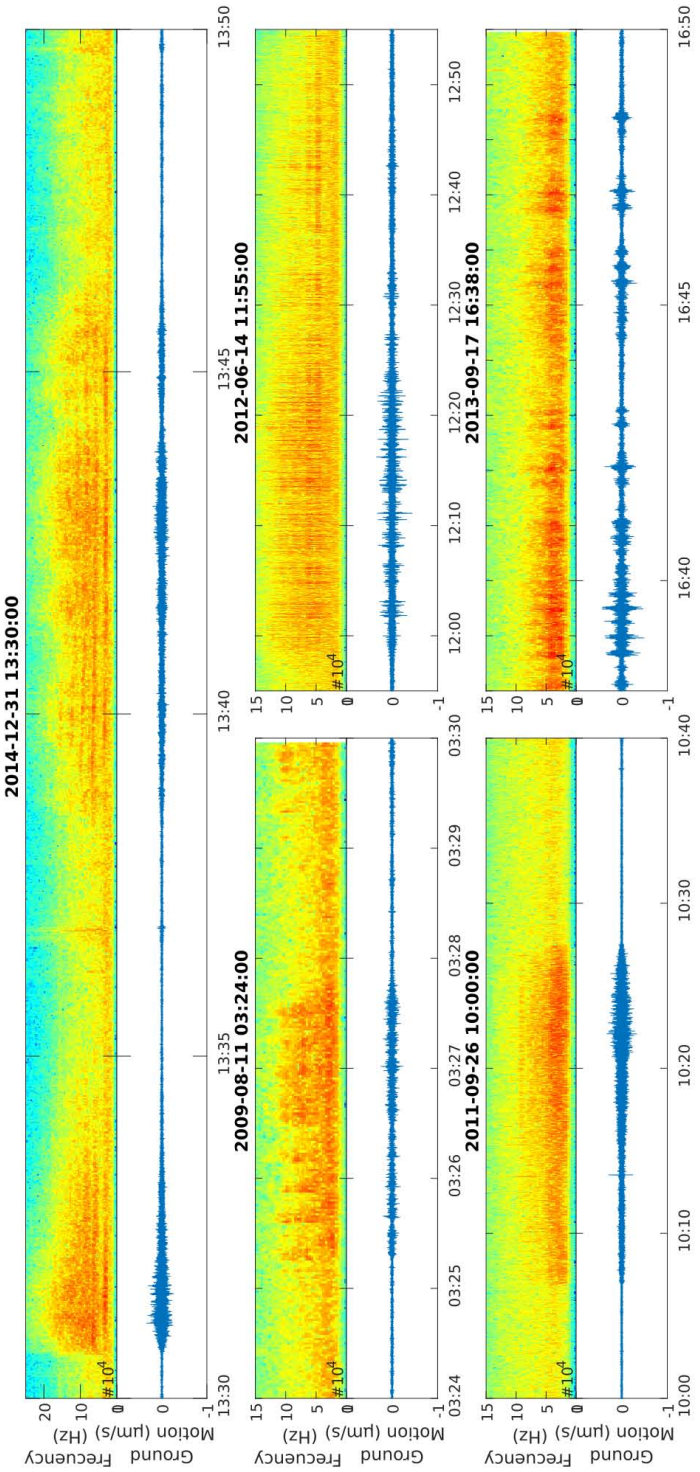

Figura 5.8: Examples of different types of TR episodes recorded at the DCP station. In all panels, we show the vertical-component seismogram, and the corresponding spectrogram on top. The times on the top axis are the start times of the windows displayed.

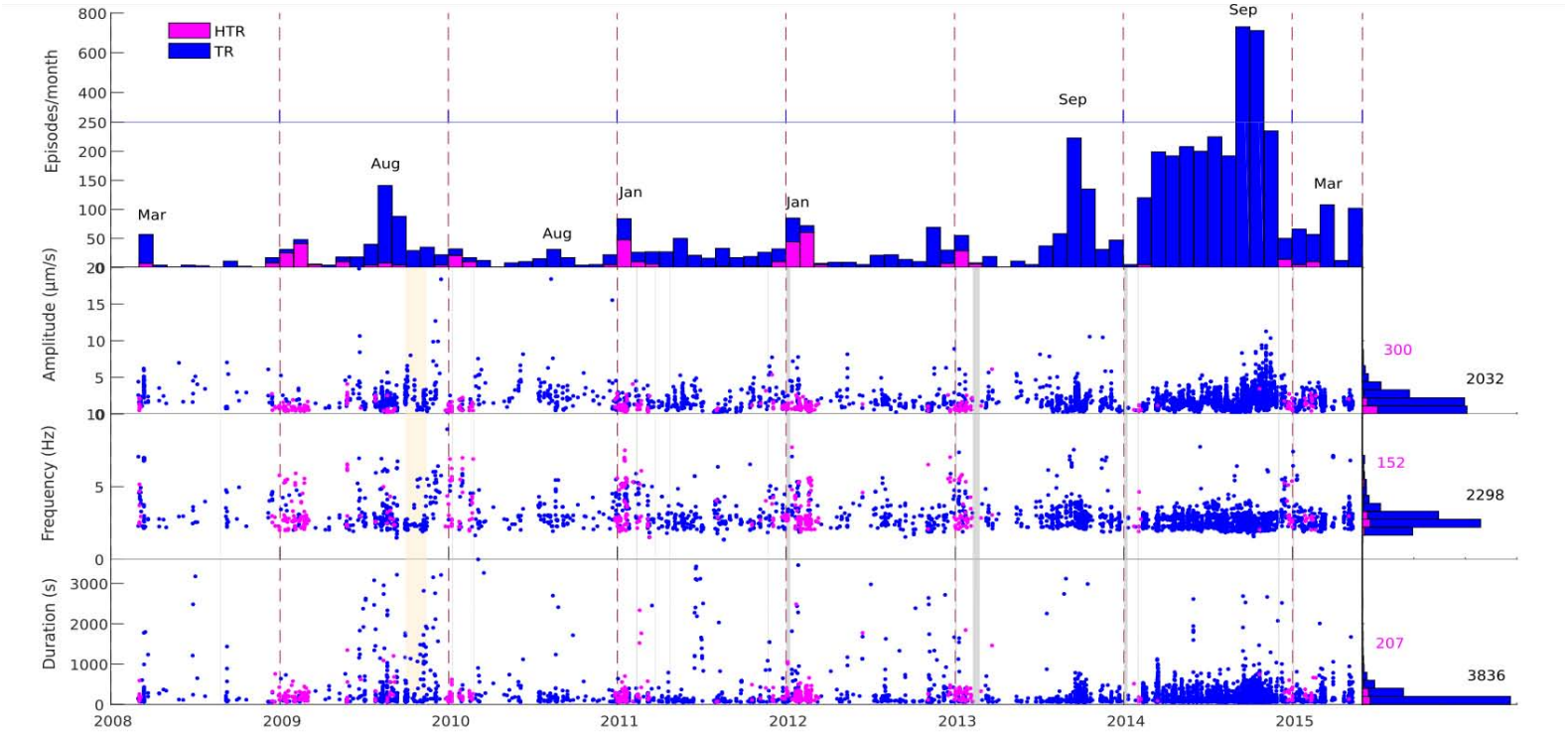

Figura 5.9: Summary of results for TR and HTR episodes at station DCP during 2008-2015. From top to bottom we show the number of tremor episodes per month, maximum amplitudes, dominant frequencies and durations. On the right, we display histograms of the distribution of these characteristics. Numbers indicate the maximum values reached in each case. Colors identify TR (blue) and HTR (magenta) signals. The labels in the top panel represent the month when the annual maximum is reached.

series of clearly isolated LP events to sustained-amplitude volcanic tremors.

5.5.3. Tectonic and volcano-tectonic earthquakes (VT, RE)

Regional tectonic earthquakes (RE) and local volcano-tectonic (VT) earthquakes are very common as well at Deception Island. We recorded 11099 earthquakes at station DCP during 2008-2015, of which 3974 are VT earthquakes and 7125 are RE earthquakes. They are characterized by relatively impulsive P-wave onsets, clear S-wave arrivals, and broadband spectral content (Figure 5.10). The separation between these two types relies on the hypocentral distances, which in our case is directly related to the difference between the P and S phase arrivals. VT earthquakes occur within the Deception Island volcanic edifice and have a small value of $t_S - t_P$, while regional earthquakes associated to fault systems outside Deception Island should have larger values. The $t_S - t_P$ threshold is set at 5 s, which implies a source distance of about 30 km (Equation 5.1).

The temporal distribution of the VT and RE events is shown in Figure 5.11. It shows a low level of activity in the first years, and a gradual increase in activity in recent years. On one hand, the VT activity since 2011 increases considerably, and it is especially high in 2014-2015. Before 2011 this activity was low, always below 100 events per year (Table 5.1), with small peaks in 2008 (12 event /month), in 2009 (14 event /month), and 2010 (38 event/month). Since 2011 the activity becomes greater and increases with time from 154 events in 2011 to 1536 events in 2014 (Table 5.1), with maxima of 229 events/month in 2013, 714 events/month in 2014, and 586 events/month in 2015. On the other hand, the rate of RE earthquakes increases moderately after 2013 and escalates during the 2014-2015 series at Livingston Island (Table 5.1 and Figure 5.11). The distribution of RE events maintains a behavior similar to the distribution of VTs. They are recorded regularly, although at a low rate in the first years (<40 events/year), with maxima of 3 events/month in 2008, 7 events/month in 2009, and 8 events/month in 2010. After 2013, this rate increases to >110 events/year, with maxima of 25 events/month in 2013 and 131 events/month in 2015. In 2014, there was a significant increase

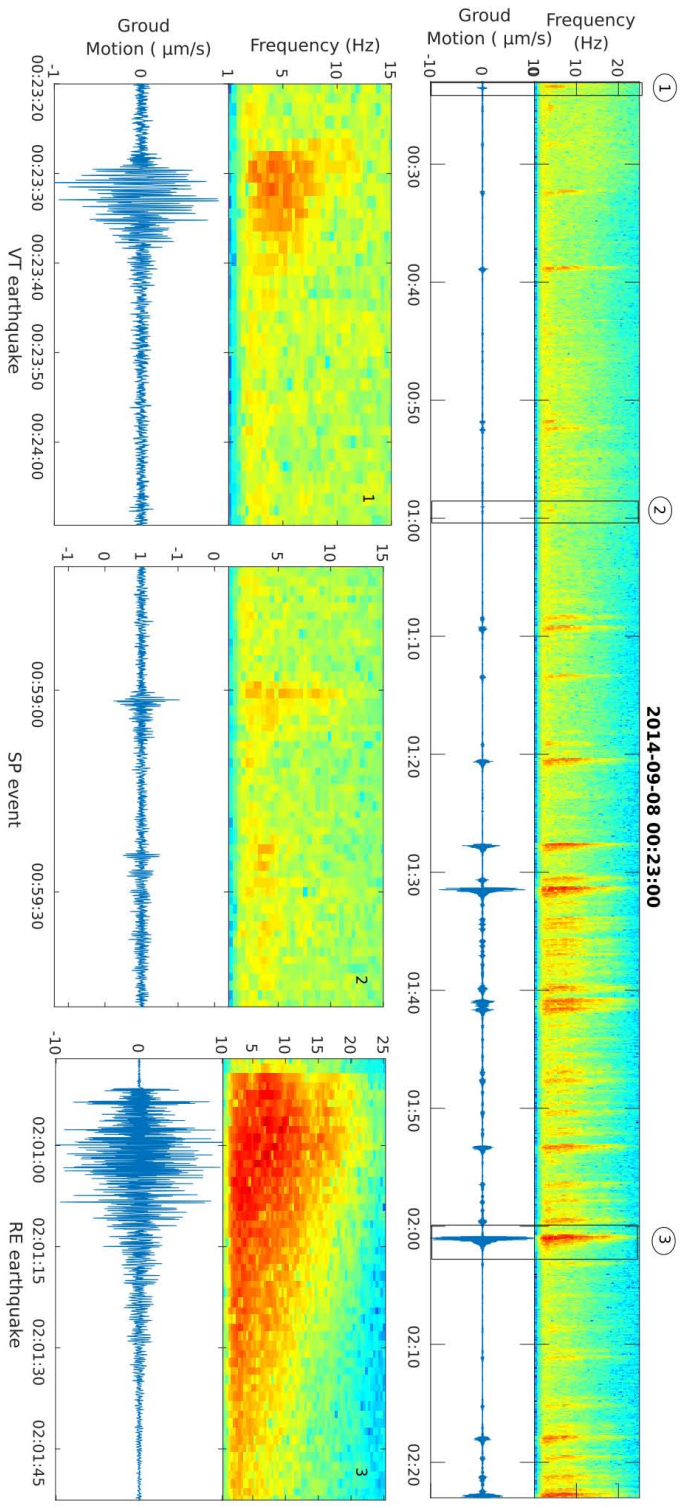

Figura 5.10: (Top) Two hours of seismic data recorded by the DCP station, containing examples of a VT earthquake (1); an SP event (2); and a RE earthquake (3). In all panels, we show the vertical-component seismogram, and the corresponding spectrogram on top. The times on the top axis are the start times of the windows displayed.

in the number and energy of REs, reporting 6579 events and a peak rate of 5252 events/month.

S-P times of VT events are concentrated around 0.8-2.3 s (Figure 5.11). This range represents a hypocentral distance of 3-11 km. We observe a high concentration of S-P times around 7-8 s in the last part of the selected period. These S-P delays imply a distance of ∼50 km from DCP, and correspond to the Livingston series detected between September 2014 and May 2015 [11].

The durations of the VT earthquakes range between 10 and 50 s, with an average around 20 s. Magnitudes vary between 0.5 and 3.3, although most events lay in the range 0.5-1.5 (Figure 5.11). RE earthquakes display durations between 15 and 360 s, with an average around 52 s. Estimated magnitudes vary between 0.5 and 4.5, with the most frequent magnitudes in the range 1-2.5 (Figure 5.11).

Figure 5.12 shows the cumulative number of events and cumulative seismic moment for VT and RE earthquakes during 2008-2015. In Table 5.2 we report the average rates of event production and seismic moment release for selected time periods.

We observe that for most of the 2008-2015 period the production of RE earthquakes is stable, with average rates of 0.09 earthquakes per day from February 2008 to January 2013 and 0.33 earthquakes per day from January 2013 to August 2014. In terms of seismic moment, and although the largest earthquakes obviously produce steps in the cumulative seismic moment, the average release is roughly constant, at a rate of $3.4 \cdot 10^{12}$ N·m/day. However, in September 2014 the earthquake rate rockets up to almost 200 events per day, as a consequence of the Livingston series. In October the earthquake production relaxes to 43 events per day, and then to about 4 events per day in November. This decreasing trend continues except for a brief period in February 14-22, when the rate reaches 14 events per day. From September 2014 to February 2015 the total seismic moment release is $\sim 4.24 \cdot 10^{16}$ N·m. Therefore 82 % of the total moment release related to RE earthquakes occurs in just 7 % of the time period (6 months). The earthquake production rate reached $1.4 \cdot 10^{15}$ N·m/day in September. This rate reduces to $2.1 \cdot 10^{14}$ N·m/day in October and keeps reducing from $3.1 \cdot 10^{13}$ N·m/day after November to $4.3 \cdot 10^{12}$ N·m/day at the end of the recording period.

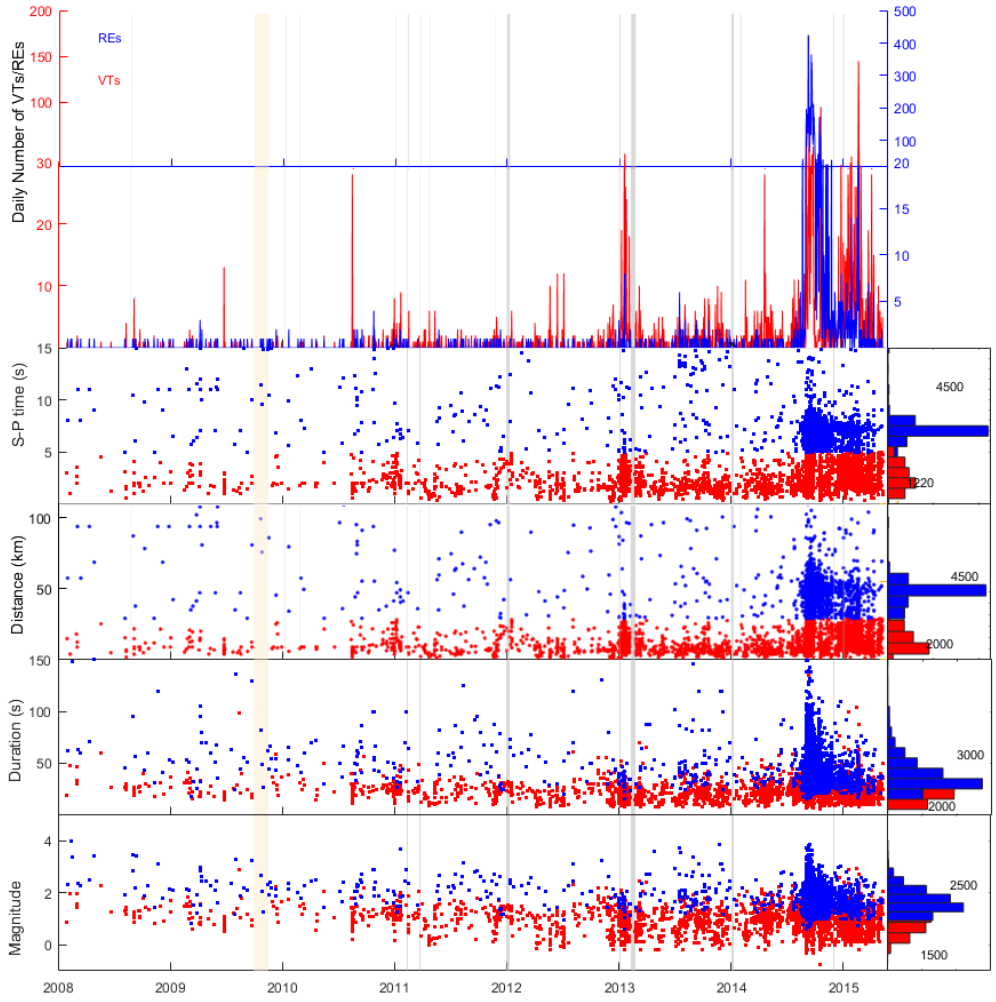

Figura 5.11: Summary of results for VT and RE earthquakes at station DCP during 2008-2015. From top to bottom we show the daily number of earthquakes, S-P time delays, distances, durations, and magnitudes for RE (blue) and VT (red) earthquakes. On the right, we display histograms of the distribution of these characteristics. Numbers indicate the maximum values reached in each case.

The number of VT earthquakes increased at more variable rates. Initially the earthquake production rate was small (0.16 earthquakes per day in 2008-2010). However, this rate increased steadily during the following years, to 0.43 earthquakes per day in 2011-2012, 1.12 events per day in February 2013-

April 2014, and 1.80 events/day in April-August 2014. The only exception to this steady trend is the occurrence of a VT swarm in January 2013, with a production rate of about 11 earthquakes per day. In any case, in September 2014 we witness a sudden increase of the VT earthquake production rate at Deception Island, reaching 26 events per day, which represents ∼15 times more earthquakes than in the previous period. In October the production rate decreased to 4.2 earthquakes per day, but in December the rate increased again, reaching 12 events per day in December-February, and a peak rate of 55 events per day during February 14-22. Finally, during the remaining period the rate went down to 4.8 earthquakes per day. The cumulative seismic moment also varied at rates increasingly higher. In 2008-2012 the moment rates were about 2-5·10^{10} N·m/day. In February 2013 the rate increases to $1.1 \cdot 10^{11}$ N·m/day, and in April 2014 there was yet another increment to a rate of $2.6 \cdot 10^{11}$ N·m/day. Again, the January 2013 swarm was an exception to this smoothly increasing trend, and produced about $1.0 \cdot 10^{12}$ N·m/day. The moment rate during September 2014 increased to $8.7 \cdot 10^{12}$ N·m/day. Although the moment release in October relaxed to a lower rate of about $1.9 \cdot 10^{11}$ N·m/day, there was another surge to come. At the end of December the moment rate increased to $1.9 \cdot 10^{12}$ N·m/day, and from February 14 to 22 it reaches a peak rate of $1.0 \cdot 10^{13}$ N·m/day. After that, the rate of moment release drops to a value of $3.2 \cdot 10^{11}$ N·m/day.

5.5.4. Short-period events (SP)

SP events are a characteristic signal often recorded at Deception Island, specially after 2012. They have a very short duration (a few seconds), and a broadband frequency content up to very high frequencies of 30-50 Hz (Figure 5.10). We have identified 3591 SP events at DCP during 2008-2015 (Figure 5.13). Durations range between 1 and 8 s, with most events lasting 2-4 s. They present amplitudes up to tens of μm/s, although about 87 % of the SP events have small amplitudes below 5 μm/s. Assuming that their energy scales with duration similarly to the VT earthquakes, we can assign magnitudes using Equation 5.3. In this way, we find that they are low-energy signals, characterized by negative magnitudes down to -2.5 and an average

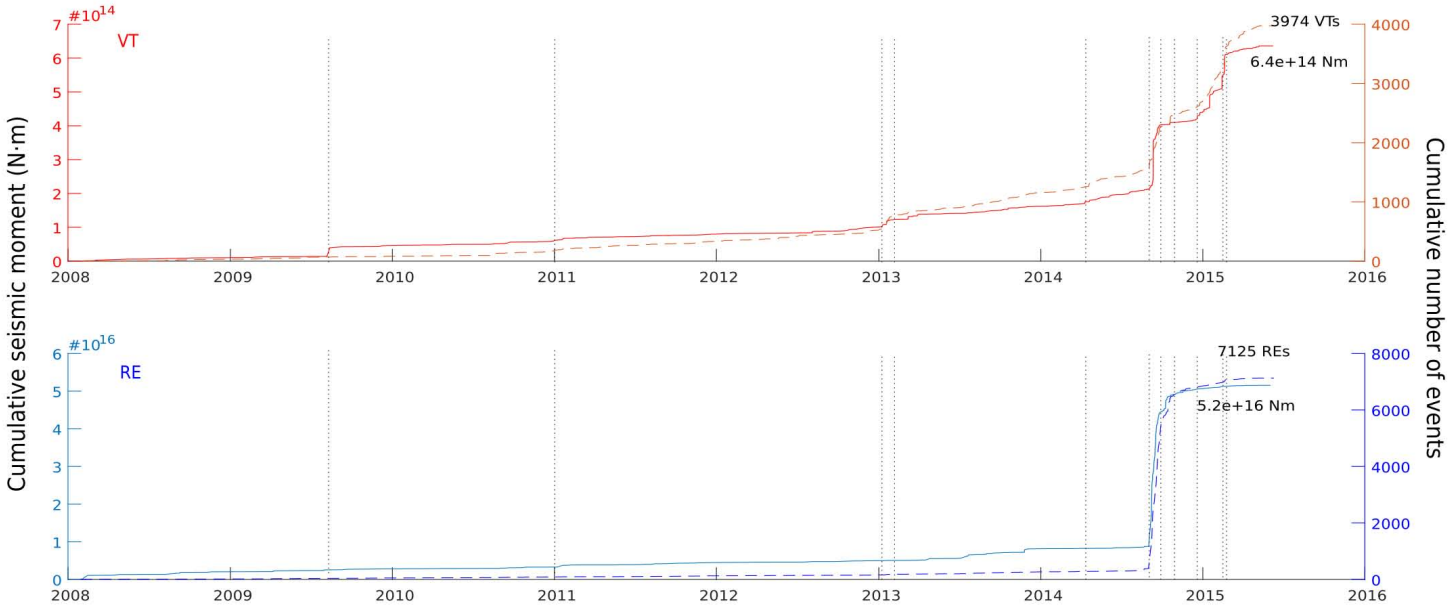

Figura 5.12: Cumulative seismic moment (solid line) and cumulative number (dashed line) of volcano-tectonic earthquakes (top, red) and regional earthquakes (bottom, blue). The gray lines bound the periods displayed in Table 5.2

.

Period	dM_0/dt VT 10^{10}Nm/day	dN/dt VT events/day	dM_0/dt RE 10^{12}Nm/day	dN/dt RE events/day
2008-01-01 - 2009-08-10	2.2	0.16	3.4	0.09
2009-08-10 - 2011-01-01	4.9			
2011-01-01 - 2013-01-07		0.43		
2013-01-07 - 2013-02-02	101.6	10.73		0.33
2013-02-02 - 2014-04-11	10.9	1.12		
2014-04-11 - 2014-09-01	26.1	1.80		
2014-09-01 - 2014-09-27	872.5	25.70	1400.3	194.0
2014-09-27 - 2014-10-28	19.3	4.19	211.3	42.89
2014-10-28 - 2014-12-18			30.8	3.78
2014-12-18 - 2015-02-14	187.0	11.99	12.1	
2015-02-14 - 2015-02-22	994.1	54.96		14.23
2015-02-22 - 2015-05-10	31.5	4.75	4.3	0.90

Cuadro 5.2: Average earthquake production and seismic moment release rates for VTs and REs during significant periods.

magnitude of about -1.3. Given these small magnitudes, they must be very local signals originating in the close vicinity of the seismic station.

In Figure 5.13 we show the monthly occurrence of SP events. Although the distribution is heterogeneous, in general the activity was low from February 2008 to November 2012 with <180 events/year (Table 5.1). The maxima of the annual distributions occurred in November 2008 (3 events/month), June 2009 (36 events/month), August 2010 (93 events/month) and March 2011 (40 events/month). Since December 2012 the activity increased significantly, often reaching values of several hundred events per month, and an average of over 500 events/year (Table 5.1). In this period the annual maxima occur in December 2012 (359 events/month), August 2013 (408 event/month), October 2014 (218 event/month) and January 2015 (92 events/month).

5.6. Discussion

We have quantified the seismic activity recorded at Deception Island volcano by a permanent seismic station during the period 2008-2015. It is the first time that such a long, continuous time series has been recorded and analyzed. Although there were some (analog) seismometers at Deception Is-

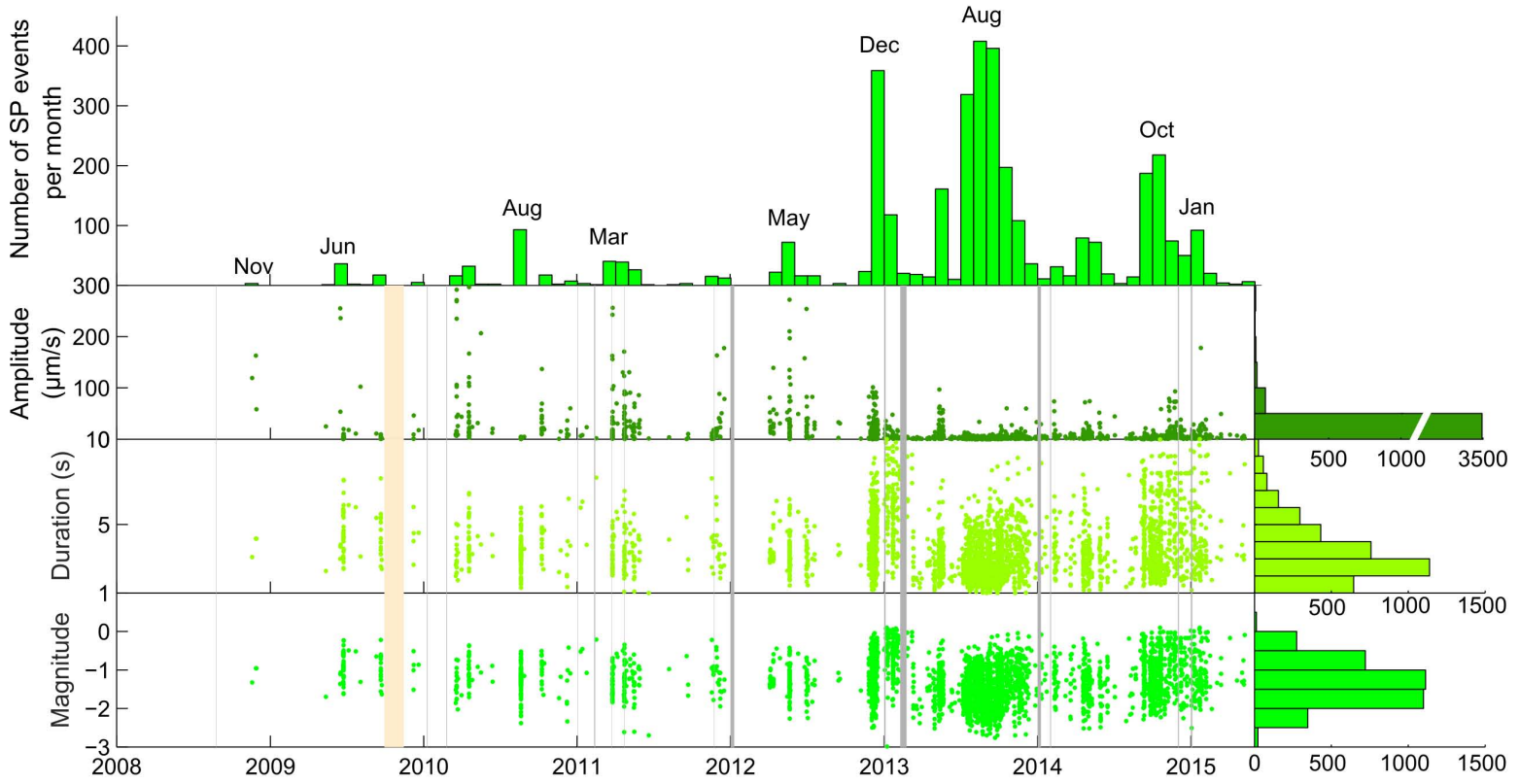

Figura 5.13: Summary of results for SP events at station DCP during 2008-2015. From top to bottom we show the number of events per month, amplitude, duration, and magnitude. On the right, we display histograms of the distribution of these characteristics. The labels in the top panel represent the month when the annual maximum is reached.

land before the 1967-1970 eruptions, they were discontinued and no seismic data was collected again until 1986. From 1986 to 2008, seismic monitoring has been intermittent, covering just the austral summer months and thus leaving out about 75 % of the time. Moreover, during those years seismic instruments have been diverse; they have been deployed at different locations; and analysts throughout this period have not been the same, therefore might not apply exactly the same criteria. In our case, we use a permanent broadband station, located at the same site for many years. In order to extract the most information from this dataset, a single operator has reviewed all data, applying the same criteria and standards. This ensures that the results are comparable and that we have a homogeneous, complete, and detailed seismic database.

Event detection and classification was based on the visual observation of the waveform characteristics, frequency content, and duration of the signals. Although this method is robust, it is also laborious and time-consuming. We are aware of other alternatives, for example based on automatic detection and recognition methods [79, 33, 119, 149, 82], which would have saved time and effort, even if the database would not be as complete. These methods are quickly improving, but they still have some problems, such as the discrimination of events in noisy conditions, the dependency on the training datasets (often short and heterogeneous, analyzed by multiple operators, using multiple instruments with different responses and different distances to the source), etc. In particular, the identification of volcanic tremors is difficult to address, due to their duration, although recent work has improved their detectability [308]. Given its homogeneity, temporal extent, and the variety of signals included, our database may constitute a significant contribution to test and improve automatic methods [159].

The availability of a continuous time series allows for the characterization of the temporal evolution of the seismicity, the detection of patterns and trends in the types of events and level of seismicity, and the assessment of the relationship between the seismic and volcanic activity. This is specially interesting if we consider that the selected period precedes the 2015 unrest of Deception Island, when the volcano underwent a series of changes suggesting the intrusion of a large volume of magma into the plumbing system [11].

In the following, we first describe the long-term evolution of the seismic activity in the period 2008-2015, the seven years preceding the 2015 seismic unrest at Deception Island volcano, and how Deception Island evolved from a background seismicity level in 2008 to an intense seismic swarm in 2015. We also discuss some temporal variations that appear in the data but are unrelated to the intrusion process. And finally, we provide a volcanological interpretation of the changes in the seismicity patterns observed during 2008-2015.

5.6.1. Behavior of the seismicity preceding the 2015 seismic crisis at Deception Island volcano

The most striking feature of the temporal distribution of the seismicity during the period 2008-2015 is that the number and energy of seismic events generally increased with time. This can be seen in Figure 5.14, where we summarize the numbers of events per month for all event types during 2008-2015, including the long-duration tremors reported by Jiménez-Morales et al. [157]. The increase in the seismicity started around 2011 and slowly accelerated until the seismic swarms that took place in Livingston and Deception Islands at the end of 2014 and beginning of 2015. This trend is clearest for those event types that are considered the most significant proxies for volcano monitoring (VT earthquakes, LP seismicity).

Different types of earthquakes correspond to different sections of the volcano. VT and RE earthquakes occur in the upper crust, and therefore may reflect the changes occurring in the deep plumbing system. LP events and TR are linked to shallow sources within the hydrothermal system, and thus limited to the shallowmost part of the volcanic edifice. Therefore they are most sensitive to changes in the shallow conduits and the effect of gas and heat supply on the hydrothermal system. With this in mind, we view the panels of Figure 5.14 as roughly sorted by source depth, from top to bottom: temperature, SP events, LP seismicity, VT & RE earthquakes, and deformation.

Based on the evolution of the seismic events, we distinguish three periods with roughly homogeneous behavior: Phase 1 (from the beginning of 2008

to the end of 2010) characterized by a background level of seismic activity; Phase 2 (from the beginning of 2011 to August 2014), when the seismicity increased gradually; and Phase 3 (from August 2014 to May 2015), when the seismicity reached its climax. In Table 5.3 we show the average numbers of events per month for the different phases, that are described below. These numbers have been already estimated for VT and RE earthquakes (Table 5.2) from the slopes of the cumulative number of events (Figure 5.12). In Table 5.3 we report simple averages, i.e. the ratio between the total number of events during the selected period and the number of months, for all event types. This allows for a more significant comparison of VT and RE earthquakes with the remaining types.

5.6.1.1. Phase 1 (2008-2010): background seismicity

During the first three years of observations, the seismic activity of Deception Island volcano was relatively low (Figure 5.14). It was dominated by LP seismicity, with very few instances of VT earthquakes. We report 12041 LP events, which implies an average rate of 335 events/month (Table 5.3). TR episodes were common as well, specially during the second half of 2009. VTs were scarce and sporadic, and displayed mostly small magnitudes below 1. We detected 180 VT events, i.e. an average rate of about 5 events/month. Seismic moment was released at $\sim 1.7 \cdot 10^{12}$ N·m/month (Table 5.3). RE earthquakes were similarly scarce with a total of 90 events in three years. The average rate was ∼2.5 events/month and the seismic moment release was $0.9 \cdot 10^{14}$ N·m/month.

5.6.1.2. Phase 2 (2011-2014): increasing trends

After three years of background behavior, between January 2011 and July 2014 the level of seismicity increased gradually (Figure 5.14). We can roughly differentiate three subphases from January 2011 to December 2012 (Phase 2a), from January 2013 to March 2014 (Phase 2b), and from April to July 2014 (Phase 2c). The first noticeable changes occur during Phase 2a. LP events became more frequent, with average rates of about 1326 events/month, four times larger than in Phase 1. VT earthquakes became more numerous

as well, around 15 events/month, a three-fold increase compared to Phase 1. This increase was not accompanied by a change in the seismic moment release, indicating that they were still low-magnitude events. During Phase 2b, the number of LP events increased again to an average of 1924 events/month. VT earthquakes were produced at a rate of 48 events/month, a three-fold increase compared to Phase 2a. In this period, and after a small VT swarm on January 2013, the seismic moment release rate also tripled from $1.6 \cdot 10^{12}$ N·m/month to $4.6 \cdot 10^{12}$ N·m/month (Table 5.3), indicating that there was also a generalized increase in the magnitudes of the VT events (Figure 5.11). Finally, in Phase 2c LP events reached an average production of 2606 events/month. In this period the number of VT earthquakes increased to 61 events/month, and their energy doubled to a seismic moment release rate of $9.0 \cdot 10^{12}$ N·m/month.

While the acceleration of the VT earthquake activity during Phase 2 is obvious, for LP events the changes may seem more subtle. For example from Phase 2a to Phase 2c we report a four-fold increase in the number of VT earthquakes and a six-fold increase in the moment release rate. However, the number of LP events barely doubled from Phase 2a to Phase 2c. Nevertheless, we note that the number of TR episodes escalates, growing from 23 episodes/month in Phase 2a to 206 episodes/month in Phase 2c. There is a close relationship between LP and TR signals, in the sense that when LP events occur closely in time, they overlap and are no longer considered as individual events, but as a TR episode. Therefore we believe that these variations in the TR numbers, combined with the trends of LP events, indicate an acceleration of the LP seismicity rate similar to the one observed for VT earthquakes.

RE earthquakes maintained a similar behavior during Phases 1 and 2a, with the same earthquake production and moment release rates. However, we note that their numbers increased slightly during Phases 2b and 2c from 3 to about 8 events/month. Although the seismic moment release during most of Phases 1 and 2 stayed below $1.0 \cdot 10^{14}$ N·m/month, we observe that in Phase 2b there was a temporary increment in the seismic moment to $2.2 \cdot 10^{14}$ N·m/month, corresponding to the occurrence of relatively large (M 3.5-4.0) but distant earthquakes (see Figure 5.11). Overall, the number of RE earthquakes in Phases 1 and 2 is small, and we do not find any significant

trends in their temporal evolution.

Other types of signals did not show the acceleration observed for VT earthquakes and LP seismicity. This is the case of SP and LPH events, that reached their maximum rates during Phase 2b, but then displayed a decrease of activity during Phase 2c and beyond.

Previous studies based on temporary summer surveys showed that during the 2012-2013 survey the number of VT events was quite large, while in 2013-2014 survey it dropped again to background levels [11, 118]. Looking at Figures 5.11 and 5.14 we realize that the 2012-2013 survey included the January 2013 cluster of VT earthquakes that started Phase 2b. On the contrary, the 2013-2014 survey coincided with a brief period of low VT activity at the beginning of 2014. This example emphasizes the need for continuous monitoring to understand the long-term behavior of the volcano, otherwise the partial sampling may lead to errors in the interpretation.

5.6.1.3. Phase 3 (2014-2015): seismic swarms

The third stage extended from August 2014 to May 2015 (Figure 5.14). The period started with the onset of the Livingston series that reached its maximum in September-October 2014 [11]. After a relatively quiet period, there was a second outburst of seismicity around February 2015. These events define the Phases 3a (August-November 2014) and 3b (December 2014-May 2015).

Since the Livingston series occurred relatively far from Deception Island, with S-P times at DCP in the range 5-7 s, these seismic events are classified as RE earthquakes. Therefore, during Phase 3a we observed a sudden increase in the number and energy of RE earthquakes (note the changes in scale in Figure 5.14). Their numbers raised to more than 5000 earthquakes/month in September 2014, with an average rate of 1615 events/month during Phase 3a. The seismic moment release in this period reached a maximum value around $1.4 \cdot 10^{15}$ N·m/day (Table 5.2).

Nevertheless, a most important observation is that the Livingston swarm was not independent of the local seismic activity at Deception Island. The numbers of VT earthquakes, LP events, TR episodes, DLDS, and even SP

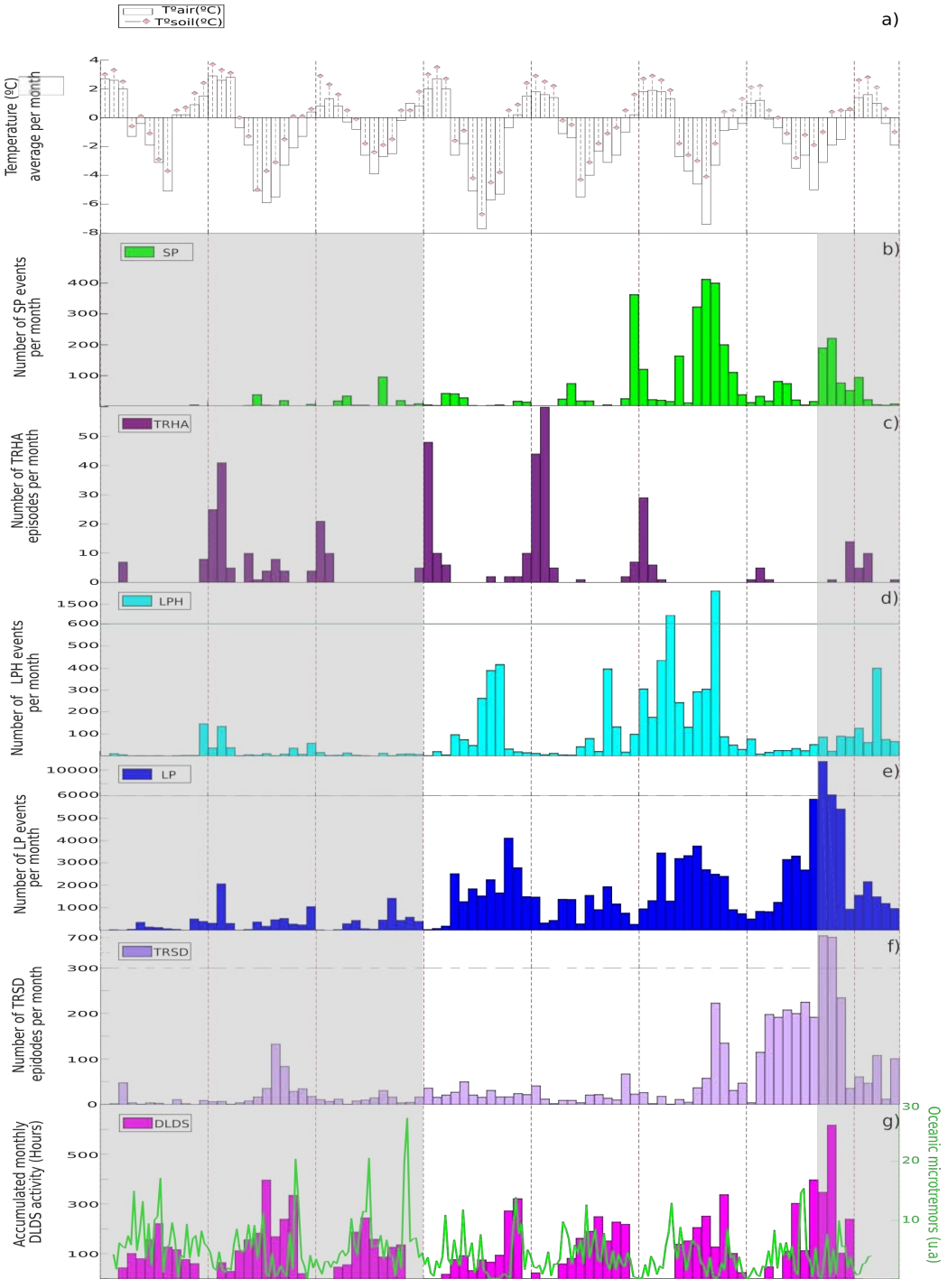

events, also increased drastically during Phase 3a (Figure 5.14, Table 5.3). In particular, during September 2014 we detected 714 VT earthquakes, the

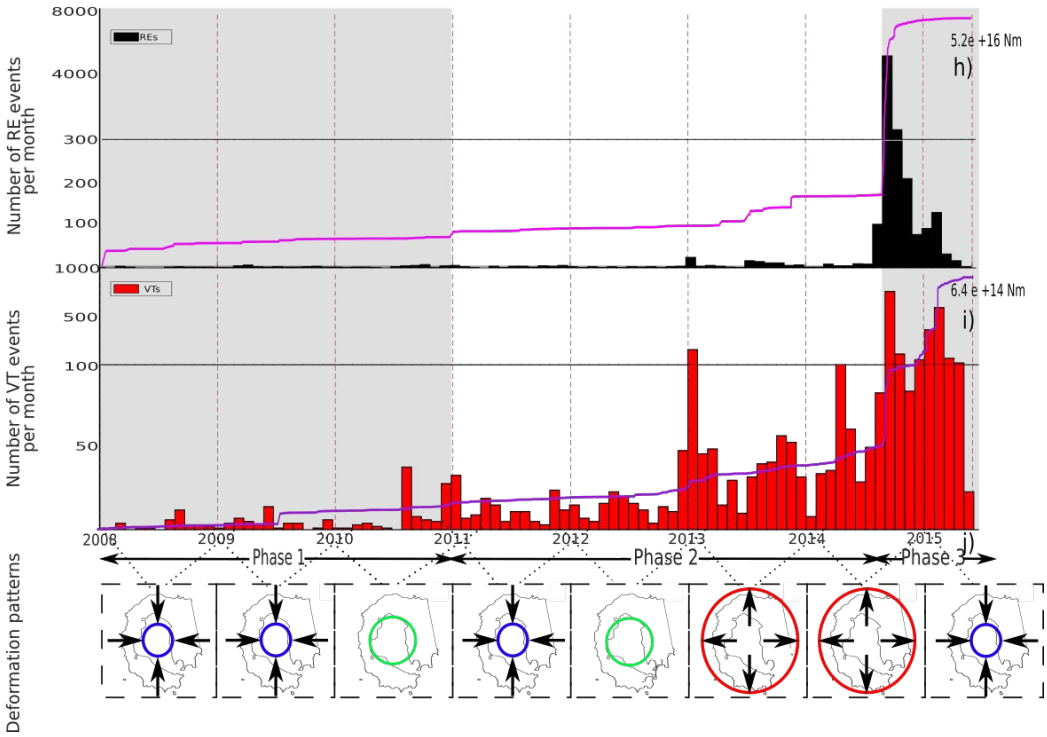

Figura 5.14: Comparison of the temporal evolution of monthly averaged temperatures, monthly number of seismic events, and annual deformation patterns during the 2008-2015 period. (a) Soil temperature (dashed line) and air temperature (empty bars); (b) SP events; (c) HTR episodes; (d) LPH events; (e) LP events; (f) TR episodes; (g) long-duration tremors (from Jiménez-Morales et al. [157]); (h) RE earthquakes; and (i) VT earthquakes. The green line in (g) represents the average amplitude of the oceanic microseisms. The black and red lines in (h) and (i) represent the cumulative seismic moment. (j) Sketch of the deformation produced during each year: red for inflation-uplift, blue for deflation-subsidence, green for transitional processes (from Rosado et al. [274]).

highest monthly rate in the entire analyzed period. The seismic moment release reached a value of $8.7 \cdot 10^{12}$ N·m/day. Similarly, there were over 11000 LP events that month. The average earthquake production rates in this Phase 3a are 268 events/month for VTs and 7260 events/month for LPs, much larger than in Phases 1 and 2.

In Phase 3b there was a second burst of VT activity at Deception Island.

The number of VT earthquakes started to increase in December and January, and reached a maximum of 586 events in February 2015, with average production rates of 283 events/month, even larger than in Phase 3a. Additionally, in February the earthquakes began to display large magnitudes above 3, resulting in a peak moment release rate of $1.0 \cdot 10^{13}$ N·m/day during February 14-22, the largest rate reported for VT earthquakes in the 2008-2015 period (Figure 5.12, Table 5.2). Since this happened when the Gabriel de Castilla Base was open, and therefore the volcanic alert system of Deception Island was in operation, at this point a change in the alert level from green to yellow was issued [10]. Shortly after that, the VT swarm started to decay, although by the end of the recording period the number of earthquakes was still well above the background level.

The VT swarm during Phase 3b was accompanied by a small increase in the number of RE earthquakes, confirming again the interconnection between the Livingston series and Deception Island. There was also a small peak in the LP seismicity, with a level of activity similar to the Phase 2. However, this second VT swarm did not involve a generalized increase of the seismicity of Deception Island and surrounding areas, as the first one had done. This is an important difference, that may be related to the underlying mechanisms triggering the seismic series, and will be discussed below.

5.6.1.4. Temporal variations unrelated to the intrusion process

Although the most important observation in Figure 5.14 is the acceleration of the seismic activity that accompanies the magmatic intrusion, we also realize that some variations in the temporal distributions of seismic events seem to be utterly unrelated to the volcanic activity.

For example, we note that the temporal evolution of some event types display cycles with a period of one year. This annual modulation is evident in most of the LP seismicity. In some cases, we observe maximum activity in summer and minimum in winter (pattern S). The most obvious example is the distribution of HTR episodes, which clearly occur preferentially during the summer, with the only exception of a winter peak in 2009 (Figure 5.14c). It is also observed for LPH events during Phase 1. In other cases, we observe

Phase	LP	LPH	TR	HTR	SP	VT	RE	VT 10^{12}Nm/month	RE 10^{14}Nm/month
1 (Jan08-Dec10)	334.5	16.8	16.7	4.3	6.6	5.0	2.5	1.7	0.9
2a (Jan11-Dec12)	1325.8	92.1	22.6	5.8	27.2	14.4	2.8	1.6	0.7
2b (Jan13-Mar14)	1923.5	351.5	60.7		124.2	47.5	8.3	4.6	2.2
2c (Apr14-Jul14)	2605.5	27.0	206.3		43.3	60.5	7.3	9.0	0.7
3a (Aug14-Nov14)	7259.8	64.3	466.8	3.4	123.3	268.3	1614.5	52.1	103.9
3b (Dec14-May15)	1682.8	165.4	73.4		34.8	284.4	71.2	44.4	2.9

Cuadro 5.3: Average number of events per month for all event types and average seismic moment release per month for VT and RE earthquakes during Phase 1 (2008-2010), Phase 2 (2011-2014), and Phase 3 (2014-2015).

maximum activity in winter and minimum in summer (pattern W). This is quite clear for DLDS, that are basically missing during the summer, and for LP events during Phase 2. It might also be observed for LPH during Phase 2, and perhaps for TR episodes that display winter peaks in 2009 and 2013, but these cases are not as obvious. During Phase 1, LP events seem to have a bimodal behavior, with peaks both in summer and winter.

The annual variations of the LP seismicity could be a response to the seasonal cycle. We assume that LP seismicity is generated by interactions within the shallow hydrothermal system of Deception Island. Seasonal changes in environmental variables (temperature, pressure, water influx) may alter the conditions of the hydrothermal system, and produce the modulations observed in the data.

For example, the relatively high temperatures reached in the austral summers (Figure 5.14a) may produce the melting of the glaciers that cover the island, and increased rainfalls. These phenomena increase the volume of thaw water that percolates into the shallow aquifers, altering the equilibrium of the unstable hydrothermal system and producing enhanced LP seismicity [13, 146, 150, 65]. This could be a mechanism that generates the pattern S, for example in HTR episodes. And indeed, we observe that there is a correlation between the number of HTR episodes and the duration and temperature of the summer, with highest activity during the longer and warmer summers (e.g. 2008-2009) and lowest activity during the shorter and colder summers (e.g. 2013-2014).

Another example could be the effect of the oceanic microtremors, whose amplitude has seasonal cycles and is generally larger during the winter (Figure 5.14g). Microtremors may induce pressure variations in volcanic and hydrothermal fluids, favoring the occurrence of LP seismicity [298, 157]. This mechanism could explain the occurrence of pattern W, and has been invoked for example to explain the temporal distribution of DLDS [157]. The same could apply to the generation of LP events. However, the correlation between oceanic microtremors and LP seismicity is not complete. For example, during Phase 1 the microtremor levels are high, although the LP seismicity is low. On the contrary, during Phase 2 the oceanic microtremors have lower amplitudes, but the LP seismicity increases. This indicates that the LP seismicity

is not only triggered by the oceanic effect, but mainly by the dynamics of the volcanic system.

In any case, the seasonal cycle is not the only annual cycle at Deception Island. We must consider also the human presence, which is intense during the summer and practically negligible during the winter. This may affect the number of seismic events in two ways. First, the human activity could be responsible for some of the signals, that would then display a pattern S. Second, the human activity might contribute to decrease the signal to noise ratio at station DCP, and reduce the detectability of small-amplitude seismic events during the summer, producing a pattern W. Since HTR occur during the months when the Gabriel de Castilla Base is open, we wonder if these signals are produced by human activity. The Base is close to station DCP (∼200 m). However, after years of seismic monitoring we are able to recognize several base-related noise sources (electric generator, engines, heavy machinery and vehicles, etc), and none presents a harmonic signature. Moreover, some HTR occur during rest (nocturnal) periods when the anthropic activity is negligible; or when the Base is closed, for example in May and July 2009, August 2011, or April 2015. Therefore, we can safely rule out the human factor produced by the activities at the Base.

The temporal evolution of SP and LPH events (Figure 5.14b,d) seem to be also unrelated to the volcanic activity. These events were very scarce during Phase 1. They did increase during Phase 2 like the remaining earthquake types, reaching a maximum activity in Phase 2b. However, in Phase 2c their numbers started to decrease and did not maintain the accelerating trends displayed by VT earthquakes and LP seismicity. During the climactic Phase 3, their numbers were not significant or did not display increasing trends as the rest of the seismicity. These temporal distributions suggest that SP and LPH events were produced by source mechanisms that were not driven by, or a consequence of, the magmatic intrusion.

SP events have been interpreted as icequakes by Ibáñez and Carmona [146] and Carmona et al. [65]. Icequakes are earthquakes produced in brittle ice Sprenke et al. [295], for example associated with extensional failure (crevassing) of glacier cracks [319, 275, 62]. However, since the station DCP is located more ∼2 km away from the nearest glacier (Figure 5.1), we believe

that the source of SP events could not be realistically linked to glaciers. Still, there might be other likely mechanisms, also related to the cryosphere. For example we propose the dynamics of the permafrost layer that covers most of the island [125, 154]. Sudden changes in the permafrost, related to freezing and thawing cycles, or permafrost degradation, may induce brittle failure along microcracks, which could be the source of SP events.

The similar temporal distributions observed for SP and LPH events suggest that their sources might share some characteristics, i.e. both event types could be related to the cryosphere. Thus LPH events might also have a glacial origin. LP events have been reported in glacial environments [263, 162]. As in volcanic or hydrothermal environments, they could be produced by the acoustic resonance of fluid-filled cavities within an elastic matrix; in this case, the fluid would be thaw water, and the solid would be ice [221]. The high-frequency spectral content of LPH, compared to the volcanic and hydrothermal LPs, may be related to a combination of smaller crack sizes and lower gas content [178, 75].

5.6.2. Volcanological interpretation

The 2014-2015 seismic activity at Deception Island and surrounding areas has been investigated by Almendros et al. [11]. The seismic swarm recorded near Livingston Island in 2014-2015 comprised ∼9000 earthquakes with magnitudes up to 4.6 over a period of 8 months, although the most important part of the swarm took place in September-October 2014. Between December 2014 and May 2015, the seismic activity at Deception Island volcano was anomalously high as well, with swarms of VT earthquakes and increasingly large and recurring LP events and TR episodes. Almendros et al. [11] proposed two hypotheses to explain the relationship between the Livingston series and the Deception Island activity. In the first one, the Livingston swarm is a tectonic series related to the extension of the Bransfield rift that acts as a trigger of the VT swarm at Deception Island. The dynamic stresses associated with the largest earthquakes [141] may have induced an over-pressure in the unstable volcanic system of Deception Island, leading to a magmatic intrusion that in turn may have triggered the VT swarm.

However, Almendros et al. [11] favor a second hypothesis, in which the Livingston earthquakes and the VT swarm could be both the result of a magmatic intrusion beneath Deception Island. The Livingston series would be a distal VT precursory swarm, which appears to be a common feature that precedes volcanic eruptions in long-dormant volcanoes [325]. The magmatic intrusion could have started some time during 2014, while its consequences started to reveal in September (distal VT seismicity near Livingston) and February (proximal VT swarm at Deception Island).

There are other evidences suggesting that the magmatic intrusion could have started earlier. For example, Rosado et al. [274] analyzed GPS measurements at Deception Island during 1991-2018, and described changes and trends in the volcano deformation. Figure 5.14j shows a sketch of their results during the 2008-2015 period. In the first five years, Deception Island was either undergoing processes of decompression (deflation-subsidence) or transitional processes without a clear deformation pattern. However, in 2013 the deformation patterns changed to inflation and uplift, revealing an increase in the internal pressure within the volcano. Rosado et al. [274] interpreted this uplift process during 2013-2015 as a consequence of a magmatic intrusion, and a precursor of the 2015 seismic unrest.

Additionally, in the austral winter of 2012, Berrocoso et al. [40] detected an increase in seawater temperatures at Colatinas Point and in soil temperatures at Cerro Caliente, near the location of fumaroles and hot springs. Both phenomena suggest an increase in the gas flux from depth, carrying heat by advection. Again, they interpreted these observation as a precursor of the 2015 unrest.

These evidences suggest that the intrusion process may have started as early as 2012, about 2.5 years before the 2015 seismic unrest of Deception Island volcano. And yet, our results demonstrate that the changes in the seismicity started even earlier. At the end of 2010 or beginning of 2011, we observe several phenomena indicating that the volcano was showing signs of a renewed activity. What may have been happening at Deception Island volcano during this 2008-2015 period? In order to include all observations, we propose the following model.

After the 1999 unrest [150], Deception Island volcano entered into a quiet

period. Carmona et al. [65] studied the seismic activity at Deception during austral summers from 1999 to 2011. They concluded that the volcano was in a low-activity mode that they described as a dormant state. This dormant state was characterized by a moderate level of seismicity dominated by LP events and TR episodes produced in the shallow hydrothermal system, and very few VT earthquakes distributed across the volcanic edifice. Our data overlaps with this period for three years (2008-2010) corresponding to Phase 1, and we observe precisely the same behavior. Therefore, during Phase 1 Deception Island was still in a dormant state.

The situation changed in 2011. During Phase 2, fresh magma was emplaced at deep crustal levels beneath Deception Island. The supply of fresh magma into a magma reservoir at depth could increase the amount of degassing. These gases permeate through the volcanic edifice. When they reach a brittle volume, perhaps with pre-existing fractures, the increase in the pore pressure may decrease the normal stress across the faults and act as a lubricant favoring the fault motion [e.g. 55, 284]. Therefore the gradual increase in the number and energy of VT earthquakes could be due to an increment in the gas flux through the volcanic edifice produced by the fresh magma supply. Similarly, the increase in the gas flux could also justify the changes in the number of LP events and TR episodes. LP seismicity increased suddenly in Phase 2, with average numbers that were several times larger than in Phase 1. LP seismicity is related to fluid-solid interactions within the hydrothermal system of Deception Island [13, 6, 147]. The increase of gas coming through the hydrothermal system would result in a larger number of LP events. Additionally, the advective heat carried by the gas can alter the thermal equilibrium of the hydrothermal system, producing anomalous variations in the temperatures of hot springs and soils, as the ones reported by Berrocoso et al. [40].

There is a delay of some months between the increase of the VT earthquakes and the increase of LP events. This may be due to the differences in source depth. VT earthquakes are produced in the upper crust, at depths on the order of several km. Therefore they are close to the magma reservoirs and the gas pulse reaches the VT source regions promptly. On the contrary, LP events are produced in the shallow hydrothermal system, at depths of

hundreds of meters, where the gas front arrives later. The observed delay would be related to the time needed by the gas to percolate from the VT source region to the hydrothermal system.

The absence of deformation during Phase 2a suggests that the initial batches of magma may have entered the plumbing system at large depths near the crust-mantle boundary, that for Deception Island is located at a depth around 15 km [242, 117]. Conversely, the observation of uplift during Phases 2b and 2c indicates that in 2013 the magma intrusion became shallower. Rosado et al. [274] estimated the parameters of the deformation source using a Mogi model. For the process observed during 2014, the volume change was 0.01 km^3 and the center of the deformation was located beneath the north half of Port Foster, at a depth of about 6 km.

The degassing rates were apparently stable until a new batch of magma rised, increasing the degassing (and the seismicity). The enhanced gas supply could explain the increasing rates of VT and LP seismicity during Phases 2b and 2c. Additionally, the extensional stress produced by the intrusion increased the permeability of the medium, which further favored the circulation of hydrothermal fluids and the generation of LP activity [103].

The increase in the number of SP and LPH events during Phases 2a and specially 2b may be related to the enhanced heat supply brought by the volcanic gas permeating the island. Even if the sources of these event types are basically external to the volcano, they could still be influenced by the gas and heat flux through the surface. Indeed, the thermal anomalies reported by Berrocoso et al. [40] during 2012 apparently triggered the most active period of SP and LPH activity. However, the number of events decreased during Phase 2c and 3, indicating that the relationship with the volcanic activity is poor or even nonexistent. There are many factors controlling this seismic activity including atmospheric and climatic variables, therefore a more detailed study is required to understand their source mechanisms and temporal variations.

The unrest process reached a climax during Phase 3, with the occurrence of intense seismic swarms at Deception Island and surrounding areas. Fresh magma intruded into shallower levels, not only increasing the volume of gas permeating through Deception Island, but also destabilizing the stress

state of the volcanic edifice. This translated into peaks of VT earthquakes and enhanced LP seismicity. Additionally, the pressure pulses propagated through crustal fluids. They generally expand faster in horizontal direction, following the layering of the crust [80]. A preferential direction for this propagation would be the Bransfield rift, oriented SW-NE. When the perturbation reached a seismogenetic region SE of Livingston Island, perhaps related to the Bransfield rift or Humpback volcano [11], it produced distal VT seismicity, that we observe as RE earthquakes.

The second swarm of VT earthquakes at Deception Island during Phase 3b was similar to the first in terms of earthquake numbers and magnitudes. However, the simultaneous levels of LP seismicity and distal VT activity were much smaller than during Phase 3a. This difference is significant, and suggests that the intrusion might have already started to slow down or even decay. In fact, the deformation reported by Rosado et al. [274] indicates that during 2015 Deception Island underwent a fast subsidence process (Figure 5.14j) with horizontal deformation rates of ∼2.3 cm/year. We hypothesize that this process may have already started during Phase 3b, hence the differences between the behavior of the volcano during the September 2014 and February 2015 VT swarms.

The minimum depth reached by the magma might be estimated from the depth of the earthquake hypocenters during Phase 3b. The comparison among the 1992, 1999, and 2015 seismic unrest episodes shows that the 1992 and 1999 episodes were produced by shallow (<4 km), short-lived (months), low-volume ($\sim 4 \cdot 10^4$ m^3) intrusions, while the 2015 unrest was due to a deep (<10 km), long-lasting (years), large-volume ($\sim 5 \cdot 10^6$ m^3) intrusion (A. Moreno-Vacas, submitted manuscript). An additional constraint comes from the depth of the Mogi source estimated by Rosado et al. [274] for the 2014 inflation, which is about 6 km. These depths are consistent with the characteristics of the Deception Island plumbing system described by Geyer et al. [117]. Therefore, it is likely that the magmatic intrusion might have reached a minimum depth in the range 6-10 km.

We have to underline that the occurrence of a VT swarm at Deception Island, simultaneous with the Livingston series, has not been reported before. Almendros et al. [11] investigated the seismic activity at Deception

and Livingston Islands during this period, combining the information from the permanent stations DCP and LVN and a temporary network deployed at Deception Island during the 2014-2015 austral summer. Although they described the sporadic occurrence of a few dozens of VT earthquakes from August to November, on their data there is no indication of a swarm of VT earthquakes at Deception Island in that period. The reason for this is that they used an automated algorithm to detect the VT earthquakes recorded at station DCP. However, given the large number of earthquakes from the Livignston series that were being simultaneously detected, the signals very often overlapped and it was quite difficult to individuate each earthquake, especially the smaller ones, using automatic, unsupervised methods. After a careful revision of the data, we have been able to determine the occurrence of a large number of VT earthquakes at Deception Island during this period.

The model described here is consistent with the phenomena observed in similar volcanic environments. White and McCausland [326] used long-term datasets preceding eruptions at long-dormant (>20 years) volcanoes to propose a model with a 4-step progression of geological and seismological stages. The first stage is a deep intrusion, sometimes revealed by deep seismicity under the volcano edifice. In a second stage, magma ascends to the upper crust and produces distal VT seismicity. A third stage is characterized by local seismicity in the volcano edifice including VT earthquakes and LP seismicity. Finally, in the fourth stage repetitive seismicity accompanies the final magma ascent to the surface. In the case of Deception Island, the observations indicate that the activity has gone through the deep intrusion stage (during Phase 2), and through distal and proximal seismicity, i.e. stages 2 and 3 (during Phase 3), with magma accumulating in the upper crust and producing VT and LP seismicity. However, there was no final ascent of magma, and therefore no eruption. In this sense, the 2015 unrest of Deception Island can be described as a failed eruption [223], since the magmatic intrusion producing anomalous seismicity, deformation, and degassing, stalled at 6-10 km and was not able to reach the surface.

5.7. Conclusions

In this paper we analyzed the seismic activity of Deception Island volcano and surrounding areas using data from a permanent seismic station operating during 2008-2015. This period precedes the 2015 seismic unrest, and therefore we were able to address the long-term evolution of the seismicity and the likely precursors observed in the data.

Overall, the most important observation is that VT earthquakes and LP seismicity started to increase years before the 2014-2015 seismic crisis at Deception Island. We can distinguish three periods with more or less homogeneous behavior: Phase 1 (2008-2010), Phase 2 (2011-2014), and Phase 3 (2014-2015). Phase 1 is characterized by a low level of seismic activity. In Phase 2 we observe a gradual increase of the seismic activity, that can be considered a precursor of the 2015 unrest. There are three different stages defined by successive increments in the rates of seismicity. Finally, in Phase 3 this increase accelerates until we reach a failed eruption that was accompanied by enhanced LP seismicity and proximal and distal VT swarms.

We propose a model in which the volcano starts at a dormant state during Phase 1. In Phase 2 there is a deep magmatic intrusion that increases the amount of gas permeating the volcanic edifice. This gas is responsible for the increase in the VT and LP rates. In Phases 2b and 2c the magma starts to intrude to shallower levels yielding enhanced degassing, thermal anomalies, higher seismicity rates, and an observable inflation of the volcanic edifice. Finally, in Phase 3 (2014-2015) the magma intrusion increases its volume and produces a generalized alteration of the stress field at Deception Island, giving rise to the earthquake swarms. However, the upward progression of magma stalled, and no eruption was finally observed.

With these results, we need to modify the dormant vs restless paradigm describing the activity of Deception Island volcano [65]. The 1992 and 1999 unrest episodes had been short-lived processes lasting a few months, with sharp onsets and localized effects on the volcanic edifice, mostly within the caldera. On the contrary, the 2015 unrest was preceded by a gradual increase of seismicity (and other indications of renewed activity) lasting several years, and had continuing effects also in the following years [11, 91]. This long-term

volcanic process does not properly fit within the dormant/restless dichotomy. Deception was definitely dormant during Phase 1 and restless during Phase 3. During Phase 2 it had already departed from the dormant state, without truly becoming restless yet. The volcano was in a state that we could define as awakening. This intermediate awakening phase was characterized by increasing precursory activity (seismicity, deformation), and it is crucial to understand the behavior of the volcanic system.

Additionally, we have detected and characterized signal types that are not usually reported, such as SP, LPH, and HTR events. These signals may not be wholly significant for the volcano dynamics, since they probably have an external origin related to the cryosphere (e.g. glaciers, permafrost). Nevertheless, and although a detailed study is beyond the scope of the present paper, they have an impact in other disciplines such as glacial studies or atmospheric sciences. Given that they are strongly affected by external factors such as the seasonal cycle and other atmospheric variations, their long-term evolution might be indicators of climatic trends.

At Deception Island, monitoring surveys during austral summers have been carried out since 1986 up to the present. However, they are essentially discontinuous. This is the first time that a long (7.5 years) time series of continuous seismic data is available. Moreover, the data are obtained with the same type of instrument; at the same location; and the analysis has been performed by the same operator applying the same criteria and techniques. Thus, we have produced a homogeneous seismic catalog that we use to characterize the evolution of the seismic activity during the years preceding the 2015 seismic unrest. In addition, this catalog constitutes an excellent tool to train and test the methods for automatic recognition and classification of seismo-volcanic signals.

The maintenance of permanent seismic stations in a remote Antarctic island, subject to harsh weather and prolonged night periods, is a technical challenge for seismologists. In any case, our results demonstrate that it is a worthwhile effort, since the continuous data, even with a single station, allow for a quantitative leap in our ability to characterize and understand the volcanic behavior. Therefore, we emphasize the need for a permanent seismic network at Deception Island volcano. Ideally it should be a multi-parameter

instrumental network, monitoring at least seismology, deformation, and gas, with real-time transmission and analysis. The continuous data provided by such a network would definitely boost our knowledge of the volcano dynamics and expand our ability to assess volcanic hazards.

Capítulo 6

Conclusiones y trabajo futuro

En resumen, las principales contribuciones de mi trabajo al estudio y la comprensión del comportamiento de la isla Decepción son:

(1) Se ha mejorado los estudios de ruido observando la estabilidad de los picos y se ha obtenido un modelo del subsuelo de la costa y Bahía interior de la Isla más completo. Lo que aporta más información sobre las propiedades del medio cuyo conocimiento es importante para mejorar la interpretación de la actividad sísmica del volcán como por ejemplo la actividad de largo periodo que es más superficial y está relacionada con el sistema hidrotermal de la isla [6].

(2) Identificación de una nueva señal sísmica llamada DLDS utilizando un enfoque basado en la evaluación de la energía sísmica promedia contenida en bandas de frecuencia seleccionadas. Se necesita una cantidad suficiente de datos sísmicos durante todo el año para el análisis de las DLDS debido a su larga duración y a su modulación estacional.

(3) Se distingue un enjambre precursor de terremotos VT distales al SE de la isla Livingston que comienza en septiembre 2014. Los enjambres de VT distales parecen ser una característica común que precede a las erupciones volcánicas y a las intrusiones de magma en volcanes. Se determina el inicio, las características y la duración de la crisis sísmica de Livingston a través del análisis de los registros continuos de las estaciones permanentes, ya que sin la presencia de estos datos continuos no hubiera sido posible la detección de este enjambre.

(4) Reconocimiento de una modulación anual para algunas de las señales sísmicas de Decepción. Esta modulación anual está relacionada con el ciclo estacional y otras variaciones atmosféricas, influenciada por factores externos, que pueden inducir variaciones de presión en los fluidos volcánicos/hidrotermales, o ser un indicador de tendencias climáticas.

(5) Identificación de un aumento y aceleración de la actividad sísmica desde 2011 hasta la crisis sísmica registrada en Decepción en 2015.

(6) Se presenta un modelo volcánico para el comportamiento del volcán Decepción durante los 7.5 años de registro continuo de DCP. El volcán inicia este periodo en un estado durmiente (fase 1), con un bajo nivel de actividad sísmica. En la fase 2 comienza a despertarse con un aumento gradual de la actividad sísmica debido a una intrusión magmática profunda que aumenta la cantidad de gas que penetra en el edificio volcánico. Finalmente, en la fase 3 el volcán está definitivamente inquieto, con una aceleración de la sismicidad que culmina en una erupción fallida, acompañada por un aumento de sismicidad de largo periodo y enjambres de VT proximales y distales.

(7) Se enfatiza la importancia de la elaboración de un catálogo sísmico homogéneo. Este constituye una herramienta muy útil para la caracterización de la evolución de la sismicidad de Decepción, ya que puedes comparar la actividad de unos años con otros. Además de entrenar y probar los métodos de reconocimiento y clasificación automática de señales sismo-volcánicas. A partir de datos obtenidos con el mismo tipo de instrumento; en el mismo lugar; y analizado por la misma operadora aplicando los mismos criterios y técnicas.

(8) El registro continuo de datos sísmicos en Decepción, incluso en una sola estación (DCP), permite un salto cuantitativo y cualitativo en nuestra capacidad para caracterizar y comprender el comportamiento volcánico. Por lo tanto, se enfatiza la necesidad de una red sísmica permanente en el volcán Isla Decepción para la evaluación de riesgos volcánicos.

6.1. Trabajo futuro

En la Isla Decepción, se han realizado diversos estudios multidisciplinares para estudiar las características geológicas, químicas y físicas del volcán.

Estos estudios o experimentos realizados han sido de corta duración o discontinuos como la vigilancia volcánica realizada durante los veranos australes desde 1986 hasta la actualidad. Hemos insistido durante la exposición de este trabajo de la importancia del uso de instrumentos permanentes en Decepción. Así, mejorar la vigilancia y el estudio de la dinámica del volcán y poder mitigar los peligros en el área.

Se considera que para ampliar el conocimiento del volcán isla Decepción deberíamos conocer todas las variables que interactúan con el sistema volcánico que generan distintas señales sísmicas. Estas variables son por ejemplo los glaciares, acuíferos, sistema atmosférico, mareas deshielo, permafrost etc. Para ello se proponen diversos estudios e instalaciones que facilitan la diferenciación, la identificación, clasificación y localización de las señales sismo-volcánicas en el volcán.

La instrumentación y tecnología recomendada es:

(1) Instalación y mantenimiento de estaciones sísmicas permanentes en el área del Bransfield o como mínimo mantener las estaciones permanentes de Isla Livingston y Caleta Cierva ya que estas estaciones nos han permitido diferenciar señales sísmicas propias de Decepción como las DLDS e identificar precursores de la erupción fallida ocurrida en el volcán en 2015 como los enjambres VT distales ocurridos al SE de Isla Livingston cinco meses antes.

(2) Desplegar una red sísmica densa y permanente en la isla Decepción constituida por estaciones sísmicas que abarquen el perímetro interior de la isla, junto a tres arrays sísmicos permanentes instalados en el área de Bahía Fumarolas, Cráteres del 70 y glacial negro. Estas estaciones son necesarias ya que las señales sísmicas de Decepción se caracterizan por ser muy locales y registrarse en una o dos estaciones.

(3) A estas estaciones símicas se recomienda instalarle sensores de viento y cámaras. Estos sensores se usarían para descartar señales producidas por rachas de viento, animales e incluso identificar señales inusuales como por ejemplo las generadas por el movimiento de la Banquisa. (4) Desplegar una red de OBS a largo plazo en la Bahía del volcán Isla Decepción incluidos los períodos de invierno austral. Debido a los avances tecnológicos actuales es posible el mantenimiento y el registro continuo de datos procedentes de estaciones de fondo marino. Esto ampliaría la red sísmica de la isla

Los estudios recomendados son:

Realizar un estudio sismológico de las estaciones permanentes desplegadas en el Bransfield junto a las de Decepción. Así, se puede establecer las diferencias de sismicidad, tipo de señales y fuentes que originan dicha sismicidad en cada estación. De modo que se pueda determinar las señales generadas sólo por la actividad volcánica. Una de las posibles dificultades que podemos encontrar en este estudio es la distinción entre señales glaciares y volcánicas. Estas señales presentan características muy similares, como por ejemplo las señales de largo periodo (LP, TR) que se registran tanto en glaciares como en volcanes y la única forma de diferenciarlas es poder localizarlas.

Analizar los datos del ruido ambiental registrados en la red sísmica permanente para desarrollar modelos de velocidad superficiales más completos mediante la inversión conjunta de las curvas experimentales de HV y de dispersión. Así como realizar estudios de inversión conjunta de telesismos y curvas HVs para obtener un modelo de velocidad más profundo. De modo que se pueda establecer la profundidad de las fallas, determinar el espesor del permafrost, establecer la configuración del sistema magmático, etc. Un obstáculo que se puede encontrar es no alcanzar la profundidad de la cámara magmática en los modelos de velocidad, como ha ocurrido en el Capítulo 2 de este trabajo. Se recomienda calcular una curva de dispersión experimental propia de la bahía o realizar correlaciones entre las estaciones de los arrays para llegar a frecuencias más bajas en la curva de dispersión calculada.

Realizar campañas de símicas activas para desarrollar nuevos estudios de reflexión, refracción y una nueva tomografía y compararla con la realizadas anteriormente. Esto nos permitiría por ejemplo determinar la profundidad en la que se detuvo la erupción fallida registrada en Decepción en 2015.

Realizar estudios hidrogeológicos para caracterizar los acuíferos de la isla. Así como realizar estudios glaciológicos y mejorar el conocimiento de todos los glaciares de la isla y su comportamiento. Con ello, se mejora el conocimiento de la isla, las interacciones que se producen entre las distintas variables del volcán y las señales que generan.

Capítulo 7

Conclusions and outlook

In summary, the main contributions of my work to the study and understanding of the behavior of Deception Island are:

(1) Determination of 1D models of the shallow structure along the coast and inner bay of Deception Island. Long series of ambient noise recordings from different land stations deployed on the inner coast and from marine stations deployed on the seafloor of Port Foster have been used, thereby improving noise studies observing the stability of the peaks.

(2) Identification of a new seismic signal called DLDS using an approach based on the evaluation of the average seismic energy contained in selected frequency bands. Continuous records from permanent stations are used for DLDS detection. Due to its long duration and seasonal modulation, the analysis of DLDS require a sufficient amount of seismic data throughout the year.

(3) A precursory swarm of distal VT earthquakes has been identified. The swarm occurred SE of Livingston Island, and started five months before the 2015 seismic crisis at Deception Island. The onset, characteristics and duration of this crisis are determined by the analysis of continuous records from permanent stations. Without these continuous data it would not have been possible to detect this crisis and its significance.

(4) Recognition of an annual modulation for part of the seismicity at Deception Island. This annual modulation is related to the seasonal cycle and other atmospheric variations, influenced by external factors, which can

induce pressure variations in volcanic/hydrothermal fluids, or be an indicator of climatic trends.

(5) Identification of a generalized increase of the seismic activity, starting in 2011 and accelerating during 2011-2014, reaching a climax during the seismic crisis recorded at Deception Island in 2015.

(6) The importance of the elaboration of a long homogeneous seismic catalog is emphasized. It constitutes a very powerful tool to characterize the evolution of the seismicity at Deception Island volcano. The results are homogeneous in the sense that data were obtained with the same type of instrument; in the same place; and analyzed by the same operator applying the same criteria and techniques. In addition, the catalog can be used to train and test the capabilities of automatic methods for the recognition and classification of seismic-volcanic signals.

(7) A volcanological model is proposed for the behaviour of Deception Island during the 7.5 years preceding the 2015 crisis. The volcano is in a dormant state up to 2010 (Phase 1), with a low level of seismic activity. In 2011 the activity shifts to an awakening state (Phase 2) characterized by a gradual increase in seismic activity as a consequence of a deep magmatic intrusion that increases the amount of gas permeating the volcanic edifice. Finally, in 2014-2015 the volcano becomes restless (Phase 3) and the activity accelerates, suggesting the occurrence of a failed eruption.

(8) The continuous recording of seismic data at Deception Island, even just one station (DCP), allows a quantitative leap in our ability to characterize and understand the volcanic behaviour of Deception Island. It therefore underlines the need for a permanent seismic network on the Deception Island volcano for the assessment of volcanic hazard is emphasized.

7.1. Outlook

At Deception Island, several multidisciplinary studies have been carried out to study the geological, chemical and physical characteristics of the volcano. These studies or experiments have been usually of short duration or discontinuous, such as the volcanic surveillance carried out during the austral summers from 1986 to the present. This work underlines the importance

of the use of permanent instruments in Deception Island to improve our knowledge of the dynamics of the volcano, and to help mitigate the volcanic hazards in the area.

In order to expand the knowledge of the Deception Island volcano we should know all the variables that interact with the volcanic system responsible for the generation of different seismic signals. These variables are related for example to glaciers, aquifers, atmospheric system, tides, permafrost dynamics, etc. For this purpose, several studies and tools are proposed that facilitate the differentiation, identification, classification and localization of seismo-volcanic signals in the volcano.

The recommended instrumentation and technology are:

(1) Installation and maintenance of permanent seismic stations in the Bransfield area, at least the stations in Livingston Island and Cierva Cove, since these stations have allowed us to discriminate seismic signals from Deception Island, such as the DLDS, and identify precursors of climactic volcanic activity. This happened in the volcano in 2015, i.e. the distal VT swarms that occurred SE of Livingston Island five months earlier.

(2) To deploy a dense, permanent seismic network on Deception Island made up of at least 8-10 seismic stations that cover the inner perimeter of the island, together with three permanent seismic arrays installed in the area of Fumarole Bay, Craters of 70s and Black Glacier. These stations are necessary because the seismic signals of Deception Island volcano are very local and registered at one or two stations.

(3) Together with these seismic stations, it is recommended to install wind sensors and video cameras. These sensors would be used to discard signals produced by gusts of wind, animals and even identify unusual signals such as those generated by the movement of the ice floe.

(4) Deploy a long-term OBS network at inner bay of Deception Island, including austral winter periods. With the current technological advances, the maintenance and continuous recordings of data from seafloor stations is feasible. This would expand the seismic network on the island.

The recommended studies are:

A seismological study of the permanent stations deployed in the Bransfield Strait together with those at Deception Island. With this information it is

possible to establish the differences in seismicity, type of signals, and sources that originate the seismicity in each station. This may help discriminate the signals generated by volcanic activity at Deception Island. One of the possible difficulties that we can find in this kind of study is the distinction between glacial and volcanic signals. They share some characteristics, such as the long-period character of signals recorded in both glaciers and volcanoes. A good estimate of source location might help in the classification and interpretation of these signals.

Analyze the ambient seismic noise recorded in the permanent seismic network to develop more complete velocity models by joint inversion of the experimental HV and dispersion curves. As well as conducting joint inversion studies of teleseisms and HV curves to obtain a deeper velocity model. These models can aid in the interpretation of the shallow structure, including the depth of the faults, the thickness of the permafrost layer, the configuration of the magmatic system, etc. Reaching the depth of the magmatic chamber in the velocity models is a challenge, as evidenced in Chapter 2. It is recommended to calculate an experimental dispersion curve typical of the bay, or to make correlations between the stations of the arrays to reach lower frequencies in the calculated dispersion curve.

Active seismic experiments to develop new studies of reflection, refraction and tomography and compare the results with previous models. For example, this would allow us to determine the depth at which the 2015 failed eruption stalled.

Carry out hydro-geological studies to characterize the aquifers in the island. Similarly, we recommend conducting detailed studies to improve our knowledge of the glaciers and their behavior regarding the interactions between the cryosphere and the volcano.

Apéndice A

Resultados H/V

A.1. Inversión conjunta

A continuación mostramos en detalle los resultados de inversiones conjuntas a partir de curvas empíricas de H/V y dispersión (líneas negras) para todas las estaciones. Las curvas teóricas se colorean como sus correspondientes modelos de velocidad y densidad. El mejor modelo conseguido se resalta en rojo.

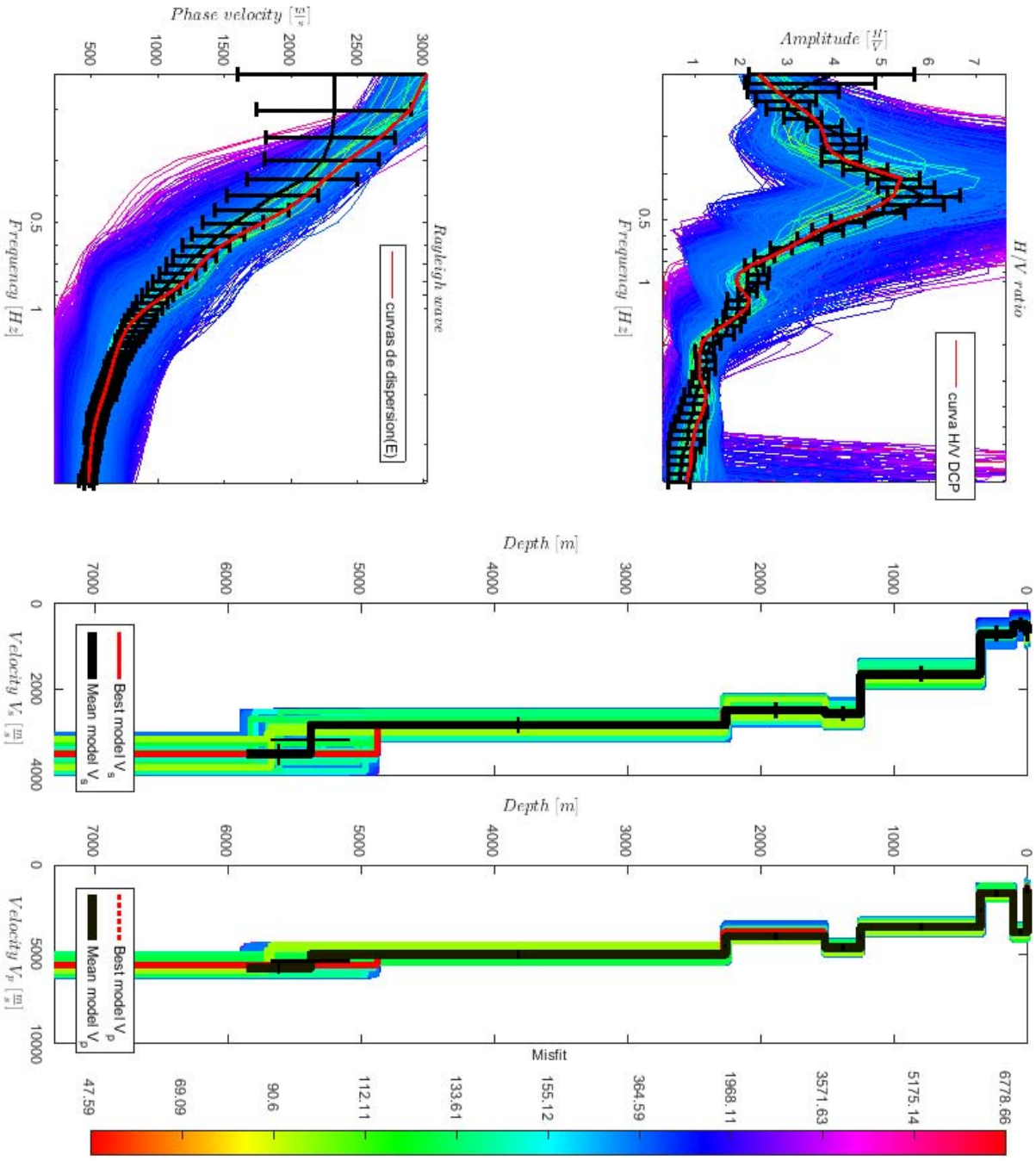

Figura A.1: Resultados de inversiones conjuntas a partir de curvas empíricas de H/V y dispersión (líneas negras) para la estación DCP.

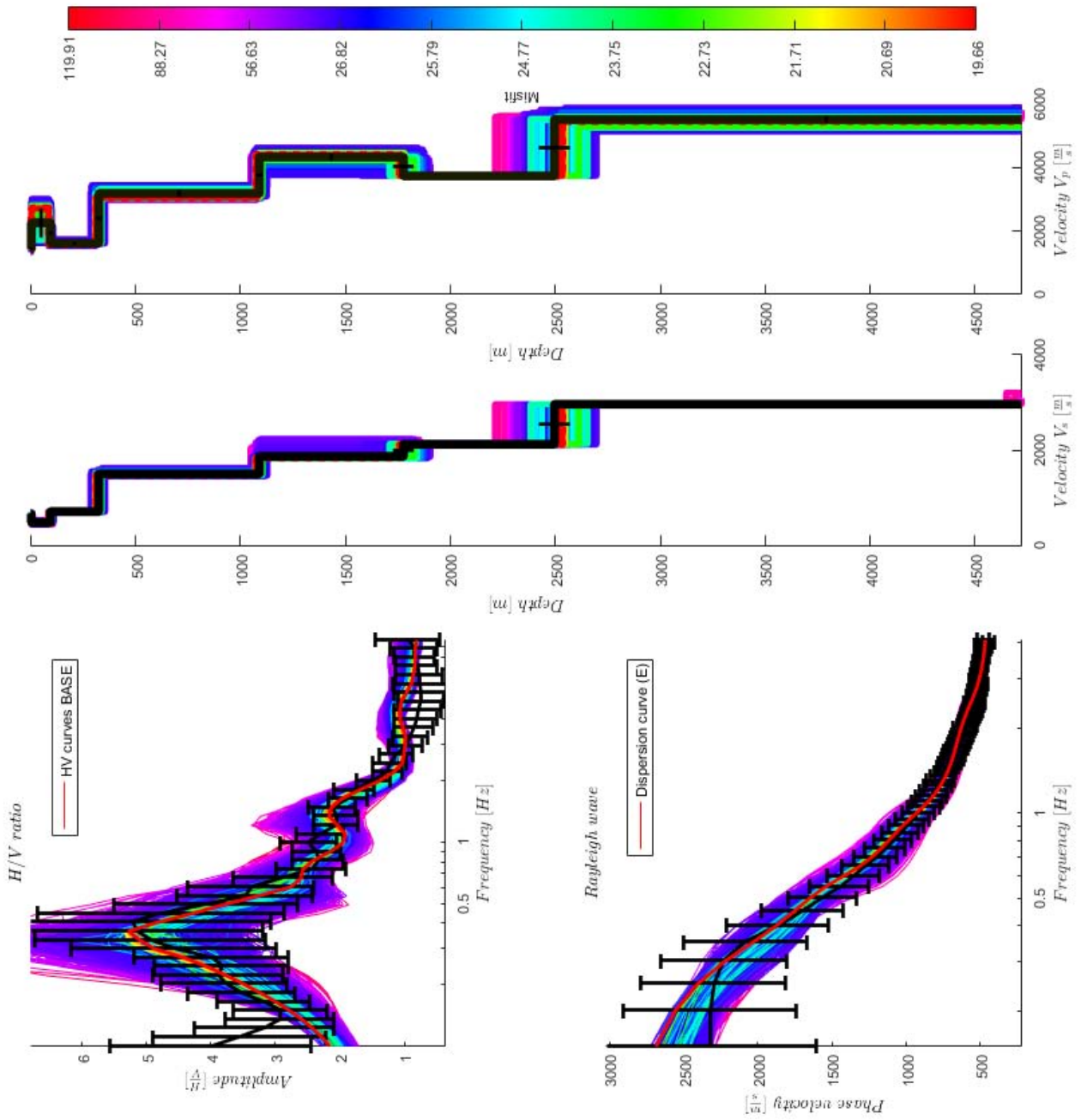

Figura A.2: Resultados de inversiones conjuntas a partir de curvas empíricas de H/V y dispersión (líneas negras) para la estación BASE

.

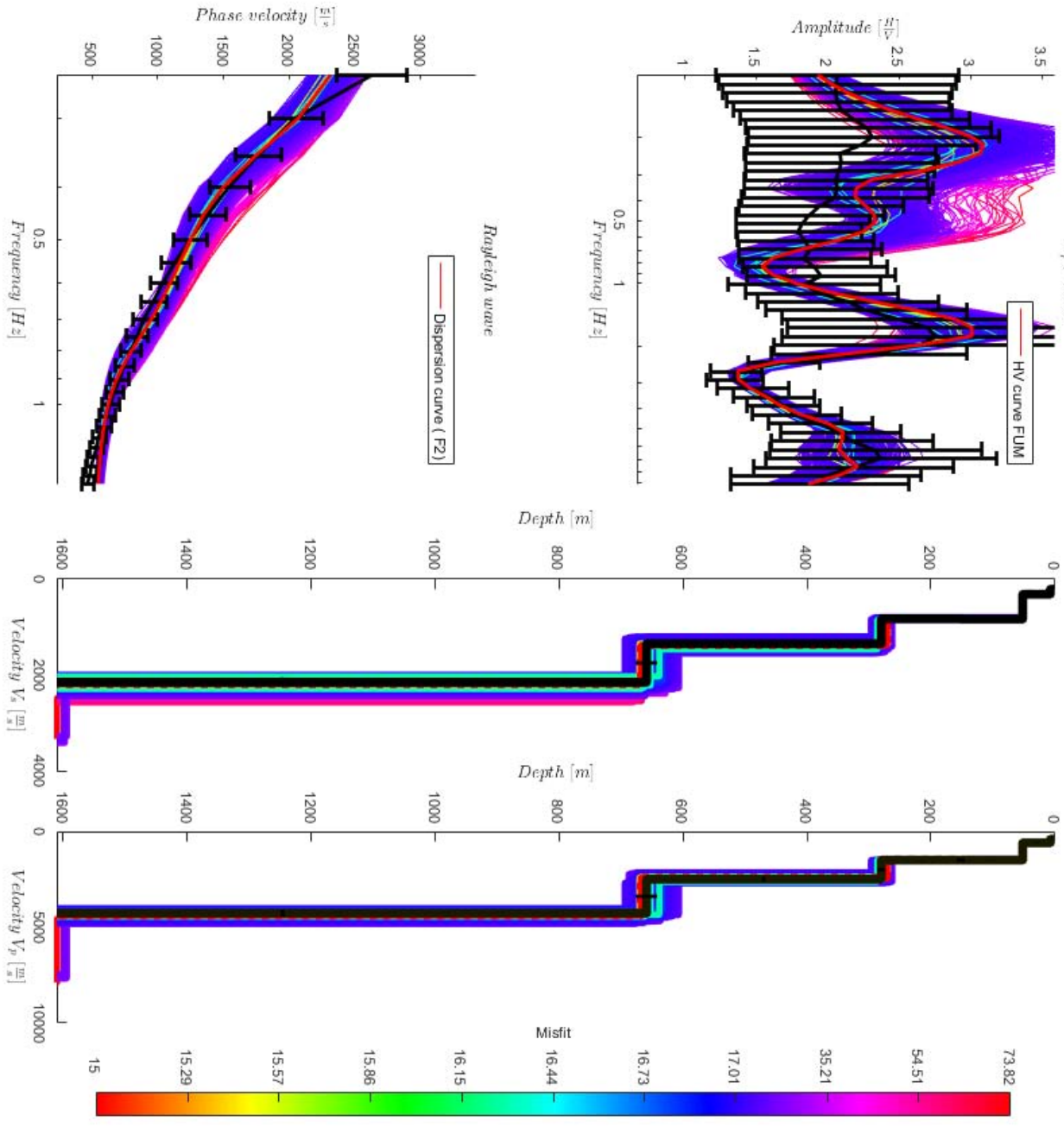

Figura A.3: Resultados de inversiones conjuntas a partir de curvas empíricas de H/V y dispersión (líneas negras) para la estación FUM.

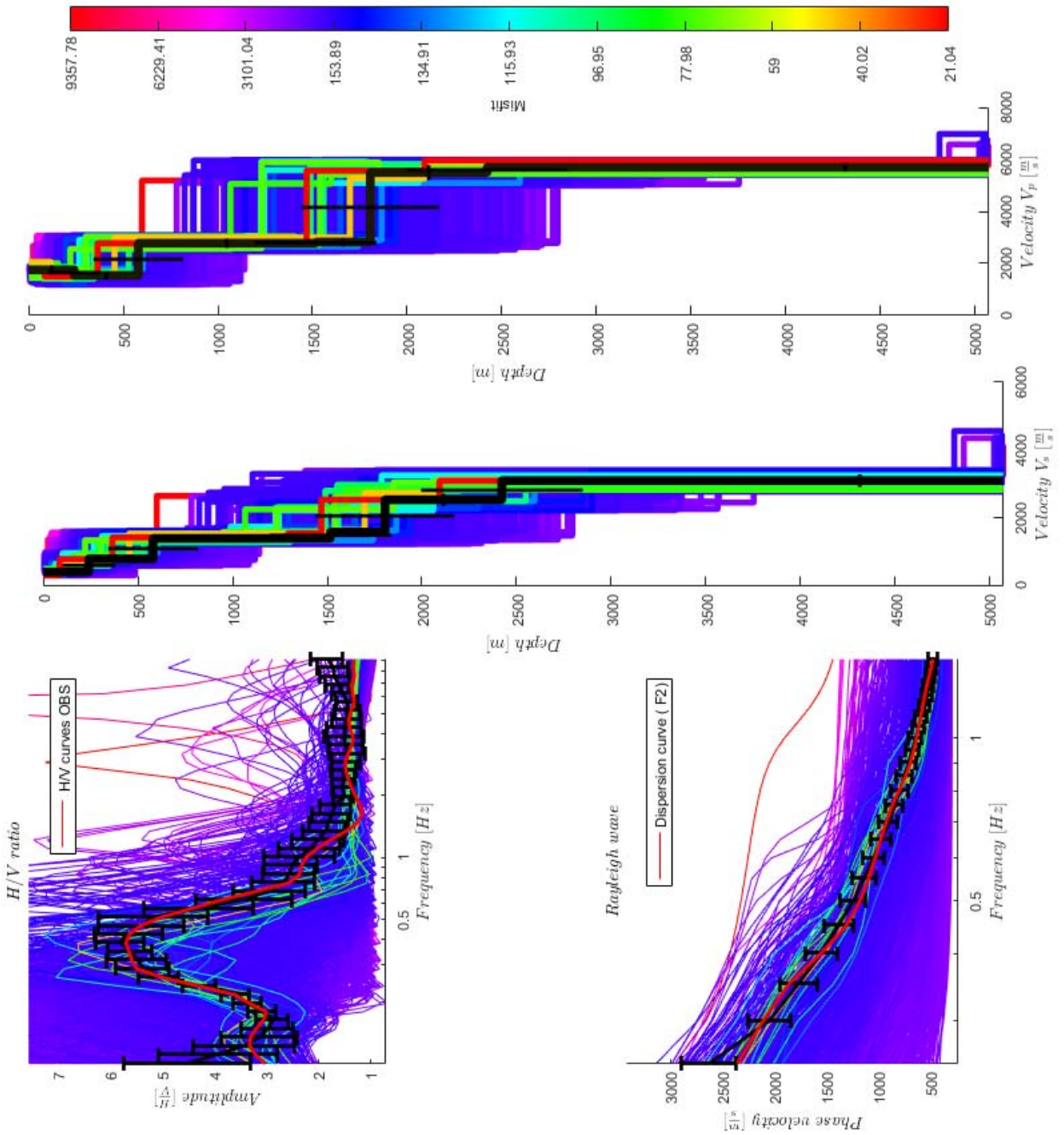

Figura A.4: Resultados de inversiones conjuntas a partir de curvas empíricas de H/V y dispersión (líneas negras) para la estación OBS.

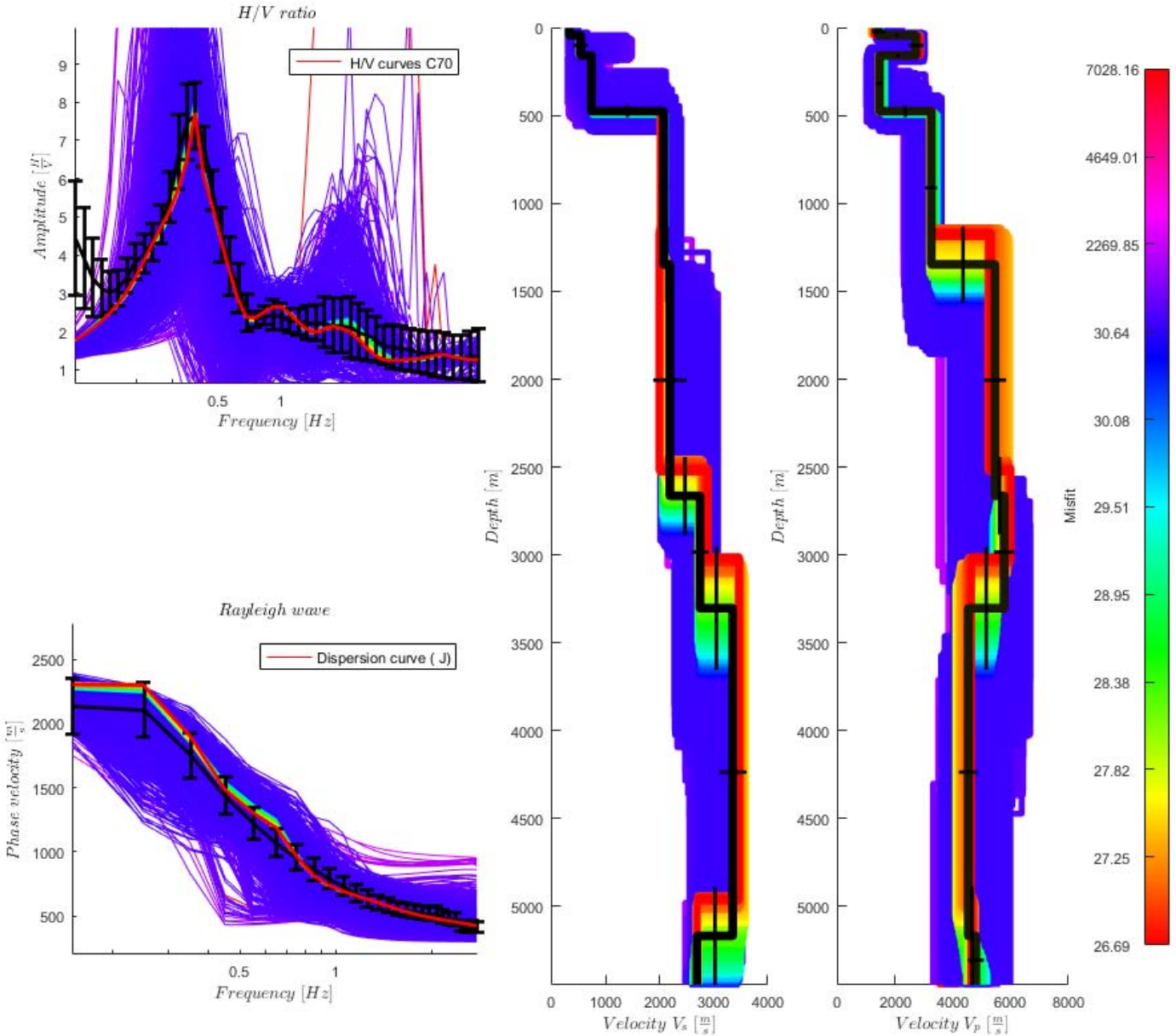

Figura A.5: Resultados de inversiones conjuntas a partir de curvas empíricas de H/V y dispersión (líneas negras) para la estación C70.

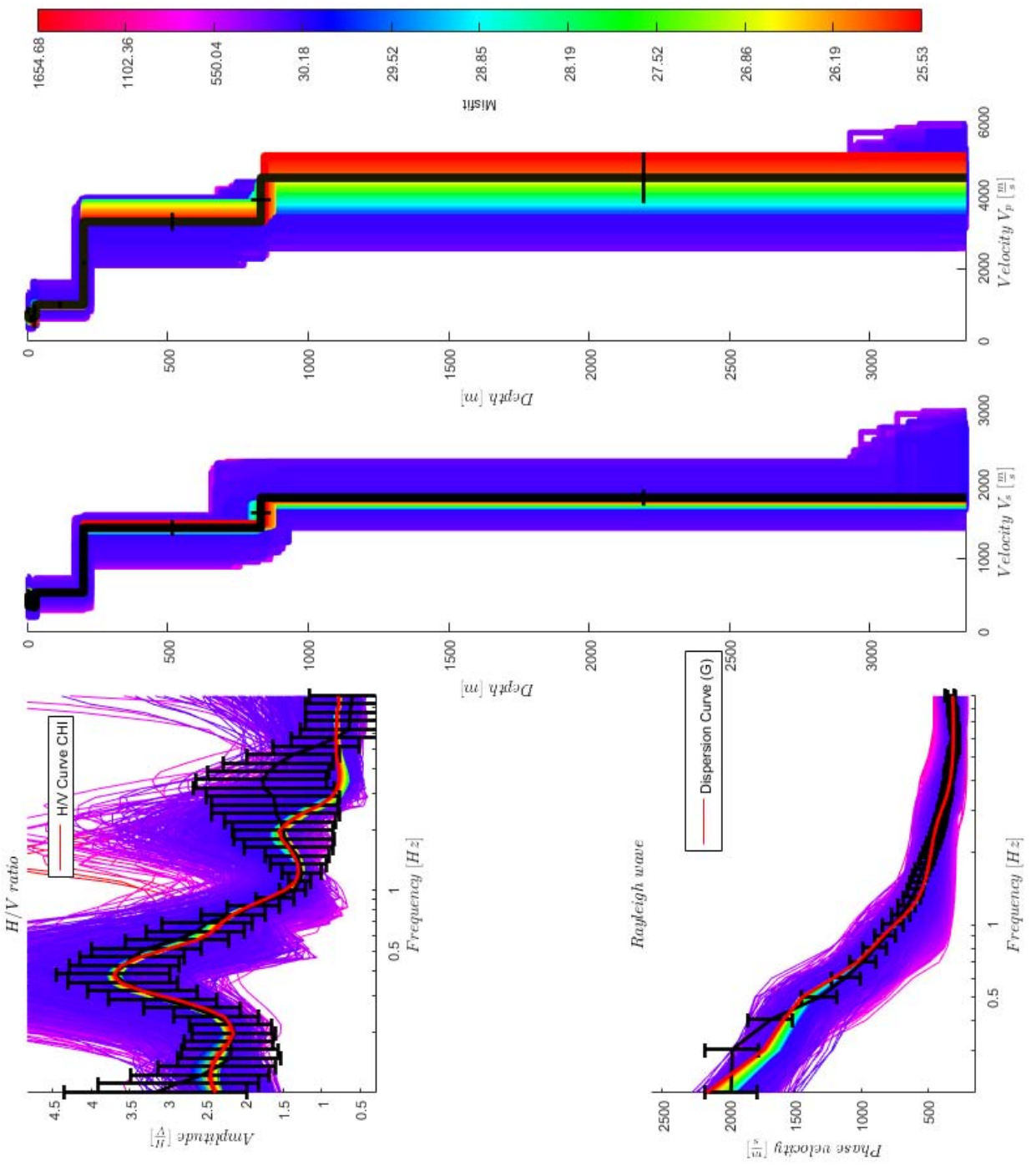

Figura A.6: Resultados de inversiones conjuntas a partir de curvas empíricas de H/V y dispersión (líneas negras) para la estación CHI.

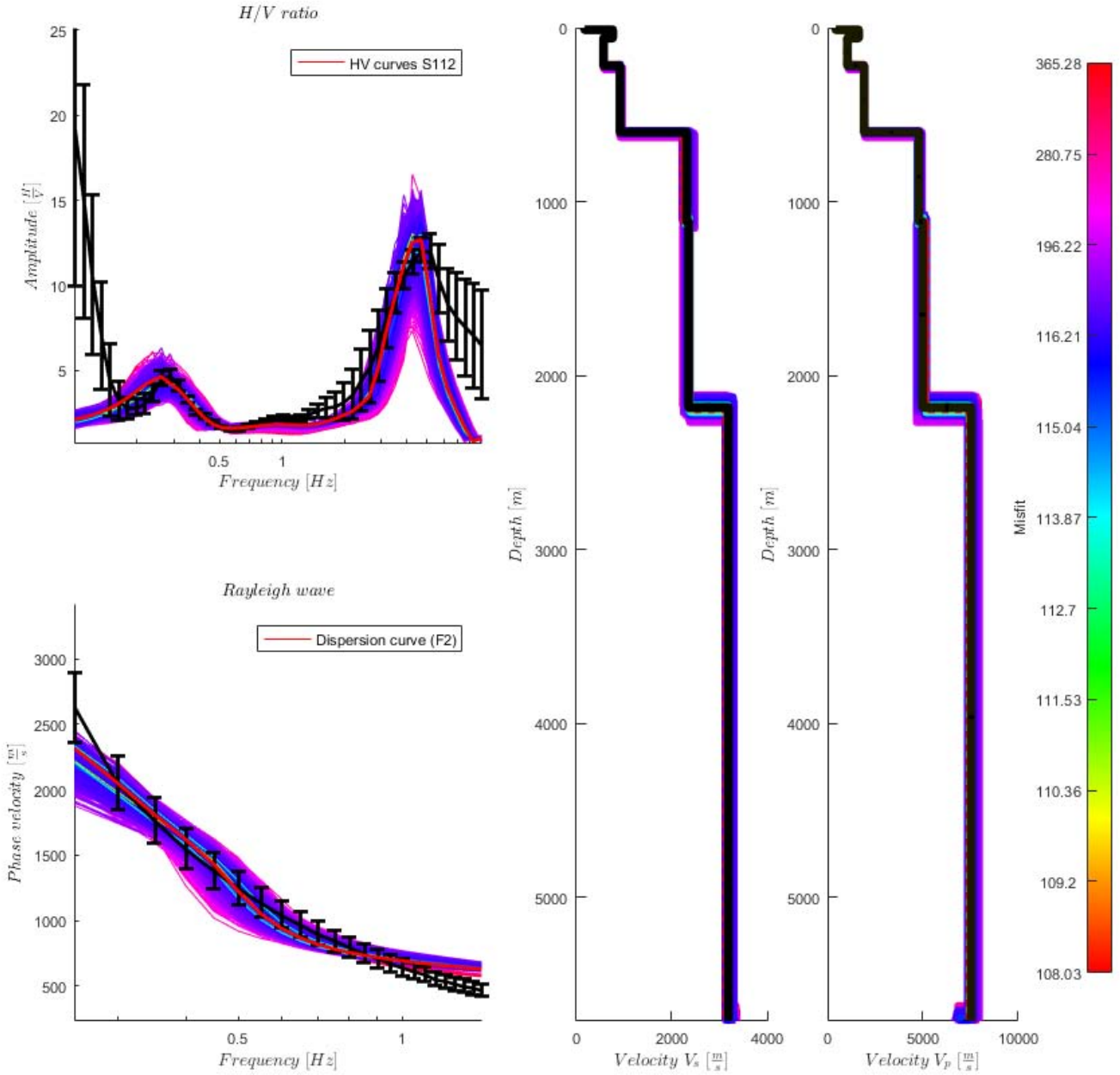

Figura A.7: Resultados de inversiones conjuntas a partir de curvas empíricas de H/V y dispersión (líneas negras) para la estación S112.

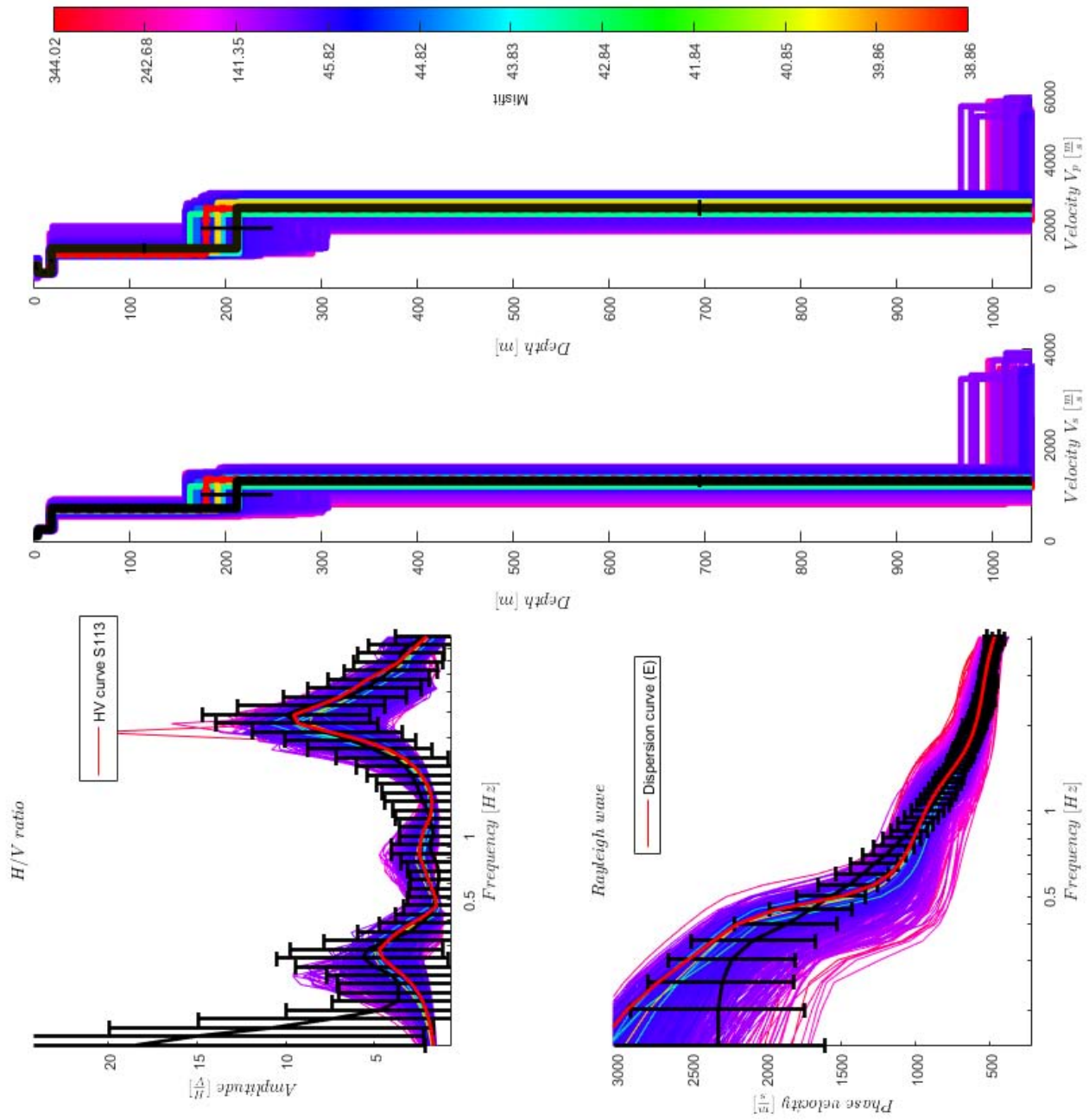

Figura A.8: Resultados de inversiones conjuntas a partir de curvas empíricas de H/V y dispersión (líneas negras) para la estación S113.

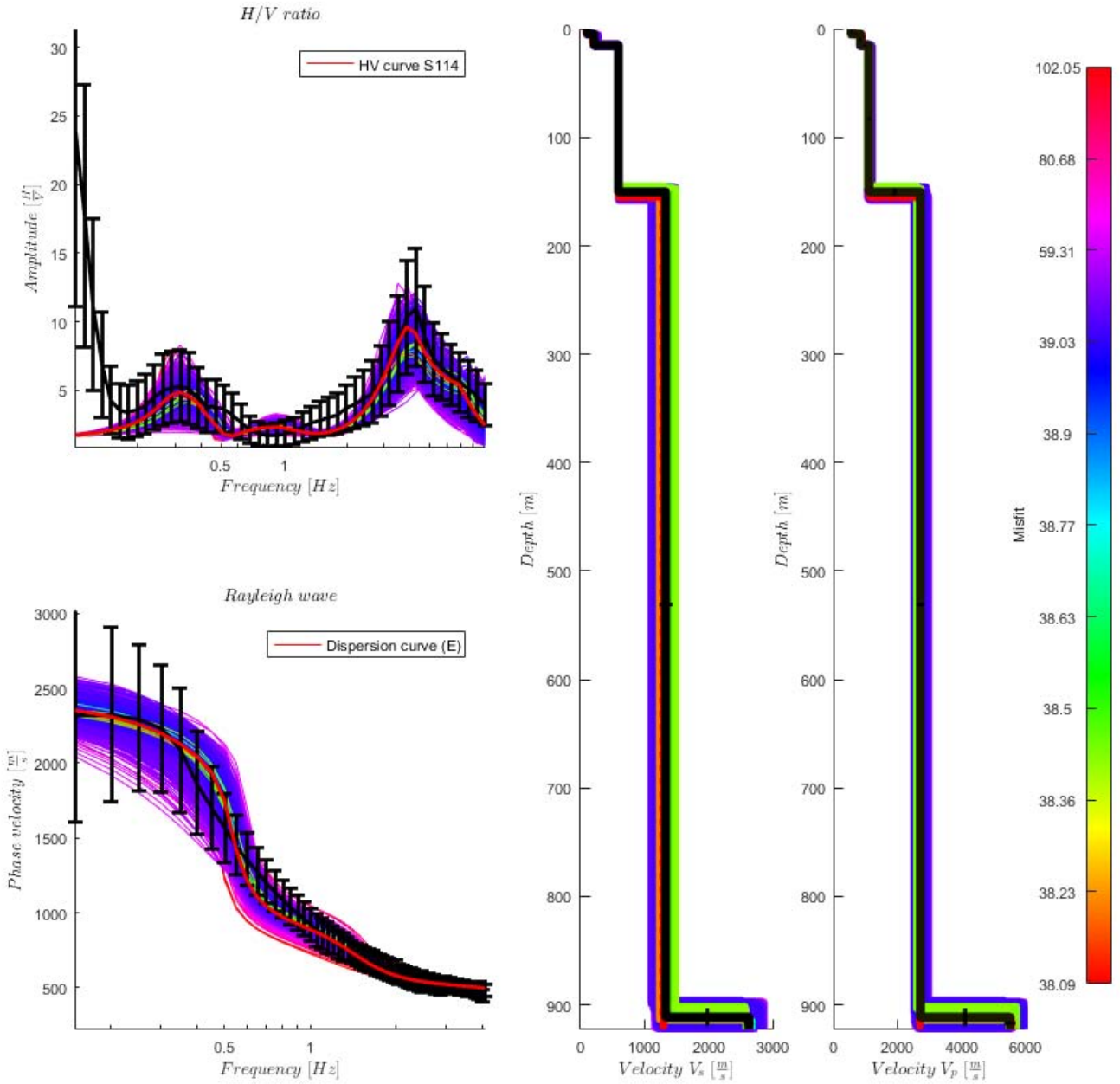

Figura A.9: Resultados de inversiones conjuntas a partir de curvas empíricas de H/V y dispersión (líneas negras) para la estación S114.

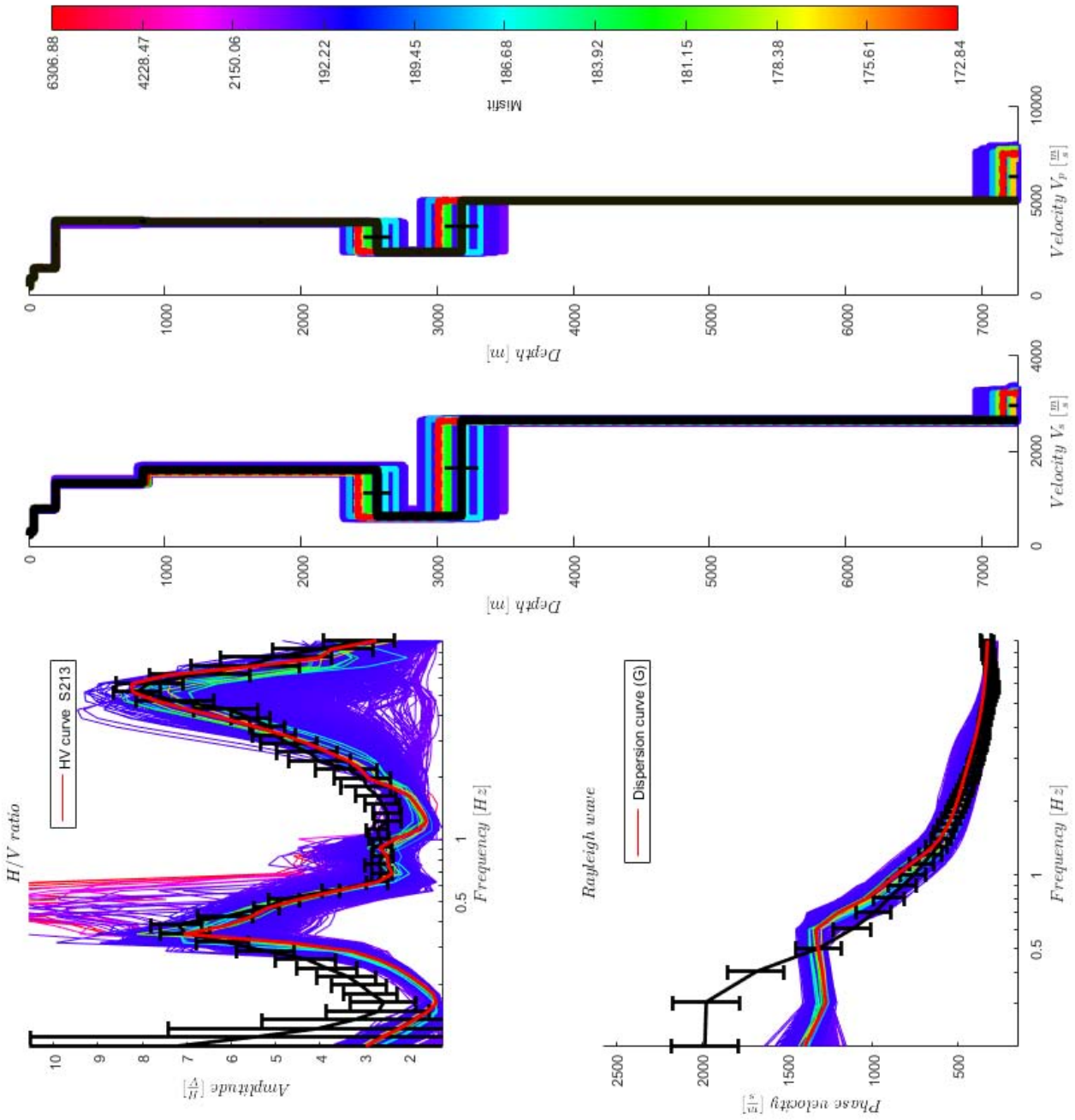

Figura A.10: Resultados de inversiones conjuntas a partir de curvas empíricas de H/V y dispersión (líneas negras) para la estación S213.

A.2. Modelos

A continuación mostramos los modelos de la estructura de velocidad ubicada debajo de todas las estaciones del estudio.

Modelo	Espesor (m)	V_p (m/s)	V_s (m/s)	Densidad (kg/m^3)
DCP	3.5	1167	696.5	912
	105.6	3759	494.9	673.6
	245.2	1522	706.4	996.7
	891.6	3457	1650	841.6
	269.9	4673	2567	1795
	791.4	3742	2376	1460
	2508	4973	2918	1539
	0	5595	3786	2799
BASE	6.15	1176	718.6	912.9
	87.5	3757	478.3	748.3
	241.8	1375	724.1	1085
	911.7	3383	1638	817.2
	227.8	4669	2583	1811
	1057	3748	2461	1489
	2439	4951	2921	1496
	0	5592	3439	2761
FUM	5.999	344.8	197	2085
	49.02	686.8	404.2	2094
	87.72	1508	870.9	2134
	238.6	1756	1086	2315
	162.4	2269	1345	2140
	155.9	2140	1345	2140
	0	3021	1787	2465

Cuadro A.1: Modelos de la estructura por capas que muestran los valores de espesor, V_p, V_s y densidad obtenidos de la inversión conjunta de las estaciones de tierra del lado Este DCP, BASE, FUM y las curvas de dispersión E, E y F2 , respectivamente.

Modelo	Espesor (m)	V_p (m/s)	V_s (m/s)	Densidad (kg/m^3)
OBS	84.91	1743	300.2	1052
	279.2	1493	785.5	493.7
	929.3	2775	1425	978.1
	175.2	2806	1546	679.8
	624.3	5575	2534	2000
	3971	5974	3093	926.2
	0	6986	4505	1382
C70	43.68	1344	322.5	990.3
	116.6	2872	517.7	990.3
	308.9	1428	753.1	1177
	706.1	3302	2041	1000
	1344	5318	1985	1750
	496	6037	2903	1706
	1938	4660	3469	1463
	0	4632	2700	1112
CHI	5.198	676.9	450.4	2709
	9.917	950.4	356.1	3420
	10.43	424.1	281.8	1950
	193.6	1239	589.7	1692
	585	2471	1314	1261
	1690	3113	1914	1753
	0	5445	2744	1248

Cuadro A.2: Modelos de la estructura por capas que muestran los valores de espesor, V_p, V_s y densidad obtenidos de la inversión conjunta de las estaciones de tierra del lado Noroeste OBS, C70 y CHI y las curvas de dispersión F2, J y G , respectivamente.

Modelo	Espesor (m)	V_p (m/s)	V_s (m/s)	Densidad (kg/m^3)
S112	3.072	573.9	100.1	1623
	12.71	895.3	307.9	2898
	136	1169	996.2	2586
	866.1	2822	1313	1284
	0	5417	3674	1567
S113	4.608	748.3	108.9	1167
	12.8	512.9	261.9	1493
	162.9	1071	675.3	1810
	958.8	2510	1296	1770
	0	5953	3966	1464
S114	3.999	573.9	100.1	1623
	10.74	895.3	224.7	2898
	140.6	1169	606.4	2586
	762.6	2822	1358	1284
	0	5417	2842	1567
S213	3.934	573.9	145.6	1623
	11.85	895.3	288.8	2898
	136	1169	996.2	2586
	926	2822	1313	1284
	0	5417	2458	1567

Cuadro A.3: Modelos de la estructura por capas que muestran los valores de espesor, V_p, V_s y densidad obtenidos de la inversión conjunta de las estaciones de marinas S112, S113, S114 y S213 y las curvas de dispersión F2, E, E, G, respectivamente.

A.3. Modelo 3D

A continuación mostramos los modelos 3D de la estructura de velocidad ubicada debajo de todas las estaciones del estudio.

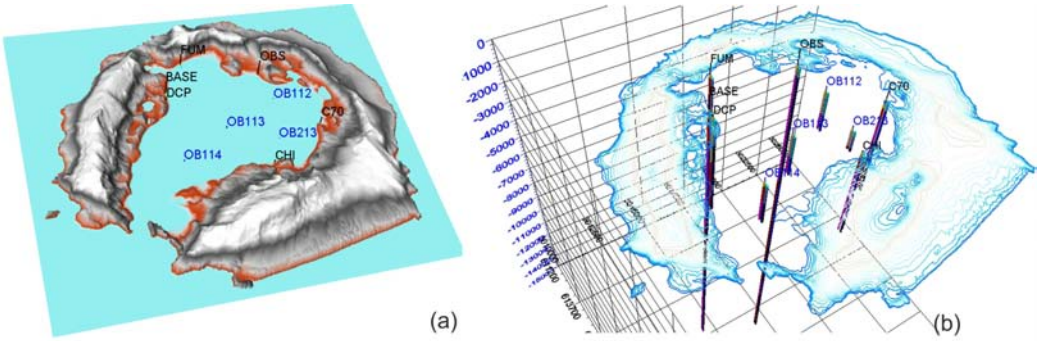

Figura A.11: Situación de las estaciones sísmicas analizadas. (a) Las estaciones marcadas como OB (en azul) son OBS emplazados en el fondo de la bahía. El resto son las estaciones terrestres , todas ellas cercanas a la orilla. (b) La imagen muestra de forma general los modelos de velocidad 1D obtenidos.

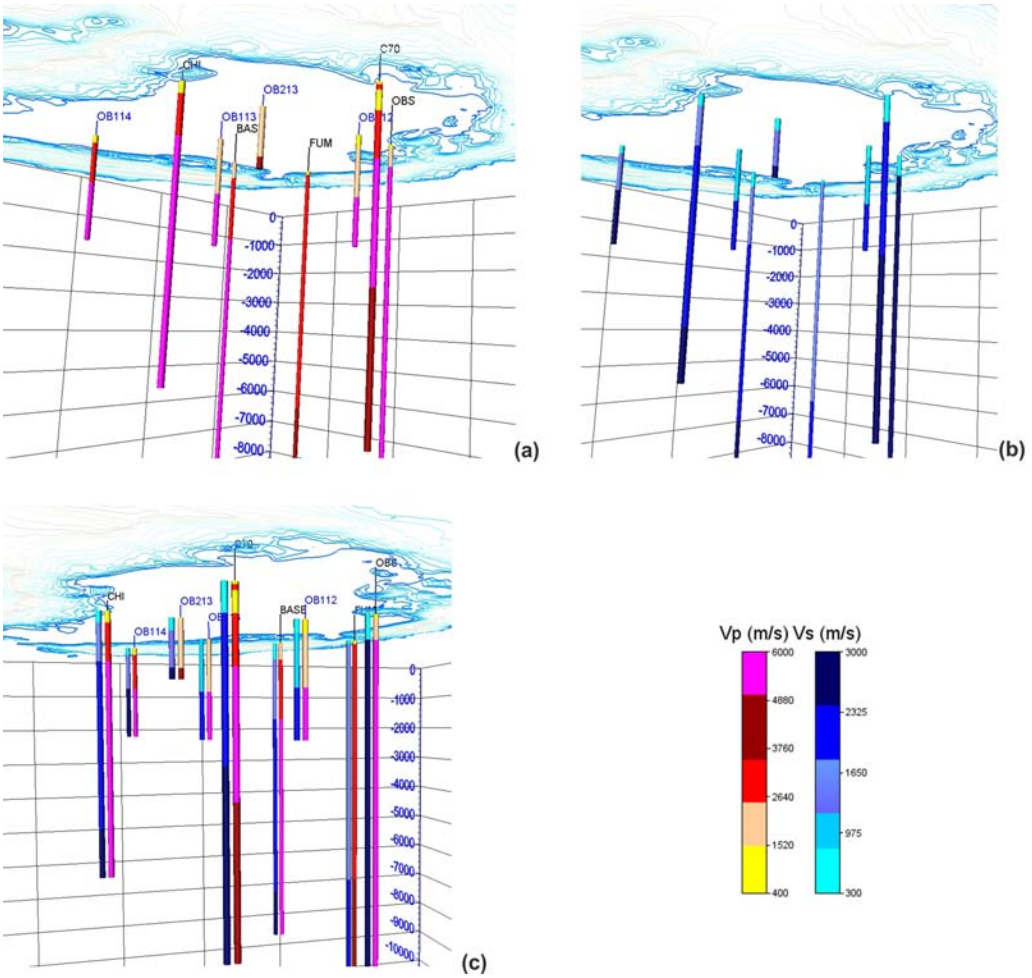

Figura A.12: Modelos de velocidades 1D: (a) para las Vp, (b) para las Vs; y (c) imagen conjunta.

Apéndice B

Catálogo de señales

A continuación vamos a mostrar distintos ejemplos de señales exóticas registradas en la estación DCP durante el curso de tiempo que nos compete en este trabajo.

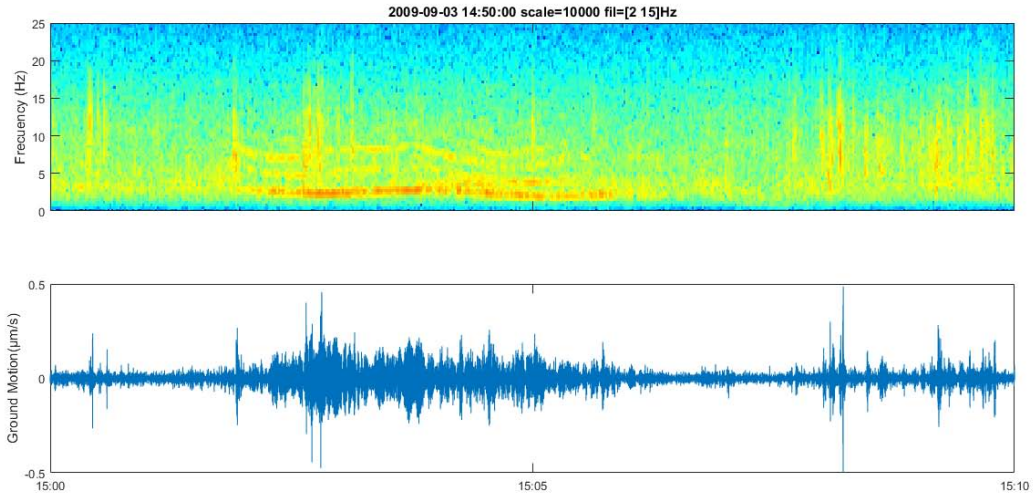

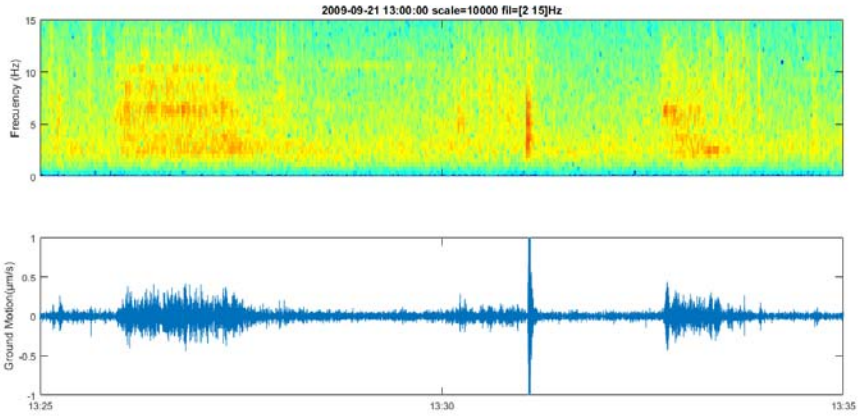
2009-09-21 13:00:00 scale=10000 fil=[2 15]Hz
Frequency (Hz)
Ground Motion(μm/s)
13:25
13:30
13:35

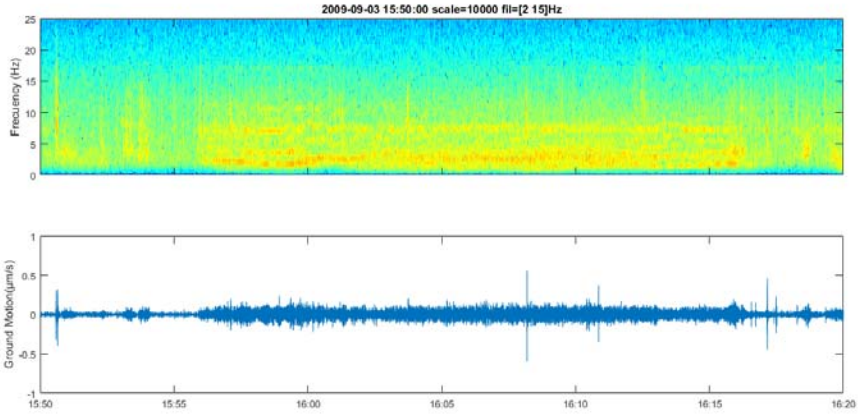
2009-09-03 15:50:00 scale=10000 fil=[2 15]Hz
Frequency (Hz)
Ground Motion(μm/s)
15:50
15:55
16:00
16:05
16:10
16:15
16:20

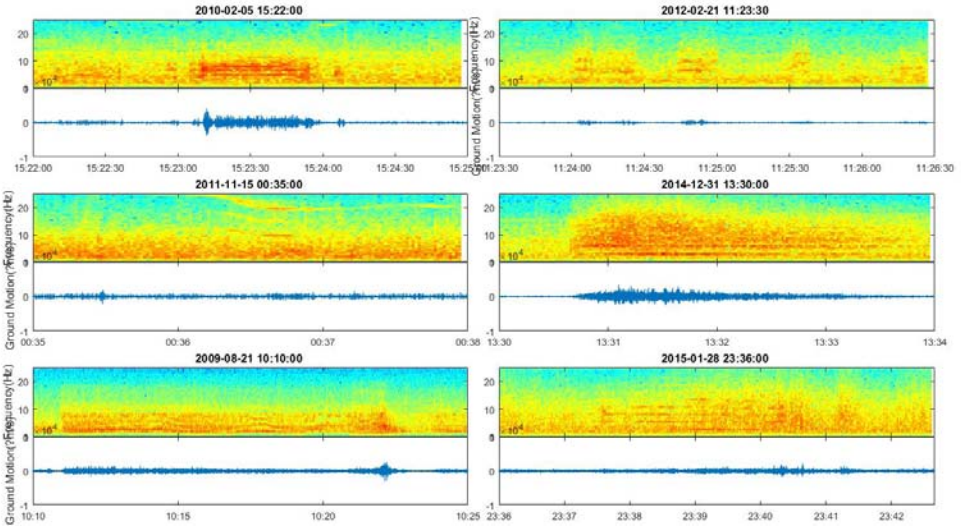
2010-02-05 15:22:00
2012-02-21 11:23:30
2011-11-15 00:35:00
2014-12-31 13:30:00
2009-08-21 10:10:00
2015-01-28 23:36:00

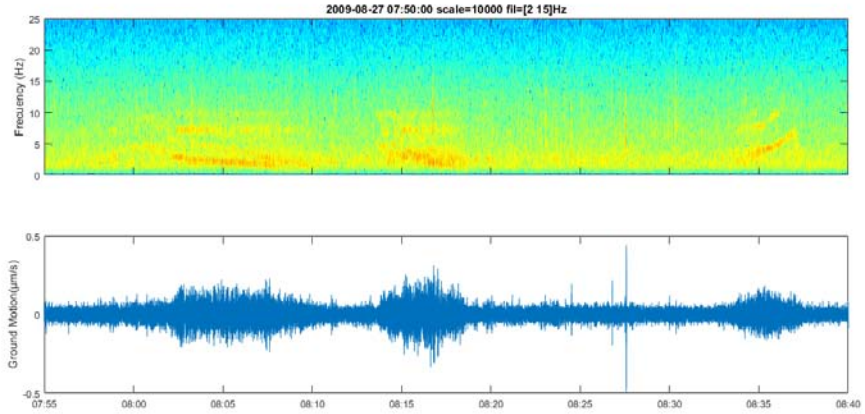
2009-08-27 07:50:00 scale=10000 fil=[2 15]Hz
Frequency (Hz)
Ground Motion(µm/s)
07:55
08:00
08:05
08:10
08:15
08:20
08:25
08:30
08:35
08:40

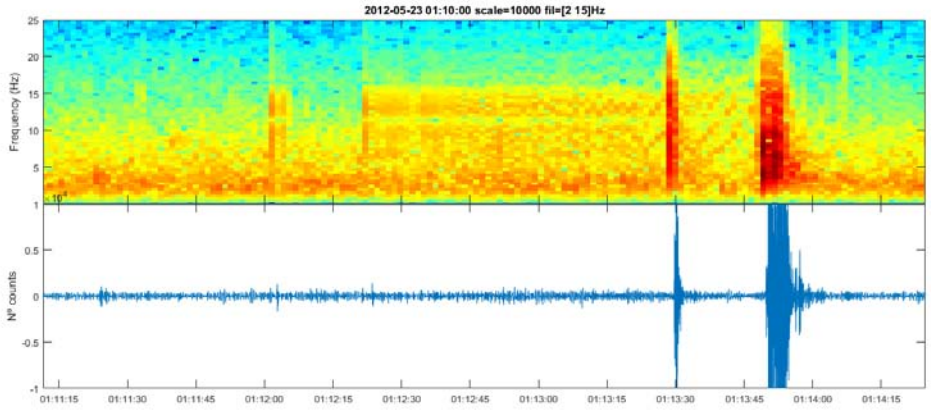
2012-05-23 01:10:00 scale=10000 fil=[2 15]Hz
Frequency (Hz)
Nº counts
01:11:15
01:11:30
01:11:45
01:12:00
01:12:15
01:12:30
01:12:45
01:13:00
01:13:15
01:13:30
01:13:45
01:14:00
01:14:15

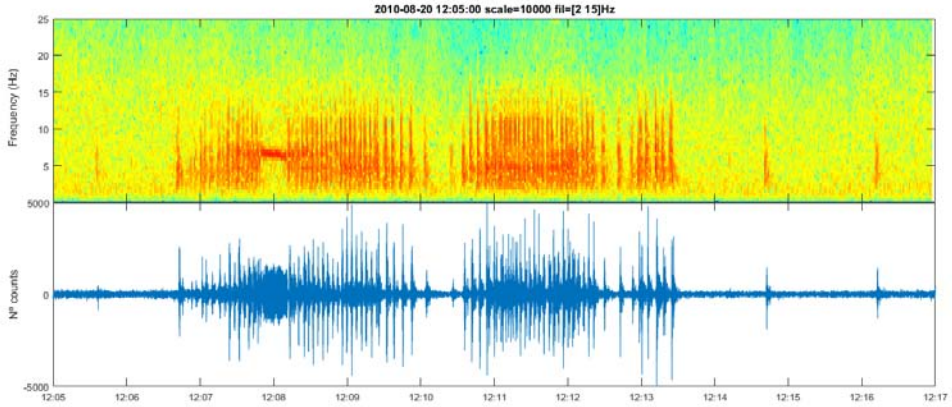
2010-08-20 12:05:00 scale=10000 fil=[2 15]Hz
Frequency (Hz)
Nº counts
12:05
12:06
12:07
12:08
12:09
12:10
12:11
12:12
12:13
12:14
12:15
12:16
12:17

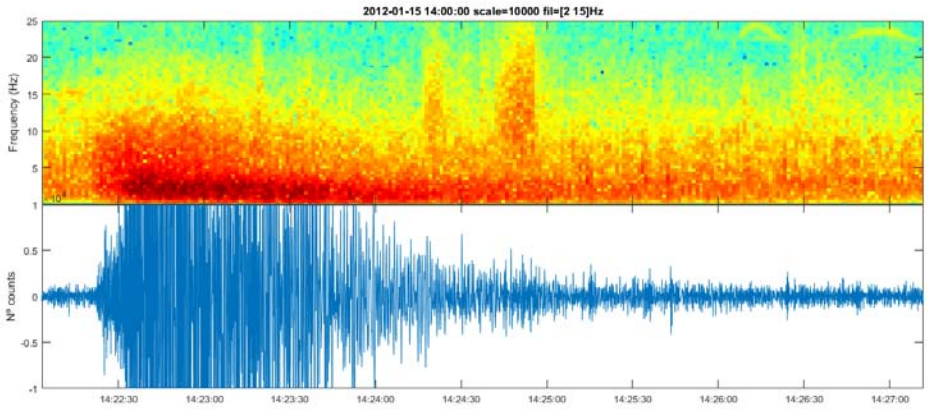
2012-01-15 14:00:00 scale=10000 fil=[2 15]Hz
Frequency (Hz)
N° counts
14:22:30
14:23:00
14:23:30
14:24:00
14:24:30
14:25:00
14:25:30
14:26:00
14:26:30
14:27:00

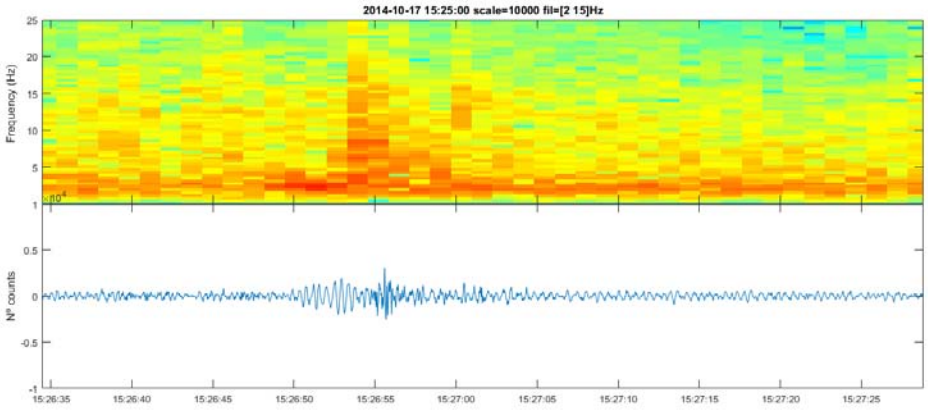
2014-10-17 15:25:00 scale=10000 fil=[2 15]Hz
Frequency (Hz)
N° counts
15:26:35
15:26:40
15:26:45
15:26:50
15:26:55
15:27:00
15:27:05
15:27:10
15:27:15
15:27:20
15:27:25

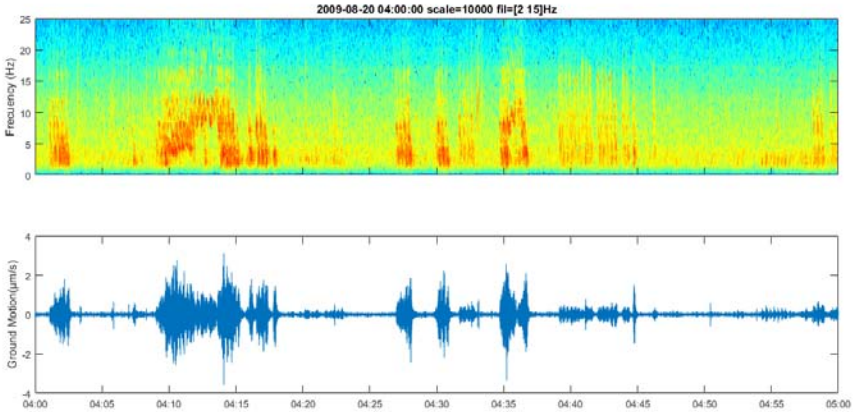
2009-08-20 04:00:00 scale=10000 fil=[2 15]Hz
Frequency (Hz)
Ground Motion(µm/s)
04:00
04:05
04:10
04:15
04:20
04:25
04:30
04:35
04:40
04:45
04:50
04:55
05:00

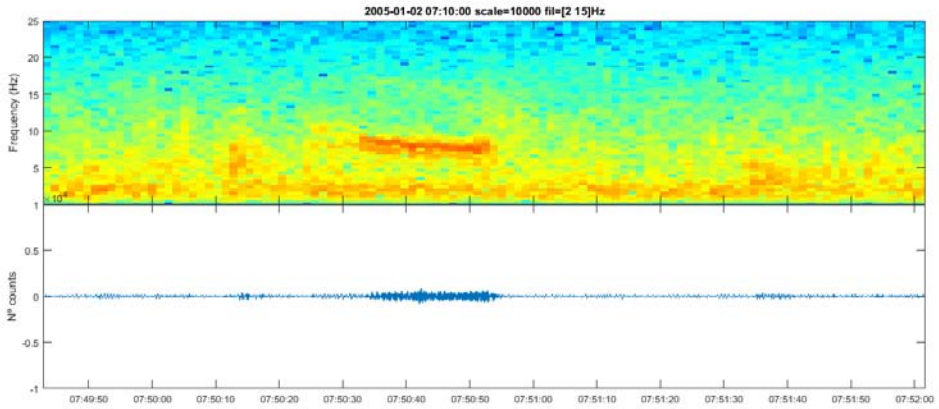
2005-01-02 07:10:00 scale=10000 fil=[2 15]Hz
Frequency (Hz)
N° counts
07:49:50
07:50:00
07:50:10
07:50:20
07:50:30
07:50:40
07:50:50
07:51:00
07:51:10
07:51:20
07:51:30
07:51:40
07:51:50
07:52:00

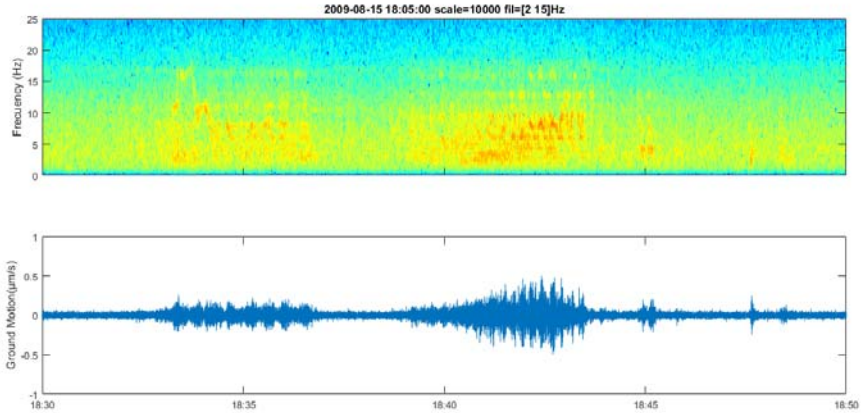
2009-08-15 18:05:00 scale=10000 fil=[2 15]Hz
Frequency (Hz)
Ground Motion(μm/s)
18:30
18:35
18:40
18:45
18:50

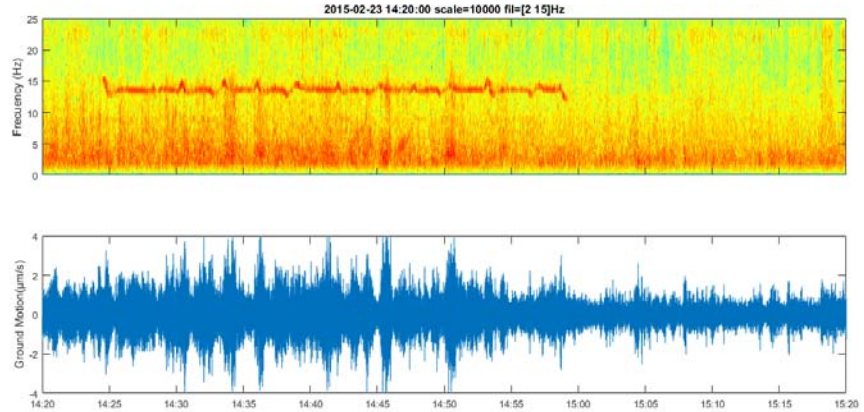
2015-02-23 14:20:00 scale=10000 fil=[2 15]Hz
Frequency (Hz)
Ground Motion(μm/s)
14:20
14:25
14:30
14:35
14:40
14:45
14:50
14:55
15:00
15:05
15:10
15:15
15:20

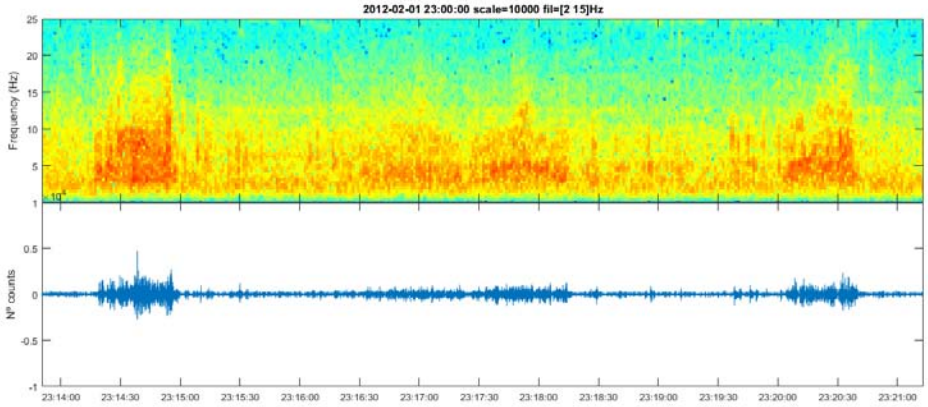
2012-02-01 23:00:00 scale=10000 fil=[2 15]Hz
Frequency (Hz)
Nº counts
23:14:00
23:14:30
23:15:00
23:15:30
23:16:00
23:16:30
23:17:00
23:17:30
23:18:00
23:18:30
23:19:00
23:19:30
23:20:00
23:20:30
23:21:00

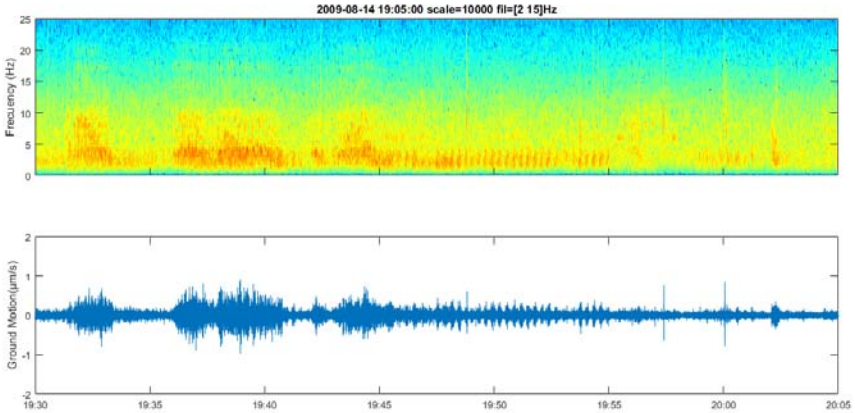
2009-08-14 19:05:00 scale=10000 fil=[2 15]Hz
Frecuency (Hz)
Ground Motion(µm/s)
19:30
19:35
19:40
19:45
19:50
19:55
20:00
20:05

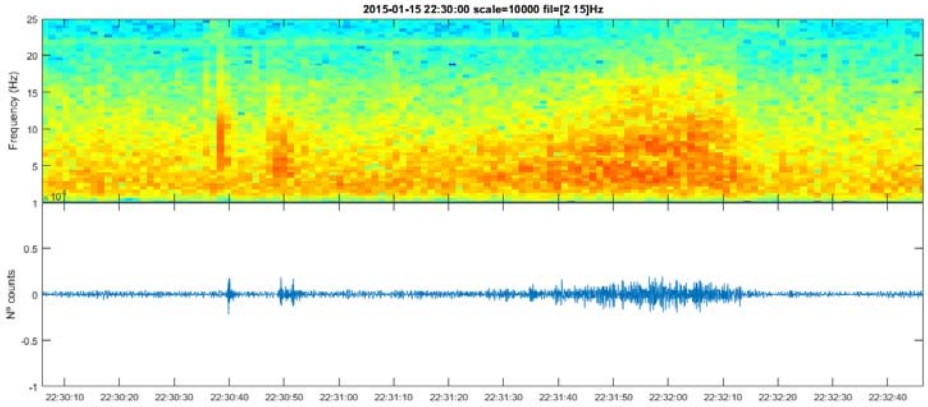
2015-01-15 22:30:00 scale=10000 fil=[2 15]Hz
Frequency (Hz)
Nº counts
22:30:10
22:30:20
22:30:30
22:30:40
22:30:50
22:31:00
22:31:10
22:31:20
22:31:30
22:31:40
22:31:50
22:32:00
22:32:10
22:32:20
22:32:30
22:32:40

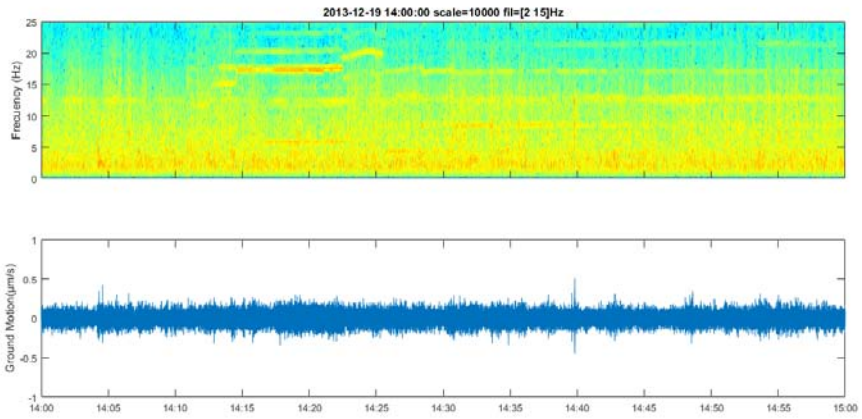
2013-12-19 14:00:00 scale=10000 fil=[2 15]Hz
Frecuency (Hz)
Ground Motion(μm/s)
14:00
14:05
14:10
14:15
14:20
14:25
14:30
14:35
14:40
14:45
14:50
14:55
15:00

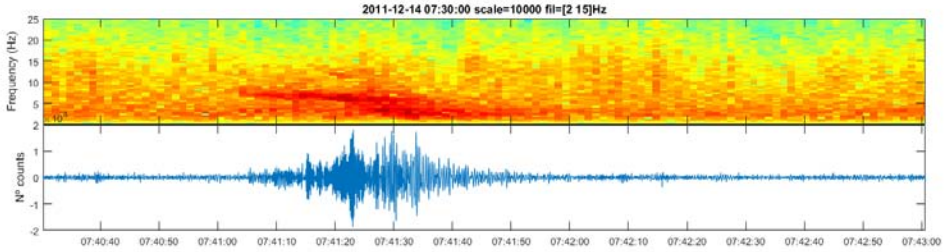
2011-12-14 07:30:00 scale=10000 fil=[2 15]Hz
Frequency (Hz)
Nº counts
07:40:40
07:40:50
07:41:00
07:41:10
07:41:20
07:41:30
07:41:40
07:41:50
07:42:00
07:42:10
07:42:20
07:42:30
07:42:40
07:42:50
07:43:00

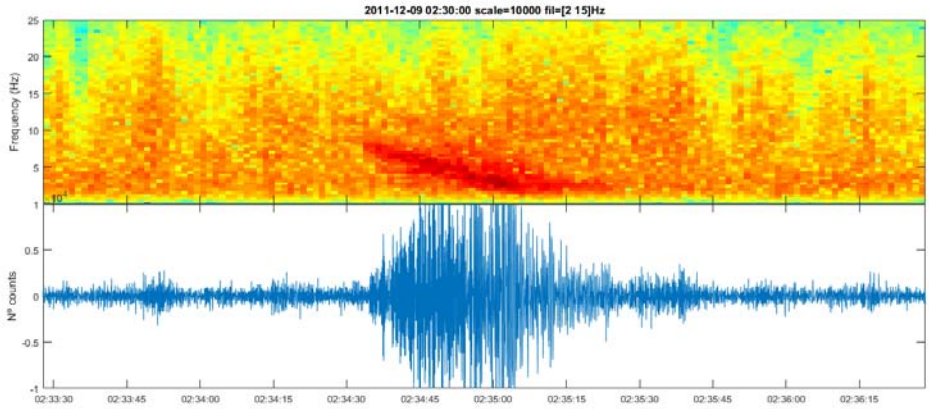
2011-12-09 02:30:00 scale=10000 fil=[2 15]Hz
Frequency (Hz)
Nº counts
02:33:30
02:33:45
02:34:00
02:34:15
02:34:30
02:34:45
02:35:00
02:35:15
02:35:30
02:35:45
02:36:00
02:36:15

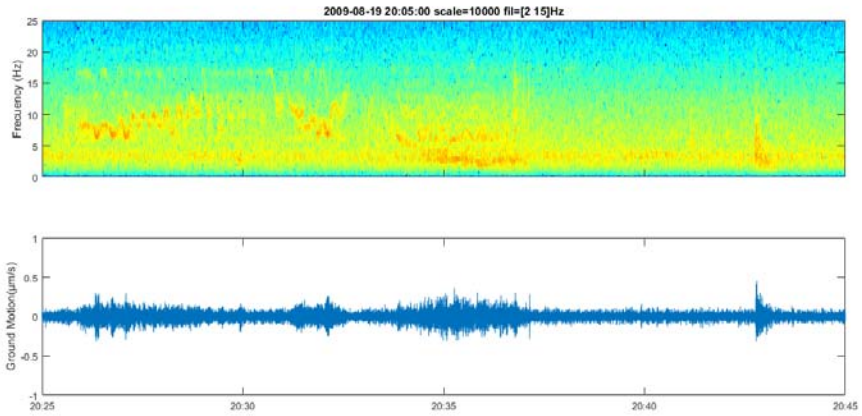
2009-08-19 20:05:00 scale=10000 fil=[2 15]Hz
Frequency (Hz)
Ground Motion(μm/s)
20:25
20:30
20:35
20:40
20:45

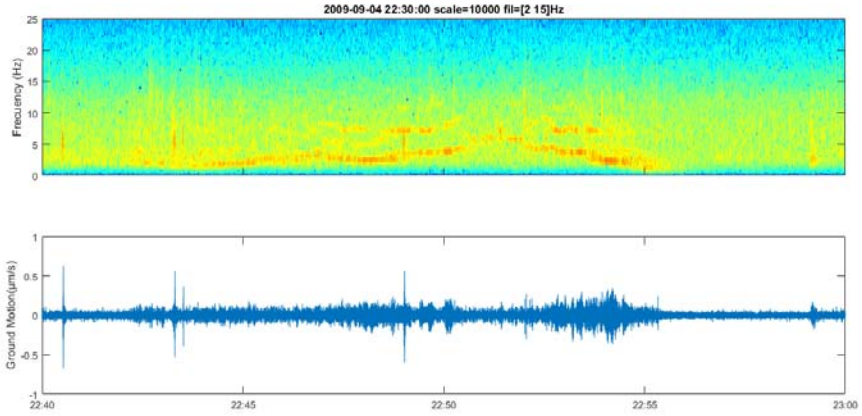
2009-09-04 22:30:00 scale=10000 fil=[2 15]Hz
Frequency (Hz)
Ground Motion(μm/s)
22:40
22:45
22:50
22:55
23:00

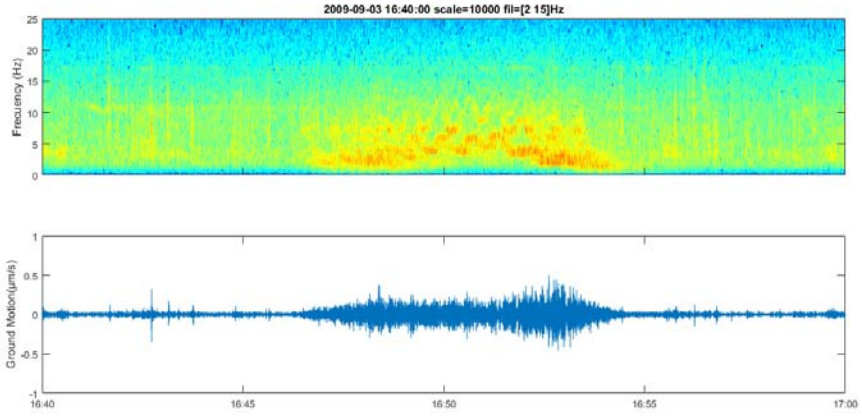
2009-09-03 16:40:00 scale=10000 fil=[2 15]Hz
Frequency (Hz)
Ground Motion(μm/s)
16:40
16:45
16:50
16:55
17:00

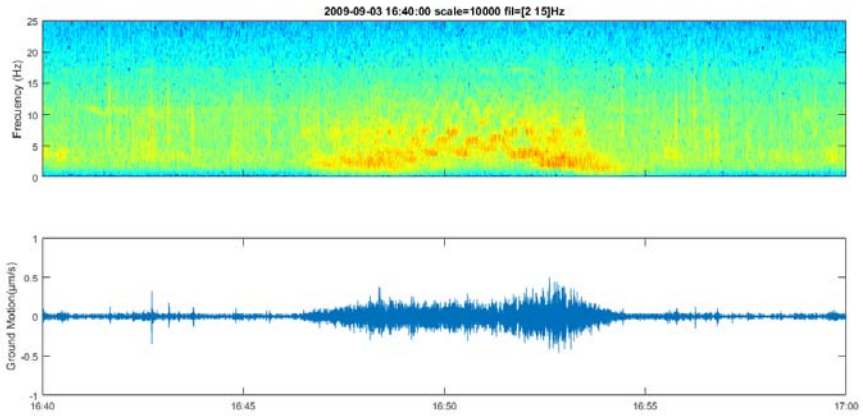
2009-09-03 16:40:00 scale=10000 fil=[2 15]Hz
Frequency (Hz)
Ground Motion(µm/s)
16:40
16:45
16:50
16:55
17:00

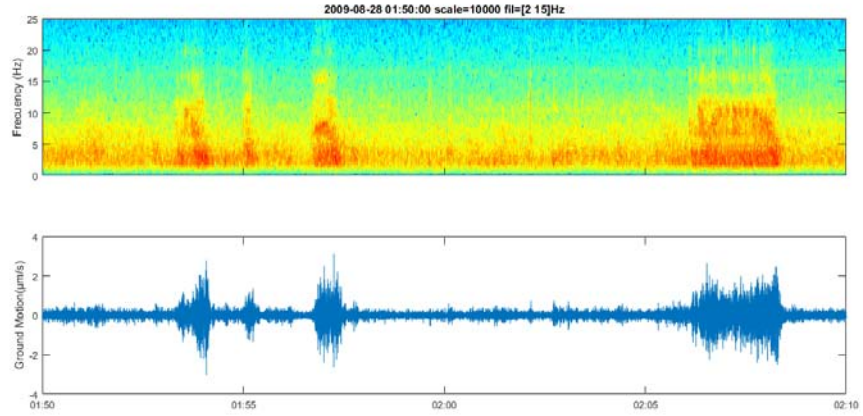
2009-08-28 01:50:00 scale=10000 fil=[2 15]Hz
Frequency (Hz)
Ground Motion(µm/s)
01:50
01:55
02:00
02:05
02:10

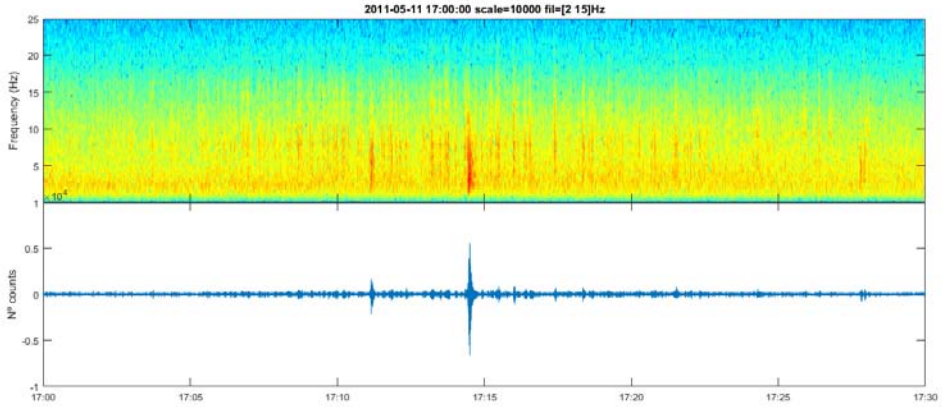
2011-05-11 17:00:00 scale=10000 fil=[2 15]Hz
Frequency (Hz)
Nº counts
17:00
17:05
17:10
17:15
17:20
17:25
17:30

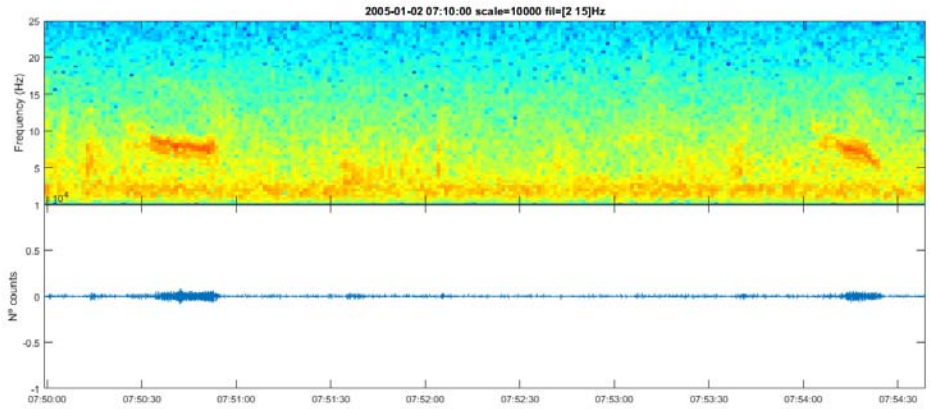
2005-01-02 07:10:00 scale=10000 fil=[2 15]Hz
Frequency (Hz)
N° counts
07:50:00
07:50:30
07:51:00
07:51:30
07:52:00
07:52:30
07:53:00
07:53:30
07:54:00
07:54:30

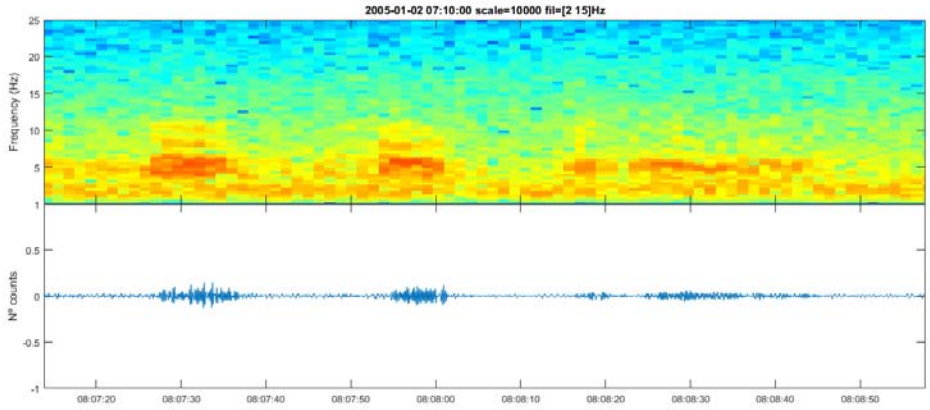
2005-01-02 07:10:00 scale=10000 fil=[2 15]Hz
Frequency (Hz)
N° counts
08:07:20
08:07:30
08:07:40
08:07:50
08:08:00
08:08:10
08:08:20
08:08:30
08:08:40
08:08:50

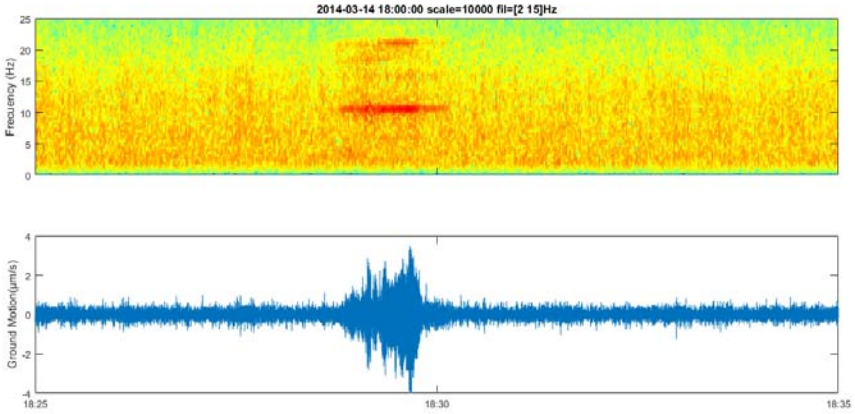
2014-03-14 18:00:00 scale=10000 fil=[2 15]Hz
Frequency (Hz)
Ground Motion(µm/s)
18:25
18:30
18:35

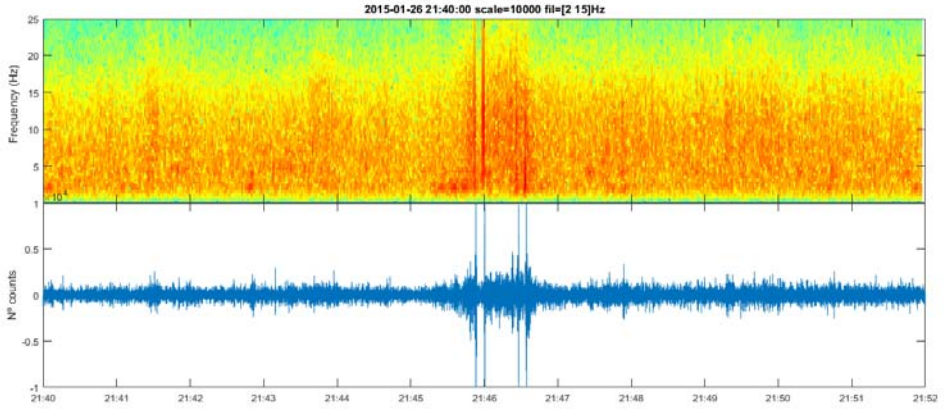
2015-01-26 21:40:00 scale=10000 fil=[2 15]Hz
Frequency (Hz)
Nº counts
21:40
21:41
21:42
21:43
21:44
21:45
21:46
21:47
21:48
21:49
21:50
21:51
21:52

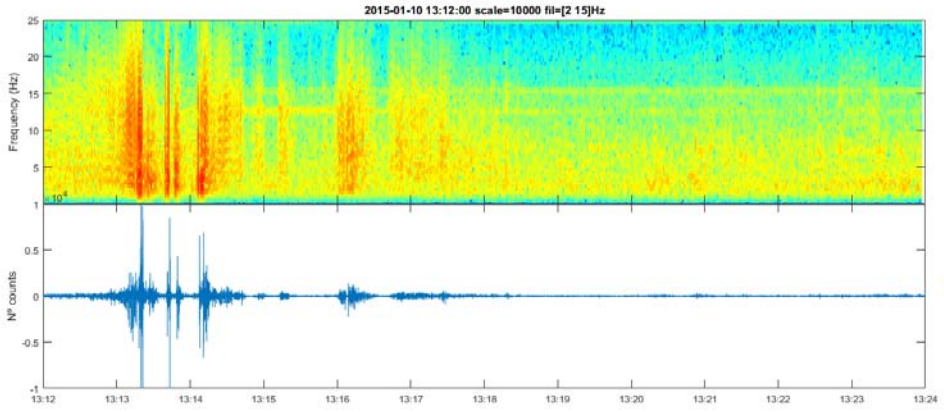
2015-01-10 13:12:00 scale=10000 fil=[2 15]Hz
Frequency (Hz)
Nº counts
13:12
13:13
13:14
13:15
13:16
13:17
13:18
13:19
13:20
13:21
13:22
13:23
13:24

Bibliografía

[1] Abril Martí, M. (2007). Evolución, diseño y desarrollo de antenas sísmicas. Las antenas del Gran Sasso, del Vesubio y las nuevas antenas sísmicas portátiles del Instituto Andaluz de Geofísica. Aplicación a zonas tectónicas y volcánicas. PhD thesis, University of Granada, Spain.

[2] Ahern, T., Casey, R., Barnes, D., Benson, R., Knight, T., and Trabant, C. (2007). SEED Reference Manual, version 2.4. IRIS (http://www. iris. edu/software/pqlx/).

[3] Aiken, C. and Peng, Z. (2014). Dynamic triggering of microearthquakes in three geothermal/volcanic regions of california. Journal of Geophysical Research: Solid Earth, 119(9):6992–7009.

[4] Aki, K. and Chouet, B. (1975). Origin of coda waves: source, attenuation, and scattering effects. Journal of Geophysical Research, 80(23):3322–3342.

[5] Aki, K., Fehler, M., and Das, S. (1977). Source mechanism of volcanic tremor: fluid-driven crack models and their application to the 1963 Kilauea eruption. Journal of Volcanology and Geothermal Research, 2(3):259–287.

[6] Almendros, J. (1999). Análisis de señales sismo- volcánicas mediante técnicas de array. PhD thesis, Universidad de Granada (Spanish).

[7] Almendros, J., Abella, R., Mora, M. M., and Lesage, P. (2014). Array analysis of the seismic wavefield of long-period events and volcanic tremor at Arenal volcano, Costa Rica. Journal of Geophysical Research: Solid Earth, 119(7):5536–5559.

[8] Almendros, J., Carmona, E., Agui, J. F. ., Moreno, J. ., Martos, A. ., Alguacil, G. ., Martin, J. B. ., Jimenez, V., Diaz-Moreno, A., and Lorenzo, F. (2018a). Seismic network at Deception Island Volcano, Antarctica, 2014/2015. Australian Antarctic Data Centre, Australia.

[9] Almendros, J., Carmona, E., Ibánez, J., and Ibáñez, J. (2004). Precise determination of the relative wave propagation parameters of similar events using a small-aperture seismic array. Journal of Geophysical Research B: Solid Earth, 109(11):1–15.

[10] Almendros, J., Carmona, E., Jiménez, V., Díaz, A., Lorenzo, F., Berrocoso, M., de Gil, A., Fernández-Ros, A., and Rosado, B. (2015). Deception Island (Antarctica): Sustained deformation and large increase in seismic activity during 2014-2015. Technical report, Smithsonian Institution.

[11] Almendros, J., Carmona, E., Jiménez, V., Díaz-Moreno, A., and Lorenzo, F. (2018b). Volcano-Tectonic Activity at Deception Island Volcano Following a Seismic Swarm in the Bransfield Rift (2014-2015). Geophysical Research Letters, 45(10):4788–4798.

[12] Almendros, J., Chouet, B., and Dawson, P. (2001). Spatial extent of a hydrothermal system at Kilauea Volcano , Hawaii , determined from array analyses of shallow long - period seismicity 2 . Results. Journal of Geophysical Research, 106(10):581–13.

[13] Almendros, J., Ibáñez, J. M., Alguacil, G., Del Pezzo, E., and Ortiz, R. (1997). Array tracking of the volcanic tremor source at Deception Island, Antarctica. Geophysical Research Letters, 24(23):3069–3072.

[14] Anthony, R. E. (2016). Studies of oceanic, atmospheric, cryospheric, and fluvial processes through spectral analysis of seismic noise. PhD thesis, Colorado State University.

[15] Antoniades, D., Giralt, S., Geyer, A., Álvarez-Valero, A. M., Pla-Rabes, S., Granados, I., Liu, E. J., Toro, M., Smellie, J. L., and Oliva, M. (2018). The timing and widespread effects of the largest holocene volcanic eruption in antarctica. Scientific Reports, 8(1):1–11.

[16] Arai, H. and Tokimatsu, K. (2004). S-wave velocity profiling by inversion of microtremor h/v spectrum. Bulletin of the Seismological Society of America, 94(1):53–63.

[17] Ardhuin, F., Balanche, A., Stutzmann, E., and Obrebski, M. (2012). From seismic noise to ocean wave parameters: General methods and validation. Journal of Geophysical Research, 117(C5):1–19.

[18] Ardhuin, F., Stutzmann, E., Schimmel, M., and Mangeney, A. (2011). Ocean wave sources of seismic noise. Journal of Geophysical Research: Oceans, 116(May):1–21.

[19] Arintalofa, V., Yuliyanto, G., and Harmoko, U. (2020). Subsurface characterization of diwak-derekan geothermal field by hvsr analysis method based on mictrotremor data. In AIP Conference Proceedings, volume 2296, page 020057. AIP Publishing LLC.

[20] Aster, R. C., McNamara, D. E., and Bromirski, P. D. (2008). Multidecadal Climate-induced Variability in Microseisms. Seismological Research Letters, 79(2):194–202.

[21] Aster, R. C., McNamara, D. E., and Bromirski, P. D. (2010). Global trends in extremal microseism intensity. Geophysical Research Letters, 37(14):1–5.

[22] Baker, P. E., Davies, T. G., and Roobol, M. J. (1969). Volcanic activity at Deception Island in 1967 and 1969. Nature, 224:553–560.

[23] Baraldo, A., Rapalini, A. E., Böhnel, H., and Mena, M. (2003). Paleomagnetic study of Deception Island, South Shetland Islands, Antarctica. Geophysical Journal International, 153(2):333–343.

[24] Baraldo, A. and Rinaldi, C. (2000). Stratigraphy and structure of Deception Island, South Shetland Islands, Antarctica. Journal of South American Earth Sciences, 13(8):785–796.

[25] Barclay, A., Wilcock, W., and Ibáñez, J. (2009). Bathymetric constraints on the tectonic and volcanic evolution of Deception Island Volcano, South Shetland Islands. Antarctic Science, 21(02):153.

[26] Bard, P.-Y., Anastasiadis, A., Atakan, K., and Azzara, R. M. (2008). "Guidelines for the Implementation of the H/V Spectral Ratio Technique on Ambient Vibrations Measurement , Processing and Interpretation SESAME European research project". Bulletin of Earthquake EngineeringEngineering, 6(March):1–63.

[27] Barnes, D. K., Linse, K., Enderlein, P., Smale, D., Fraser, K. P., and Brown, M. (2008). Marine richness and gradients at deception island, antarctica. Antarctic Science, 20(3):271–280.

[28] Bartolini, S., Geyer, A., Martí, J., Pedrazzi, D., and Aguirre-Díaz, G. (2014). Volcanic hazard on Deception Island (South Shetland Islands, Antarctica). Journal of Volcanology and Geothermal Research, 285:150–168.

[29] Battaglia, J., Aki, K., and Ferrazzini, V. (2005). Location of tremor sources and estimation of lava output using tremor source amplitude on the Piton de la Fournaise volcano: 1. Location of tremor sources. Journal of Volcanology and Geothermal Research, 147(3):268–290.

[30] Battaglia, J., Thurber, C. H., Got, J.-L., Rowe, C. A., and White, R. A. (2004). Precise relocation of earthquakes following the 15 June 1991 eruption of Mount Pinatubo (Philippines). Journal of Geophysical Research: Solid Earth, 109(B7).

[31] Bean, C. J., De Barros, L., Lokmer, I., Métaxian, J. P., O'Brien, G., and Murphy, S. (2014). Long-period seismicity in the shallow volcanic edifice formed from slow-rupture earthquakes. Nature Geoscience, 7(1):71–75.

[32] Bebbington, M. (2008). Incorporating the eruptive history in a stochastic model for volcanic eruptions. Journal of Volcanology and Geothermal Research, 175(3):325–333.

[33] Bebbington, M. S. (2012). Models for temporal volcanic hazard. Statistics in Volcanology, 1:1–24.

[34] Ben-Zvi, T., Wilcock, W. S. D., Barclay, A. H., Zandomeneghi, D., Ibáñez, J. M., and Almendros, J. (2009). The P-wave velocity structure of Deception Island, Antarctica, from two-dimensional seismic tomography. Journal of Volcanology and Geothermal Research, 180(1):67–80.

[35] Benítez, M. C., Ramírez, J., Segura, J. C., Ibanez, J. M., Almendros, J., Garcíia-Yeguas, A., and Cortes, G. (2006). Continuous HMM-based seismic-event classification at Deception Island, Antarctica. IEEE Transactions on Geoscience and remote sensing, 45(1):138–146.

[36] Berger, J., Davis, P., and Ekström, G. (2004). Ambient Earth noise: A survey of the Global Seismographic Network. Journal of Geophysical Research: Solid Earth, 109(B11):B11307.

[37] Beroza, G. C. and Ide, S. (2011). Slow Earthquakes and Nonvolcanic Tremor. Annual Review of Earth and Planetary Sciences, 39(1):271–296.

[38] Berrocoso, M., Fernández-Ros, A., Prates, G., García, A., and Kraus, S. (2016). Geodetic implications on block formation and geodynamic domains in the South Shetland Islands, Antarctic Peninsula.

[39] Berrocoso, M., Fernández-Ros, A., Ramírez, M., Salamanca, J., Torrecillas, C., Pérez-Peña, A., Páez, R., García-García, A., Jiménez-Teja, Y.,

García-García, F., Soto, R., Gárate, J., Martín-Davila, J., Sánchez-Alzola, A., de Gil, A., Fernández-Prada, J., and Jigena, B. (2008). Geodetic Research on Deception Island and its Environment (South Shetland Islands, Bransfield Sea and Antarctic Peninsula) During Spanish Antarctic Campaigns (1987–2007). In Geodetic and Geophysical Observations in Antarctica, pages 97–124. Springer Berlin Heidelberg, Berlin, Heidelberg.

[40] Berrocoso, M., Prates, G., Fernández-Ros, A., Peci, L., de Gil, A., Rosado, B., Páez, R., and Jigena, B. (2018). Caldera unrest detected with seawater temperature anomalies at Deception Island, Antarctic Peninsula. Bulletin of Volcanology, 80(4).

[41] Berrocoso, M., Ramírez, M., and Fernández, A. (2006). Horizontal deformation models for deception island (south shetland islands, antarctica). In Geodetic Deformation Monitoring: From Geophysical to Engineering Roles, pages 217–221. Springer.

[42] Berrocoso, M., Torrecillas, C., Jigena, B., and Fernández-Ros, a. (2012). Determination of geomorphological and volumetric variations in the 1970 land volcanic craters area (Deception Island, Antarctica) from 1968 using historical and current maps, remote sensing and GNSS. Antarctic Science, 24(04):367–376.

[43] Beyreuther, M., Carniel, R., and Wassermann, J. (2008). Continuous Hidden Markov Models: Application to automatic earthquake detection and classification at Las Can??das caldera, Tenerife. Journal of Volcanology and Geothermal Research, 176(4):513–518.

[44] Birkenmajer, K. (1992). Volcanic succession at deception island, west antarctica: a revised lithostratigraphic standard. Studia Geologica Polonica, 101:27–82.

[45] Birkenmajer, K. (1994). Evolution of the Pacific margin of the northern Antarctic Peninsula: an overview. Geologische Rundschau, 83(2):309–321.

[46] Birkenmajer, K., Guterch, A., Grad, M., Janik, T., and Perchuc, E. (1990). Lithospheric transect Antarctic Peninsula — South Shetland Islands, West Antartica. Polish Polar Research, 11:241–258.

[47] Bisztricsany, E. (1958). A new method for the determination of the magnitude of earthquakes. Geofiz. Kozlemen, 7(2).

[48] Bisztricsany, E. (1959). On a new method of determining earthquake magnitudes. UGGI Serie A, Travaux Sci., Fasc, 20:9–15.

[49] Bó, M. S. and Copello, S. (2001). Distribution and abundance of breeding birds at deception island, south shetland islands, antarctica, february to april 2000. Marine Ornithology, 29:39–42.

[50] Bohnenstiehl, D., Tolstoy, M., Dziak, R., Fox, C., and Smith, D. (2002). Aftershock sequences in the mid-ocean ridge environment: An analysis using hydroacoustic data. Tectonophysics, 354(1-2):49–70.

[51] Bohnenstiehl, D. R., Dziak, R. P., Tolstoy, M., Fox, C. G., and Fowler, M. (2004). Temporal and spatial history of the 1999–2000 endeavour segment seismic series, juan de fuca ridge. Geochemistry, Geophysics, Geosystems, 5(9).

[52] Bonaccorso, A., Currenti, G., and Del Negro, C. (2013). Interaction of volcano-tectonic fault with magma storage, intrusion and flank instability: A thirty years study at Mt. Etna volcano. Journal of Volcanology and Geothermal Research, 251:127–136.

[53] Bonali, F. (2013). Earthquake-induced static stress change on magma pathway in promoting the 2012 copahue eruption. Tectonophysics, 608:127–137.

[54] Bonali, F., Tibaldi, A., Corazzato, C., Tormey, D., and Lara, L. (2013). Quantifying the effect of large earthquakes in promoting eruptions due to stress changes on magma pathway: the chile case. Tectonophysics, 583:54–67.

[55] Brodsky, E. E. and Kanamori, H. (2001). Elastohydrodynamic lubrication of faults. Journal of Geophysical Research: Solid Earth, 106(B8):16357–16374.

[56] Brodsky, E. E. and Prejean, S. G. (2005). New constraints on mechanisms of remotely triggered seismicity at long valley caldera. Journal of Geophysical Research: Solid Earth, 110(B4).

[57] Brodsky, E. E., Sturtevant, B., and Kanamori, H. (1998). Earthquakes, volcanoes, and rectified diffusion. Journal of Geophysical Research: Solid Earth, 103(B10):23827–23838.

[58] Brodsky, E. E. and van der Elst, N. J. (2014). The uses of dynamic earthquake triggering. Annual Review of Earth and Planetary Sciences, 42:317–339.

[59] Bromirski, P. D. (2001). Vibrations from the "Perfect Storm". Geochemistry, Geophysics, Geosystems, 2(7):1030.

[60] Bromirski, P. D. and Duennebier, F. K. (2002). The near-coastal microseism spectrum: Spatial and temporal wave climate relationships. Journal of Geophysical Research, 107(B8):2166.

[61] Burges, C. J. (1998). A Tutorial on Support Vector Machines for Pattern Recognition. Data Mining and Knowledge Discovery, 2(2):121–167.

[62] Canassy, P. D., Faillettaz, J., Walter, F., and Huss, M. (2012). Seismic activity and surface motion of a steep temperate glacier: a study on triftgletscher, switzerland. Journal of Glaciology, 58(209):513–528.

[63] Carmona, E., Almendros, J., Martín, R., Cortés, G., Alguacil, G., Moreno, J., Martín, J. B., Martos, A., Serrano, I., Stich, D., and Ibáñez, J. M. (2014). Advances in seismic monitoring at deception island volcano (Antarctica) since the international polar year. Annals of Geophysics, 57(3):SS0321.

[64] Carmona, E., Almendros, J., Peña, J. A., and Ibáñez, J. M. (2010). Characterization of fracture systems using precise array locations of earthquake multiplets: An example at Deception Island volcano, Antarctica. Journal of Geophysical Research: Solid Earth, 115(6):1–20.

[65] Carmona, E., Almendros, J., Serrano, I., Stich, D., and Ibáñez, J. M. (2012). Results of seismic monitoring surveys of Deception Island volcano, Antarctica, from 1999–2011. Antarctic Science, 24(05):485–499.

[66] Caselli, A., Badi, G., Bonatto, A., Bengoa, C., Agusto, M., Bidone, A., and Ibáñez, J. (2007a). Actividad sísmica y composición química fumarólica anómala debido a posible efecto sello en el sistema volcánico, isla decepción (antártida). Revista de la Asociación Geológica Argentina, 62(4):545–552.

[67] Caselli, A. T., Badi, G., Bonatto, A. L., Bengoa, C. L., Agusto, M. R., Bidone, A., and Ibáñez, J. (2007b). Actividad sísmica y composición química fumarólica anómala debido a posible efecto sello en el sistema volcánico, Isla Decepción (Antártida). Revista de la Asociacion Geologica Argentina, 62(4):545–552.

[68] Caselli, A. T., Dos Santos Afonso, M., and Agusto, M. R. (2004). Gases fumarólicos de la isla Decepción (Shetland del Sur, Antártida): Variaciones

químicas y depósitos vinculados a la crisis sísmica de 1999. Revista de la Asociacion Geologica Argentina, 59(2):291–302.

[69] Catalán, M., Galindo-Zaldivar, J., Davila, J. M., Martos, Y. M., Maldonado, A., Gambôa, L., and Schreider, A. A. (2013). Initial stages of oceanic spreading in the bransfield rift from magnetic and gravity data analysis. Tectonophysics, 585:102–112.

[70] Catalán, M., Martos, Y. M., Galindo-Zaldívar, J., and Funaki, M. (2014). Monitoring the evolution of Deception Island volcano from magnetic anomaly data (South Shetland Islands, Antarctica). Global and Planetary Change, 123:199–212.

[71] Chapp, E., Bohnenstiehl, D. R., and Tolstoy, M. (2005). Sound-channel observations of ice-generated tremor in the Indian Ocean. Geochemistry, Geophysics, Geosystems, 6((6)):Q06003.

[72] Chouet, B. (1992). A Seismic Model for the Source of Long-Period Events and Harmonic Tremor. In Volcanic seismology, pages 133–156. Springer, Berlin, Heidelberg.

[73] Chouet, B., De Luca, G., Milana, G., Dawson, P., Martini, M., and Scarpa, R. (1998). Shallow velocity structure of Stromboli volcano, Italy, derived from small-aperture array measurements of Strombolian tremor. Bulletin of the Seismological Society of America, 88(3):653–666.

[74] Chouet, B. A. (1996). Long-period volcano seismicity: its source and use in eruption forecasting. Nature, 380(6572):309–316.

[75] Chouet, B. A. (2003). Volcano Seismology. Pure and Applied Geophysics, 160(3):739–788.

[76] Christeson, G. L., Barker, D. H. N., Austin, J. A., and Dalziel, I. W. D. (2003). Deep crustal structure of Bransfield Strait: Initiation of a back arc basin by rift reactivation and propagation. Journal Of Geophysical Research-Solid Earth, 108(B10):2492.

[77] Cooper, A. R. P. R., Smellie, J. L., and Maylin, J. (1998). Evidence for shallowing and uplift from bathymetric records of Deception Island, Antarctica. Antarctic Science, 10(04).

[78] Correig, A. M., Urquizu, M., Vila, J., and Marti, J. (1997). Analysis of the Temporal Occurrence of Seismicity at Deception Island (Antarctica). A Nonlinear Approach. pure and applied geophysics, 149:553–574.

[79] Cortés, G., Carniel, R., Mendoza, M., and Lesage, P. (2019). Standardization of Noisy Volcanoseismic Waveforms as a Key Step toward Station-Independent, Robust Automatic Recognition. Seismological Research Letters, 90(2 A):581–590.

[80] Coulon, C., Hsieh, P., White, R., Lowenstern, J., and Ingebritsen, S. (2017a). Causes of distal volcano-tectonic seismicity inferred from hydrothermal modeling. Journal of Volcanology and Geothermal Research, 345:98–108.

[81] Coulon, C. A., Hsieh, P. A., White, R., Lowenstern, J. B., and Ingebritsen, S. E. (2017b). Causes of distal volcano-tectonic seismicity inferred from hydrothermal modeling. Journal of Volcanology and Geothermal Research, 345:98–108.

[82] Curilem, G., Vergara, J., Fuentealba, G., Acuña, G., and Chacón, M. (2009). Classification of seismic signals at Villarrica volcano (Chile) using neural networks and genetic algorithms. Journal of Volcanology and Geothermal Research, 180(1):1–8.

[83] Custodio, S. I. S., Fonseca, J. F. B. D., D'Oreye, N. F., Faria, B. V. E., and Bandomo, Z. (2003). Tidal modulation of seismic noise and volcanic tremor. Geophysical Research Letters, 30(15):1816.

[84] Dalziel, I. W. D. (1984). The Scotia Arc: An international geological laboratory. Episodes, 7(3):8–13.

[85] De Rosa, R., Mazzuoli, R., Omarini, R., Ventura, G., and Viramonte, J. (1995). A volcanological model for the historical eruptions at Deception Island (Bransfield Strait, Antarctica), volume 2. Terra Antarctica.

[86] Di Lieto, B., Saccorotti, G., Zuccarello, L., Rocca, M. L., and Scarpa, R. (2007). Continuous tracking of volcanic tremor at Mount Etna, Italy. Geophysical Journal International, 169(2):699–705.

[87] Díaz Gato, D. (2016). Análisis de terremotos volcánicos de la Isla Decepción (Antártida), con técnicas de array.

[88] Díaz-Moreno, A., Ibáñez, J. M., De Angelis, S., García-Yeguas, A., Prudencio, J., Morales, J., Tuvè, T., and García, L. (2015). Seismic hydraulic fracture migration originated by successive deep magma pulses: The 2011–2013 seismic series associated to the volcanic activity of El Hierro Island. Journal of Geophysical Research: Solid Earth, 120(11):7749–7770.

[89] Dibbern, J. S. (2010). Fur seals, whales and tourists: a commercial history of deception island, antarctica. Polar Record, 46(3):210–221.

[90] Dietrich, R., Rülke, A., Ihde, J., Lindner, K., Miller, H., Niemeier, W., Schenke, H.-W., and Seeber, G. (2004). Plate kinematics and deformation status of the Antarctic Peninsula based on GPS. Global and Planetary Change, 42(1-4):313–321.

[91] Dimitrova, L., Georgieva, G., Raykova, R., Dimitrov, D., Gurev, V., Solakov, D., Georgiev, I., Raykova, P., Protopopova, V., Aleksandrova, I., and Popova, M. (2017). Exploring seismicity of livingston island (antarctica) and surroundings using records of bulgarian broadband seismological station livv during the astral summer 2015-2016. Comptes Rendus of the Bulgarian Academy of Sciences, 70(12):1709–1718.

[92] Dowla, F. U. (1996). Neural networks in seismic discrimination. In Monitoring a Comprehensive Test Ban Treaty, pages 777–789. Springer Netherlands., Dordrecht.

[93] Dziak, R. P., Bohnenstiehl, D. R., Stafford, K. M., Matsumoto, H., Park, M., Lee, W. S., Fowler, M. J., Lau, T. K., Haxel, J. H., and Mellinger, D. K. (2015). Sources and levels of ambient ocean sound near the Antarctic Peninsula. PLoS ONE, 10(4):1–23.

[94] Dziak, R. P., Park, M., Lee, W. S., Matsumoto, H., Bohnenstiehl, D. R., and Haxel, J. H. (2010). Tectonomagmatic activity and ice dynamics in the Bransfield Strait back-arc basin, Antarctica. Journal of Geophysical Research, 115:1–14.

[95] Eibl, E. P., Lokmer, I., Bean, C. J., Akerlie, E., and Vogfjörd, K. S. (2015). Helicopter vs. volcanic tremor: Characteristic features of seismic harmonic tremor on volcanoes. Journal of Volcanology and Geothermal Research, 304:108–117.

[96] Endo, E. T. and Murray, T. (1991). Real-time Seismic Amplitude Measurement (RSAM): a volcano monitoring and prediction tool. Bulletin of Volcanology, 53(7):533–545.

[97] Faillettaz, J., Funk, M., and Sornette, D. (2011). Icequakes coupled with surface displacements for predicting glacier break-off. Journal of Glaciology, 57(203):453–460.

[98] Fernández-Ibáñez, F., Pérez-López, R., Martinez-Diaz, J. J., Paredes, C., Giner-Robles, J. L., Caselli, A. T., and Ibáñez, J. M. (2005). Costa

Recta beach, Deception Island, West Antarctica: a retreated scarp of a submarine fault? Antarctic Science, 17(03):418.

[99] Fernández-Ros, A., Berrocoso, M., Ramírez, M. E., Ramírez, M. E., Berrocoso, M., Fernández-Ros, A., González, M. J., Berrocoso, M., de Salamanca, J. M. E., Ramírez, M. E., and others (2007). Volcanic deformation models for Deception Island (South Shetland Islands, Antarctica). In Antarctica: a keystone in a changing world. Proceedings for the 10th International Symposium on Antarctic Earth Sciences.

[100] Ferrán, O. G. (1995). Volcanes de Chile. Instituto Geográfico Militar.

[101] Ferrazzini, V. and Aki, K. (1987). Slow waves trapped in a fluid-filled infinite crack: Implication for volcanic tremor. Journal of Geophysical Research, 92(10):9215–9223.

[102] Fetterer, F., Knowles, K., Meier, W., Savoie, M., and Windnagel, A. K. (2016). Sea ice index, version 2. Boulder, Colorado USA. NSIDC: National Snow and Ice Data Center.

[103] Fournier, N. and Chardot, L. (2012). Understanding volcano hydrothermal unrest from geodetic observations: Insights from numerical modeling and application to White Island volcano, New Zealand. Journal of Geophysical Research B: Solid Earth, 117(11):1–16.

[104] Freed, A. M. (2005). Earthquake triggering by static, dynamic, and postseismic stress transfer. Annu. Rev. Earth Planet. Sci., 33:335–367.

[105] Gabrieli, A., Wilson, L., and Lane, S. (2015). Volcano–tectonic interactions as triggers of volcanic eruptions. Proceedings of the Geologists' Association, 126(6):675–682.

[106] Galgaro, A., Boaga, J., and Rocca, M. (2014). Hvsr technique as tool for thermal-basin characterization: a field example in ne italy. Environmental Earth Sciences, 71(10):4433–4446.

[107] Galindo-Zaldívar, J., Gamboa, L., Maldonado, A., Nakao, S., and Bochu, Y. (2004). Tectonic development of the Bransfield Basin and its prolongation to the South Scotia Ridge, northern Antarctic Peninsula. Marine Geology, 206(1-4):267–282.

[108] Gamboa, L. A. P. and Maldonado, P. R. (1990). Geophysical investigations in the Bransfield Strait and in the Bellingshausen Sea, Antarctica. In Antarctica as an Exploration Frontier: Hydrocarbon Potential, Geology,

and Hazards, volume 31, chapter 9, pages 127–141. AAPG Special Volumes.

[109] Gao, S., Silver, P., Linde, A., and Sacks, I. (2000). Annual modulation of triggered seismicity following the 1992 Landers earthquake in California. Nature, 406(6795):500–504.

[110] García, A., Blanco, I., Torta, J. M., Astiz, M. M., Ibáñez, J. M., and Ortiz, R. (1997). A search for the volcanomagnetic signal at Deception volcano (South Shetland I., Antarctica).

[111] García-Jerez, A., Luzón, F., Navarro, M., and Pérez-Ruiz, J. A. (2006). Characterization of the sedimentary cover of the zafarraya basin, southern spain, by means of ambient noise. Bulletin of the Seismological Society of America, 96(3):957–967.

[112] García-Jerez, A., Piña-Flores, J., Sánchez-Sesma, F. J., Luzón, F., and Perton, M. (2016). A computer code for forward calculation and inversion of the H/V spectral ratio under the diffuse field assumption. Computers and Geosciences, 97:67–78.

[113] García-Jerez, A., Seivane, H., Navarro, M., Martínez-Segura, M., and Piña-Flores, J. (2019). Joint analysis of rayleigh-wave dispersion curves and diffuse-field hvsr for site characterization: the case of el ejido town (se spain). Soil Dynamics and Earthquake Engineering, 121:102–120.

[114] García-Yeguas, A., Almendros, J., Abella, R., and Ibáñez, J. M. (2011). Quantitative analysis of seismic wave propagation anomalies in azimuth and apparent slowness at Deception Island volcano (Antarctica) using seismic arrays. Geophysical Journal International, 184(2):801–815.

[115] Garcia-Yeguas, A., Almendros, J., Abella, R., and Ibáñez, J. M. (2011). Quantitative analysis of seismic wave propagation anomalies in azimuth and apparent slowness at Deception Island volcano (Antarctica) using seismic arrays. Geophysical Journal International, 184(2):801–815.

[116] Gerstoft, P. and Tanimoto, T. (2007). A year of microseisms in southern California. Geophysical Research Letters, 34(20):2–7.

[117] Geyer, A., Alvarez-Valero, A. M., Gisbert, G., Aulinas, M., Hernandez-Barreña, D., Lobo, A., and Marti, J. (2019). Deciphering the evolution of Deception Island's magmatic system. Scientific Reports, 9(1):373–.

[118] Geyer, A., Pedrazzi, D., Almendros, J., Berrocoso, M., Lopez-Martinez, J., Maestro, A., Carmona, E., Alvarez-Valero, A. M., and de Gill, A. (2021). Deception island. In Smellie, J. L., Panter, K. S., and Geyer, A., editors, Volcanism in Antarctica: 200 Million Years of Subduction, Rifting and Continental Break-up, volume 55 of Memoirs, chapter 7.1, pages M55–2018–56–. Geological Society of London.

[119] Giacco, F., Esposito, A. M., Scarpetta, S., Giudicepietro, F., Marinaro, M., and Apolloni, B. (2009). Support Vector Machines and MLP for automatic classification of seismic signals at Stromboli volcano. In Proceedings of the 2009 conference on Neural Nets WIRN09, volume 204, pages 116–123. IOS Press.

[120] Goldstein, P. and Chouet, B. (1994). Array measurements and modeling of sources of shallow volcanic tremor at Kilauea Volcano, Hawaii. Journal of Geophysical Research: Solid Earth, 99(B2):2637–2652.

[121] González-Casado, J. M., Giner Robles, J. L., and López-Martínez, J. (2000). Bransfield Basin, Antarctic Peninsula: Not a normal backarc basin. Geology, 28(11):1043–1046.

[122] Górski, M. (1997). Seismicity of the Hornsund region Spitzbergen. Pol. akad. nauk, Inst. geofizyki Warszawa.

[123] Górski, M. (2014a). Application of the Shear-Band Model to the Determination of Focal Parameters. In Seismic Events in Glaciers, pages 87–97. Springer Berlin Heidelberg.

[124] Górski, M. (2014b). Introduction: Scope of the Book. In Seismic Events in Glaciers, pages 1–4. Springer Berlin Heidelberg.

[125] Goyanes, G., Vieira, G., Caselli, A., Cardoso, M., Marmy, A., Santos, F., Bernardo, I., and Hauck, C. (2014). Local influences of geothermal anomalies on permafrost distribution in an active volcanic island (Deception Island, Antarctica). Geomorphology, 225:57–68.

[126] Gracia, E., Canals, M., Farràn, M. L., Jose Prieto, M., Sorribas, J., and Team, G. (1996). Morphostructure and evolution of the central and Eastern Bransfield Basins (NW Antarctic Peninsula). Marine Geophysical Researches, 18(Figure 1):429–448.

[127] Gràcia, E., Canals, M., Farràn, M. L., Prieto, M. J., Sorribas, J., and Team, G. (1996). Morphostructure and evolution of the central and eastern Bransfield basins (NW Antarctic Peninsula). Marine Geophysical Researches, 18(2-4):429–448.

[128] Grad, M., Guterch, a., and Sroda, P. (1992). Upper crustal structure of Deception Island area, Bransfield Strait, West Antarctica. Antarctic Science, 4(04):469–476.

[129] Grad, M., Shiobara, H., Janik, T., Guterch, A., and Shimamura, H. (1997). Crustal model of the Bransfield Rift, West Antarctica, from detailed OBS refraction experiments. Geophysical Journal International.

[130] Grob, M., Maggi, A., and Stutzmann, E. (2011). Observations of the seasonality of the Antarctic microseismic signal, and its association to sea ice variability. Geophysical Research Letters, 38(11):1–6.

[131] Guéguen, P., Cornou, C., Garambois, S., and Banton, J. (2007). On the limitation of the h/v spectral ratio using seismic noise as an exploration tool: application to the grenoble valley (france), a small apex ratio basin. Pure and applied geophysics, 164(1):115–134.

[132] Harmoko, U., Gernowo, R., and Yuliyanto, G. (2021). Determining the hydrothermal flow media using seismicity properties in kaliulo geothermal field, semarang, central java, indonesia. In Journal of Physics: Conference Series, volume 1943, page 012031. IOP Publishing.

[133] Harris, A. J. and Ripepe, M. (2007). Regional earthquake as a trigger for enhanced volcanic activity: evidence from modis thermal data. Geophysical Research Letters, 34(2).

[134] Hasselmann, K. (1963). A statistical analysis of the generation of microseisms. Reviews of Geophysics, 1(2):177–210.

[135] Havskov, J. and Ottemöller, L. (1999). SeisAn Earthquake Analysis Software. Seismological Research Letters, 70(5):532–534.

[136] Havskov, J. and Ottemöller, L. (2010). Routine data processing in Earthquake Seismology. Springer.

[137] Havskov, J., Pena, J. A., Ibánez, J. M., Ottemöller, L., and Martínez-Arévalo, C. (2003). Magnitude scales for very local earthquakes. Application for Deception Island Volcano (Antarctica). Journal of Volcanology and Geothermal Research, 128(1-3):115–133.

[138] Hawkes, D. D. (1961). The geology of the South Shetland Islands: II. The geology and petrology of Deception Island, volume 27. HMSO.

[139] Henriet, J., Meissner, R., Miller, H., and Team, T. G. (1992). Active margin processes along the antarctic peninsula. Tectonophysics, 201(3-4):229–253.

[140] Hill, D. and Prejean, S. (2015a). 4.11 - dynamic triggering. In Schubert, G., editor, Treatise on Geophysics (Second Edition), pages 273–304. Elsevier, Oxford, second edition edition.

[141] Hill, D. and Prejean, S. (2015b). Dynamic triggering. In Schubert, G., editor, Treatise on Geophysics (2nd Edition), volume 4 of Treatise on Geophysics, chapter 11, pages 273–304. Elsevier, Oxford, 2nd edition edition.

[142] Hill, D. P. (2008). Dynamic stresses, coulomb failure, and remote triggering. Bulletin of the Seismological Society of America, 98(1):66–92.

[143] Hill, D. P., Pollitz, F., and Newhall, C. (2002). Earthquake-volcano interactions. Physics Today, 55(11):41.

[144] Hill, D. P., Reasenberg, P., Michael, A., Arabaz, W., Beroza, G., Brumbaugh, D., Brune, J., Castro, R., Davis, S., dePolo, D., et al. (1993). Seismicity remotely triggered by the magnitude 7.3 landers, california, earthquake. Science, 260(5114):1617–1623.

[145] Hotovec, A. J., Prejean, S. G., Vidale, J. E., and Gomberg, J. (2013). Strongly gliding harmonic tremor during the 2009 eruption of Redoubt Volcano. Journal of Volcanology and Geothermal Research, 259:89–99.

[146] Ibáñez, J. and Carmona, E. (2000). Sismicidad volcánica. In Curso Internacional de Volcanología y Geofísica Volcanica., pages 269–282. Curso Internacional de Volcanología y Geofísica Volcanica, Serie Casa de los Volcanes.

[147] Ibanez, J., Del Pezzo, E., Almendros, J., La Rocca, M., Alguacil, G., Ortiz, R., and Garcia, A. (2000). Seismovolcanic signals at Deception Island volcano, Antarctica: wave field analysis and source modeling. J. Geophys. Res., 105(B6):13905–13931.

[148] Ibáñez, J. M., Almendros, J., Carmona, E., Martínez-Arévalo, C., and Abril, M. (2003a). The recent seismo-volcanic activity at Deception Island volcano. Deep-Sea Research Part II: Topical Studies in Oceanography, 50(10-11):1611–1629.

[149] Ibáñez, J. M., Benítez, C., Gutiérrez, L. A., Cortés, G., García-Yeguas, A., and Alguacil, G. (2009). The classification of seismo-volcanic signals using Hidden Markov Models as applied to the Stromboli and Etna volcanoes. Journal of Volcanology and Geothermal Research, 187:218–226.

[150] Ibáñez, J. M., Carmona, E., Almendros, J., Saccorotti, G., Del Pezzo, E., Abril, M., and Ortiz, R. (2003b). The 1998-1999 seismic series at Deception Island volcano, Antarctica. Journal of Volcanology and Geothermal Research, 128(1-3):65–88.

[151] Ibáñez, J. M., Díaz-Moreno, A., Prudencio, J., Zandomeneghi, D., Wilcock, W., Barclay, A., Almendros, J., Benítez, C., García-Yeguas, A., and Alguacil, G. (2017). Database of multi-parametric geophysical data from the tomo-dec experiment on deception island, antarctica. Scientific data, 4(1):1–18.

[152] Ibáñez, J. M., Morales, J., Alguacil, G., Almendros, J., Ortiz, R., and Del Pezzo, E. (1997). Intermediate-focus earthquakes under South Shetland Islands (Antarctica). Geophysical Research Letters, 24(5):531–534.

[153] ISC (2017). On-line bulletin. Retrieved from http://www.isc.ac.uk. Internatl. Seismol. Cent., Thatcham, UK.

[154] James, S., Knox, H., Abbott, R., Panning, M., and Screaton, E. (2019). Insights into permafrost and seasonal active-layer dynamics from ambient seismic noise monitoring. Journal of Geophysical Research: Earth Surface, 124(7):1798–1816.

[155] Janik, T. (1997). Seismic crustal structure of the Bransfield Strait , West Antarctica. Polish Polar Research, 18(3-4):171–225.

[156] Janik, T., Grad, M., Guterch, A., and Sroda, P. (2014). The deep seismic structure of the Earth's crust along the Antarctic Peninsula-A summary of the results from Polish geodynamical expeditions. Global and Planetary Change, 123:213–222.

[157] Jiménez-Morales, V., Almendros, J., and Carmona, E. (2017). Detection of long-duration tremors at Deception Island volcano, Antarctica. Journal of Volcanology and Geothermal Research, 347:234–249.

[158] Jiménez Morales, V., Almendros, J., and Carmona, E. (2021). New insights into the structure of Deception island from analysis of long time series of ambient noise New. not published, page In preparing.

[159] Jimenez-Morales, V., Almendros, J., Carmona, E., Melchor, I., Agui, F., and Abella, R. (2019). Deception Island: a challenging test database for automatic recognition systems. Workshop of the ESC Working Group on Volcano Seismology, Tenerife, Spain.

[160] Johnston, M., Prejean, S., and Hill, D. (2004). Triggered deformation and seismic activity under mammoth mountain in long valley caldera by the 3 november 2002 m w 7.9 denali fault earthquake. Bulletin of the Seismological Society of America, 94(6B):S360–S369.

[161] Jolly, A. D., Lokmer, I., Thun, J., Salichon, J., Fry, B., and Chardot, L. (2017). Insights into fluid transport mechanisms at White Island from analysis of coupled very long-period (VLP), long-period (LP) and high-frequency (HF) earthquakes. Journal of Volcanology and Geothermal Research, 343:75–94.

[162] Jónsdóttir, K., Roberts, R., Pohjola, V., Lund, B., Shomali, Z. H., Tryggvason, A., and Böovarsson, R. (2009). Glacial long period seismic events at katla volcano, iceland. Geophysical research letters, 36(11).

[163] Julian, B. (2000). Period doubling and other nonlinear phenomena in volcanic earthquakes and tremor. Journal of Volcanology and Geothermal Research, 101(1-2):19–26.

[164] Julian, B. R. (1994). Volcanic tremor: Nonlinear excitation by fluid flow. Journal of Geophysical Research, 99:11859–11877.

[165] Kang, S. Y., Kim, K.-H., Chiu, J.-M., and Liu, L. (2020). Microtremor HVSR analysis of heterogeneous shallow sedimentary structures at Pohang, South Korea. Journal of Geophysics and Engineering, 17(5):861–869.

[166] Kao, H. ., Shao-Ju, S. ., Dragert, H. ., and Rogers, G. (2005). A wide depth distribution of seismic tremors along the northern Cascadia margin. Nature, 436(7052):841–844.

[167] Kasahara, J. (2002). Tides, Earthquakes, and Volcanoes. Science (New York, N.Y.), 297(5580):348–349.

[168] Kedar, S. (1996). Kedar_s_1996.pdf. PhD thesis, Caltech Pasadena ;California.

[169] Kedar, S., Longuet-Higgins, M., Webb, F., Graham, N., Clayton, R., and Jones, C. (2008). The origin of deep ocean microseisms in the

North Atlantic Ocean. Proceedings of the Royal Society of London A: Mathematical, Physical and Engineering Sciences., 464(2091):777–793.

[170] Keller, R. A., Fisk, M. R., White, W. M., and Birkenmajer, K. (1992). Isotopic and trace element constraints on mixing and melting models of marginal basin volcanism, Bransfield Strait, Antarctica. Earth and Planetary Science Letters, 111(2-4):287–303.

[171] Kendal, L. (1831). Account of the island of deception, one of the new shetland isles. Journal of the Royal Geographical Society of London, 1:62–66.

[172] Kisslinger, C. and Jones, L. M. (1991). Properties of aftershock sequences in southern California. Journal of Geophysical Research: Solid Earth, 96(B7):11947–11958.

[173] Köhler, A., Maupin, V., Nuth, C., and Van Pelt, W. (2019). Characterization of seasonal glacial seismicity from a single-station on-ice record at holtedahlfonna, svalbard. Annals of Glaciology, 60(79):23–36.

[174] Köhler, A. and Weidle, C. (2019). Potentials and pitfalls of permafrost active layer monitoring using the hvsr method: a case study in svalbard. Earth Surface Dynamics, 7(1):1–16.

[175] Konno, K. and Ohmachi, T. (1998). Ground-motion characteristics estimated from spectral ratio between horizontal and vertical components of microtremor. Bulletin of the Seismological Society of America, 88(1):228–241.

[176] Konstantinou, K. I. and Schlindwein, V. (2003). Nature, wavefield properties and source mechanism of volcanic tremor: a review. Journal of Volcanology and Geothermal Research, 119(1-4):161–187.

[177] Koper, K. D., Seats, K., and Benz, H. (2010). On the Composition of Earth ' s Short-Period Seismic Noise Field. Bulletin of the Seismological Society of America, 100(2):606–617.

[178] Kumagai, H. and Chouet, B. A. (2000). Acoustic properties of a crack containing magmatic or hydrothermal fluids. Journal of Geophysical Research: Solid Earth, 105(B11):25493–25512.

[179] Kumagai, H., Palacios, P., Maeda, T., Castillo, D. B., and Nakano, M. (2009). Seismic tracking of lahars using tremor signals. Journal of Volcanology and Geothermal Research, 183(1-2):112–121.

[180] Kusakabe, M., Nagao, K., Ohba, T., Seo, J. H. U. N., and Park, S.-h. (2009). Noble gas and stable isotope geochemistry of thermal fluids from Deception Island , Antarctica. Antarctic Science, 21(3):255–267.

[181] La Rocca, M., Creager, K. C., Galluzzo, D., Malone, S., Vidale, J. E., Sweet, J. R., and Wech, A. G. (2009). Cascadia Tremor Located Near Plate Interface Constrained by S Minus P Wave Times. Science (New York, N.Y.), 323(5914):620–623.

[182] Lahr, J. C., Chouet, B. A., Stephens, C. D., Power, J. A., and Page, R. A. (1994). Earthquake classification, location, and error analysis in a volcanic environment: implications for the magmatic system of the 1989-1990 eruptions at redoubt volcano, Alaska. Journal of Volcanology and Geothermal Research, 62(1-4):137–151.

[183] Lawrence, L. A., Sloan, B. J., Barker, D. H., Ghidella, M., Von Herzen, R. P., Keller, R. A., Klinkhammer, G. P., and Chin, C. S. (1996). Distributed, Active Extension in Bransfield Basin, Antarctic Peninsula: Evidence from Multibeam Bathymetry. Geological Society of America, 6,nº11(SSN 1052-5173):1–6.

[184] Lee, W. H. K., Bennett, R. E., and Meagher, K. L. (1972). A method of estimating magnitude of local earthquakes from signal duration. US Department of the Interior, Geological Survey.

[185] Lee, Y. I., Lim, H. S., Yoon, H. I., and Tatur, A. (2007). Characteristics of tephra in Holocene lake sediments on King George Island, West Antarctica: implications for deglaciation and paleoenvironment. Quaternary Science Reviews, 26(25-28):3167–3178.

[186] Lees, J. M., Gordeev, E. I., and Ripepe, M. (2004). Explosions and periodic tremor at Karymsky volcano, Kamchatka, Russia. Geophysical Journal International, 158(3):1151–1167.

[187] Lemarchand, N. and Grasso, J.-R. (2007). Interactions between earthquakes and volcano activity. Geophysical Research Letters, 34(24).

[188] LeMasurier, W. E. and Thomson, J. W. (1990). Antarctic Research Series. Antarctic Research Series, 48:1–17.

[189] Lermo, J. and Chávez-García, F. J. (1994). Are microtremors useful in site response evaluation? Bulletin of the seismological society of America, 84(5):1350–1364.

[190] Lesage, P. (2009). Interactive Matlab software for the analysis of seismic volcanic signals. Computers & Geosciences, 35(10):2137–2144.

[191] Lesage, P., Mora, M. M., Alvarado, G. E., Pacheco, J., and Métaxian, J.-P. (2006). Complex behavior and source model of the tremor at Arenal volcano, Costa Rica. Journal of Volcanology and Geothermal Research, 157:49–59.

[192] Lienert, B. R. and Havskov, J. (1995). A computer program for locating earthquakes both locally and globally. Seismological Research Letters, 66(5):26–36.

[193] Linde, A. T. and Sacks, I. S. (1998). Triggering of volcanic eruptions. Nature, 395(6705):888.

[194] Longuet-Higgins, M. S. (1950). A Theory of the Origin of Microseisms. Philosophical Transactions of the Royal Society of London A: Mathematical, Physical and Engineering Sciences, 243(857).

[195] Lontsi, A. M., García-Jerez, A., Molina-Villegas, J. C., Sánchez-Sesma, F. J., Molkenthin, C., Ohrnberger, M., Krüger, F., Wang, R., and Fäh, D. (2019). A generalized theory for full microtremor horizontal-to-vertical [H/V(z, f)] spectral ratio interpretation in offshore and onshore environments. Geophysical Journal International, 218(2):1276–1297.

[196] Lopes, F. C., Caselli, A., Machado, A., and Barata, M. (2015). The development of the deception island volcano caldera under control of the bransfield basin sinistral strike-slip tectonic regime (nw antarctica). Geological Society, London, Special Publications, 401(1):173–184.

[197] Lunedei, E. and Albarello, D. (2010). Theoretical hvsr curves from full wavefield modelling of ambient vibrations in a weakly dissipative layered earth. Geophysical Journal International, 181(2):1093–1108.

[198] Lunedei, E. and Malischewsky, P. (2015). A review and some new issues on the theory of the h/v technique for ambient vibrations. Perspectives on European earthquake engineering and seismology, pages 371–394.

[199] Luzón, F., Almendros, J., and García-Jerez, A. (2011). Shallow structure of Deception Island, Antarctica, from correlations of ambient seismic noise on a set of dense seismic arrays. Geophysical Journal International, 185(2):737–748.

[200] MacAyeal, D. R., Okal, E. A., Aster, R. C., and Bassis, J. N. (2008). Seismic and hydroacoustic tremor generated by colliding icebergs. Journal of Geophysical Research, 113(F3):F03011.

[201] Maestro, A., Somoza, L., Rey, J., Martínez-Frías, J., and López-Martínez, J. (2007). Active tectonics, fault patterns, and stress field of Deception Island: A response to oblique convergence between the Pacific and Antarctic plates. Journal of South American Earth Sciences, 23(2-3):256–268.

[202] Maldonado, A., Dalziel, I. W. D., and Leat, P. T. (2015). The global relevance of the Scotia Arc: An introduction. Global and Planetary Change, 125:A1–A8.

[203] Manga, M. and Brodsky, E. (2006). Seismic triggering of eruptions in the far field: Volcanoes and geysers. Annu. Rev. Earth Planet. Sci, 34:263–291.

[204] Martí, J. and Baraldo, A. (1990). Pre-caldera pyroclastic deposits of deception island (south shetland islands). Antarctic Science, 2(4):345–352.

[205] Martí, J., Geyer, A., and Aguirre-Diaz, G. (2013). Origin and evolution of the Deception Island caldera (South Shetland Islands, Antarctica). Bulletin of Volcanology.

[206] Martí, J., Rey, J., and Baraldo, A. (1990). Origen y estructura de la isla decepcion (islas shetland del sur). Actas del Tercer Simposium de Estudios Antárticos. Comisión Interminister-ial de Ciencia y Tecnologia, Madrid, Spain, pages 187–194.

[207] Martí, J., Vila, J., and Rey, J. (1996). Deception island (bransfield strait, antarctica): an example of a volcanic caldera developed by extensional tectonics. Geological Society, London, Special Publications, 110(1):253–265.

[208] Martínez-Arévalo, C., Bianco, F., Ibáñez, J. M., Del Pezzo, E., Martínez-Arévalo, C., Bianco, F., Ibánez, J. M., and Del Pezzo, E. (2003). Shallow seismic attenuation and shear-wave splitting in the short period range of Deception Island volcano (Antarctica). Journal of Volcanology and Geothermal Research, 128(1-3):89–113.

[209] Martini, M. and Giannini, L. (1988). Deception island (south shetlands): an area of active volcanism in antarctica. Memorie della Societa Geologica Italiana, 43:117–122.

[210] Marzocchi, W. (2002). Remote seismic influence on large explosive eruptions. Journal of Geophysical Research: Solid Earth, 107(B1):EPM–6.

[211] Matoza, R. S. (2018). The Inaudible Rumble of Volcanic Eruptions. A Publication of the Acoustical Society of America, 14(1):17–25.

[212] Matsumoto, H., Dziak, R., Bohnenstiehl, D., Park, M., Haxel, J., Lee, W., and Lau, T. (2007). Ambient noise in the bransfield strait and the drake passage, antarctica: Temporal and spatial variations. In Abstract presented at Pacific Rim Underwater Acoustic Conference, Office of Naval Research and Acoustic Society of America, Vancouver BC, Canada.[Available at http://pruac. apl. washington. edu/abstracts/Matsumoto. pdf.].

[213] Matthews, A. J., Barclay, J., and Johnstone, J. E. (2009). The fast response of volcano-seismic activity to intense precipitation: Triggering of primary volcanic activity by rainfall at Soufrière Hills Volcano, Montserrat. Journal of Volcanology and Geothermal Research, 184(3-4):405–415.

[214] McCausland, W., Malone, S., and Johnson, D. (2005). Temporal and spatial occurrence of deep non-volcanic tremor: From Washington to northern California. Geophysical Research Letters, 32(24):1–4.

[215] Mcnamara, D. E., Buland, R. P., Boaz, R. I., Weertman, B., Ahern, T., and Mcnamara, D. E. (2004). Ambient Seismic Noise. www. mcnamara@ usgs. gov.

[216] McNutt, S. R. (1992). Volcanic Tremor. In Encyclopedia of Earth System Science, volume 4, pages 417–425. Elsevier, New York., w. a. nier edition.

[217] McNutt, S. R. (2005). Volcanic seismology. Annu. Rev. Earth Planet. Sci., 32:461–491.

[218] McNutt, S. R. and Roman, D. C. (2015). Volcanic seismicity. In Sigurdsson, H., editor, The Encyclopedia of Volcanoes, pages 1011–1034. Elsevier.

[219] Melguizo-Mejías, D. (2011). Análisis de sismicidad volcánica en Isla Decepción mediante técnicas de array (campaña 2009-2010). Master's thesis, Universidad de Granada (Spanish).

[220] Métaxian, J.-P. (2002). Locating sources of volcanic tremor and emergent events by seismic triangulation: Application to Arenal volcano, Costa Rica. Journal of Geophysical Research, 107:1–18.

[221] Métaxian, J.-P., Araujo, S., Mora, M., and Lesage, P. (2003). Seismicity related to the glacier of cotopaxi volcano, ecuador. Geophysical Research Letters, 30(9).

[222] Montanaro, C., Scheu, B., Gudmundsson, M. T., Vogfjörd, K., Reynolds, H. I., Dürig, T., Strehlow, K., Rott, S., Reuschlé, T., and Dingwell, D. B. (2016). Multidisciplinary constraints of hydrothermal explosions based on the 2013 Gengissig lake events, Kverkfjöll volcano, Iceland. Earth and Planetary Science Letters, 434:308–319.

[223] Moran, S. C., Newhall, C., and Roman, D. C. (2011). Failed magmatic eruptions: late-stage cessation of magma ascent. Bulletin of Volcanology, 73(2):115–122.

[224] Muller, C. (2005). Singing Icebergs. Science, 310(5752):1299–1299.

[225] Muñoz-Martín, A., Catalán, M., Martín-Dávila, J., Carbó, A., Munoz-Martin, A., Catalan, M., Martin-Davila, J., and Carbo, A. (2005). Upper crustal structure of Deception Island area (Bransfield Strait, Antarctica) from gravity and magnetic modelling. Antarctic Science, 17(2):213–224.

[226] Nakamura, Y. (2000). Clear identification of fundamental idea of Nakamura's technique and its applications. Proceedings of the 12th world conference on . . . , page Paper no. 2656.

[227] Nardone, L., Esposito, R., Galluzzo, D., Petrosino, S., Cusano, P., La Rocca, M., Di Vito, M. A., and Bianco, F. (2020). Array and spectral ratio techniques applied to seismic noise to investigate the campi flegrei (italy) subsoil structure at different scales. Advances in Geosciences, 52:75–85.

[228] Naveen, R., Lynch, H. J., Forrest, S., Mueller, T., and Polito, M. (2012). First direct, site-wide penguin survey at deception island, antarctica, suggests significant declines in breeding chinstrap penguins. Polar Biology, 35(12):1879–1888.

[229] Neuberg, J., Luckett, R., Baptie, B., and Olsen, K. (2000). Models of tremor and low-frequency earthquake swarms on Montserrat. Journal of Volcanology and Geothermal Research, 101(1-2):83–104.

[230] Nishimura, T. (2017). Triggering of volcanic eruptions by large earthquakes. Geophysical Research Letters, 44(15):7750–7756.

[231] Obara, K. (2002). Nonvolcanic Deep Tremor Associated with Subduction in Southwest Japan. Science (New York, N.Y.), 296(5573):1679–1681.

[232] Oliva-Urcia, B., Gil-Peña, I., Maestro, A., López-Martínez, J., Galindo-Zaldívar, J., Soto, R., Gil-Imaz, A., Rey, J., and Pueyo, O. (2016). Paleomagnetism from deception island (south shetlands archipelago, antarctica), new insights into the interpretation of the volcanic evolution using a geomagnetic model. International Journal of Earth Sciences, 105(5):1353–1370.

[233] Olsacher, J., Díaz, H., and Teruggi, M. E. (1956). Contribución a la geología de la Antártida Occidental. Instituto Antártico Argentino.

[234] Orheim, O. (1972a). A 200-year record of glacier mass balance at Deception Island, southwest Atlantic Ocean, and its bearing on models of global climatic change. Technical Report 42, The Ohio State University.

[235] Orheim, O. (1972b). Volcanic activity on Deception Island, South Shetland Islands. Ohio State University, Institute of Polar Studies, Oslo.

[236] Ortiz, R., García, A., Aparicio, A., Blanco, I., Felpeto, A., Del Rey, R., Villegas, M. T., Ibáñez, J. M., Morales, J., Del Pezzo, E., and Others (1997). Monitoring of the volcanic activity of Deception Island, South Shetland Islands, Antarctica (1986–1995).

[237] Ortiz, R., Vila, J., García, A., Camacho, A. G., Diez, J. L., Aparicio, A., Soto, R., Viramonte, J. G., Risso, C., Menegatti, N., and others (1992). Geophysical features of Deception Island. Recent Progress in Antarctic Earth Science, pages 143–152.

[238] Ottemöller, L., Voss, P., and Havskov, J. (2011). Seisan earthquake analysis software for Windows, Solaris, Linux and MacOsX. Dept. Earth Sci., Univ. Bergen, Bergen, Norway, 335.

[239] Overduin, P. P., Haberland, C., Ryberg, T., Kneier, F., Jacobi, T., Grigoriev, M. N., and Ohrnberger, M. (2015). Submarine permafrost depth from ambient seismic noise. Geophysical Research Letters, 42(18):7581–7588.

[240] Padrón, E., Hernández, P. A., Carmona, E., Pérez, N. M., Melián, G., Sumino, H., Almendros, J., Kusakabe, M., Wakita, H., and Padilla, G. D. (2015). Geochemical evidence of different sources of long-period seismic

events at Deception volcano, South Shetland Islands, Antarctica. Antarctic Science, 27(6):557–565.

[241] Pallàs, R., Smellie, J. L., Casas, J. M., and Calvet, J. (2001). Using tephrochronology to date temperate ice: correlation between ice tephras on Livingston Island and eruptive units on Deception Island volcano (South Shetland Islands, Antarctica). The Holocene, 11(2):149–160.

[242] Parera-Portell, J. A., Mancilla, F. d. L., Morales, J., Almendros, J., and Jimenez-Morales, V. (2021). Structure of the crust and upper mantle beneath the bransfield strait (antarctica) using p receiver functions. Tectonophysics, 802:228744–.

[243] Park, Y., Kim, K. H., Lee, J., Yoo, H. J., and Plasencia L., M. P. (2012). P-wave velocity structure beneath the northern Antarctic Peninsula: Evidence of a steeply subducting slab and a deep-rooted low-velocity anomaly beneath the central Bransfield Basin. Geophysical Journal International, 191(3):932–938.

[244] Parolai, S., Picozzi, M., Richwalski, S., and Milkereit, C. (2005). Joint inversion of phase velocity dispersion and h/v ratio curves from seismic noise recordings using a genetic algorithm, considering higher modes. Geophysical research letters, 32(1).

[245] Pastén, C., Sáez, M., Ruiz, S., Leyton, F., Salomón, J., and Poli, P. (2016). Deep characterization of the santiago basin using hvsr and cross-correlation of ambient seismic noise. Engineering Geology, 201:57–66.

[246] Patrick, M. R., Orr, T., Sutton, A. J., Lev, E., Thelen, W., and Fee, D. (2016). Shallowly driven fluctuations in lava lake outgassing (gas pistoning), Kilauea Volcano. Earth and Planetary Science Letters, 433:326–338.

[247] Pedrazzi, D., Aguirre-Díaz, G., Bartolini, S., Martí, J., and Geyer, A. (2014). The 1970 eruption on Deception Island (Antarctica): Eruptive dynamics and implications for volcanic hazards. Journal of the Geological Society, 171(6):765–778.

[248] Pedrera, A., Ruiz-Constán, A., Heredia, N., Galindo-Zaldívar, J., Bohoyo, F., Marín-Lechado, C., Ruano, P., and Somoza, L. (2012). The fracture system and the melt emplacement beneath the Deception Island active volcano, South Shetland Islands, Antarctica. Antarctic Science, 24(02):173–182.

[249] Pelayo, A. M. and Wiens, D. A. (1989). Seismotectonics of the Scotia Sea region. Journal of Geophysical Research, 94:7293–7320.

[250] Peng, Z., Vidale, J. E., Wech, A. G., Nadeau, R. M., and Creager, K. C. (2009). Remote triggering of tremor along the San Andreas Fault in central California. Journal of Geophysical Research, 114:B00A06.

[251] Petrosino, S., Damiano, N., Cusano, P., Di Vito, M. A., de Vita, S., and Del Pezzo, E. (2012). Subsurface structure of the solfatara volcano (campi flegrei caldera, italy) as deduced from joint seismic-noise array, volcanological and morphostructural analysis. Geochemistry, Geophysics, Geosystems, 13(7).

[252] Picotti, S., Francese, R., Giorgi, M., Pettenati, F., and Carcione, J. M. (2017). Estimation of glacier thicknesses and basal properties using the horizontal-to-vertical component spectral ratio (hvsr) technique from passive seismic data. Journal of Glaciology, 63(238):229–248.

[253] Picozzi, M., Parolai, S., and Richwalski, S. (2005). Joint inversion of h/v ratios and dispersion curves from seismic noise: Estimating the s-wave velocity of bedrock. Geophysical Research Letters, 32(11).

[254] Piña-Flores, J., Perton, M., García-Jerez, A., Luzón, F., Molina Villegas, J. C., and Sánchez-Sesma, F. J. (2016). The inversion of spectral ratio H/V in a layered system using the Diffuse Field Assumption (DFA). Geophysical Journal International, 1(1):1–38.

[255] Podolskiy, E. A. and Walter, F. (2016). Cryoseismology. Reviews of Geophysics, 54(4):708–758.

[256] Power, J. A., Lahr, J. C., Page, R. A., Chouet, B. A., Stephens, C. D., Harlow, D. H., Murray, T. L., and Davies, J. N. (1994). Seismic evolution of the 1989–1990 eruption sequence of Redoubt Volcano, Alaska. Journal of Volcanology and Geothermal Research, 62(1-4):69–94.

[257] Power, J. A., Murray, T. L., Marso, J. N., and Laguerta, E. P. (1996). Preliminary observations of seismicity at Mount Pinatubo by use of the seismic spectral amplitude measurement (SSAM) system, May 13–June 18, 1991. In Newhall, C. G. and Punongbayan, R. S., editors, Fire and Mud: Eruptions and Lahars of Mount Pinatubo, Philippines, pages 269–283. University of Washington Press, Seattle.

[258] Prates, G., Berrocoso, M., Fernández-Ros, A., and García, A. (2013). Enhancement of sub-daily positioning solutions for surface deformation

monitoring at Deception volcano (South Shetland Islands, Antarctica). Bulletin of Volcanology, 75(2):1–10.

[259] Prejean, S., Hill, D., Brodsky, E., Hough, S., Johnston, M., Malone, S., Oppenheimer, D., Pitt, A., and Richards-Dinger, K. (2004). Remotely triggered seismicity on the united states west coast following the m w 7.9 denali fault earthquake. Bulletin of the Seismological Society of America, 94(6B):S348–S359.

[260] Privitera, E., Villari, L., and Gambino, S. (1992). An approach to the seismicity of Mt. Melbourne Volcano (Northern Victoria Land, Antarctic-Privitera, E., Villari, L., Gambino, S., 1992. An approach to the seismicity of Mt. Melbourne Volcano (Northern Victoria Land, Antarctica). Recent Prog. Antarct. Eart. Recent Progress in Antarctic Earth Sciences, edited by Y. Yoshida, K. Kaminuma, and K. Shiraishi, page 499505.

[261] Prudencio, J., De Siena, L., Ibáñez, J. M., Del Pezzo, E., García-Yeguas, A., and Díaz-Moreno, A. (2015). The 3D Attenuation Structure of Deception Island (Antarctica). Surveys in Geophysics, 36(3):371–390.

[262] Prudencio, J., Ibáñez, J. M., García-Yeguas, A., Del Pezzo, E., and Posadas, A. M. (2013). Spatial distribution of intrinsic and scattering seismic attenuation in active volcanic islands-II: Deception Island images. Geophysical Journal International, 195(3):1957–1969.

[263] Qamar, A. (1988). Calving icebergs: A source of low-frequency seismic signals from columbia glacier, alaska. Journal of Geophysical Research: Solid Earth, 93(B6):6615–6623.

[264] Ramos, M., Vieira, G., de Pablo, M. A., Molina, A., Abramov, A., and Goyanes, G. (2016). Recent shallowing of the thaw depth at Crater Lake, Deception Island, Antarctica (2006–2014). Catena, 149:519–528.

[265] Rey, J., Maestro, A., Somoza, L., Smellie, J. L., Lopez, M. J., Headland, R. K., Hernandez, C. F., Millar, I. L., Serrano, E., Thomson, J. W., Thomson, M. R. A., and British Antarctic Survey Cambridge compiler (2002). Submarine morphology and seismic stratigraphy of Port Foster In: Geology and geomorphology of Deception Island. BAS Geomap Series.

[266] Rey, J., Somoza, L., and Martínez-Frías, J. (1995). Tectonic, volcanic, and hydrothermal event sequence on Deception Island (Antarctica). Geo-Marine Letters, 15:1–8.

[267] Richardson, J. P., Waite, G. P., and Palma, J. L. (2014). Varying seismic-acoustic properties of the fluctuating lava lake at Villarrica volcano, Chile. Journal of Geophysical Research: Solid Earth, 119(7):5560–5573.

[268] Ripepe, M., De Angelis, S., Lacanna, G., and Voight, B. (2010). Observation of infrasonic and gravity waves at Soufrière Hills Volcano, Montserrat. Geophysical Research Letters, 37(8).

[269] Ripepe, M. and Gordeev, E. (1999). Gas bubble dynamics model for shallow volcanic tremor at Stromboli. Journal of Geophysical Research: Solid Earth, 104(B5):10639–10654.

[270] Ripepe, M., Poggi, P., Braun, T., and Gordeev, E. (1996). Infrasonic waves and volcanic tremor at Stromboli. Geophysical Research Letters, 23(2):181–184.

[271] Roberts, N. S., Bell, A. F., and Main, I. G. (2015). Are volcanic seismic b-values high, and if so when? Journal of Volcanology and Geothermal Research, 308:127–141.

[272] Robertson Maurice, S., Wiens, D., Shore, P., Vera, E., and Dorman, L. (2003). Seismicity and tectonics of the South Shetland Islands and Bransfield Strait from a regional broadband seismograph deployment. Journal of Geophysical Research, 108(B10):1–12.

[273] Roobol, M. (1973). Historic volcanic activity at deception island. British Antarctic Survey Bulletin, 32:23–30.

[274] Rosado, B., Fernández-Ros, A., Berrocoso, M., Prates, G., Gárate, J., de Gil, A., and Geyer, A. (2019). Volcano-tectonic dynamics of Deception Island (Antarctica): 27 years of GPS observations (1991-2018). Journal of Volcanology and Geothermal Research, 381:57–82.

[275] Roux, P.-F., Walter, F., Riesen, P., Sugiyama, S., and Funk, M. (2010). Observation of surface seismic activity changes of an alpine glacier during a glacier-dammed lake outburst. Journal of Geophysical Research: Earth Surface, 115(F3).

[276] Rubinstein, J. L., Shelly, D. R., and Ellsworth, W. L. (2009). Non-volcanic Tremor: A Window into the Roots of Fault Zones. In New Frontiers in Integrated Solid Earth Sciences, pages 287–314. Springer Netherlands, Dordrecht.

[277] Rundquist, D. V. and Sobolev, P. O. (2002). Seismicity of mid-oceanic ridges and its geodynamic implications: a review. Earth-Science Reviews, 58(1-2):143–161.

[278] Saccorotti, G., Almendros, J., Carmona, E., Ibáñez, J. M., and Del Pezzo, E. (2001). Slowness anomalies from two dense seismic arrays at Deception Island Volcano, Antarctica. Bulletin of the Seismological Society of America, 91(3):561–571.

[279] Saccorotti, G., Ventura, G., and Vilardo, G. (2002). Seismic swarms related to diffusive processes: The case of somma-vesuvius volcano, italy. Geophysics, 67(1):199–203.

[280] Saccorotti, G., Zuccarello, L., Del Pezzo, E., Ibáñez, J., and Gresta, S. (2004). Quantitative analysis of the tremor wavefield at Etna Volcano, Italy. Journal of Volcanology and Geothermal Research, 136(3):223–245.

[281] Sánchez-Sesma, F. J. and Campillo, M. (2006). Retrieval of the green's function from cross correlation: the canonical elastic problem. Bulletin of the Seismological Society of America, 96(3):1182–1191.

[282] Sánchez-Sesma, F. J., Rodríguez, M., Iturrarán-Viveros, U., Luzón, F., Campillo, M., Margerin, L., García-Jerez, A., Suarez, M., Santoyo, M. A., and Rodríguez-Castellanos, A. (2011). A theory for microtremor H/V spectral ratio: Application for a layered medium. Geophysical Journal International, 186(1):221–225.

[283] Schlindwein, V., Wassermann, J., and Scherbaum, F. (1995). Spectral analysis of harmonic tremor signals at Mt. Semeru Volcano, Indonesia. Geophysical Research Letters, 22(13):1685–1688.

[284] Shapiro, S. A. (2003). Elastic piezosensitivity of porous and fractured rocks. Geophysics, 68(2):482–486.

[285] Shearer, P. M. (2019). Introduction to seismology. Cambridge university press.

[286] Shelly, D. R., Beroza, G. C., and Ide, S. (2007). Non-volcanic tremor and low-frequency earthquake swarms. Nature, 446(7133):305–307.

[287] Shultz, C. H. (1972). Eruption at Deception Island, Antarctica, August 1970. Geological Society of America Bulletin, 83(9):2837–2842.

[288] Smellie, J., López-Martínez, J., Headland, R., Hernández-Cifuentes, F., Maestro, A., Millar, I., Rey, J., Serrano, E., Somoza, L., and Thomson, J. (2002). Geology and geomorphology of Deception Island. British Antarctic Survey.

[289] Smellie, J. L. (1988). Recent observations on the volcanic history of Deception Island, South Shetland Islands.

[290] Smellie, J. L. (2002). The 1969 subglacial eruption on Deception Island (Antarctica): events and processes during an eruption beneath a thin glacier and implications for volcanic hazards. Geological Society, London, Special Publications, 202(1):59–79.

[291] Smellie, J. L., Baker, P., and Thomson, J. (1990). D. Graham Land and South Shetland Islands. Volcanoes of the Antarctic plate and Southern oceans, pages 302–359.

[292] Smith, R. L. (2005). The thermophilic bryoflora of deception island: unique plant communities as a criterion for designating an antarctic specially protected area. Antarctic Science, 17(1):17–27.

[293] Spica, Z., Caudron, C., Perton, M., Lecocq, T., Camelbeeck, T., Legrand, D., Piña-Flores, J., Iglesias, A., and Syahbana, D. K. (2015). Velocity models and site effects at kawah ijen volcano and ijen caldera (indonesia) determined from ambient noise cross-correlations and directional energy density spectral ratios. Journal of Volcanology and Geothermal Research, 302:173–189.

[294] Spica, Z. J., Perton, M., Nakata, N., Liu, X., and Beroza, G. C. (2018). Site characterization at groningen gas field area through joint surface-borehole h/v analysis. Geophysical Journal International, 212(1):412–421.

[295] Sprenke, K. F., Adema, G. W., and & Miller, M. M. (1997). Brittle ice deformation on the Juneau Icefield, an analog for icequake activity on other planetary bodies. American Geophysical Union, 78(46, Suppl.):409.

[296] Steacy, S., Gomberg, J., and Cocco, M. (2005). Introduction to special section: Stress transfer, earthquake triggering, and time-dependent seismic hazard. Journal of Geophysical Research: Solid Earth, 110(B5).

[297] Stephens, C. D., Chouet, B. A., Page, R. A., Lahr, J. C., and Power, J. A. (1994). Seismological aspects of the 1989–1990 eruptions at Redoubt Volcano, Alaska: the SSAM perspective. Journal of Volcanology and Geothermal Research, 62(1):153–182.

[298] Stich, D., Almendros, J., Jiménez, V., Mancilla, F. D. L., and Carmona, E. (2011). Ocean noise triggering of rhythmic long period events at Deception Island volcano. Geophysical Research Letters, 38(22):L22307.

[299] Stutzmann, E., Schimmel, M., Patau, G., and Maggi, A. (2009). Global climate imprint on seismic noise. Geochemistry, Geophysics, Geosystems., 10(11):Q11004.

[300] Sudjono, D. S., Harmoko, U., and Yuliyanto, G. (2019). Delineation of geothermal manifestation in sangubanyu area based on microtremor hvsr method. In E3S Web of Conferences, volume 125, page 14012. EDP Sciences.

[301] Sylvette, B.-C., Cécile, C., Pierre-Yves, B., Fabrice, C., Peter, M., Jozef, K., and Fäh, D. (2006). H/v ratio: a tool for site effects evaluation. results from 1-d noise simulations. Geophysical Journal International, 167(2):827–837.

[302] Talandier, J., Hyvernaud, O., Okal, E. A., and Piserchia, P. F. (2002). Long-range detection of hydroacoustic signals from large icebergs in the Ross Sea, Antarctica. Earth and Planetary Science Letters, 203(1):519–534.

[303] Tanimoto, T. (2007). Excitation of microseisms. Geophysical Research Letters, 34(5):L05308.

[304] Taron, J., Elsworth, D., Thompson, G., and Voight, B. (2007). Mechanisms for rainfall-concurrent lava dome collapses at Soufrière Hills Volcano, 2000-2002. Journal of Volcanology and Geothermal Research, 160(1-2):195–209.

[305] Tejedo, P., Gutiérrez, B., Pertierra, L. R., and Benayas, J. (2015). Analysis of published scientific research from deception island, south shetland islands. Antarctic Science, 27(2):134–149.

[306] Torrese, P., Rossi, A. P., Unnithan, V., Pozzobon, R., Borrmann, D., Lauterbach, H., Luzzi, E., and Sauro, F. (2020a). Hvsr passive seismic stratigraphy for the investigation of planetary volcanic analogues. Icarus, 351:113970.

[307] Torrese, P., Rossi, A. P., Unnithan, V., Pozzobon, R., Borrmann, D., Lauterbach, H., Luzzi, E., and Sauro, F. (2020b). Hvsr passive seismic stratigraphy for the investigation of planetary volcanic analogues. Icarus, 351:113970.

[308] Unglert, K. and Jellinek, A. M. (2017). Feasibility study of spectral pattern recognition reveals distinct classes of volcanic tremor. Journal of Volcanology and Geothermal Research, 336:219–244.

[309] Utheim, T., Havskov, J., Ozyazicioglu, M., Rodriguez, J., and Talavera, E. (2014). Rtquake, a real-time earthquake detection system integrated with seisan. Seismological Research Letters, 85(3):735–742.

[310] Utsu, T., Ogata, Y., and others (1995). The centenary of the Omori formula for a decay law of aftershock activity. Journal of Physics of the Earth, 43(1):1–33.

[311] Valencio, D. A., Mendia, J., and Vilas, J. F. (1979). Palaeomagnetism and K sbnd Ar age of Mesozoic and Cenozoic igneous rocks from Antarctica. Earth and Planetary Science Letters, 45:61–68.

[312] Van Der Elst, N. J. and Brodsky, E. E. (2010). Connecting near-field and far-field earthquake triggering to dynamic strain. Journal of Geophysical Research: Solid Earth, 115(B7).

[313] Vandemeulebrouck, J., Roux, P., and Cros, E. (2013). The plumbing of Old Faithful Geyser revealed by hydrothermal tremor. Geophysical Research Letters, 40(10):1989–1993.

[314] Vassallo, M., Satriano, C., and Lomax, A. (2012). Automatic picker developments and optimization: A strategy for improving the performances of automatic phase pickers. Seismological Research Letters, 83(3):541–554.

[315] Vila, J., Marti, J., Ortiz, R., Garcia, A., and Correig, A. M. (1992a). Volcanic tremors at Deception Island (South Shetland Islands, Antarctica). Journal of Volcanology and Geothermal Research, 53(1):89–102.

[316] Vila, J., Ortiz, R., Correig, A. M., and Gracia, A. (1992b). Seismic activity on Deception Island. Journal of Volcanology and Geothermal Research, 53(1-4):89–102.

[317] Vuan, A., Robertson Maurice, S. D., Wiens, D. A., and Panza, G. F. (2005). Crustal and upper mantle S-wave velocity structure beneath the Bransfield Strait (West Antarctica) from regional surface wave tomography. Tectonophysics, 397(3-4):241–259.

[318] Walker, R. T., Parizek, B. R., Alley, R. B., Anandakrishnan, S., Riverman, K. L., and Christianson, K. (2013). Ice-shelf tidal flexure and subglacial pressure variations. Earth and Planetary Science Letters., 361:422–428.

[319] Walter, F., Deichmann, N., and Funk, M. (2008). Basal icequakes during changing subglacial water pressures beneath gornergletscher, switzerland. Journal of Glaciology, 54(186):511–521.

[320] Walter, T. R., Wang, R., Acocella, V., Neri, M., Grosser, H., and Zschau, J. (2009). Simultaneous magma and gas eruptions at three volcanoes in southern italy: An earthquake trigger? Geology, 37(3):251–254.

[321] Walter, T. R., Wang, R., Zimmer, M., Grosser, H., Lühr, B., and Ratdomopurbo, A. (2007). Volcanic activity influenced by tectonic earthquakes: Static and dynamic stress triggering at mt. merapi. Geophysical Research Letters, 34(5).

[322] Webb, S. C. (1998). Broadband seismology and noise under the ocean. Reviews of Geophysics, 36(1):105–142.

[323] Weber, B., Becker, J., Hanka, W., Heinloo, A., Hoffmann, M., Kraft, T., Pahlke, D., Reinhardt, J., Saul, J., and Thoms, H. (2007). SeisComP3—Automatic and interactive real time data processing. In Geophysical Research Abstracts, volume 9, page 219.

[324] White, R. and Mccausland, W. (2016). Volcano-tectonic earthquakes : A new tool for estimating intrusive volumes and forecasting eruptions. Journal of Volcanology and Geothermal Research, 309:139–155.

[325] White, R. and McCausland, W. (2016). Volcano-tectonic earthquakes: A new tool for estimating intrusive volumes and forecasting eruptions. Journal of Volcanology and Geothermal Research, 309:139–155.

[326] White, R. A. and McCausland, W. A. (2019). A process-based model of pre-eruption seismicity patterns and its use for eruption forecasting at dormant stratovolcanoes. Journal of Volcanology and Geothermal Research, 382:267–297.

[327] Wilkes, C. (1845). Narrative of the United States exploring expedition during the years 1838, 1839, 1840, 1841, and 1842. Lea and Blanchard, Philadelphia.

[328] Winberry, J. P., Anandakrishnan, S., and Alley, R. B. (2009). Seismic observations of transient subglacial water-flow beneath MacAyeal Ice Stream, West Antarctica. Geophysical Research Letters, 36(11):L11502.

[329] Yan, P., Li, Z., Li, F., Yang, Y., Hao, W., and Bao, F. (2018). Antarctic ice sheet thickness estimation using the horizontal-to-vertical spectral

ratio method with single-station seismic ambient noise. The Cryosphere, 12(2):795–810.

[330] Zandomeneghi, D., Barclay, A., Almendros, J., Godoy, J. M. I., Wilcock, W. S. D., and Ben-Zvi, T. (2009). Crustal structure of Deception Island volcano from P wave seismic tomography: Tectonic and volcanic implications. Journal of Geophysical Research: Solid Earth, 114(6):1–16.

[331] Zobin, V. M. (2012). Introduction to Volcanic Seismology. Elsevier.

[332] Özalaybey, S., Zor, E., Ergintav, S., and Tapırdamaz, M. C. (2011). Investigation of 3-D basin structures in the İzmit Bay area (Turkey) by single-station microtremor and gravimetric methods. Geophysical Journal International, 186(2):883–894.

Agradecimientos

¡¡¡¡¡Bueno por fin termino!!!!! aún no me lo creo, pero familia sí esto es el final del periplo llamado tesis doctoral.

Me gustaría comenzar a agradecer a todas a las personas e instituciones que han permitido el desarrollo de este trabajo.

Gracias al Ministerio de Ciencia de España que concedió el proyecto CORSHET con el que se subvencionó la compra e instalación de las estaciones permanentes CCV, LVN y DCP en las que baso mi trabajo.

Gracias al personal técnico laboral y científico del Instituto Andaluz de Geofísica (IAG) que instalaron las estaciones permanentes y por el mantenimiento durante 8 años que permitió su correcto funcionamiento. Además, agradezco a las instituciones que subvencionaron las expediciones a la Antártida para hacerlo posible.

Gracias al Comité Polar, a la Unidad de Tecnología Marina, al Ejército de Tierra, la Armada de España y al Consejo Superior de Investigaciones Científicas, por brindar un apoyo logístico crucial para las actividades de investigación.

El desarrollo de esta tesis se ha subvencionado gracias a las distintas empresas que me han contratado a lo largo de los años y han sido flexibles para poder compatibilizar el realizar este trabajo de investigación con el trabajo de camarera, artesana, cocinera, limpiadora e investigadora. Estas empresas son: Bar Salao, Bar Rinconcillo, Tartas Mara, Consentidos Naturales, Javivi ya es hora de entregar y al Instituto Andaluz de Geofísica.

Gracias a la música y los programas de radio que me ha acompañado durante estos años que sin ella no podría ser posible este trabajo. Gracias a Cuando los elefantes sueñan con la música y Saltamontes que me acompañaron en la identificación y clasificación de más de 140000 señales. Gracias a Turbo tres, Alma de león y Sonideros que me inspiraron para escribir este trabajo.

Seguidamente le agradezco a la familia y amigos que me han apoyado, aguantado y animado durante este trabajo, que según a quien preguntes es más la historia interminable o misión imposible que una tesis doctoral.

Gracias a mi director de tesis Javier Almendros por darme la oportunidad de cumplir dos de mis sueños, investigar un volcán e ir a la Antártida. Gracias Javier por tu paciencia, tu tiempo y por compartir tus conocimientos conmigo. Gracias por darme todas las facilidades posibles para poder realizar este trabajo, como ordenadores, discos duros, libros, etc. Por contratarme e incluso dejar que ocupe tu despacho de Ciencias. Gracias a mi tutor de tesis José Morales por prestar su tiempo y su criterio en la conducción de este trabajo.

Gracias a todos los componentes de IAG desde el personal técnico al científico por aceptarme con los brazos abiertos y mucho cariño. Gracias por ayudarme, por contestar a todas mis preguntas, apoyarme y animarme. Gracias por los ratitos del cafelito, la comida y el cigarrito. Muchas gracias en especial a Teresa, Oier, Luis, Daniel, Antonio, Javier, Paco, Benito, Rafa, Antonio, José María, Pepe, Feli, Alex y por supuesto al Enrique por enseñarme desde el Seisan a trabajar en la Antártida, por ver mis señales raras sin poner caras demasiado raras y sobre todo por estar ahí y aguantarme con mis cosas.

Gracias a la familia Antártica por acompañarme en una de las experiencias más mágicas de mi vida. Gracias por los ratos de alegría y de maravilla. Muchas gracias a todos en especial a mis compañeros de fatigas de la universidad de Cádiz Amós, Mirenchu y Belén gracias por salvarme mi cordura más de una vez, por el cariño y vuestra sabiduría. Gracias a Rafa, Enrique y Loreno por vuestras clases magistrales de electrónica, Matlab y sismicidad además de por ser vosotros. Gracias a Carlos por la alegría y los bailes en Ushuaia y Punta Arenas. Gracias a Feli, Manolo, Gabi, Olga, Rafa, Manuel, Miguel Ángel de Pablo y tantos compañeros que han estado ahí, no puedo ponerlos a todos, pero gracias Antárticos.

Gracias a mi familia del Master Mara, Alice, Flavio, Juan, Caro, yuyi, Patricia, Rafa, Vero y Martin gracias por acompañarme en las vicisitudes del mundo de la investigación, gracias por las cenas, por las barbacoas y los ratos de alegría.

Gracias a mi familia de Cádiz por llamarme, quererme, aguantarme y apoyarme durante todo este tiempo. Gracias por venir a visitarme y perdonarme que no vaya yo. Gracias Tamara, Luzma, Naza, Susana, Jesica y Vicente os veré pronto. Gracias a Mariela por todo su apoyo y hacer unas acuarelas preciosas a partir de fotos y dejar que la use para mi tesis.

Gracias a mi familia granaína a Laura, Pepa, Atxé, Caro, Al-les, Raquel, Javier, Sito y a tantos amigos que me han hecho reír cuando no tenía ganas, por dedicarme tiempo en los malos y buenos momentos. Gracias por acompañarme, apoyarme y compartirme con una tesis doctoral y en general por ser vosotras.

Gracias a mi tito Rafa y sus compañeros por su colaboración en desarrollar una idea, aunque finalmente no se haya incluido en este trabajo de investigación.

¡Gracias a mi familia que os quiero!! Gracias a mi yaya, a mi madre, a mis hermanas Teresa y Laura, a mi hermano Arturo, a mi cuñado Álvaro y a mis sobrinos. Gracias por vuestro amor y alegría. Gracias por tolerarme cuando estoy de mal humor, por respaldarme, por pelearme y perdonarme por pasar poco tiempo con ustedes.

Finalmente, muchas gracias a mi compañero de vida Javivi, gracias por el amor que me has dado estos años, gracias por levantarte cada mañana para hacerme el desayuno y poder pasar un rato juntos, gracias por estar ahí en los malos y buenos tiempos y en apoyarme en esta montaña rusa de emociones que te provoca el hacer una tesis doctoral, gracias cariño por todo.

Esta tesis doctoral ha sido parcialmente financiada por el Ministerio de Ciencia español a través de los proyectos CORSHET (POL2006-08663) y BRAVOSEIS (CTM2016-77315). Agradezco a todos los investigadores que han colaborado en el mantenimiento de las estaciones sísmicas permanentes desde 2008. Agradezco al programa de doctorado de Ciencias de la Tierra de la Universidad de Granada. También agradezco a mi tutor José Morales, a mi director Javier Almendros y al coordinador del programa de doctorado José Benavente.